



UNIVERSITÉ DU
LUXEMBOURG

PhD-FSTM-2025-110

Faculty of Science, Technology and Medicine

DISSERTATION

Defence held on 23 September 2025 in Esch-sur-Alzette

to obtain the degree of

DOCTEUR DE L'UNIVERSITÉ DU LUXEMBOURG EN PHYSIQUE

by

Ashwath Aravindhan

Born on 17 October 1997 in Chromepet, Tamil Nadu (India)

NONLINEAR PYROELECTRIC MATERIALS FOR ELECTRO-THERMAL ENERGY HARVESTING

Dissertation defence committee

Prof. Dr. Jorge Íñiguez-González, Chair

*Affiliate Professor, University of Luxembourg; Group leader Modelling of functional materials,
Luxembourg Institute of Science and Technology*

Prof. Dr. Gael Sebald, Vice Chair

Professor, INSA Lyon, CNRS; Tohoku University

Prof. Dr. Emmanuel Defay, Supervisor

*Affiliate Professor, University of Luxembourg; Head of Smart Materials Unit,
Luxembourg Institute of Science and Technology*

Prof. Dr. Brahim Dkhil,

Professor, CentraleSupélec, Université Paris-Saclay

Prof. Dr. Hana Uršič

Professor, Jožef Stefan Institute

Affidavit / Statement of originality

I declare that this thesis:

- is the result of my own work. Any contribution from any other party, and any use of generative artificial intelligence technologies have been duly cited and acknowledged;
- is not substantially the same as any other that I have submitted, and;
- is not being concurrently submitted for a degree, diploma or other qualification at the University of Luxembourg or any other University or similar institution except as specified in the text.

With my approval I furthermore confirm the following:

- I have adhered to the rules set out in the University of Luxembourg's Code of Conduct and the Doctoral Education Agreement (DEA)¹, in particular with regard to Research Integrity.
- I have documented all methods, data, and processes truthfully and fully.
- I have mentioned all the significant contributors to the work.
- I am aware that the work may be screened electronically for originality.

I acknowledge that if any issues are raised regarding good research practices based on the review of the thesis, the examination may be postponed pending the outcome of any investigation of such issues. If a degree was conferred, any such subsequently discovered issues may result in the cancellation of the degree.

Approved on 2025-08-14

Abstract

Nearly two-thirds of the global energy derived from primary resources is dissipated as low-grade waste heat, which remains a largely untapped source of recoverable energy. As global energy demand continues to increase, it is imperative to adopt alternative and sustainable energy conversion technologies that focus on reducing energy losses. One such technology is pyroelectric energy harvesting, which converts the heat directly into electrical energy by utilizing the intrinsic pyroelectric effect in certain polar dielectric materials. Moreover, this technology serves niche application areas where thermoelectric energy harvesting becomes ineffective, especially in harnessing low-grade heat. Unlike thermoelectric materials, which require a steady-state temperature difference, pyroelectric devices operate under temperature fluctuations, making them especially suitable for applications involving temperature variations over time. Although the concept of pyroelectric energy harvesting has been known for several decades, there is limited understanding of how nonlinear behaviour of pyroelectric materials, as a function of temperature and electric field, influences energy conversion performance.

This work investigates the nonlinear pyroelectric conversion potential of a prototypical pyroelectric material, lead scandium tantalate (PST) in different device geometries, from thin films to bulk samples. Despite its excellent electrocaloric and pyroelectric properties, PST thin films were not widely studied due to the challenges associated with high processing temperatures. In this work, the processing conditions were carefully optimized to yield high quality PST thin films. Indeed, thin films can withstand high electric fields which directly enhance the pyroelectric energy output and are also suitable for integration in microelectronic devices. High-quality PST thin films developed in this work achieved a pyroelectric energy density of up to $9 \text{ J}\cdot\text{cm}^{-3}$ under optimized thermal and electrical conditions. Furthermore, to expand the operating temperature range, the transition temperature of PST thin films was shifted to higher temperatures by systematically doping with Ti^{4+} ions.

While thin films offer numerous advantages, their limited active volume restricts their applicability in macroscopic energy harvesting systems. To overcome this challenge, the study expanded to include both PST bulk ceramics and PST multilayer capacitors (MLCs). These geometries benefit from high B-site cation ordering, resulting in a first-order phase transition and high pyroelectric coefficient. In addition to the detailed electrical characterizations, direct pyroelectric energy conversion cycles were implemented on PST MLCs using a dedicated experimental setup. The results indicate that PST MLCs can achieve a maximum of 50% Carnot efficiency for a 5 K temperature span near their phase transition temperature, compared to 22% achieved by PST bulk ceramics for a ΔT of 10 K at their transition. These results were obtained under the Olsen pyroelectric conversion cycle without any heat regeneration.

Based on these results, PST MLCs were selected to demonstrate two proofs of concept to highlight the practical feasibility of non-linear pyroelectric energy harvesting devices. First, a standalone autonomous pyroelectric energy harvester was developed using only two PST MLCs. The device automatically initiates the Stirling pyroelectric conversion cycle based on the temperature profile of the material obtained from a thermocouple and the energy harvested by the materials is reused to initiate successive cycles without drawing energy from external power sources. Following the same device concept, a macroscopic self-powered pyroelectric energy harvester consisting of 60 PST MLCs was developed. To successfully implement this system, a closed-loop fluidic control system was introduced for the first time, enabling nonlinear pyroelectric energy harvesting in a macroscopic device without relying on heat regeneration or large volumes of heat transfer fluid. The energy extracted from the device was used not only to sustain the autonomous operation of the device but also to continuously power an external Bluetooth communication module for more than 30 minutes, thereby demonstrating a fully self-sustaining pyroelectric energy harvesting device.

The results presented in this dissertation highlight the practical feasibility of nonlinear pyroelectric energy conversion, showing that high electrical output and efficiency can be achieved by carefully tuning both the material properties and the device architecture. Furthermore, the macroscopic self-powered pyroelectric energy harvester indicate that this technology can be used to develop autonomous devices or serve as a supplementary energy source to extend device lifetime by harnessing energy from ambient sources such as the ubiquitous waste heat. These outcomes not only open new avenues for real-world applications but also suggest that future efforts in nonlinear pyroelectric energy harvesting should shift from purely material-focused improvements toward system-level design and integration.

Acknowledgements

First and foremost, I would like to thank my PhD supervisor, Dr. Emmanuel Defay for his guidance and support throughout these years. I am deeply grateful for the opportunity to work on this fascinating topic. Thank you for your supervision, time, dedication, patience and most importantly your passion for research. I will carry forward all the valuable lessons I have learned from you over the years. I would also like to thank my co-supervisor, Dr. Veronika Kovacova for her continuous support. My journey in this group wouldn't have been possible without you, as you were the first person to give me the opportunity to step into the world of caloric materials. I have fond memories of my internship days, and I am very grateful for that opportunity and for your guidance along the way. Secondly, I would like to acknowledge the members of my doctoral thesis committee, Dr. Jorge Íñiguez and Dr. Gael Sebald. Thank you for your time, patience and constructive feedback, which helped me improve the quality of my work and also my scientific rigor.

I would like to extend my gratitude to all the former and present colleagues of the EC team, now changed to FMEH group. Thanks to Pierre Lhéritier and Àlvar Torelló, who introduced me to this topic and took the time to patiently explain me all the fundamentals. Thank you for being the foundation in my research journey, it was a pleasure to work alongside both of you and learn from your experience. I would also like to thank Youri Nouchokgwe for his invaluable guidance, scientific discussions and support throughout these years. Thank you for being a wonderful and considerate colleague, who constantly motivates everyone in the group. I will always cherish our conversations, the fun and laughter both at work and outside, and most importantly thank you for being a great gym bro, salsa teacher and a good friend.

Special thanks to Junning Li and Longfei Song for showing me the true meaning of hard work and perseverance. I am grateful to have had the opportunity to work with you guys and learn about prototyping. To Longfei, who has been like a brother and a close friend, thank you for constantly motivating me during the challenging days. I would like to thank you for involving me in your seminal work, which also gave me an opportunity to directly work on these exciting macroscopic devices. Thank you for all the great memories and hope our paths cross again in the future. I would also like to express my gratitude to the rest of the FMEH group members (Nischay Saurabh, Omar Ramirez, Uros Prah, Fan Ni, Moiz Khalil, Mayara Cardozo & Amandine Helt) for all the insightful scientific discussions, friendly banter and for maintaining a positive work environment. Furthermore, I would like to extend my appreciation to Oliver Bouton and Nouredine Bousri for their crucial assistance in prototyping. I thoroughly enjoyed working with both of you and learning throughout this duration. If it weren't for you guys, the project might have not been a success. A heartfelt thanks to both of you.

I extend my gratitude and appreciation to all the colleagues from the parent group, the ferroic materials group. Thanks to Dr. Sebastjan Glinsek for teaching me all the processing techniques related to ferroelectric thin film fabrication. Many thanks to Dr. Stéphanie Girod for teaching me lithography. Thank you, Steph, it was a pleasure to work with you on MLA in the clean room. I really appreciate it. I am also thankful to Dr. Torsten Granzow for his invaluable support, especially with the dielectric spectroscopy. Honestly, you saved me from 'reviewer 2' on more than one occasion, but truth be told, you were unofficially our 'reviewer 2'. On a serious note, thank you for teaching me about relaxor materials. I will remember our technical discussions and the funny movie references. I would also like to acknowledge other senior researchers Dr. Jorge Íñiguez, Dr. Hugo Aramberri and Dr. Natalya Fedorova for their technical and theoretical insights, particularly in the context of pyroelectric energy harvesting. In addition, I extend my thanks to Dr. Mael Guennou and his team for actively participating in all the technical meetings and discussions.

My appreciation also goes to the rest of the colleagues – Monica Graf, Binayak Mukherjee, Alfredo Martinez, Naveen Aruchamy, Cosme Milesi-Brault, Sangita Dutta, Christina Hill, Diana Murillo, Mauro Pulzone, Barnik Mandal, Krishna Patel, Nicolaei Cernov, Angelina Gudima, Georgy Gordeev, Suraj Manikandan, Mohamad Shoker, with whom I shared many pleasant conversations and some truly great memories. Thanks to Cosme for always including people and maintaining a positive work environment. I want to thank Sangita for being a positive role model and the best office mate. I would like to extend my heartfelt thanks to Nicolaei for his kind gesture that I will always remember and wishing you the best of luck with your thesis. I would also like to take a moment to thank my Corsica summer school buddies (Mauro, Angelina, Barnik, Binayak and Natalya) for making it such a memorable experience filled with both engaging technical discussions and fun memories. It was a pleasure guys.

I would also like to express my gratitude to other colleagues from LIST – Athira, Rakibul, Poorani, Marco, Alireza, Ashwini, Zahra, Vishnu, Andreas, Jonah, Leonard, Flavie, Arpan, and Ahilan for all the meaningful interactions and fun afterwork parties we have had throughout these years. Thank you, Marco, for all the fun memories and random conversations, I will always remember them. Thank you, Poorani for patiently listening to all my complaints and your friendly advice during challenging times. A special mention goes to Athira, Krishna, and Rakibul, who have not only been my closest friends but also treated me like family and helped me navigate this chapter of my life in Luxembourg. Thank you, guys, for everything.

My appreciation also goes to all the professors and teachers who directly or indirectly motivated me to pursue a PhD. Special thanks to Dr. Balasivanandha Prabu, who inspired me to pursue a master's degree in Europe. I still vividly remember all the concepts from nanostructured materials course. I would also like to thank Dr. Imants Dirba for placing his trust in me and giving me an opportunity to work with him in the functional materials group. Thank you, Imants, I really enjoyed working with you. Thanks to Dr. Mael Guennou and Dr. Jorge Íñiguez for teaching me about ferroelectrics. I can honestly say you that you

are among the best teachers I have ever had so far. I would also like to acknowledge our collaborator, Dr. Sakyō Hirose for providing us the gold standard PST MLCs. I extend the same gratitude to all the researchers I met during the course of this journey.

I also would like to thank my friends outside work, Vaidya, Ekaterina, Ali, Ariel, and Utkir for all the wonderful memories. I will cherish all our late night talks and banter. Also special thanks to Mrs. Veronika Wilhelm and her family for their genuine kindness and support. Thank you, Veronika, I will always remember your kind gesture when I first arrived in Luxembourg. Next, I would like to thank my cricket buddies – Naveen, Rishikesh, Neeraj, and Vijay for the fun and competitive matches that brought much needed work-life balance. Thanks to Ranjani, Namit and Lakshmi for their kindness and support. I would also like to thank my senior, Monish, who became a close friend over time. Your support and friendship meant a lot throughout this journey. Thank you for being both a good friend and a brother, always looking out for me. I am also grateful for all the spontaneous hiking trips, even if they ended in miserable fatigue, they gave us some unforgettable stories. I wish to extend my appreciation to Nagaarjhuna for his support and friendship. Thank you for all the pleasant memories. I would also like to acknowledge my peers from AMIS and FAME, especially Khasan and Akarshana for all the fun hiking trips and discussions. Likewise, I would like to extend my appreciation to my friends and peers from CEG for all the wonderful memories. I cannot finish this paragraph without thanking my childhood friends, Goutham, Surya and Durga for their support. Thank you for always wishing the best for me. I hope I did not miss out anyone in this list. In general, thanks to all my friends and acquaintances for all the nice moments.

Last but not least, I am deeply grateful to my family. I owe everything to my parents for their unwavering support, hard work, and countless sacrifices they made for me and my brother. None of this would have been possible without them. Thank you, Appa and Amma, for everything. I would also like to thank my little brother, Avinash, and my grandmother for their support and love. Honestly, I am at a loss for words to express the depth of love and gratitude I feel for my family and relatives.

Finally, I would like to acknowledge FNR Luxembourg for funding this project, University of Luxembourg and LIST for providing the necessary infrastructure and facilities to carry out this work with ease. I really appreciate it.

Table of Contents

Abstract	ii
List of figures.....	xii
List of tables.....	xix
Abbreviations and Notations.....	xx
1. Introduction	
1.1 Motivation	1
1.2 Research questions	5
1.3 Objectives and Structure of the thesis	5
2. Fundamentals of pyroelectric energy harvesting	
2.1 Phenomenology of polar materials.....	8
2.1.1 Pyroelectric effect	9
2.1.2 Correlation between pyroelectric and electrocaloric effect.....	10
2.1.3 Classification of ferroelectric, relaxor and anti-ferroelectric materials	11
2.2 Linear pyroelectric energy harvesting	12
2.3 Non-linear pyroelectric energy harvesting.....	13
2.3.1 Electro-thermodynamic cycles	13
2.3.2 Role of phase transition	19
2.3.3 Influence of material geometry	22
2.3.4 Nonlinear pyroelectric materials	24
2.3.5 Figures-of-merit.....	30
2.3.6 Effect of losses and material degradation.....	35
2.4 State-of-the-art pyroelectric energy harvesting devices	39
2.4.1 Principle of heat regeneration	39
2.4.2 Macroscopic pyroelectric energy harvesters	42
2.4.3 Role of thermal control devices.....	47
2.4.4 Significance of power interface systems	49
3. Pyroelectric conversion potential of pure and doped $\text{Pb}(\text{Sc}_{1/2}\text{Ta}_{1/2})\text{O}_3$ thin films	
3.1 Motivation	51
3.2 Lead Scandium Tantalate – $\text{Pb}(\text{Sc}_{1/2}\text{Ta}_{1/2})\text{O}_3$ (PST)	53
3.3 Preparation of PST solution and thin films	56
3.4 Results and discussion.....	59
3.4.1 XRD analysis	59
3.4.2 Microstructure analysis	60
3.4.3 Dielectric measurements and analysis	61
3.4.4 Maximum harvestable energy density.....	62

3.5	Ti-doped PST thin films.....	67
3.6	Synthesis of Ti-doped PST thin films	68
3.7	Results and discussion.....	69
3.7.1	XRD analysis	69
3.7.2	SEM analysis	70
3.7.3	Dielectric measurement.....	72
3.7.4	Pyroelectric energy density.....	76
3.7.5	Electrocaloric effect	77
3.7.6	Pyroelectric conversion efficiency.....	79
3.7.7	Multistage device using PSTT thin films: A conceptual study	81
4.	From thin films to bulk: Pyroelectric conversion efficiency of $\text{Pb}(\text{Sc}_{1/2}\text{Ta}_{1/2})\text{O}_3$ ceramics and multi-layer capacitors	
4.1	Motivation	85
4.2	Methods	87
4.2.1	Sample preparation and characterization.....	87
4.2.2	Nonlinear pyroelectric characterization setup.....	88
4.3	Investigation of PST bulk ceramics.....	90
4.3.1	Characterization of $D - E$ loops.....	90
4.3.2	Electrocaloric measurements	92
4.3.3	Pyroelectric efficiency of PST ceramic.....	93
4.4	Nonlinear pyroelectric performance of PST MLC.....	95
4.4.1	Permittivity measurements.....	95
4.4.2	Measurement of $D - E$ loops.....	95
4.4.3	Direct implementation of the Olsen cycle.....	97
4.4.4	Evaluation of the pyroelectric conversion efficiency	100
4.4.5	Pyroelectric efficiency of PST MLC at high electric fields.....	102
4.5	Influence of frequency on the performance of PST MLC	106
5.	Proof-of-concept: Pyroelectric energy harvesting devices using $\text{Pb}(\text{Sc}_{1/2}\text{Ta}_{1/2})\text{O}_3$ multi-layer capacitors	
5.1	Motivation	112
5.2	Stirling cycle.....	114
5.3	Autonomous pyroelectric energy harvester	119
5.3.1	Low-voltage converter.....	120
5.3.2	Description of the autonomous system.....	124
5.3.3	Results and discussion.....	127
5.4	Self-powered macroscopic pyroelectric energy harvester – GEN 1.....	129
5.4.1	Design of GEN 1	130
5.4.2	Autonomous system implementation	132
5.4.3	External communication module device	135

5.4.4 Overall power consumption of the demonstrator	136
5.4.5 Functioning of the self-powered pyroelectric energy harvester	139
5.5 Summary and conclusions	143
6. Conclusion and perspectives	
Future perspectives	147
Appendix A	
A.1 Chemical solution deposition	150
A.2 X-ray techniques	152
A.3 Scanning electron microscopy	153
A.4 Electrical characterization	154
A.5 Dielectric spectroscopy	156
A.6 Infrared thermography	158
Appendix B	
Appendix C	
C.1 Indirect estimation of Olsen cycles at low electric fields	164
C.2 Direct Olsen cycle under slow charging and discharging conditions	166
C.3 Direct Brayton cycle.....	167
PhD Output	169
References	171

List of figures

Figure 1.1 Annual number of scientific publications related to pyroelectric energy harvesting (1976–present), retrieved from the Dimensions bibliographic database using the keyword "pyroelectric energy" in titles and abstracts.	4
Figure 2.1 Temperature dependence of the spontaneous polarization and the absolute value of the zero-field pyroelectric coefficient of a ferroelectric dP_s/dT . Adapted from [17].	9
Figure 2.2 Heckmann diagram depicting the thermal, electrical, and mechanical coupling of a ferroelectric with respect to stress, strain, temperature, and electric field with the respective effects. Adapted from [20].	11
Figure 2.3 Schematic of linear pyroelectric energy conversion when the pyroelectric material is subjected to temperature fluctuations without a bias field. Figure reconstructed from [24].	13
Figure 2.4 Schematic representation of the entropy–temperature profile (left) and the electric displacement (D) – electric field (E) (right) for four thermodynamic cycles used in pyroelectric energy conversion: (a) Carnot, (b) Ericsson/Olsen, (c) Stirling, and (d) Brayton. $D - E$ loops were experimentally measured on PST multilayer capacitors and these graphs were taken from our previous work [30]. In the $D - E$ graphs, the colours represent isothermal curves (blue = cold, red = hot). The respective cycles are marked using a bold dark line with their cycle steps marked inside the graph. In the entropy–temperature diagrams, the two inclined lines represent the iso-field (at $E = 0$ and $E_{\max} > 0$) conditions.	19
Figure 2.5 Entropy versus temperature with and without an electric field, showing how a phase transition increases the energy harvesting area (large green area) compared to when no transition is present (small blue area). It must be noted that the ferroelectric (FE) – paraelectric (PE) transition varies according to the field. Adapted from [30].	20
Figure 2.6 Specific heat from iso-field DSC measurements on PST bulk ceramic showing a clear shift in the phase transition temperature. Adapted from [41].	22
Figure 2.7 Schematic of bulk ceramics (left), multilayer capacitor (middle) and thin films (right). The red and blue area represents the inactive and active regions respectively. The electrodes are marked with silver. Adapted from [49].	23
Figure 2.8 Schematic representation of P(VDF), P(VDF-TrFE) and P(VDF-TrFE) terpolymers. Adapted from [89].	29

Figure 2.9 Schematic representation of the non-linear figure of merit (FOM_e) from the $D - E$ loops.....	31
Figure 2.10 Schematic of unipolar $D-E$ loops for a ferroelectric with low hysteresis (left) and high hysteresis (right). The shaded area shows the harvested energy.....	35
Figure 2.11 Unipolar $D-E$ loops of PST MLC at different temperatures at 195 kV cm^{-1} . (b) Leakage current time evolution data of PST multilayer capacitors under the same field after fitting with Curie-von Schweidler empirical law. Adapted from [30].	37
Figure 2.12 Schematic of macroscopic degradation in ferroelectrics due to (a) aging - typical of acceptor doped materials (b) fatigue – predominant in donor doped materials. Adapted from [113].	37
Figure 2.13 (a) Energy and power densities generated by 9.5/65/35 PLZT as a function of cycle number. (b) $D-E$ loops of Olsen cycles collected after different numbers of cycles [63].	38
Figure 2.14 Illustration of three types of pyroelectric energy harvesting cycles: (a) non-regenerative, (b) passive regenerative, and (c) active regenerative. In (a) and (b), the arrow shows the movement of the green pyroelectric element from one end to other. In (c), the arrows indicate that the two steps repeat continuously.....	40
Figure 2.15 Schematic representation of cascaded or multistage pyroelectric energy harvester. The arrows means that the process is cycled.....	41
Figure 2.16 Schematic of macroscopic pyroelectric devices by Olsen et al. [28,116]: (a) regenerative device made of ceramic stacks and (b) isometric view of the ceramic stack used in the cascaded energy converter (redrawn for clarity).	42
Figure 2.17 Picture of PST MLCs assembled in the parallel plate heat exchanger configuration. Taken from [126].	44
Figure 2.18 (a) Experimental set-up of pyroelectric energy harvester based on 28 1-mm thick PST MLCs (4 rows \times 7 columns). (b) Energy harvested by the prototype for different temperature spans and input voltages. Adapted from [30].	44
Figure 2.19 Working principle of thermal diode/switch under Olsen pyroelectric cycle. .	49
Figure 2.20 (a) Circuit diagram of parallel SSHI device and (b) typical waveform [36].	50
Figure 3.1 Perovskite structure $A(B'B'')O_3$ of disordered and ordered PST (drawn using VESTA software [165]).	55

Figure 3.2 Spontaneous polarization change in disordered and ordered PST samples as a function of temperature (graph replotted from [154]).	55
Figure 3.3 (a) Spin coating process flow for fabricating PST thin films. (b) Schematic of an IDE configuration along with the optical microscopy image of a PST thin film patterned with platinum IDEs.	59
Figure 3.4 XRD pattern of sol-gel deposited PST thin film (a) $\theta - 2\theta$ scan at $\chi = 0^\circ$; (b) $\theta - 2\theta$ scan at $\chi = 54.7^\circ$.	60
Figure 3.5 SEM images of the PST thin film (a) Top-view; (b) Cross-section.	61
Figure 3.6 Temperature and frequency dependence of PST thin films (a) dielectric constant; (b) loss tangent.	61
Figure 3.7 Dielectric constant and loss tangent behaviour of PST thin films under different bias fields across various temperatures.	62
Figure 3.8 $D - E$ loop (in black) and $j - E$ loop (in red) of PST thin films.	63
Figure 3.9 Indirect estimation of energy density using Olsen cycle between 0°C and 100°C at different frequencies.	64
Figure 3.10 Maximum pyroelectric energy density in PST thin films using Olsen cycle between 0°C and 150°C .	65
Figure 3.11 (a) Schematic depicting the $(1-x)\text{PST} - (x)\text{PT}$ solid solution system [x : mole fraction of PT]; (b) Dielectric constant of poled $(1-x)\text{PST} - (x)\text{PT}$ specimens for $x = 0.3 - 0.5$ at 1 kHz. Adapted from [181].	68
Figure 3.12 (a) XRD pattern of PSTT thin films ($x = 0, 0.05, \text{ and } 0.1$) on c-sapphire substrate; (b) magnified image of (200) peak.	69
Figure 3.13 $\theta - 2\theta$ scans of PSTT thin films ($x = 0, 0.05, \text{ and } 0.1$) performed at different χ angles.	70
Figure 3.14 SEM images showing the top-view and cross section of PSTT thin films (a, b) $x = 0$; (c, d) $x = 0.05$; (e, f) $x = 0.1$.	71
Figure 3.15 Temperature dependent permittivity measurements of PSTT thin films at 1 kHz.	72
Figure 3.16 Dielectric constant (ϵ) and loss tangent ($\tan \delta$) values of PSTT thin films (a) $x = 0$, (b) $x = 0.05$, (c) $x = 0.1$, at different frequencies and temperatures.	74

Figure 3.17 Logarithmic plots of the reciprocal permittivity ($1/\varepsilon - 1/\varepsilon_m$) vs. temperature ($T - T_m$) at 1 kHz and 1 MHz of PSTT thin films (a) $x = 0$, (b) $x = 0.05$, and (c) $x = 0.1$	75
Figure 3.18 Bipolar $D - E$ loops (magnified) and energy densities of PSTT thin films: (a, b) $x = 0$, (c, d) $x = 0.05$, and (e, f) $x = 0.1$, at various initial temperatures and temperature spans for a ΔE of $560 \text{ kV}\cdot\text{cm}^{-1}$	77
Figure 3.19 ΔT_{ad} versus temperature of PST thin film for a ΔE of $667 \text{ kV}\cdot\text{cm}^{-1}$	78
Figure 3.20 Maximum polarization (P_{max}) and adiabatic temperature change (ΔT_{ad}) of PSTT thin films (a, b) $x = 0.05$; (c, d) $x = 0.1$ as a function of temperature.....	79
Figure 3.21 Efficiency and relative efficiency of PSTT thin films: (a, b) $x = 0$, (c, d) $x = 0.05$, and (e, f) $x = 0.1$, as a function of different temperature spans and initial temperature for a ΔE of $560 \text{ kV}\cdot\text{cm}^{-1}$	81
Figure 3.22 Energy densities of PSTT thin films ($x = 0, 0.05$, and 0.1) calculated using the Olsen cycle, as a function of the starting temperature for a ΔT_{span} of 20 K	82
Figure 3.23 A three-stage device composed of (a) undoped sample ($x = 0$) and (b) with $x = 0, 0.05$, and 0.1 operating at different temperatures in stages.....	83
Figure 4.1 Picture of the nonlinear pyroelectric characterization experimental setup (Insert) Top-view image of the Linkam temperature stage used for thermally cycling the material.....	89
Figure 4.2 $D - E$ loops of PST ceramic at 1 Hz measured from 20 to 60°C for a maximum ΔE of $130 \text{ kV}\cdot\text{cm}^{-1}$	91
Figure 4.3 Indirect estimation of pyroelectric energy density at 1 Hz for a ΔE of $130 \text{ kV}\cdot\text{cm}^{-1}$	91
Figure 4.4 Adiabatic temperature variation of PST bulk ceramic at 30°C as a function of different electric field. [<i>This measurement was performed by Dr. Uros Prah</i>].....	92
Figure 4.5 (a) Efficiency and (b) relative efficiency of PST ceramic using the Olsen cycle as a function of different temperature spans and initial temperatures.....	94
Figure 4.6 Relative permittivity and loss tangent measurements of 0.5 mm thick PST MLC performed at 1 kHz under a zero bias field condition. [<i>This measurement was performed by Dr. Uros Prah</i>].....	95
Figure 4.7 $D-E$ loops of 0.5 mm thick PST MLC for a ΔE of $130 \text{ kV}\cdot\text{cm}^{-1}$ at 1 Hz	96
Figure 4.8 Energy density estimation from the isothermal $D-E$ loops.....	96

Figure 4.9 (a) Voltage (in black) and current (in red) temporal profiles of the 0.5 mm thick PST MLC subjected to an Olsen cycle; (Insert) Zoomed in view of current vs time profile during the isoelectric heating phase. (b) Corresponding energy profile (in maroon) of the material as a function of time. The inserted numbers (1,2,3 and 4) correspond to the different steps of the Olsen cycle. Negative energy represents the harvested energy.....99

Figure 4.10 Correlation between indirect and direct Olsen cycle measurements on 0.5 mm thick PST MLC.....100

Figure 4.11 ECE of 0.5 mm thick PST MLC at a starting temperature of 30°C for different electric fields. [*This result is adapted from the supplementary information (Figure 12.2) of reference [30]*].100

Figure 4.12 (a) Efficiency and (b) relative efficiency of a 0.5 mm thick PST MLC under the Olsen cycle for different temperature spans and starting temperatures at 130 kV·cm⁻¹ and 1 Hz.....101

Figure 4.13 (a) Unipolar *D – E loops* of 0.5 mm thick PST MLC between 20 and 70°C for a ΔE of 205 kV·cm⁻¹ at 1 Hz. (b) Estimated energy density across different temperature spans and initial temperatures.102

Figure 4.14 (a) Temperature profile of the PST MLC undergoing Olsen cycle between 20 and 70°C; (b) Corresponding voltage and current profile of the sample during different stages of the Olsen cycle; (c) Energy profile of the sample throughout the cycle as a function of time.104

Figure 4.15 Comparison between directly implemented and indirectly estimated Olsen cycles for a 0.5 mm thick PST MLC at an initial temperature of 20 °C across different temperature spans (ΔT_{span}).....105

Figure 4.16 Estimated (a) η and (b) η_r of the 0.5 mm thick PST MLC under Olsen cycle at 1 Hz for a ΔE of 205 kV·cm⁻¹.....106

Figure 4.17 Adiabatic *D – E loops* (a) unipolar , (b) bipolar of 0.5 mm thick PST MLC measured at 10 Hz for a ΔE of 205 kV·cm⁻¹.....108

Figure 4.18 Pyroelectric energy density across different temperature spans and initial temperatures estimated from the bipolar *D – E loops* at 10 Hz and $\Delta E = 205$ kV·cm⁻¹. ...109

Figure 4.19 (a) η and (b) η_r of the 0.5 mm thick PST MLC under Brayton cycle at 10 Hz for a ΔE of 205 kV·cm⁻¹.110

Figure 5.1 Direct implementation of the Stirling cycle on 0.5 mm thick PST MLC between 5 and 95°C. (a) Voltage and current profile as a function of time (b) Energy profile as a function of time.116

Figure 5.2 Isothermal unipolar $D - E$ loops of 0.5 mm thick PST MLC measured at 5 and 95°C for an applied field of 170 kV·cm⁻¹. The blue region corresponds to the input energy. The blue and orange regions corresponds to the total energy output of the material and the orange area alone corresponds to the amount of harvested energy from heat.....116

Figure 5.3 (a) Electrical gain in 0.5 mm thick PST MLC under Stirling (in black) and Olsen (in red) cycle. (b) Estimated efficiency with respect to Carnot for the Stirling (in black) and Olsen (in red), as a function of the applied field.118

Figure 5.4 Energy harvested by 0.5 mm thick PST MLC under Stirling cycle across various temperature spans as a function of output voltage. The initial temperature was kept at 5°C and the input voltage was varied from 5 to 20 V, which are annotated with different symbols. The final temperature for each cycle is indicated by different colour legends. 120

Figure 5.5 Schematic of the low-voltage converter circuit drawn using LTspice software.121

Figure 5.6 Energy harvested by 0.5 mm-PST MLC (filled squares) and the energy stored in the capacitors (open squares) as a function of the output voltage during Stirling cycle operation at different temperature spans. The corresponding final temperatures for each cycle are indicated in the colour legend. The right Y-axis represents the percentage of transmitted energy from the PST MLC to the storage capacitor as a function of the final output voltage for each temperature span.122

Figure 5.7 Voltage profile of LTC 3588-1 DC/DC converter board monitored using the LabView software. The black line corresponds to the voltage of LTC board’s internal capacitor while the red line indicates the output voltage from the LTC board, which is at 3.6 V.....124

Figure 5.8 Overall schematic of the autonomous piezoelectric energy harvester.....124

Figure 5.9 Experimental set-up of the autonomous piezoelectric energy harvester: (a) the harvester block comprising of two 0.5 mm thick PST MLCs, (b) the autonomous control circuit with all components clearly labelled.....125

Figure 5.10 Power consumption of the autonomous system at different stages of the Stirling cycle.....127

Figure 5.11 Voltage profile of the storage capacitors (left – in blue) and two PST MLCs of 0.5 mm thickness (right – in red) as a function of time.....129

Figure 5.12 Voltage profile of the storage capacitors (left – in blue) and two PST MLCs of 1 mm thickness (right – in red) as a function of time.....129

Figure 5.13 Pictures of self-powered pyroelectric energy harvester. (a) Top view image of GEN 1, (b) Side view showing the stacked structure and spacing between MLCs (c, d) Experimental setup showing the enclosed prototype, peristaltic pump and solenoid valves.131

Figure 5.14 Schematic of the self-powered macroscopic pyroelectric energy harvester system.132

Figure 5.15 Experimental setup of the autonomous system board.....133

Figure 5.16 Photograph of the XIAO BLE-based communication module used as the external device, along with the custom-built application in the mobile to retrieve the data transmitted via Bluetooth by the device.136

Figure 5.17 Schematic of the power measurement setup used to evaluate the power consumption of both the autonomous system and the external BLE device.137

Figure 5.18 Measured power consumption values of (a) the autonomous system and (b) both the autonomous system and external BLE device as a function of time. Different events such as the wake up, charge and discharge steps are marked in the figure. The presence of smaller peaks in 5.18 (b) correspond to the communication bursts of the Bluetooth communication module.138

Figure 5.19 Experimental setup of the self-powered macroscopic pyroelectric energy harvester.140

Figure 5.20 (a) Inlet and outlet temperature profiles of GEN 1, (b) Magnified view on the right. (c) Voltage evolution of the storage capacitor, (d) Zoomed-in view of the voltage profile. (e) Voltage response of GEN 1 and (f) a magnified image, as a function of operating time.....142

Figure 5.21 Data transmitted by the low power consumption BLE communication module to the custom-built mobile application as a function of time.143

List of tables

Table 2.1 Performance of several non-linear pyroelectric materials when subjected to Olsen cycle.....	25
Table 2.2 Pyroelectric energy harvesting figures of merits for different materials.....	32
Table 2.3 Performance of pyroelectric energy harvesting devices when subjected to Olsen cycle.....	45
Table 3.1 Pyroelectric energy densities of various materials using the Olsen cycle.....	65
Table 3.2 Energy density of PSTT thin films ($x = 0, 0.05, \text{ and } 0.1$) when utilized as a three-stage pyroelectric converter across different temperature intervals (values taken from Figure 3.22).....	83
Table 4.1 Properties and dimensions of PST ceramics and 0.5 mm thick PST MLC respectively.	88

Abbreviations and Notations

PST	Lead Scandium Tantalate
PSTT	Titanium doped lead scandium tantalate
FE	Ferroelectric
PE	Paraelectric
RFE	Relaxor ferroelectric
PNRs	Polar nanoregions
Ω	Long range order parameter
T_c	Curie temperature
C_p	Specific heat capacity
C_E	Volumetric heat capacity
p	Pyroelectric coefficient
P_s	Spontaneous polarization
N_d	Pyroelectric energy density
P_d	Pyroelectric power density
α	Thermal diffusivity
K	Thermal conductivity
k^2	Electro-thermal coupling factor
CSD	Chemical solution deposition
2-MOE	2-methoxy ethanol
MePro	1-methoxy 2-propanol
SEM	Scanning electron microscopy
XRD	X-ray diffraction
MLC	Multilayer capacitor
SC	Single crystal
EC	Electrocaloric
Q_{EC}	Electrocaloric heat

ΔT_{ad}	Adiabatic temperature change
Q_{hot}	Additional heat contribution due to intrinsic electrocaloric effect
τ_{th}	Thermal time constant
IR	Infrared
IDE	Interdigitated electrode
FOM	Figure of merit
MC	Microcontroller
BLE	Bluetooth low energy
UVLO	Undervoltage lockout
RSSI	Received signal strength indicator
CMOS	Complementary metal-oxide-semiconductor

Chapter 1

Introduction

1.1 Motivation

With constant technological advancements, global energy demand and consumption continue to rise, highlighting the need for efficient energy generation strategies. This growing demand necessitates the exploration of alternative energy conversion methods that can utilize untapped energy sources and significantly reduce reliance on fossil fuels, which are inherently non-renewable. Despite increasing awareness of the limitations of fossil fuels, particularly in the context of global warming, they still account for approximately 80% of the world's primary energy supply [1]. In addition to environmental consequences, fossil fuel dependence increases vulnerability to geopolitical instability, driven by uneven global distribution and market volatility.

While renewable energy technologies are gaining attention, it is equally important to improve energy generation strategies and minimize energy losses. A significant portion of these losses occurs in the form of waste heat, which is released during various industrial and energy conversion processes. Despite being one of the most abundant byproducts of primary energy use, waste heat remains largely underutilized, representing a vast yet untapped resource with considerable potential for recovery and reuse. At present, approximately 72% of the energy produced from primary sources, predominantly fossil fuels, is lost as heat due to inefficiencies in industrial processes, transportation systems, and power generation systems [2]. Of this, nearly 63% is released as low grade waste heat, typically below 200°C, which has long been considered unrecoverable due to its limited potential for conversion into useful energy [2,3]. However, recent assessments indicate that if low and medium grade waste heat (< 500°C) were effectively recovered and transformed into electricity, it could produce up to 2.5 petawatt-hours of electrical energy annually, representing an economic potential of more than 300 billion euros when supplied to industrial consumers [3]. Furthermore, the global market for waste heat to power is expected to reach around 26 billion euros by 2025, reflecting the increasing interest in harnessing heat into a useful form of energy [3].

This context raises two critical questions:

- (1) Are there existing or emerging technologies capable of efficiently converting low grade waste heat directly into usable electrical energy?
- (2) Can such a technology be developed into a sustainable solution that is practical, scalable, and relevant for specific niche applications where conventional methods are inefficient or impractical?

Among existing technologies, thermoelectric energy harvesting remains the most mature and commercially adopted method for the direct conversion of thermal energy into electricity. Solid-state thermoelectric devices operate based on the Seebeck effect [4], wherein a temperature gradient across two junctions of a thermoelectric material induces the diffusion of charge carriers from the hot side to the cold side, thereby generating an electrical voltage [5,6]. However, the main limitation of thermoelectric materials is their low conversion efficiency, particularly at small temperature differentials, as the thermoelectric figure of merit (ZT) remains modest for most materials in the low temperature range. This constraint significantly limits their applicability in harvesting low grade waste heat. Additional challenges pertain to the requirement of imposing and sustaining a substantial spatial temperature gradient, which demands high heat fluxes due to the inherently high thermal conductivity of thermoelectric materials [7]. Furthermore, achieving high conversion efficiency necessitates not only a high ZT value but also optimized heat exchange conditions, both of which are difficult to maintain in practical low temperature energy harvesting scenarios [5,8].

Due to these limitations, particularly at lower temperatures, there is growing interest in alternative solid-state thermal energy harvesting technologies that do not depend on sustaining large spatial temperature gradients. Pyroelectric energy harvesting is one such technology, which utilizes the intrinsic pyroelectric effect in polar dielectric materials to generate electricity. Although the concept of pyroelectricity and the use of pyroelectric materials have been known for several decades, primarily in applications such as infrared sensing, fire detection, and thermal imaging [9], their potential to convert thermal energy into useful electrical energy remains largely unexplored. To directly convert thermal energy into electrical energy, pyroelectric materials must undergo temporal temperature fluctuations rather than a steady state spatial temperature gradient. When a pyroelectric material is heated or cooled, its intrinsic polarization (i.e. electric dipole moment per unit volume) changes due to the temperature dependence of the dipole alignment within the crystal lattice. This

change in polarization leads to a redistribution of bound charges at the surfaces of the material, resulting in an electric potential across the material. If the material is connected to an external circuit, this field drives the flow of free charges to maintain electrostatic equilibrium, thereby generating an electric current. The magnitude of this current is proportional to the rate of temperature change and the material's pyroelectric coefficient. Recent reports indicate that the conversion efficiency of pyroelectric materials can exceed that of thermoelectric counterparts under small temperature differentials, making them particularly well suited for the recovery of low temperature waste heat [7].

In this context, pyroelectric energy harvesting presents a niche application target where conventional energy conversion technologies face practical limitations. These include self-powered sensing systems in remote or inaccessible environments, low power electronics in industrial monitoring, wireless sensor networks, wearable or flexible devices, and embedded electronics in data centres [10]. In such settings, the intermittent and low intensity nature of available waste heat makes it difficult to maintain the spatial temperature gradients required by thermoelectric systems. Pyroelectric materials, by contrast, can respond effectively to temporal temperature fluctuations, allowing them to extract useful electrical energy even from low temperature variations that would otherwise be discarded. This opens new possibilities for integrating energy harvesting functionalities into compact and lightweight systems tailored for localized power generation. Moreover, by employing appropriate thermal control mechanisms [7], it is possible to convert a spatial temperature gradient into temporal temperature fluctuations, thereby enabling continuous operation of pyroelectric harvesters. This strategy not only facilitates scalability but also paves the way for the development of macroscopic pyroelectric devices. With further advancements, such systems could deliver power outputs in the range of several watts.

Despite their promise, pyroelectric energy harvesting has received relatively limited research attention compared to other thermal energy conversion approaches as shown in Figure 1.1.

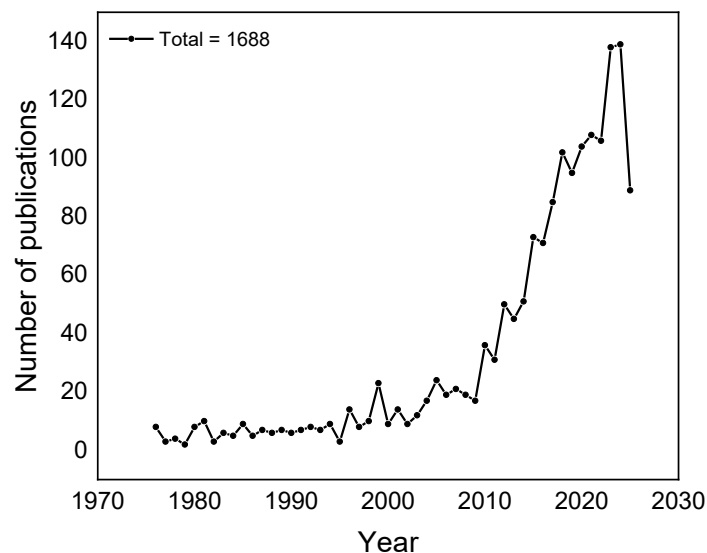


Figure 1.1 Annual number of scientific publications related to pyroelectric energy harvesting (1976–present), retrieved from the Dimensions bibliographic database using the keyword "pyroelectric energy" in titles and abstracts.

In recent years, there has been renewed interest in pyroelectric energy harvesting, largely driven by the development of advanced ferroelectric materials that exhibit high pyroelectric response and enhanced energy conversion capabilities. This resurgence is also attributed to the discovery of the giant electrocaloric effect [11,12] in certain ferroelectric materials in 2006, which is the thermodynamic inverse of the pyroelectric effect, where the application of an electric field induces a temperature variation in the material. By controlling the temperature- and field-dependent properties of ferroelectric materials, it is possible to execute a closed loop thermodynamic cycle, analogous to conventional heat engines, for converting thermal energy into useful work [13]. This approach forms the basis of nonlinear pyroelectric energy harvesting, in which the intrinsic nonlinear behaviour of ferroelectric materials with respect to temperature and electric field is harnessed to significantly enhance electrical work output.

While the direct use of the linear pyroelectric effect for energy harvesting has demonstrated potential, its practical viability remains limited by low power output. In contrast, nonlinear pyroelectric energy harvesting offers a more promising pathway, enabling higher work output by leveraging field-driven thermodynamic transitions. Nevertheless, research in this area is still in its early stages, with considerably fewer studies reported compared to linear pyroelectric energy harvesting. To address this gap, this thesis investigates the design, fabrication, and evaluation of nonlinear pyroelectric harvesters using advanced ferroelectric materials. The subsequent chapters present the theoretical background, material development, device architecture, and experimental results underpinning this work.

1.2 Research questions

The primary research questions of this doctoral dissertation are as follows:

- (1) Can nonlinear pyroelectric materials achieve high electrical work outputs i.e., pyroelectric energy densities greater than $5 \text{ J}\cdot\text{cm}^{-3}$ under optimized thermodynamic cycling conditions?
- (2) Can the conversion efficiency of nonlinear pyroelectric materials reach 50% of Carnot efficiency when subjected to a specific pyroelectric conversion cycle?
- (3) Can nonlinear pyroelectric materials be integrated into a macroscopic thermal energy harvester capable of continuously powering an external electronic device?

Addressing these research questions necessitates a multidisciplinary strategy that unifies material development, thermodynamic cycle design, and power interface optimization to develop a functional macroscopic pyroelectric energy harvester.

1.3 Objectives and Structure of the thesis

The main objective of this doctoral dissertation is to investigate the nonlinear pyroelectric conversion potential of $\text{Pb}(\text{Sc}_{1/2}\text{Ta}_{1/2})\text{O}_3$ (PST), which is an excellent pyroelectric material.

(1) High pyroelectric energy density:

To fabricate and characterize high-quality PST thin films exhibiting strong nonlinear pyroelectric response capable of delivering a harvestable energy density exceeding $5 \text{ J}\cdot\text{cm}^{-3}$ per cycle.

(2) Investigation of pyroelectric conversion efficiency:

To evaluate the pyroelectric conversion efficiency of PST in various geometries under different thermodynamic cycles and identify the configuration that achieves the highest efficiency relative to the Carnot limit.

(3) Develop a macroscopic pyroelectric energy harvester

To design and develop a macroscopic pyroelectric energy harvester based on PST multilayer capacitors and demonstrate its ability to continuously power an external electronic device as a proof of concept for the practical viability of this technology.

Based on these objectives, this dissertation is organized into six chapters.

Chapter 1 introduces the context and motivation for pyroelectric energy harvesting.

Chapter 2 presents the theoretical background, beginning with an overview of polar materials and the thermodynamic principles underlying the pyroelectric effect. It then discusses conventional (linear) energy harvesting, followed by a detailed examination of nonlinear energy harvesting, with emphasis on electro-thermodynamic cycles, phase transitions, geometric influences, and figures of merit for material selection. The chapter concludes with a review of current device-level implementations, including strategies for heat regeneration, macroscopic device implementation, and the integration of thermal control and power management systems.

Chapter 3 focuses on the nonlinear pyroelectric energy harvesting performance of PST thin films, aiming to address the research question concerning the maximum harvestable energy density achievable in this material system. PST thin films were fabricated using sol-gel synthesis and systematically characterized to evaluate their structural, dielectric, and ferroelectric properties. Furthermore, to examine whether the phase transition temperature could be tailored through chemical modification, PST was doped with Ti^{4+} at varying concentrations based on earlier reports. Additionally, a conceptual study was proposed to assess the potential of Ti-doped PST in multistage device architectures aimed at enhancing energy harvesting performance.

Chapter 4 investigates the pyroelectric conversion efficiency of PST bulk ceramics and multilayer capacitors. To this end, a nonlinear pyroelectric measurement setup was developed to directly implement thermodynamic cycles on these samples. The chapter examines how factors such as geometry, cycling frequency, and cation ordering influence the energy harvesting performance. In particular, the comparative analysis between bulk ceramics and 0.5 mm thick PST multilayer capacitors under Olsen cycle operation provides key insights into optimizing material configuration for high efficiency. The findings from this chapter specifically contribute toward addressing the second research question, concerning the achievable pyroelectric conversion efficiency relative to the Carnot limit.

Chapter 5 presents the design, development, and experimental demonstration of macroscopic pyroelectric energy harvesters based on PST multilayer capacitors. The chapter introduces an autonomous pyroelectric energy harvesting system, designed using only two PST multilayer capacitors as active materials. Building upon this initial system, a scaled-up, self-powered harvester comprising 60 PST multilayer capacitors is developed, demonstrating its capability to continuously power an external electronic device over several hours without external energy input. This chapter directly addresses the third research question by showcasing the practical feasibility

of nonlinear pyroelectric harvesting through the realization of functional macroscopic devices.

Chapter 6 provides a general conclusion along with a summary of the key findings from each chapter. Finally, future perspectives are discussed, highlighting potential research directions to further enhance the performance, scalability, and practical applicability of nonlinear pyroelectric energy harvesting systems.

The content of this dissertation is primarily based on my first-author publications, alongside other works to which I contributed significantly as a coauthor, particularly in the experimental design, implementation, investigation, analysis, and written contributions related to nonlinear pyroelectric energy harvesting systems. In addition to published works, the dissertation incorporates original, unpublished experimental results generated during the course of my doctoral research. This thesis follows a unified, monograph-style format while integrating and expanding upon key findings from these works. Each chapter begins with a short introduction outlining its scope and structure. Collaborative efforts are acknowledged where applicable, and all core conceptual, experimental, and analytical work presented herein represents my primary contribution. Additional experimental results relevant to this dissertation are included in the appendices.

Chapter 2

Fundamentals of pyroelectric energy harvesting

This chapter provides an overview of the fundamentals of pyroelectric energy harvesting. Section 2.1 discusses the phenomenology of polar materials, including key thermodynamic concepts. Section 2.2 outlines the principles of linear pyroelectric energy harvesting. Section 2.3 highlights the core concepts of nonlinear energy harvesting, focusing on electro-thermodynamic cycles, the role of phase transitions, geometric influences, nonlinear pyroelectric materials and relevant figures of merit for selecting them. Finally, Section 2.4 reviews state-of-the-art pyroelectric energy harvesting devices, covering heat regeneration strategies, macroscopic harvester designs, and the integration of thermal control components and power electronics systems.

The content presented in this chapter is based on my first-author publication, "*Converting Heat to Electricity with Non-Linear Pyroelectrics: A Review*", which is accepted for publication in International Materials Reviews.

2.1 Phenomenology of polar materials

Of the thirty-two crystallographic point groups, twenty-one are non-centrosymmetric, meaning they lack a centre of symmetry and possess one or more unique crystallographic axes. Among these, twenty classes exhibit the direct piezoelectric effect, whereby mechanical stress induces an electric polarization within the material. The sole exception is the cubic class 432, which, despite its non-centrosymmetric nature, does not exhibit piezoelectricity due to its high-symmetry configuration. Of the piezoelectric groups, ten are classified as polar, characterized by the presence of a spontaneous electric dipole moment even in the absence of external electric fields or mechanical forces. When the polar materials are subjected to a change in temperature, a variation in its spontaneous polarization occurs. This phenomenon is known as pyroelectricity.

If the spontaneous polarization can be switched by the application of an external electric field of sufficient magnitude, the material is designated as ferroelectric. This

class of materials exhibit reversible polarization states that can be switched by an external electric field. Moreover, these materials undergo a structural transformation from a high-symmetry, non-polar parent phase (paraelectric) to a low-symmetry, polar (ferroelectric) phase at a characteristic temperature known as the Curie temperature T_c [14]. These materials are intrinsically both piezoelectric and pyroelectric, although the converse does not necessarily hold true. Moreover, ferroelectric materials possess a higher piezoelectric and pyroelectric effect compared to non-ferroelectric pyroelectric materials such as zinc oxide [14–16]. Hence, the discussions in this chapter will focus primarily on ferroelectric materials, particularly in the context of thermal energy harvesting.

2.1.1 Pyroelectric effect

As mentioned earlier, ferroelectric pyroelectric materials exhibit a change in spontaneous polarization when subjected to a temperature variation, which is known as the pyroelectric effect. This effect can be quantified using the pyroelectric coefficient (p), which is defined as:

$$dP_s = p dT \quad (2.1)$$

The temperature dependence of spontaneous polarization and pyroelectric coefficient (p) of a ferroelectric material is shown in Figure 2.1. As the material reaches the T_c , the polarization rapidly decreases resulting in a significant rise in p .

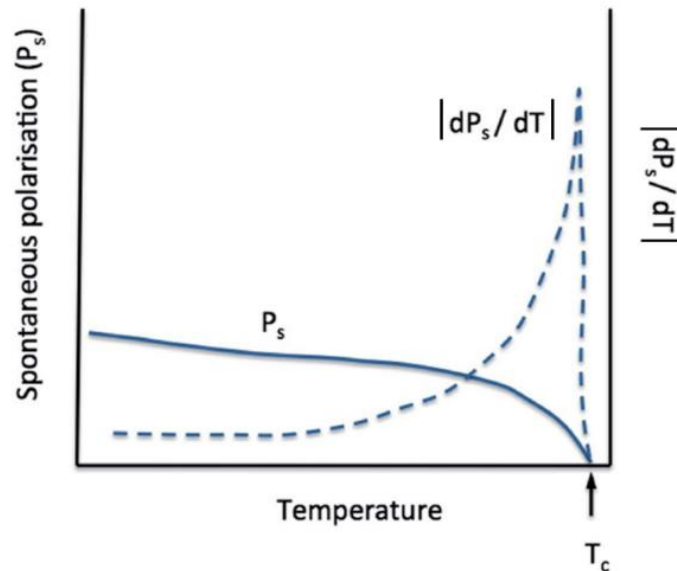


Figure 2.1 Temperature dependence of the spontaneous polarization and the absolute value of the zero-field pyroelectric coefficient of a ferroelectric dP_s/dT . Adapted from [17].

2.1.2 Correlation between pyroelectric and electrocaloric effect

To better understand the behaviour of ferroelectric materials and their coupling between thermal, elastic, and electrical properties, it is beneficial to review the thermodynamics of ferroelectrics. Here, the discussion is limited to electro-thermal coupling. The total free energy density G of a simple 1D dielectric is:

$$G = U - TS - xX - ED \quad (2.2)$$

where U is internal energy, S is entropy, T is temperature, X is stress, x is strain, D is electric displacement ($D = \epsilon_0 E + P$ where ϵ_0 is the vacuum permittivity) and E electric field. The interest of using G rather than U stems from the fact that it is practical to use T and E as variables rather than S and D . This is called a Legendre transformation of free energy [18]. Note that here we use D and not P in the description of the free energy¹, though it is very common in ferroelectric materials to consider that $D \sim P$.

As $dU = TdS + Xdx + EdD$ (intensive variable times differential extensive variable), the differential form of Gibbs' free energy becomes

$$dG = -SdT - xdX - DdE \quad (2.3)$$

From the above equations and the following state equations, the differential form of Gibbs' free energy is re-written with respect to T , E and X to obtain the Maxwell thermodynamic relations as follows:

$$dG = \left(\frac{\partial G}{\partial X}\right)_{E,T} dX + \left(\frac{\partial G}{\partial E}\right)_{X,T} dE + \left(\frac{\partial G}{\partial T}\right)_{E,X} dT \quad (2.4)$$

$$-S = \left(\frac{\partial G}{\partial T}\right)_{X,E} \quad ; \quad -D = \left(\frac{\partial G}{\partial E}\right)_{X,T} \quad (2.5)$$

$$\left(\frac{\partial^2 G}{\partial E \partial T}\right)_X = \left(\frac{\partial D}{\partial T}\right)_{E,X} = \left(\frac{\partial S}{\partial E}\right)_{X,T} = p^{E,X} \quad (2.6)$$

where the pyroelectric coefficient p indicates the coupling between temperature and dielectric displacement. From Equation (2.6), we can understand the correlations between the pyroelectric effect and its conjugate, the electrocaloric effect [19], which enables the generation of a temperature variation by the application of an electric field. In other words, a good electrocaloric material inherently qualifies as an excellent pyroelectric material. The correlation between piezoelectric, pyroelectric and thermoelastic properties of a ferroelectric material can be understood from the Heckmann diagram as shown in Figure 2.2.

¹ In a dielectric material, the electric displacement (D) and polarization (P) are related by the expression $D = \epsilon_0 E + P$, where $P = \epsilon_0 \chi E$ denotes the electric susceptibility. In ceramic ferroelectrics, the susceptibility $\chi \gg 1$ [215], implying that $D \cong P$.

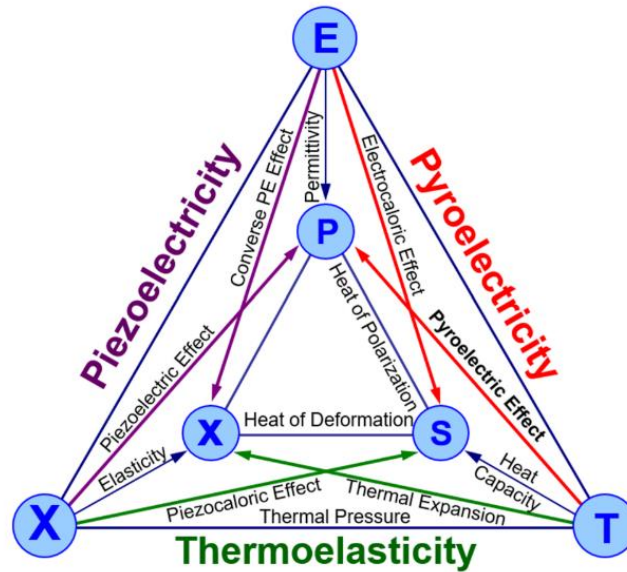


Figure 2.2 Heckmann diagram depicting the thermal, electrical, and mechanical coupling of a ferroelectric with respect to stress, strain, temperature, and electric field with the respective effects. Adapted from [20].

2.1.3 Classification of ferroelectric, relaxor and anti-ferroelectric materials

Understanding the distinctions among ferroelectric, relaxor, and antiferroelectric materials is critical for selecting suitable candidates for pyroelectric energy harvesting. Each material class exhibits unique dielectric and thermodynamic properties, significantly influencing their suitability for various applications, especially those involving thermal-to-electrical energy conversion.

Ferroelectric materials, as introduced previously, are characterized by a spontaneous electric polarization that can be reversed through the application of an external electric field. These materials can exhibit a first order transition (discontinuous change in polarization) or a second order (continuous change in polarization) phase transition. Typically, ferroelectric exhibiting first order transition are widely investigated due to their pronounced changes in polarization, dielectric permittivity, and pyroelectric response near T_c . Classic examples include barium titanate (BaTiO_3), and lead zirconate titanate (PZT).

Relaxor ferroelectrics represent a subclass of polar dielectrics characterized by diffuse phase transitions and frequency-dependent dielectric responses. Unlike conventional ferroelectrics, relaxors do not have a sharply defined Curie temperature. Instead, their dielectric permittivity peaks over a broad temperature range, with the peak temperature shifting with measurement frequency. The underlying reason for this behaviour is the presence of nanoscale polar regions or polar nanoregions (PNRs) that dynamically fluctuate in size and orientation. These dynamic heterogeneities are

responsible for the highly dispersive dielectric and piezoelectric properties observed in relaxors. Prominent examples include lead magnesium niobate–lead titanate (PMN-PT) and lead lanthanum zirconate titanate (PLZT).

Antiferroelectric materials, in contrast, exhibit a spontaneous antiparallel arrangement of dipoles, resulting in a macroscopically net-zero polarization at equilibrium. However, these materials can transition to a ferroelectric state under an applied external electric field of sufficient magnitude, leading to a reversible double-hysteresis loop. Such field-induced transitions from antiferroelectric to ferroelectric states are accompanied by large polarization changes, making antiferroelectric materials appealing for applications requiring high energy densities, such as electrocaloric cooling and energy storage. Notable examples include lead zirconate (PbZrO₃)-based antiferroelectrics and certain doped ceramics derived from this family.

Thus, recognizing and categorizing the distinctive thermodynamic and dielectric features of these three classes of polar materials enables strategic material selection and optimization in pyroelectric energy harvesting systems, as explored in the subsequent sections.

2.2 Linear pyroelectric energy harvesting

Linear pyroelectric energy harvesting consists of subjecting the pyroelectric material to cyclic temperature variations in the absence of a bias electric field [21]. As implied by the term “linear,” this method leverages the linear behaviour of the material to harness heat into electricity. Hence the temperature variations are limited to few tens of degrees (typically around $\pm 10^\circ\text{C}$). Figure 2.3 shows the principle of linear pyroelectric energy conversion, where electrodes are placed perpendicular to the polarization axis, allowing the pyroelectric coefficient (p) to be treated as a scalar.

When the material is at thermal equilibrium, there is no flow of charges from the materials to the external circuit. However, when the material is heated, the spontaneous polarization of the material decreases, resulting in a pyroelectric short-circuit current (i_p) flowing through the circuit, which is as follows:

$$i_p = Ap(T) \frac{dT}{dt} \quad (2.7)$$

where dT/dt is the rate of change of temperature T with time t and A corresponds to the surface area. Similarly, when the material is cooled, the spontaneous polarization of the material increases resulting the flow of current in the opposite direction. Here,

i_p is proportional to $\left(\frac{dT}{dt}\right)$, which has been widely exploited for a range of applications including heat sensing, thermal imaging and infrared detectors [22,23].

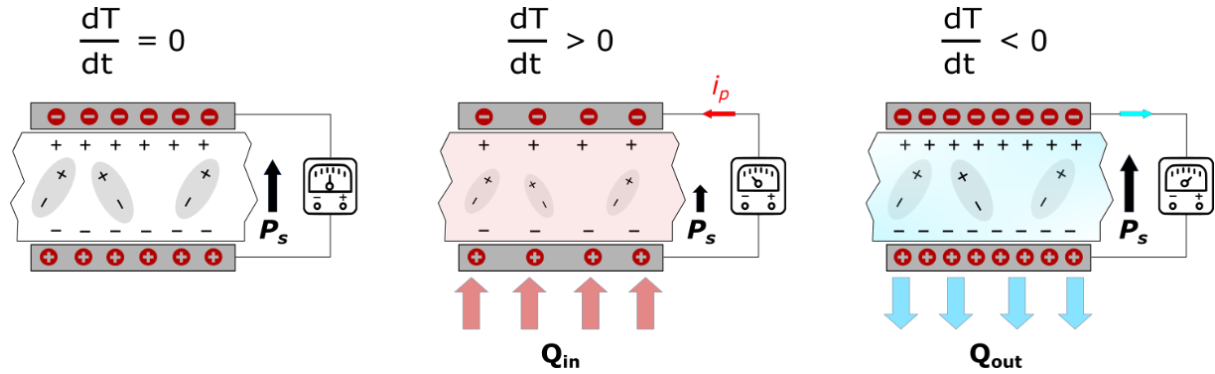


Figure 2.3 Schematic of linear pyroelectric energy conversion when the pyroelectric material is subjected to temperature fluctuations without a bias field. Figure reconstructed from [24].

While linear pyroelectric energy harvesting provides a straightforward approach by relying solely on temperature-induced polarization changes without external electric fields, its output is inherently limited due to the relatively small polarization variation over modest temperature swings. In contrast, non-linear pyroelectric energy conversion exploits the strong, field-enhanced polarization changes near the ferroelectric (FE) – paraelectric (PE) phase transition, enabling much higher energy output [25,26]. This makes non-linear methods more suitable for efficient thermal-to-electrical conversion, as discussed in the following section.

2.3 Non-linear pyroelectric energy harvesting

In contrast to linear energy harvesting, nonlinear pyroelectric materials are subjected to thermal cycling under a bias electric field. By leveraging their strong dependence on both temperature and electric field, the material can be driven sequentially in a clockwise manner to establish a closed thermodynamic cycle in electric displacement and electric field. These cycles are not confined to narrow temperature spans and typically encompass the phase transition of the material. This approach exploits the significant polarization changes that occur near phase transitions, which may be induced by temperature variations, mechanical stress, or strong electric fields.

2.3.1 Electro-thermodynamic cycles

Several thermodynamic cycles can be adapted for pyroelectric energy harvesting by coupling thermal and electrical variables. These cycles, originally developed for mechanical heat engines, can be reinterpreted for pyroelectric systems by drawing analogies: voltage is analogous to the pressure, and electric displacement is equivalent to the volume.

In this framework, the behaviour of pyroelectric materials can be described thermodynamically by considering only thermal and electrical contributions. The differential form of internal energy is given by:

$$dU = \delta W + \delta Q = T dS + E dD \quad (2.8)$$

where U denotes the internal energy, S represents the entropy, T is the temperature, D is the electric displacement, E is the electric field while W and Q correspond to the electrical work and isothermal heat respectively. Here, T and E are intensive variables, whereas S and D are extensive. The electrical work per cycle is expressed as $W = \oint E dD$, and the heat exchanged is $Q = \oint T dS$.

a) Carnot cycle

To directly convert the heat into electricity, Froom was the first to envision an electrical analogue of the Carnot cycle based on the $D - E$ characteristics of a polar dielectric material [27]. The pyroelectric Carnot cycle consists of two isothermal (1 – 2 , and 3 – 4) and two adiabatic (2 – 3 , and 4 – 1) steps, forming a closed thermodynamic cycle. This cycle is best visualized through the entropy vs temperature diagram and the $D - E$ loops of a ferroelectric material, which together illustrate the electro – thermodynamic path followed by the material for energy conversion, as shown in Figure 2.4 (a). Initially, at step 1 – 2, the electric field is increased while the material is maintained in thermal contact with a cold reservoir at a constant temperature T_1 , resulting in isothermal charging. In the next step (2 – 3), the system is thermally isolated, and the electric field is further increased rapidly. This adiabatic process leads to a rise in temperature to T_2 due to the electrocaloric effect (ECE), while the entropy of the system remains constant. At point 3, the material is brought into contact with a heat source at T_2 , and the electric field is gradually reduced, allowing isothermal heat exchange (3 – 4). This step corresponds to the warm isothermal step. Finally, the field is further decreased under adiabatic conditions while thermally isolating the material, causing it to cool back down to T_1 (4 – 1), and complete the electro-thermodynamic cycle [9].

The efficiency η_{Carnot} of this cycle is defined as the ratio of the electrical work W generated per cycle to the heat input Q required to complete the cycle. The work output is given by $W = \oint E dD = \Delta S \cdot \Delta T$, while the heat absorbed during the warm isothermal step is $Q = \Delta S \cdot T_{hot}$. Therefore, the η_{Carnot} is expressed as:

$$\eta_{Carnot} = \frac{W}{Q} = \frac{\Delta S \Delta T}{T_{hot} \Delta S} = \frac{\Delta T}{T_{hot}} = 1 - \frac{T_{cold}}{T_{hot}} \quad (2.9)$$

By definition, the Carnot cycle represents the theoretical upper limit of efficiency for any thermodynamic system converting heat into useful work. This idealized cycle depends solely on the temperatures of the hot and cold reservoirs, as the material

reaches thermal equilibrium with the hot source through adiabatic heating during step 2 – 3. This feature gives the Carnot cycle its distinct rectangular form in the entropy vs temperature diagram, which is not achievable in other thermodynamic cycles.

Indeed, Carnot cycle is an ideal cycle which assumes a completely reversible system without any losses. But in reality, it is very challenging to achieve a Carnot cycle due to these reasons:

- 1) The achievable temperature difference between the cold and hot reservoirs is limited by the magnitude of the material's adiabatic temperature variation due to its ECE, which typically spans only a few degrees. Besides, it is extremely challenging to achieve an isentropic condition (i.e., reversible and adiabatic response) as there will be heat transfer with the surroundings after a period of time. Hence, it is only possible to achieve near-adiabatic condition and there will be irreversible losses in the material due to hysteresis.
- 2) Achieving perfect isothermal conditions necessitates infinitely slow transitions, which is not practical for device operation.

While the Carnot cycle provides a valuable theoretical benchmark, practical systems often employ alternative thermodynamic cycles that better balance efficiency and power output. However, it is possible to theoretically reach close to Carnot efficiency using other thermodynamic cycles by implementing heat regeneration, which allows the system to recover and reuse thermal energy internally, thereby minimizing losses and improving overall performance. This will be detailed in the next section.

b) Olsen (electrical Ericsson) cycle

Olsen cycle can be considered as the electrical analogue of the Ericsson cycle, thereby constituting two isothermal (1 – 2, and 3 – 4) and two isoelectric (2 – 3, and 3 – 4) steps as shown in Figure 2.4 (b). In the Olsen cycle, the material is first charged isothermally at a low temperature T_1 (Step: 1 – 2). This is followed by heating to a higher temperature T_3 under constant electric field application, corresponding to the isoelectric step (Step: 2 – 3). At high temperature, the sample is discharged isothermally (Step: 3 – 4). The cycle is completed by cooling the material at a constant electric field (isoelectric condition) back to the initial state (Step: 4 – 1). This cycle was originally proposed and implemented by Olsen [28], who also pioneered the concept of heat regeneration in nonlinear pyroelectric energy harvesting devices. This topic will be covered in the following section.

One of the main challenges in realizing the Olsen cycle experimentally is maintaining true isothermal conditions during both charging and discharging stages. Nevertheless, studies have shown that the Olsen cycle can outperform most other

pyroelectric cycles in terms of electrical work output, even when operated under quasi-isothermal conditions. The net energy harvested per cycle, or electrical energy density N_d , is represented by the area enclosed in the D - E loop (see Figure 2.4. (b)) and is calculated as:

$$N_d = \oint E dD \quad (2.10)$$

The corresponding power output is given by $P_d = N_d \cdot f$, where f is the cycle frequency. To achieve high energy output, the ferroelectric material must possess a high dielectric breakdown strength and exhibit a large variation in electric displacement D .

The conversion efficiency of the Olsen cycle, η_{Olsen} is as follows:

$$\eta_{Olsen} = \frac{\oint E dD}{\int_{T_{cold}}^{T_{hot}} C_p dT + Q_{hot}} \quad (2.11)$$

Here, C_p denotes the specific heat capacity of the material, and Q_{hot} refers to the heat exchanged during the isothermal discharge at high temperature. The first term in the denominator represents the heat required to raise the temperature of active material from T_{cold} to T_{hot} while the second term accounts for the entropy-driven heat exchange during the discharge phase. This entropy change can be experimentally determined through calorimetric measurements, especially in materials exhibiting strong electrocaloric effects. To assess the performance of the Olsen cycle relative to the Carnot limit, a scaled or relative efficiency $\eta_{Olsen,r}$ is defined as:

$$\eta_{Olsen,r} = \frac{\eta_{Olsen}}{\eta_{Carnot}} = \frac{\oint E dD}{\int_{T_{cold}}^{T_{hot}} C_p dT + Q_{hot}} \left(\frac{T_{hot}}{\Delta T} \right) \quad (2.12)$$

c) Stirling cycle

The Stirling cycle, illustrated in Figure 2.4 (c), consists of two isothermal (1 – 2, and 3 – 4) and two iso-displacement steps (2 – 3, and 3 – 4). The pyroelectric Stirling cycle was first experimentally demonstrated by Childress [29]. It begins with isothermal charging at a lower temperature T_1 (step 1 – 2). Following this, the system is heated under open-circuit conditions, maintaining constant charge and thus constant electric displacement (2 – 3). Once the material reaches the higher temperature T_3 , it undergoes isothermal discharging (3 – 4), and the cycle is completed by cooling under open circuit condition (4 – 1).

One of the main practical challenges in applying the Stirling cycle lies in the substantial voltage increase that occurs during the constant-charge heating step, which can potentially exceed the dielectric breakdown strength of the material. Despite this, it has been shown that, with proper optimization of the electric field input and operating temperature range, the Stirling cycle can be implemented effectively in

practical devices [30]. An additional advantage of this cycle is its low input energy requirement to initiate operation, particularly due to the inherent voltage amplification step during the iso-displacement heating phase of the cycle.

The efficiency and relative efficiency of the Stirling cycle can be evaluated using the same expression applied to the Olsen cycle:

$$\eta_{Stirling} = \frac{\oint E dD}{\int_{T_{cold}}^{T_{hot}} C_p dT + Q_{hot}} \quad (2.13)$$

$$\eta_{Stirling,r} = \frac{\eta_{Stirling}}{\eta_{Carnot}} = \frac{\oint E dD}{\int_{T_{cold}}^{T_{hot}} C_p dT + Q_{hot}} \left(\frac{T_{hot}}{\Delta T} \right) \quad (2.14)$$

Moreover, it has been reported that the Stirling cycle is capable of achieving ideal heat regeneration, in contrast to the Olsen cycle. This advantage arises because, during the iso-displacement steps of the Stirling cycle, the specific heat capacity depends solely on temperature. In comparison, the Olsen cycle involves iso-electric field processes, where the specific heat varies with both temperature and electric field, leading to unequal heat transfer during the regenerative steps, leading to increased thermal losses [31,32].

d) Brayton cycle

The Brayton cycle, illustrated in Figure 2.4 (d), is composed of two adiabatic steps (1 – 2 , and 3 – 4) and two isoelectric steps (2 – 3, and 3 – 4). The cycle begins with adiabatic charging (step 1 – 2) of the pyroelectric material at an initial temperature T_1 , which results in a temperature increase to T_2 due to the electrocaloric effect (based on the assumption that the material exhibits a positive electrocaloric response). This is followed by isoelectric heating from T_2 to a higher temperature T_3 (step 2 – 3), during which external heat must be supplied. The heat input required for this step is $\int_{T_2}^{T_3} C_p dT$. After reaching the high temperature T_3 , the material is discharged adiabatically (step 3 – 4), resulting in a temperature drop, followed by isoelectric cooling (step 4 – 1) to return the system to its initial state and complete the cycle. The pyroelectric conversion efficiency of the Brayton cycle is as follows:

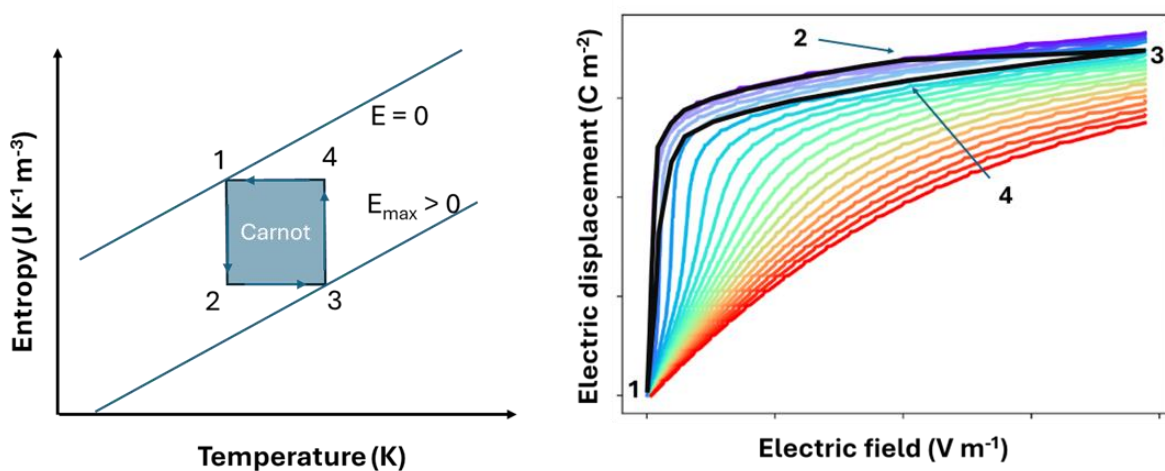
$$\eta_{Brayton} = \frac{\oint E dD}{\int_{T_2}^{T_3} C_p dT} \quad (2.15)$$

Since the material reaches adiabatic conditions during the charge and discharge steps, which implies no heat exchange between the material and the heat source, the additional heat associated with dipolar entropy change (the electrocaloric effect) is not considered for efficiency calculations. Similar to the Olsen cycle, the relative or scaled efficiency of the Brayton cycle can be defined by normalizing its actual efficiency to the Carnot limit:

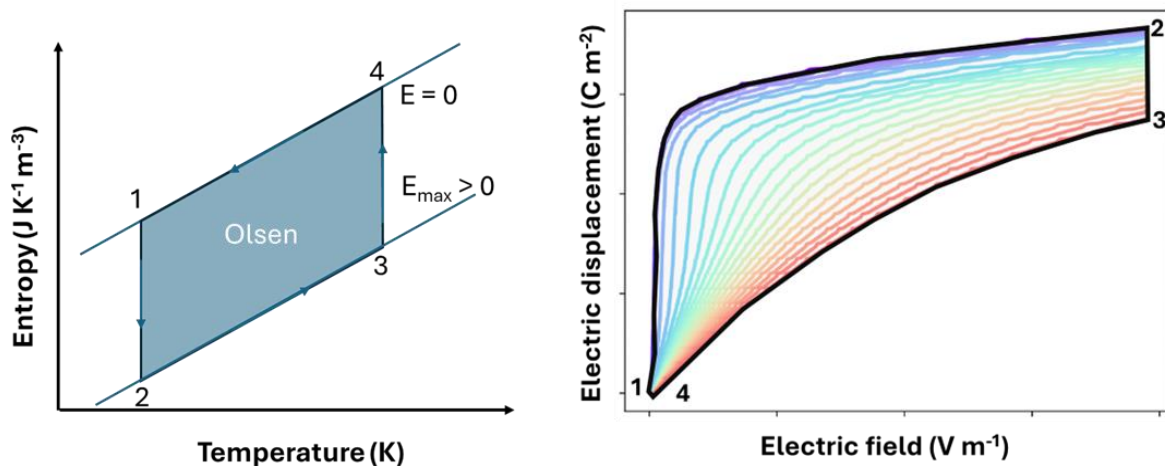
$$\eta_{Brayton,r} = \frac{\eta_{Brayton}}{\eta_{Carnot}} \quad (2.16)$$

Recently, Hanrahan et al.[33] investigated the pyroelectric performance of the Brayton and Olsen cycles using thin-film pyroelectric materials across a range of operating frequencies. Owing to the low thermal mass of these films, rapid thermal cycling was achievable. Their study demonstrated that the Brayton cycle outperformed the Olsen cycle in terms of power output at higher frequencies. This advantage was attributed to the rate-limiting nature of the isothermal steps in the Olsen cycle, which constrain its effectiveness under fast cycling conditions.

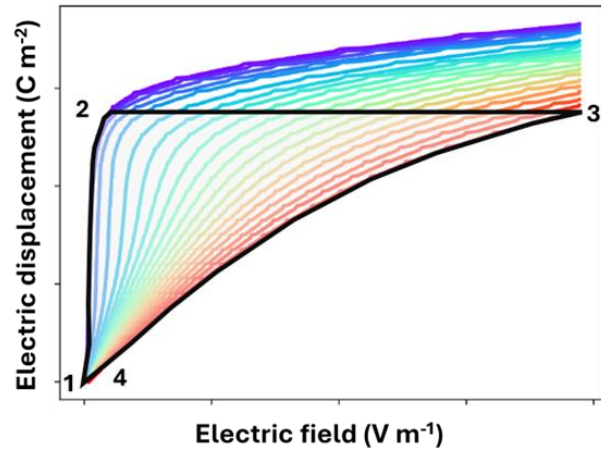
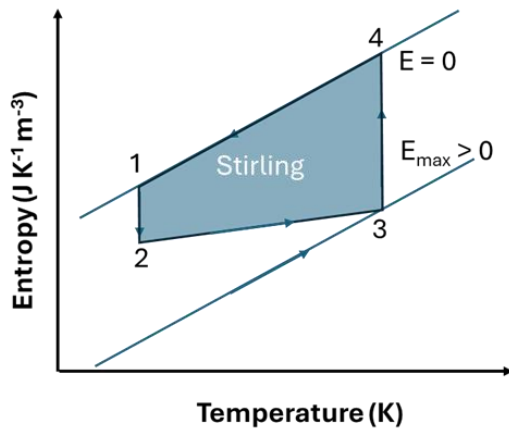
a) Carnot



b) Ericsson/Olsen



c) Stirling



d) Brayton

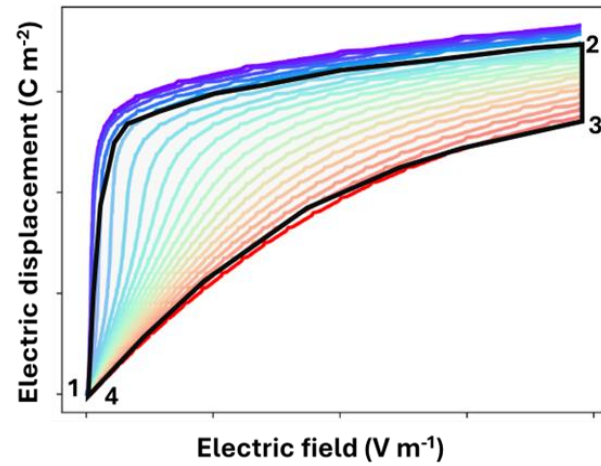
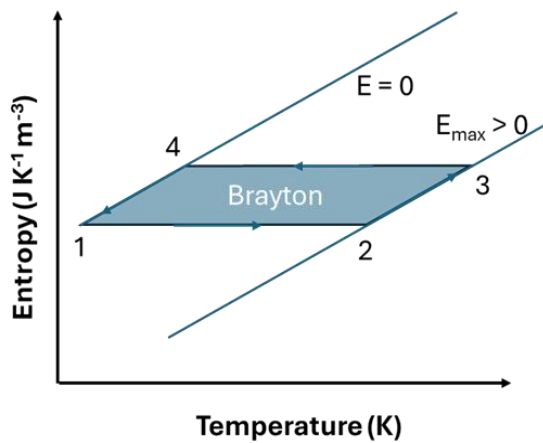


Figure 2.4 Schematic representation of the entropy–temperature profile (left) and the electric displacement (D) – electric field (E) (right) for four thermodynamic cycles used in pyroelectric energy conversion: (a) Carnot, (b) Ericsson/Olsen, (c) Stirling, and (d) Brayton. $D - E$ loops were experimentally measured on PST multilayer capacitors and these graphs were taken from our previous work [30]. In the $D - E$ graphs, the colours represent isothermal curves (blue = cold, red = hot). The respective cycles are marked using a bold dark line with their cycle steps marked inside the graph. In the entropy–temperature diagrams, the two inclined lines represent the iso-field (at $E = 0$ and $E_{\max} > 0$) conditions.

2.3.2 Role of phase transition

From the earlier sections, it is evident that to achieve maximum pyroelectric energy output, the material must be operated near its phase transition temperature. In this temperature region, substantial variations in entropy and polarization occur, significantly enhancing the harvested energy per cycle. Although the importance of

phase transitions was initially highlighted through $D - E$ loops, deeper insights can be gained by examining these processes using entropy–temperature ($S-T$) diagrams. This approach, initially proposed by Olsen et al. [34,35] and thoroughly examined by Sebald et al. [36] clearly illustrates how phase transitions influence the energy-harvesting capacity, as also emphasized by Guyomar et al.[37,38].

In a typical pyroelectric energy-harvesting cycle represented in Figure 2.5, the material starts at point A at low temperature with zero electric field. Upon applying an electric field at this temperature, the material transitions to a polarized state at point B. The temperature is then increased to a higher value at point C while maintaining the electric field. At the elevated temperature, energy is harvested by removing the electric field, bringing the system to point D. Finally, the cycle completes as the material cools back to point A. The enclosed area in the $S-T$ diagram represents the harvested energy, highlighting the importance of maximizing this area.

As depicted in Figure 2.5, the transition between ferroelectric (FE) and paraelectric (PE) phases involves a pronounced entropy increase. This transition can be shifted to higher temperatures by applying an external electric field, as indicated by the shift from the black curve (zero field) to the orange curve (non-zero field). Positioning the thermodynamic cycle within this field-induced transition region (green area) greatly enhances the harvestable energy compared to cycles occurring outside this region (blue area). Such cycles must run counter-clockwise, ideally encompassing the Curie temperature (T_c) where the entropy variation is maximal.

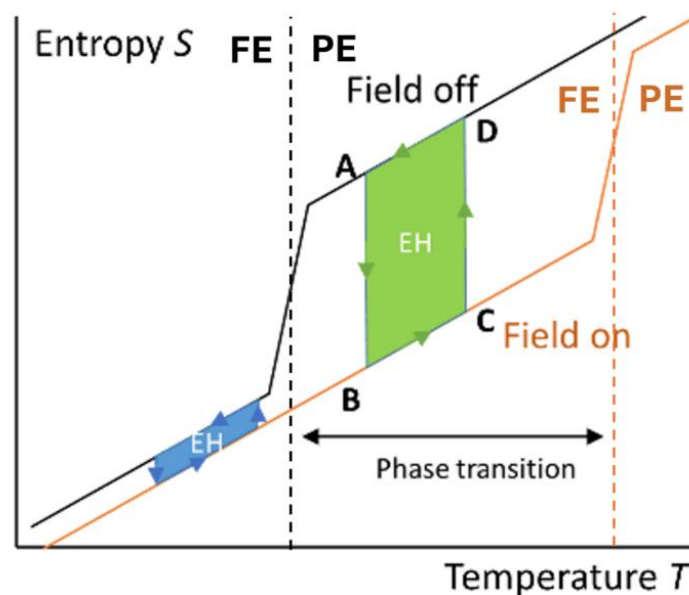


Figure 2.5 Entropy versus temperature with and without an electric field, showing how a phase transition increases the energy harvesting area (large green area) compared to when no transition is present (small blue area). It must be noted that the

ferroelectric (FE) – paraelectric (PE) transition varies according to the field. Adapted from [30].

Although the greatest harvested energy typically occurs near T_c , certain materials, such as barium titanate (BaTiO_3), exhibit additional ferroelectric–ferroelectric (FE–FE) transitions. These secondary transitions provide opportunities for energy harvesting when operation near T_c is impractical [37,39]. While the energy obtained from these transitions may be lower compared to operation around T_c , they remain beneficial for specific applications. Field-induced transitions can further enhance energy output in these scenarios.

Moreover, operating near a phase transition increases the dielectric constant, inevitably raising dielectric losses as well [40]. Another critical factor influencing harvested energy is the dielectric breakdown strength of the material. Higher breakdown fields permit the application of stronger electric fields, directly enhancing the energy recovered per cycle. Typically, thin films possess fewer defects and thus exhibit higher breakdown strengths compared to bulk ceramics. Furthermore, the breakdown strength varies significantly among different material classes; for instance, polymer-based ferroelectrics generally tolerate much higher electric fields than ceramic materials.

Figure 2.6 highlights how an external electric field shifts the phase transition temperature, significantly expanding the usable region for energy harvesting cycles. Differential Scanning Calorimetry (DSC) experiments on lead scandium tantalate (PST) ceramics [41] demonstrate this shift clearly. Under an applied field of $18 \text{ kV}\cdot\text{cm}^{-1}$, the strong first-order phase transition peak in PST shifts upwards by approximately 12 K compared to zero field conditions, underscoring the practical importance of field-driven phase transitions.

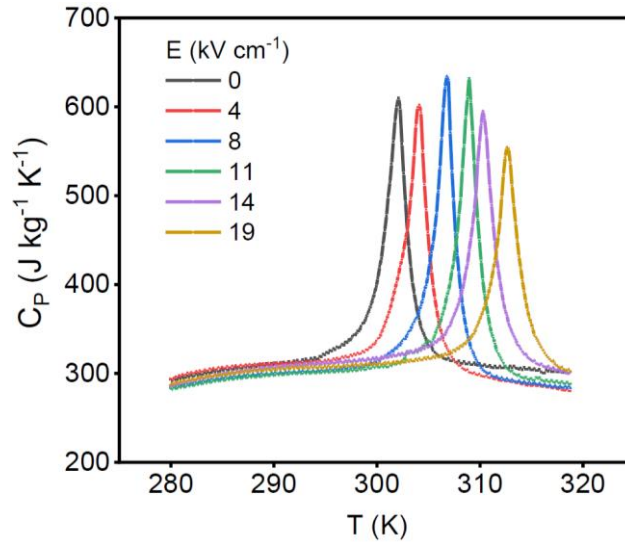


Figure 2.6 Specific heat from iso-field DSC measurements on PST bulk ceramic showing a clear shift in the phase transition temperature. Adapted from [41].

In summary, maximizing pyroelectric energy output per cycle depends critically on the magnitude of electric displacement change, electric field strength, and the operational temperature range. Leveraging the presence of phase transitions is particularly beneficial. Moreover, by restricting the operating temperature window close to the phase transition, particularly in material undergoing strong first order transition (due to their large ΔP) can be significantly enhance the thermal conversion efficiency.

2.3.3 Influence of material geometry

Ferroelectric materials can be fabricated into bulk ceramics, thin films, or multilayer capacitors (MLC), as shown in Figure 2.7. Bulk ceramics are appealing for electrothermal applications due to their relatively large active volume yielding a significantly high work output. However, bulk ceramics are limited to the magnitude of the electric field due to their increased thickness. This also reduces the breakdown field, as thicker dielectrics are more prone to defects that can trigger electrical failure. Additionally, thermal relaxation times are longer in bulk ceramics, which imposes restrictions on heat exchange conditions.

To address these limitations, thin-film ferroelectrics have garnered interest [20,42,43], as high electric fields can be induced at a very low voltage and benefit from rapid heat transfer, which can yield a high pyroelectric power density [44–46]. However, accurately measuring their performance remains complex. Standard testing methods can trigger the release of trapped charges, producing misleading signals that obscure the true pyroelectric response [47]. Moreover, due to their low thermal mass, thin films

store relatively little energy, and their integration with rigid substrates introduces mechanical constraints that reduce adiabatic conditions and limit absolute energy output values [48].

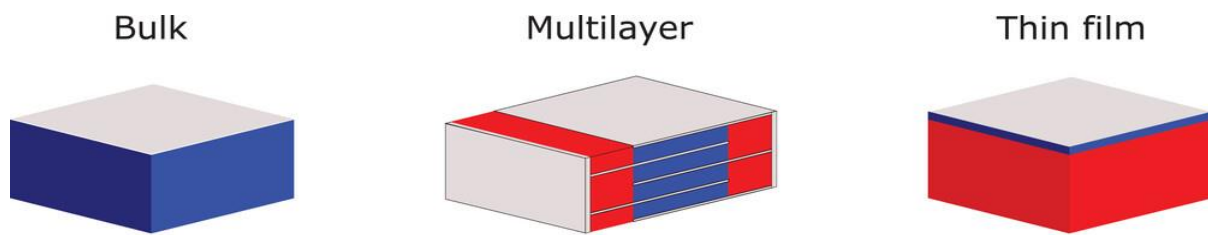


Figure 2.7 Schematic of bulk ceramics (left), multilayer capacitor (middle) and thin films (right). The red and blue area represents the inactive and active regions respectively. The electrodes are marked with silver. Adapted from [49].

To improve the thermal capacity while preserving the electrical advantages of thin films, researchers have turned to MLC geometries, commonly used in the electronics industries [50,51]. MLCs comprise stacked thin ferroelectric layers, each a few to several tens of microns thick, interleaved with electrodes and co-sintered into a compact structure. This geometry allows large electric fields at modest voltages while retaining a macroscopic volume. The electrodes are alternately connected to opposing terminals, with each internal capacitor operating in parallel. Typically, the active region accounts for 50–80% of the total volume. The interdigitated electrodes also serve as efficient thermal pathways, conducting heat from the core to the outer surfaces and enhancing thermal exchange [52,53].

MLCs have been extensively explored for electrocaloric (EC) cooling [52], although only one study has directly applied the Olsen cycle in MLC-based nonlinear pyroelectric energy conversion [30]. Kar-Narayan et al. [54] highlighted MLCs as an optimal design for EC devices, estimating a cooling capacity of 20 kW across a 0.56 m² area through lumped thermal modelling. Crossley et al. [55] examined the thermal transport across MLCs, demonstrating that silver electrodes offer better thermal performance than nickel due to higher thermal diffusivity. Faye et al. [52] showed that increasing electrode thickness fivefold improves heat flow by a factor of 2.5. In a related study, they also examined the thermal interaction between MLCs and their surroundings, identifying ways to minimize heat loss and improve integration in functional prototypes [56]. More recently, Li et al. [57] optimized MLC geometry in an EC system, achieving a 21 K temperature span. Additionally, MLCs also offer robust long-term performance, as evidenced by PST-based MLCs maintaining consistent operation through over 4 million switching cycles [57]. These findings indicate that

MLCs are the ideal geometry for electro-thermal energy interconversion, offering an optimal balance between the high thermal capacity of bulk ceramics and the rapid thermal response of thin films.

2.3.4 Nonlinear pyroelectric materials

In this section, a selected group of nonlinear pyroelectric materials is briefly presented, focusing primarily on perovskite oxides and polyvinylidene difluoride (PVDF) based polymers. As noted in Section 2.1, an excellent electrocaloric material will also exhibit excellent pyroelectric properties, making them promising candidates for thermal energy harvesting.

Table 2.1 summarizes the performance of various nonlinear pyroelectric materials subjected to the Olsen cycle under different operating conditions. The materials are broadly categorized into lead-based ceramics, lead-free ceramics and polymers. Key performance indicators such as energy density, harvested energy per cycle, and power density are reported alongside their corresponding operating temperature ranges and electric field conditions. These metrics offer a comparative view of the materials' suitability for thermal energy harvesting applications.

Energy density is particularly valuable for comparing materials of different geometries, as it normalizes the harvested energy with respect to volume. Harvested energy per cycle, on the other hand, reflects the total energy output and is critical for evaluating device-level feasibility. Power density, where available, provides insight into the material's capacity to deliver usable energy over time, which is an essential requirement for real-world applications such as powering wireless sensors or IoT devices. In cases where power density was not explicitly provided, it was calculated from energy density, active volume, and cycle frequency. The table also includes the zero-field Curie temperature (T_c) of each material, which is crucial in determining the optimal operating window for thermal energy conversion. Materials with a T_c close to the ambient or application-specific temperature range are particularly attractive for efficient heat harvesting.

Among the listed materials, $\text{Pb}(\text{Sc}_{1/2}\text{Ta}_{1/2})\text{O}_3$ (PST) demonstrates the highest reported energy density of $4.4 \text{ J}\cdot\text{cm}^{-3}$ per cycle, making it one of the most promising nonlinear pyroelectric materials. A detailed discussion of its structural, dielectric, and electrothermal properties is provided in the following chapter.

In addition to PST, lead zirconate titanate (PZT) based materials also garner attention due to the presence of a morphotropic phase boundary (MPB) and their tuneable functional properties, which can be optimized through compositional doping. For

example, Zhang et al.[58] demonstrated that doping PZT 30/70 thin films with 1% Mn enhanced the pyroelectric coefficient from $2.1 \times 10^{-4} \text{ C m}^{-2} \text{ K}^{-1}$ to $3 \times 10^{-4} \text{ C m}^{-2} \text{ K}^{-1}$, specifically for uncooled infrared detector applications. Similarly, Olsen et al.[35] achieved an energy density of $0.3 \text{ J}\cdot\text{cm}^{-3}$ per cycle using Sn^{4+} doped PZT ceramics. This performance enhancement is primarily attributed to a field-induced transition between the antiferroelectric (AFE) and ferroelectric (FE) phases in Sn^{4+} doped PZT, which facilitates a rapid release of bound charges and notable volume contraction, thereby increasing the harvested energy [59,60]. Furthermore, the PZT system can be modified to exhibit relaxor behaviour by doping with La^{3+} ions (7 to 9 mol.%), which disrupt long-range ferroelectric order and promote the formation of nanoscale polar regions [61]. Substituting Pb^{2+} with La^{3+} also increases electrical resistivity, reduces leakage currents [62,63], and lowers the Curie temperature (T_c), thereby making the PLZT system highly suitable for pyroelectric energy harvesting. Lee et al. [64] investigated several La-doped PZT compositions and reported a maximum energy density of $1.01 \text{ J}\cdot\text{cm}^{-3}$ for 7/65/35 PLZT, as shown in Table 2.1.

Another material of interest is $\text{Pb}(\text{Mg}_{1/2}\text{Nb}_{2/3})\text{O}_3 - \text{PbTiO}_3$ (PMN-PT), which undergoes a transition from a rhombohedral ferroelectric phase to a cubic paraelectric phase when the PbTiO_3 content is below 20% [65,66]. Notably, PMN-PT exhibits an MPB in the 27–33 % PbTiO_3 composition range, marking a transition between the rhombohedral and tetragonal FE phases, where enhanced piezoelectric coupling coefficients have been observed [67]. In addition, detailed structural characterizations have identified two monoclinic phases (C_m and P_m) at the MPB [67]. PMN-PT can be fabricated as single crystals, ceramics, or thin films, with the material form having a significant impact on its functional characteristics [68]. Single crystals of PMN-PT near the MPB composition are especially valued for their superior electromechanical performance [68,69], and pyroelectric coefficients as high as $1070 \mu\text{C}\cdot\text{m}^{-2}\cdot\text{K}^{-1}$ have been reported for oriented rhombohedral PMN-28PT and PMN-33PT single crystals [70].

Kandilian et al. [65] utilized PMN-32PT single crystals for nonlinear pyroelectric energy harvesting and achieved an energy density of $100 \text{ mJ}\cdot\text{cm}^{-3}$ per cycle with a 90°C temperature swing, leveraging the MPB-induced polarization variation. However, the energy output was limited by the material's relatively low breakdown strength. More recently, Pandya et al. [71] demonstrated significantly improved performance using PMN-32PT thin films, attaining a maximum energy density of $1.06 \text{ J}\cdot\text{cm}^{-3}$ and a power density of $526 \text{ W}\cdot\text{cm}^{-3}$, as listed in Table 2.1.

Table 2.1 Performance of several non-linear pyroelectric materials when subjected to Olsen cycle.

Material	Type- thickness (μm)	T_{Curie} ($^{\circ}\text{C}$)	Temperature $T_{\text{cold}} / T_{\text{hot}}$ ($^{\circ}\text{C}$)	Electric field $E_{\text{low}} / E_{\text{high}}$ ($\text{kV}\cdot\text{cm}^{-1}$)	Sample dimensions (cm^2)	Energy density/ Cycle ($\text{J}\cdot\text{cm}^{-3}$)	Harvested Energy/ Cycle (mJ)	Frequency (Hz)	Power density ($\text{mW}\cdot\text{cm}^{-3}$)	Ref
PZST	Ceramic – (250)	148	155 / 185	8 / 32	5.8	0.3	43.2	0.04	12	[35]
PMN- 10PT	Ceramic – (1000)	40	35 / 85	5 / 35	0.5	0.18	8.64	-	-	[72]
PZN- 4.5PT	Single Crystal (1000)	166	100 / 160	0 / 20	0.32	0.21	6.72	0.1	21	[26]
PZN- 5.5PT	Ceramic – (200)	165	100 / 190	0 / 12	1	0.15	3	0.035	5.1	[73]
#PNZST	Ceramic – (500)	180	150 / 220	0 / 13	6	0.77	231	0.185	144	[74]
6/65/35 PLZT	Ceramic – (180)	180	40/210	4 / 85	0.25	0.95	4.2	0.035	33.2	[75]
7/65/35 PLZT	Ceramic – (190)	120	30 / 200	2 / 70	0.32	1.01	6.16	0.025	25.3	[75]
8/65/35 PLZT	Ceramic – (290)	65	25 / 160	2 / 75	0.18	0.88	4.54	0.017	15	[75]
9/65/35 PLZT	Ceramic – (200)	15	3/150	4 / 75	0.35	0.65	4.50	0.02	13	[75]
PNNZT	Ceramic – (200)	150	20 / 220	3 / 90	20.25	0.86	348	0.09	77.4	[76]
PMN- 28PT	Single Crystal – (300)	125	90/170	2 / 7.5	0.25	0.09	6	-	-	[77]

PMN-32PT	Ceramic – (140)	150	80 / 170	0 / 9	1	0.10	1.40	-	-	[65]
PMN-32PT	Thin film – (0.15)	215	25 / 81	133 / 400	6E-05	0.526	4.73E-07	1000	526000	[71]
PST	MLC – (38 μ m per layer; 19 layers in total)	20	20 / 90	0 / 155	0.49	1.84	65	-	-	[30]
PST	MLC – (38 μ m per layer; 9 layers in total)	20	5 / 180	0 / 195	0.49	4.43	75	-	-	[30]
*BST 66/34	Ceramic – (200)	23	25 / 65	0 / 70	0.2	0.36	1.41	-	-	[78]
*BST 72/28	Ceramic – (200)	43	25 / 85	0 / 70	0.2	0.49	1.92	-	-	[78]
*BSTZ	Ceramic – (1000)	~40	30 / 90	0 / 20	1.1	0.20	22.6	-	-	[79]
60/40 P(VDF-TrFE)	Polymer – (50)	65	25 / 110	200 / 500	1	0.52	2.6	0.1	52	[80]

PZST = $\text{Pb}_{0.99}\text{Nb}_{0.02}(\text{Zr}_{0.68}\text{Sn}_{0.25}\text{Ti}_{0.07})_{0.98}\text{O}_3$, PMN - xPT = $\text{Pb}(\text{Mg}_{1/3}\text{Nb}_{2/3})\text{O}_3 - x\text{PbTiO}_3$, PZN-4.5PT = $\text{Pb}(\text{Zn}_{1/3}\text{Nb}_{2/3})_{0.955}\text{Ti}_{0.045}\text{O}_3$, PZN-5.5PT = $0.945 \text{Pb}(\text{Zn}_{1/3}\text{Nb}_{2/3})\text{O}_3 - 0.055 \text{PbTiO}_3$, PNZST = $\text{Pb}_{0.99}\text{Nb}_{0.02}(\text{Zr}_{0.637}\text{Sn}_{0.273}\text{Ti}_{0.09})_{0.98}\text{O}_3$, x/65/35 PLZT = $\text{Pb}_{1-x}\text{La}_x(\text{Zr}_{0.65}\text{Ti}_{0.35})_{1-x/4}\text{O}_3$, PNNZT = $\text{Pb}(\text{Zr}, \text{Ti})\text{O}_3 - \text{Pb}(\text{Ni}, \text{Nb})\text{O}_3$, PST = $\text{Pb}(\text{Sc}_{1/2}\text{Ta}_{1/2})\text{O}_3$, BST = $\text{Ba}_{(1-x)}\text{Sr}_x\text{TiO}_3$, BSTZ = $\text{Ba}_{0.85}\text{Sr}_{0.15}\text{Ti}_{0.9}\text{Zr}_{0.1}\text{O}_3$

Note: The # PNZST data uses a combined Olsen-Stirling cycle instead of the traditional Olsen cycle.

It must also be noted that the high absolute values of certain materials in Table 1 are due to their large sample dimensions, which must not be neglected.

Indirect measurements from the D-E loops are indicated with (*) symbol

Lead-free perovskite materials

Barium titanate (BaTiO_3 or BTO) is a well-established candidate due to its pronounced first-order ferroelectric transition, chemical stability, and non-toxicity. Li et al. [81] reported electrocaloric temperature changes of 0.9 K and 2.4 K associated with the FE-FE and FE-PE transitions, respectively, in BTO multilayer capacitors. Notably, the latent heat associated with the FE-PE transition in BTO ($\sim 1 \text{ J}\cdot\text{g}^{-1}$) is comparable to that of PST [82]. However, its relatively high specific heat and limited polarization variation under strong electric fields result in lower overall electrocaloric and pyroelectric performance compared to PST. The intrinsic pyroelectric coefficient of BTO is modest ($\sim 200 \mu\text{C}\cdot\text{m}^{-2}\cdot\text{K}^{-1}$), but dopants such as Zr^{4+} and Sr^{2+} have been shown to enhance its pyroelectric response [83,84].

To improve thermodynamic performance, compositional tuning has been extensively explored in $\text{Ba}(\text{Zr}_x\text{Ti}_{1-x})\text{O}_3$ (BZT) ceramics. Jian et al. [85] identified $x = 15 \text{ mol.}\%$ as an optimal composition near the multiphase boundary for maximizing entropy change. This finding was corroborated by Qian et al. [83], who showed that operating near the invariant critical point in BZT ($x = 0.2$) enables access to 26 polar states, resulting in a significant entropy change of approximately $8 \text{ J}\cdot\text{kg}^{-1}\cdot\text{K}^{-1}$ [83,86]. Likewise, $\text{Ba}_{1-x}\text{Sr}_x\text{TiO}_3$ (BST) ceramics exhibit high pyroelectric coefficients and notable electrocaloric effects, with temperature shifts up to 1.8 K reported for $x = 0.35$ [87]. Increasing Sr^{2+} lowers the T_c and at higher concentrations ($x > 30 \text{ mol.}\%$) the material becomes a relaxor [88].

Polyvinylidene difluoride based polymers

Apart from perovskite oxides, ferroelectric polymers based on polyvinylidene fluoride (PVDF) represent a compelling alternative for electrothermal energy conversion due to their lightweight nature, mechanical flexibility, high dielectric strength, and large entropy changes near phase transitions. PVDF exists in five crystalline phases, of which the polar β -phase is most suitable for energy harvesting applications [89]. The ferroelectric and crystallographic properties of PVDF-based

polymers are highly sensitive to molecular structure and confinement effects [89]. Blending PVDF with trifluoroethylene (TrFE) enhances crystallinity and ferroelectric order due to the structural compatibility of the two monomers. Further copolymerization with chlorofluoroethylene (CFE) or chlorotrifluoroethylene (CTFE) increases the chain spacing ($l_3 > l_2 > l_1$), inducing relaxor ferroelectric (RFE) behaviour, as depicted in Figure 2.8. These relaxor polymers exhibit both high entropy variation and large electrocaloric temperature shifts, with reported ΔT values up to 12 K for P(VDF-TrFE) and P(VDF-TrFE-CFE) [12].

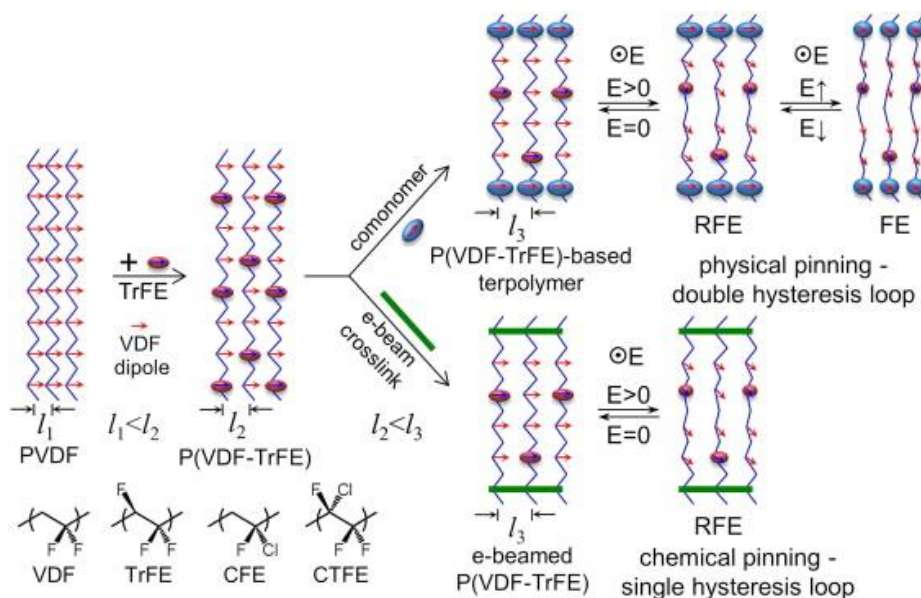


Figure 2.8 Schematic representation of P(VDF), P(VDF-TrFE) and P(VDF-TrFE) terpolymers. Adapted from [89].

Although PVDF-based polymers have been extensively investigated for electrocaloric applications [12,43,89–95], their use in nonlinear pyroelectric energy harvesting remains limited due to challenges such as high leakage currents [96–98]. However, recent work suggests that entropy variation as large as $37.5 \text{ J}\cdot\text{kg}^{-1}\cdot\text{K}^{-1}$ can be achieved in P(VDF-TrFE-CFE) through the introduction of double bonds, significantly improving their electrothermal properties [90]. These high-entropy polymers offer promising features for pyroelectric energy conversion, including enhanced crystallinity, large ΔS , minimal hysteretic losses, reduced switching barriers, and high dielectric breakdown strengths. Nevertheless, improving their thermal conductivity remains a key challenge for practical device integration.

2.3.5 Figures-of-merit

[The new nonlinear figures of merit discussed in this section were originally proposed by Dr. Emmanuel Defay during collaborative discussions. The inclusion of thermal diffusivity in the power-based figure of merit was suggested by Dr. Roger Whatmore to better reflect dynamic thermal effects]

A "figure-of-merit" (FOM) combines relevant material properties into a single value that directly indicates the potential performance of the material under certain operating conditions for specific device applications. An appropriate FOM allows straightforward comparison of pyroelectric materials for targeted applications. Although numerous pyroelectric FOM exist, most were initially developed for detectors or linear energy harvesting [99]. This section reviews the existing FOMs and introduces two new FOMs for non-linear pyroelectric energy harvesting, focusing on the energy and power produced per cycle.

In thermal imaging and pyroelectric detector applications, two primary FOMs assess the materials' capability to generate either maximum current or voltage from a given input power [23]. The FOM related to current responsivity (F_i) is defined as:

$$F_i = \frac{p}{C_E} \quad (2.17)$$

Similarly, the voltage responsivity FOM (F_v) is given by:

$$F_v = \frac{p}{\varepsilon_0 \varepsilon_r C_E} \quad (2.18)$$

Here, p is the pyroelectric coefficient ($\mu\text{C}\cdot\text{cm}^{-2}$), C_E is the volumetric heat capacity ($\text{J}\cdot\text{m}^{-3}\cdot\text{K}^{-1}$) and ε_r is the permittivity of the material ($\text{F}\cdot\text{m}^{-1}$).

These detector-focused FOMs, however, are not suitable for energy harvesting applications, where primary considerations include energy and power output, alongside the efficiency relative to the material's volume or mass. Sebald et al. [36,100] proposed two FOMs for pyroelectric energy harvesting analogous to those used in piezoelectric harvesting, assuming linear material behaviour. The energy harvesting FOM (F_E) was defined as:

$$F_E = \frac{p^2}{\varepsilon_0 \varepsilon_r} \quad (2.19)$$

They also introduced an electro-thermal coupling factor [36], akin to the electromechanical coupling factor, to estimate harvesting efficiency:

$$k^2 = \frac{p^2 T_H}{\varepsilon_0 \varepsilon_r C_E} \quad (2.20)$$

where T_H denotes the material's high operating temperature. Although (F_E) is commonly used, it excludes heat capacity, a crucial parameter for realistic heat exchange. Addressing this limitation, Bowen et al. [101,102] introduced a modified FOM that incorporates volumetric heat capacity, given by:

$$F_{E'} = \frac{p^2}{\epsilon_0 \epsilon_r (C_E)^2} \quad (2.21)$$

For non-linear pyroelectric energy harvesting, the linear FOMs which are mentioned above based on the low-field permittivity and pyroelectric coefficients do not accurately reflect performance under high-field conditions. Instead, the simplest way to evaluate non-linear materials is by examining their polarization-electric field (D - E) loops at different temperatures. As previously discussed regarding the Olsen cycle (Figure 2.4 (b)), the enclosed area between two D - E loops measured at distinct temperatures accurately represents harvestable energy. The cycle area increases with higher maximum electric fields and larger polarization changes. Thus, we propose a new figure of merit, ($FOMe$) defined as:

$$FOMe = \Delta D \times E_{max} \quad (2.22)$$

with $\Delta D = D_1(E_{max}, T_{cold}) - D_2(E_{max}, T_{hot})$ as depicted in Figure 2.9. This parameter effectively captures the material's potential for non-linear pyroelectric energy harvesting, accounting for both polarization variation and maximum operational electric field.

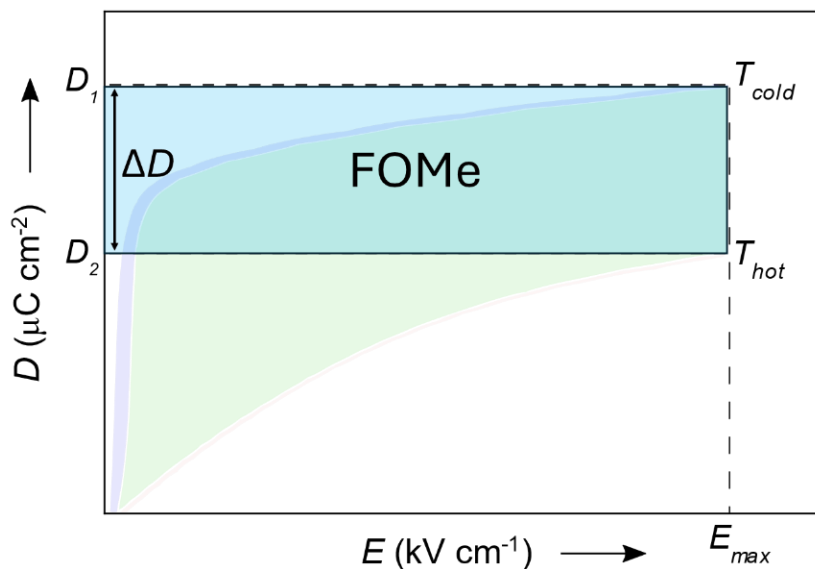


Figure 2.9 Schematic representation of the non-linear figure of merit ($FOMe$) from the D - E loops.

Although Childress first addressed the relationship between power generation and thermal conductivity [29], previous figures of merit have not explicitly considered the interplay of thermal properties and non-linear behaviour. Furthermore, the power-generating capability of pyroelectric materials has rarely been evaluated explicitly, with no existing figure of merit for this aspect. Therefore, we propose another metric (*FOM_p*) to represent power per cycle, integrating electrical and thermal characteristics by including the material's thermal diffusivity (α):

$$FOM_p = \Delta D \times E_{max} \times \alpha \quad (2.23)$$

This definition provides a more comprehensive evaluation, reflecting both electrical and thermal performance. Indeed, the thermal time scale for heat transfer in a material of thickness 'd' and thermal diffusivity α is given by d^2/α [103]. Hence, the frequency at which heat can enter or leave the material directly correlates with its thermal diffusivity, validating the relevance of this figure of merit.

Table 2.2 summarizes key properties and figures of merit for various pyroelectric materials reported in literature. Notably, PST and BST ceramics exhibit high pyroelectric coefficients under bias fields, approximately $1165 \mu\text{C}\cdot\text{m}^{-2}\cdot\text{K}^{-1}$ and $708 \mu\text{C}\cdot\text{m}^{-2}\cdot\text{K}^{-1}$ respectively. PST multilayer capacitors (MLCs) achieve significant energy densities ($\sim 2 \text{ J}\cdot\text{cm}^{-3}$) due to their ability to withstand high electric fields ($\sim 200 \text{ kV cm}^{-1}$), although polymer films such as HfO_2 and P(VDF-TrFE) can surpass these values because of their even higher breakdown fields. Despite their lower energy densities, BST ceramics offer comparable power performance to PST MLCs due to higher thermal conductivity ($> 7 \text{ W/m}\cdot\text{K}$). Additionally, lead-free ceramics, benefiting from superior thermal diffusivity, demonstrate excellent potential for high-power applications. Conversely, polymers like PVDF, despite limitations in thermal conductivity, could still perform effectively if used in ultra-thin layers. Ultimately, while linear figures of merit favour PMN-PT single crystals, nonlinear FOMs highlight the advantages of thin films and high-conductivity lead-free ceramics for practical energy harvesting.

Table 2.2 Pyroelectric energy harvesting figures of merits for different materials

Material	p ($\mu\text{C}\cdot\text{m}^{-2}\cdot\text{K}^{-1}$)	$\varepsilon / \varepsilon_0$	C_E ($\text{J}\cdot\text{m}^{-3}\cdot\text{K}^{-1}$)	K (W/mK)	α (mm^2/s)	F_E ($\text{J}\cdot\text{m}^{-3}\cdot\text{K}^{-2}$)	$F_{E'}$ ($\times 10^{-12}$) ($\text{m}^3\cdot\text{J}^{-1}$)	ΔT ($T_{\text{start}} / T_{\text{final}}$) (K)	E_{max} ($\text{kV}\cdot\text{cm}^{-1}$)	$FOMe$ $= \Delta D \times E_{\text{max}}^{(d)}$ ($\text{J}\cdot\text{cm}^{-3}$)	$FOMP$ $\times 10^{-2}$ ($\text{W}\cdot\text{cm}^{-1}$)	Ref
PZT ^(a)	533	1116	2.5	1.25	0.5	28.8	4.6	150 (150 / 300)	20	0.2	0.10	[17,104,105]
PMN-0.25PT ^(a)	746	2100	2.5	1.3	0.52	29.94	4.8	130 (40 / 170)	25	0.48	0.25	[17,106]
PMN-0.25PT SC ^(b)	1790	961	2.5	1.5	0.6	376.7	60.3	130 (40 / 170)	25	0.5	0.30	[17,100,106]
PST MLC	1165	1500	2.7	2.1	0.78	102.2	14	95 (5 / 100)	200	2	1.56	[30,107,108]
BTO	200	1200	2.5	3	1.2	3.76	0.6	120	40	0.6	0.72	[17,81,109]

BST 65/35	708	1350	2.7	7	2.6	41.94	5.75	60 (25 / 85)	70	0.6	1.56	[78,110,111]
HZO TF	60	34	2.6	1.26	0.48	12	1.77	160 (-10 / 150)	2000	14	6.70	[112]
PVDF- TrFE 55/45 ^(c)	40	8	2.2	0.14	0.06	22.60	4.67	30 (70 / 100)	2000	2	0.12	[12,17]

^(a) Poled ceramic

PMN – 0.25 PT SC ^(b) = 0.75 Pb(Mg_{1/3}Nb_{2/3})O₃ – 0.25 PbTiO₃ single crystal poled along [111] of the unit cell; PZT = Pb(Zr_xTi_{1-x})O₃, PST = Pb(Sc_{1/2}Ta_{1/2})O₃, BTO = BaTiO₃, BST 65/35 = Ba_{0.65}Sr_{0.35}TiO₃, HZO TF= Hf_{0.5}Zr_{0.5}O₂ thin film

^(c) P(VDF-TrFE) 55/45 – polyvinylidene fluoride trifluoro ethylene, ferroelectric polymer

^(d) ΔD and E_{\max} are extracted from $P - E$ loops after their definition provided in Figure 2.9.

[Note: The temperature and electric field values are not normalized, so the numbers should be interpreted with caution in the case of nonlinear figures of merit. Additionally, the hysteretic loss of the material is not taken into consideration. Nonetheless, they offer a useful perspective on the material's performance. Besides, the pyroelectric coefficient values and the volumetric heat capacities may not be accurate due to the limitations of the measurement techniques used in the literature]

2.3.6 Effect of losses and material degradation

One of the main challenges in nonlinear pyroelectric energy conversion is to reduce the material losses, particularly the hysteresis and leakage current as they can significantly reduce the harvestable energy. The detrimental role of electrical hysteresis can simply be understood from the $D - E$ loops, as material with higher hysteresis will reduce the area between the two loops, which typically corresponds to the harvestable energy, as shown in Figure 2.10.

Khodayari et al. [26] investigated the Ericsson cycle using a PZN-4.5PT single crystal within a temperature range of 25 to 50 °C and under moderate electric fields. Their simulations revealed that the energy input to the system exceeded the recoverable energy output, primarily due to hysteresis associated with the ferroelectric-to-ferroelectric (FE-FE) phase transition. This thermal hysteresis led to a crossover between the $D - E$ loops over the limited temperature span, which diminished the net harvested energy.

The effectiveness of energy conversion in such systems depends heavily on several parameters, including the thermal and electrical history of the material, the operating temperature window, the cycling frequency, and the magnitude of the applied electric field. For example, if the electric field is insufficient to drive a fully reversible phase transition, the material cannot entirely traverse the hysteresis region. This results in a partial or irreversible transition, thereby limiting the energy that can be harvested [103].

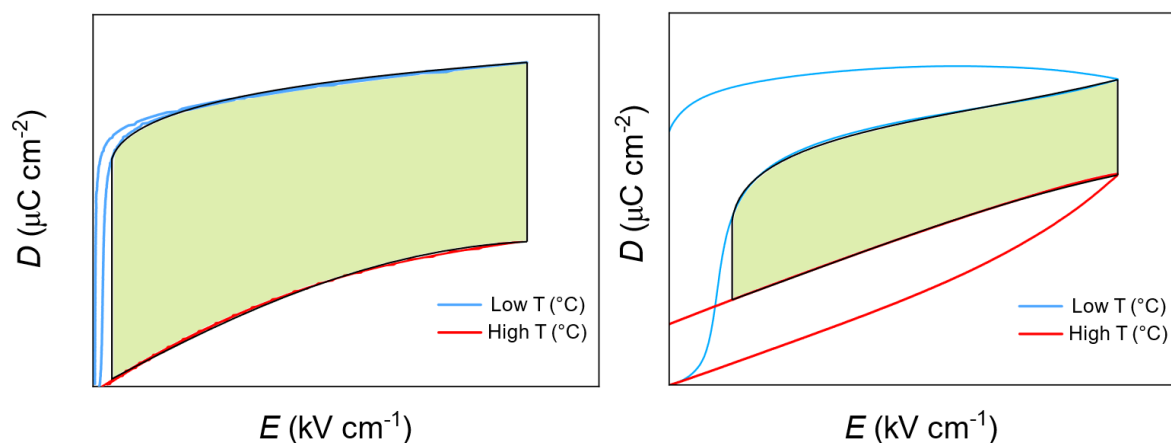


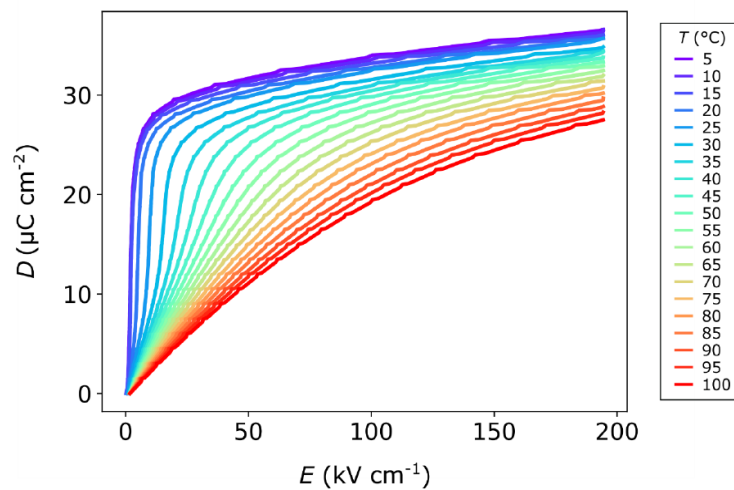
Figure 2.10 Schematic of unipolar $D-E$ loops for a ferroelectric with low hysteresis (left) and high hysteresis (right). The shaded area shows the harvested energy.

In addition to hysteresis, leakage current poses another significant limitation. Because ferroelectric materials have finite electrical resistance, prolonged cycling at high electric fields and elevated temperatures can cause accumulated surface charge to

gradually leak through the bulk of the material. This leakage disrupts the charge recovery in subsequent cycles, shrinking the area enclosed by the D - E loops and thereby reducing the total electric energy output. Olsen [34] demonstrated this behaviour experimentally by adding a parallel resistor to the system, simulating conduction losses. The resulting charge–voltage loops were broader and had reduced enclosed areas, confirming the impact of leakage.

Both hysteresis and conduction-related losses, including Joule heating, reduce the energy conversion efficiency of the material. Therefore, to maximize energy output, ferroelectric materials should exhibit both low hysteresis and minimal leakage current. An excellent example of this is provided by Lheritier et al. [29], who achieved a high energy density of $4.4 \text{ J}\cdot\text{cm}^{-3}$ per cycle using lead scandium tantalate multilayer capacitors. These devices demonstrated both low electrical hysteresis and extremely low leakage currents—less than 10^{-7} A at $195 \text{ kV}\cdot\text{cm}^{-1}$ up to $180 \text{ }^\circ\text{C}$, as shown in Figure 2.11 (a) and (b).

(a)



(b)

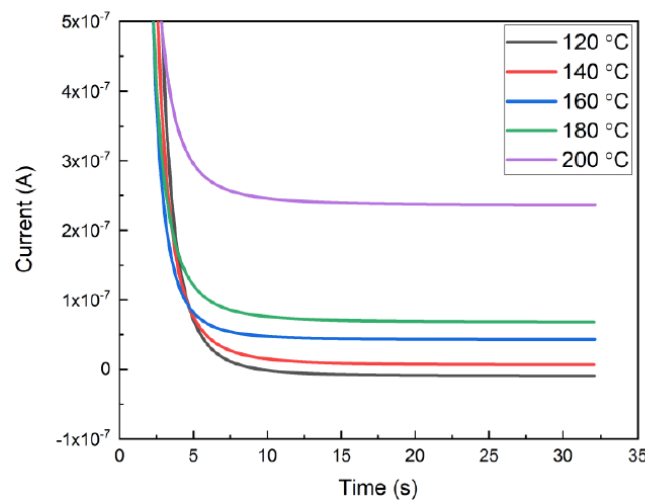


Figure 2.11 Unipolar D - E loops of PST MLC at different temperatures at 195 kV cm^{-1} . (b) Leakage current time evolution data of PST multilayer capacitors under the same field after fitting with Curie-von Schweidler empirical law. Adapted from [30].

Impact of material aging and fatigue

The long-term performance of pyroelectric materials is significantly affected by aging and fatigue. Aging refers to the gradual degradation in material properties over time without external stimuli (electrical, mechanical and thermal load), typically seen as a distortion of the D - E hysteresis loops and reductions in polarization, permittivity, and strain [113]. This degradation is primarily due to the rearrangement of charged defects and their interaction with polarization, especially at domain walls. Fatigue, by contrast, results from repeated application of the external load, leading to reduced switchable polarization, which is often linked to defect accumulation, such as oxygen vacancies, at grain boundaries.

Although re-annealing above the T_c of material can partially reverse these effects, the precise microscopic mechanisms still remain under debate [114,115]. Aging and fatigue are influenced by factors like microstructure, doping, crystallography, and external conditions such as temperature and applied fields [113]. Figure 2.12 illustrates typical degradation patterns: aging dominates in acceptor-doped materials, while fatigue is more pronounced in donor-doped systems.

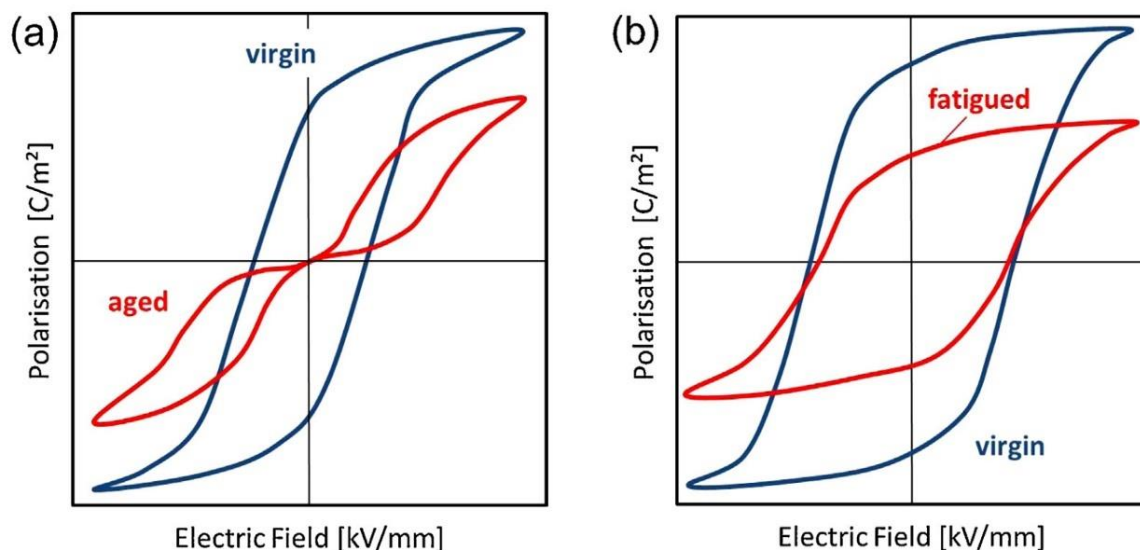


Figure 2.12 Schematic of macroscopic degradation in ferroelectrics due to (a) aging - typical of acceptor doped materials (b) fatigue - predominant in donor doped materials. Adapted from [113].

Despite their relevance, very few studies have directly examined reliability during nonlinear pyroelectric cycling. Chin et al. [63] observed a drop in energy (300 to 250 J L^{-1}) and power density (43 to 40 W L^{-1}) in PLZT 9.5/65/35 after 72 successive Olsen

cycles between 23 and 140 °C at 0.15 Hz (see Figure 2.13). They attributed this performance degradation to stress-induced microcracking, although no microstructural evidence was presented in their study. Until now, there are no reports on the fatigue/aging phenomena about macroscopic pyroelectric harvesters. Notably, the early work by Olsen and his colleagues on a large-scale energy harvester showed that the prototype could only sustain 21 operational cycles, with adjustments needed between each cycle to ensure continued operation [116]. Consequently, the system lacked the reliability necessary for assessing long-term aging or fatigue behaviour. However, further understanding of fatigue behaviour in ferroelectric materials and its implications for thermal energy harvesting can be gained by examining studies on electrocaloric fatigue.

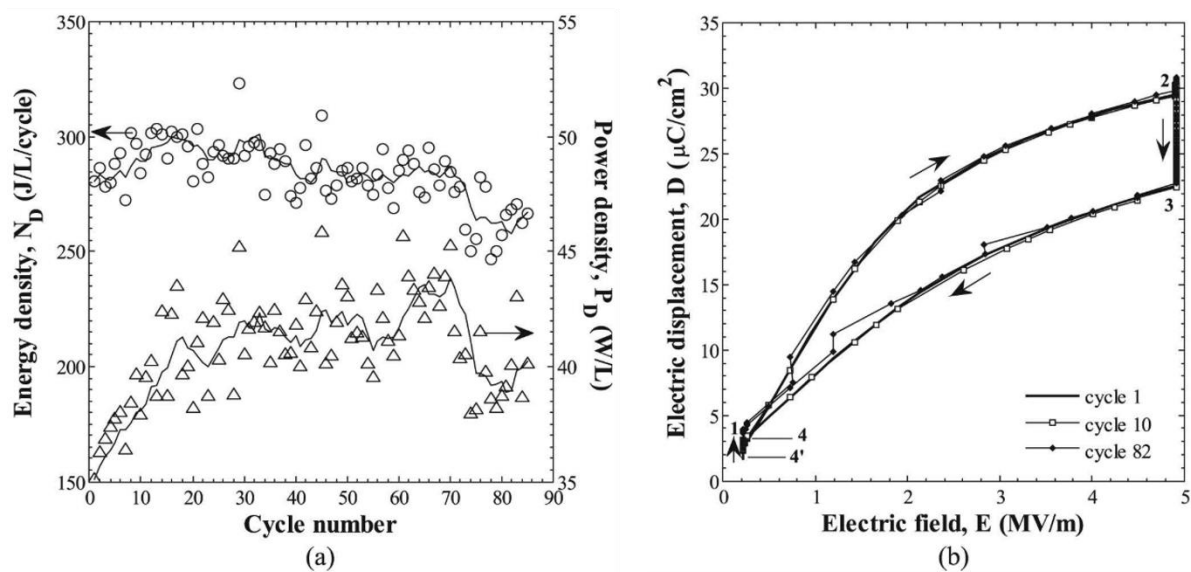


Figure 2.13 (a) Energy and power densities generated by 9.5/65/35 PLZT as a function of cycle number. (b) D - E loops of Olsen cycles collected after different numbers of cycles [63].

Bradeško et al. [117] showed that PMN samples under unipolar square waves (70 kV cm^{-1} , 2 Hz) experienced a three-order drop in resistivity after 28,000 cycles due to increased grain boundary conduction from field-induced phase changes. Fulanović et al. [118] reported only a 1% reduction in electrocaloric effect in PMN multilayer capacitors after one million cycles at 110 kV cm^{-1} , with no observed microcracking. Similarly, Li et al. [57] found less than 2% degradation in the electrocaloric effect of PST MLCs after four million cycles under 400 V unipolar pulses at 10 Hz.

These results highlight the need to better understand fatigue and aging under strong electrothermal cycling, especially in devices operating under large fields and temperature gradients. Studies on PZT and PLZT have shown that electric field-induced fatigue can cause crack propagation due to internal strain mismatch [119].

Developing detailed fatigue models, especially for multilayer geometries, is crucial for assessing device longevity.

Thermal fatigue also remains underexplored, especially in the context of electro-thermal energy harvesting. Hoh [120] emphasized the need for high thermal shock resistance in ferroelectrics used for energy harvesting [121]. Future work should focus on evaluating thermal fatigue and building predictive models to link electrothermal cycling to long-term reliability in multilayer capacitors.

2.4 State-of-the-art pyroelectric energy harvesting devices

This section presents a review of current macroscopic pyroelectric energy harvesting devices. It begins by outlining the principle of heat regeneration, followed by recent developments in large-scale pyroelectric harvesters. Finally, it highlights the role of thermal management and power electronics in improving system performance.

2.4.1 Principle of heat regeneration

The efficiency of pyroelectric energy harvesters in converting heat into electricity can be significantly improved by recycling and reusing such that the external thermal energy input can be reduced. This principle, known as heat regeneration, has been utilized in steam engines and can also be effectively applied to macroscopic pyroelectric energy harvesters, making heat transfer between active elements and thermal reservoirs more reversible [28].

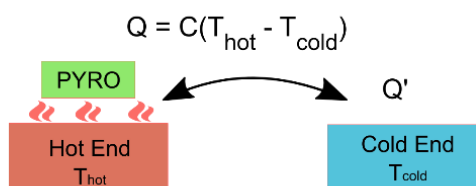
Figure 2.14 compares non-regenerative and regenerative cycles. In non-regenerative cycles, heat is directly absorbed by the pyroelectric material from the hot reservoir and subsequently released to the cold reservoir during each cycle. Due to the large temperature difference between the pyroelectric material and reservoirs, the heat flow is irreversible causing considerable energy loss. Consequently, the net harvested energy, which is the difference between the heat absorbed from the hot source (Q) and the heat released to the cold end (Q') remains relatively low. This results in suboptimal efficiency, as it is determined by the ratio of this small heat difference to the total heat input at high temperature (Q) [34].

In the regenerative cycle, the sample is moved from the hot end to the cold end through the intermediate regenerator heat reservoir ($T_1, T_2 \dots T_n$), which serves as the second thermodynamic medium. Here, the heat absorbed by the sample is relatively small due to the small temperature difference ($Q = C_p(T_h - T_1)$), where C_p is the heat capacity of the material. In this case, the heat flow is not very irreversible. As the sample moves towards the cold end, a small quantity of heat is dissipated to the regenerator reservoirs before reaching the cold reservoir. Similar to the non-regenerative case, the sample undergoes an identical temperature change from T_{hot} to T_{cold} , but the heat absorbed at hot end and released at cold end is small. To initiate the

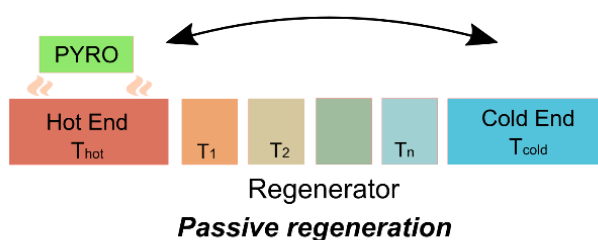
next cycle, the sample travels through the regenerator reservoirs absorbing a small amount of heat stored in them before reaching the hot reservoir [34].

Instead of moving the sample through the regenerator reservoir, heat regeneration can also be accomplished by pumping a caloric fluid between the hot and cold reservoirs to exchange heat with the active material. As the heat is transferred from the hot end to the cold end via the heat transfer fluid, a temperature gradient is established. The oscillating fluid induces cyclic temperature variations in the samples, enabling the heat required to raise the lattice temperature to be continuously regenerated between the fluid and the material, rather than being dissipated into the heat sink [122]. This type of regeneration is known as active regeneration. Through slow cycling with a large number of intermediate reservoirs and proper thermal insulation of the device, Carnot efficiency could be achieved theoretically [34]. However, it is practically very difficult to achieve Carnot efficiency, as the heat capacity is also dependent on the field and the material is cycled at different electric fields along the regenerator resulting in some heat leakage.

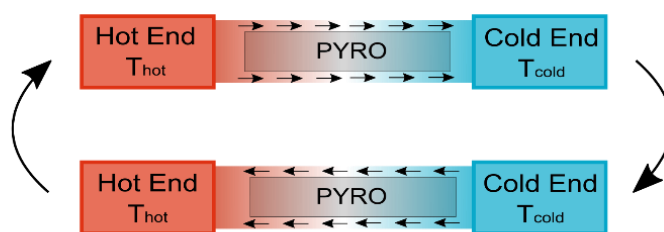
(a) **Non - regenerative cycle**



(b) **Regenerative cycle**



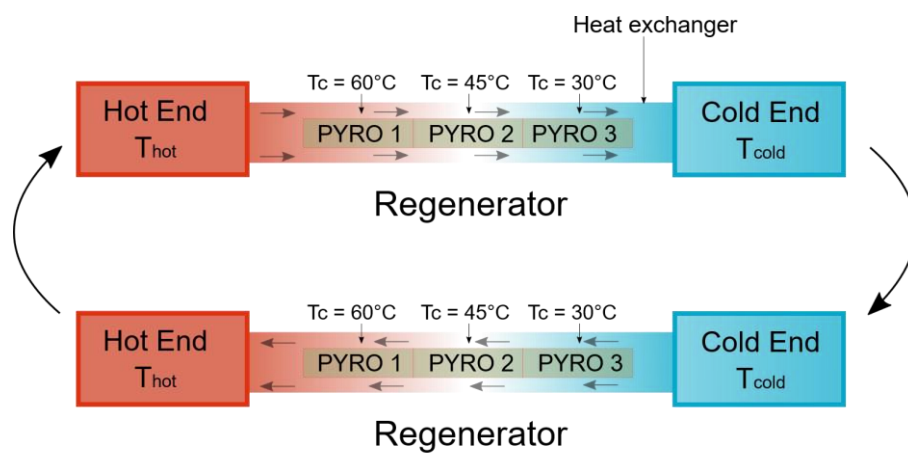
Passive regeneration



Active regeneration

Figure 2.14 Illustration of three types of pyroelectric energy harvesting cycles: (a) non-regenerative, (b) passive regenerative, and (c) active regenerative. In (a) and (b), the arrow shows the movement of the green pyroelectric element from one end to other. In (c), the arrows indicate that the two steps repeat continuously.

To further enhance the efficiency, Gonzalo [123] and Drummond et al. [124] proposed the idea of using multiple stages, in which pyroelectric materials with different transition temperatures are thermally connected in series to broaden the operational temperature range of the device. In this configuration, the heat released by the first stage serves as the input heat for the second stage, thus minimising the heat required to raise the temperature of subsequent stages. By applying a suitable method of heat regeneration, such as the circulation of a thermal fluid or the use of a thermal control system (discussed in the following section), the thermal energy can be recycled efficiently between stages, thereby reducing the total heat input from external sources. This approach contributes to a noticeable improvement in the performance of device as the energy output is enhanced due to multi-staging and heat input is reduced due to the heat regeneration between the stages as shown in Figure 2.15.



Cascading or multistage device

Figure 2.15 Schematic representation of cascaded or multistage pyroelectric energy harvester. The arrows means that the process is cycled.

Although the concept has been proposed for several decades, experimental demonstration of heat regeneration in cascading pyroelectric systems remains rare. The only reported study is by Olsen et al. [116], who evaluated system efficiency by measuring the heat supplied to a resistive heater and the electrical power generated by the pyroelectric modules. They reported a maximum absolute efficiency of 0.50 percent, corresponding to approximately 7.4 percent of the theoretical Carnot efficiency (31 K over 454 K gives 6.8 percent). Their cascaded system showed a 20 % increase in efficiency compared to a single stage device, confirming the potential of thermal regeneration combined with staged design for enhancing the performance of practical pyroelectric energy harvesters.

2.4.2 Macroscopic pyroelectric energy harvesters

In the 1980s, Olsen and his colleagues developed several regenerative macroscopic pyroelectric harvesters. Their first prototype comprised twenty-four Sn-doped $\text{Pb}(\text{Zr},\text{Ti})\text{O}_3$ ceramic plates arranged in a parallel plate configuration with 0.25 mm spacing between each stack. Silicone oil was used as the heat transfer fluid to facilitate thermal exchange between the prototype and both the heater and the aluminium sink, as shown in Figure 2.16 (a). Although energy breakeven was not achieved, the device produced $130 \text{ mJ}\cdot\text{cm}^{-3}$ per cycle and 40 mW of power for a temperature span of 33 K at a frequency of 0.13 Hz. This regenerative approach resulted in a two-thirds improvement in efficiency compared to the nonregenerative case [28]. Successively, Olsen et al. developed a cascaded pyroelectric energy harvester using Sn-doped ceramics with different transition temperatures arranged in a four stage configuration [116]. Design improvements included wider spacing (0.38 mm), lower viscosity fluid (50 cP), and reduced inactive mass. By implementing both multi staging and heat regeneration, the harvester containing 317 g of active material across eight sections (see Figure 2.16 (b)) produced 6.23 J of energy in a single cycle. Additionally, their device achieved a peak power of 1.64 W for one cycle, after which the performance could not be consistently reproduced due to the electrical breakdown of the samples.

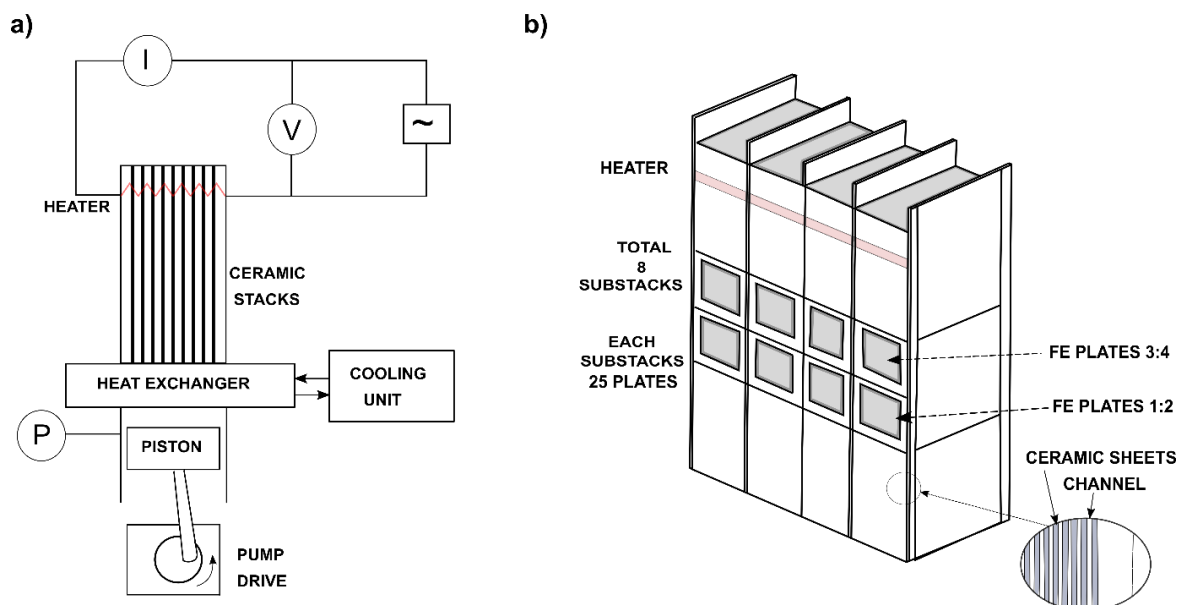


Figure 2.16 Schematic of macroscopic pyroelectric devices by Olsen et al. [28,116]: (a) regenerative device made of ceramic stacks and (b) isometric view of the ceramic stack used in the cascaded energy converter (redrawn for clarity).

Later, Olsen et al. [96] developed a device using P(VDF-TrFE) copolymers due to their high dielectric strength and desirable power-to-weight ratio. In this configuration, the copolymer was spirally wound around a rod, and nylon spacers were used to form channels for silicone oil to facilitate heat exchange. However, due to significant

conduction losses, the energy density achieved was only $30 \text{ mJ}\cdot\text{cm}^{-3}$ between 20°C and 90°C . Over the following years, research efforts focused on mitigating these losses in PVDF-based systems [97,98]. More recently, Nguyen et al. [125] demonstrated notable improvements by employing a 60/40 copolymer formulation, achieving an energy output of $130 \text{ J}\cdot\text{L}^{-1}$ per cycle.

In 2022, Lheritier et al. [30] developed two macroscopic pyroelectric energy harvesters consisting of PST multilayer capacitors undergoing Olsen cycle. Similar to earlier designs, the PST MLCs were arranged in a parallel plate configuration, allowing a heat transfer fluid to circulate between the stacks and facilitate thermal cycling, as shown in Figure 2.17. The capacitors were alternately exposed to hot and cold reservoirs through a low-viscosity silicone oil (5 cP), which enabled efficient heat exchange while maintaining electrical insulation. A notable aspect of this design was the use of a polyolefin hose, thermally shrunk to seal the system. This minimal sealing strategy significantly reduced inactive mass in the heat exchanger, a technique previously applied by the same group in electrocaloric cooling systems [57,126].

Their initial prototype, containing 28 capacitors, achieved a maximum energy output of 3.1 J per cycle at 750 V (see Figure 2.18). A larger version, integrating eight heat exchanger modules with a total of 42 g of active material, produced an electrical energy output of 11.2 J per cycle between 11 and 98°C at 500 V , which is nearly twice the output of Olsen's earlier system, achieved using seven times less active mass.

These results, along with detailed experimental conditions of all the prototypes mentioned above are summarized in Table 2.3. Harvested energy is the primary reported metric; when power is not provided, it is estimated from the product of energy per cycle and cycle frequency.

Only three materials—PZST, PST, and P(VDF-TrFE) have been studied, all in fluid-based systems, highlighting the limited material and design diversity explored to date. Ceramics are commonly used due to their suitability for parallel plate geometries, but their need for dielectric fluids like silicone oil, which has low thermal conductivity, limits heat transfer efficiency.

The choice of heat exchange medium, particularly silicone oil viscosity, significantly affects performance. Olsen et al. [116] and Lheritier et al. [30] reported improved results with lower-viscosity oils, consistent with theoretical predictions. Olsen et al.[35] also demonstrated that cycling near the Curie temperature enhances energy output. High field tolerance is essential for achieving large energy gains. While PVDF-based devices yield lower energy, they benefit from high dielectric strength, low density, and ease of fabrication into thin films.

Lheritier et al. [30] notably generated about 10 joules of energy in one cycle using 40 grams of nonlinear pyroelectric material. Key challenges ahead include enhancing efficiency via regeneration and boosting power output through improved heat exchange, as discussed in the next section.

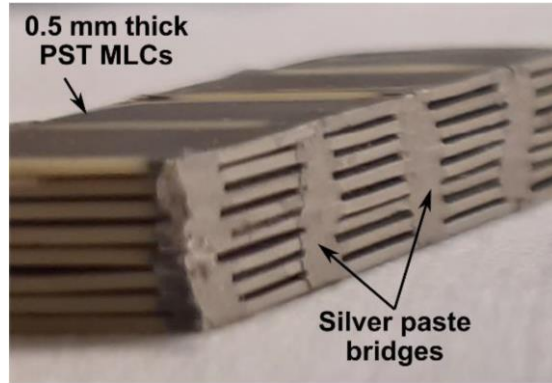


Figure 2.17 Picture of PST MLCs assembled in the parallel plate heat exchanger configuration. Taken from [126].

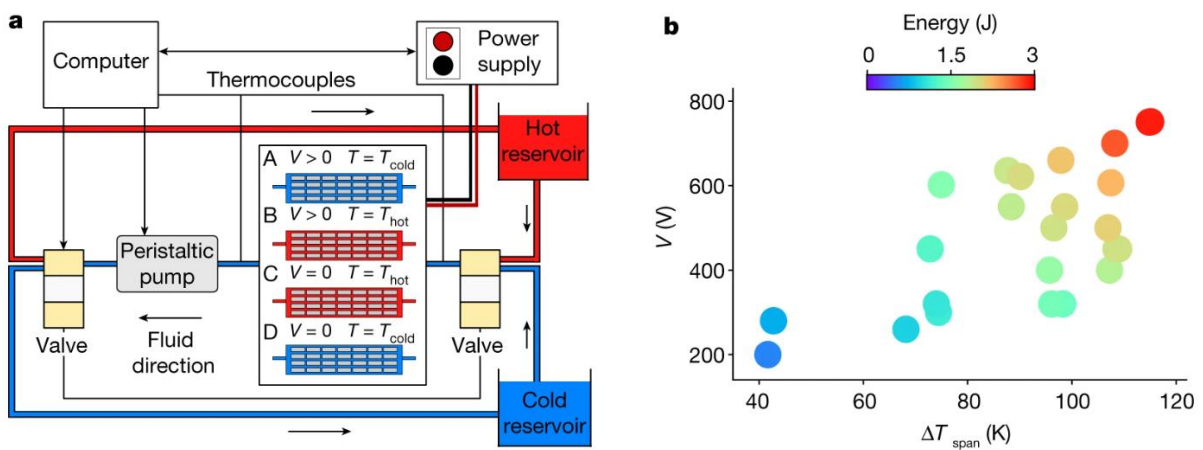


Figure 2.18 (a) Experimental set-up of pyroelectric energy harvester based on 28 1-mm thick PST MLCs (4 rows × 7 columns). (b) Energy harvested by the prototype for different temperature spans and input voltages. Adapted from [30].

Table 2.3 Performance of pyroelectric energy harvesting devices when subjected to Olsen cycle

Material	Thickness of the element (μm)	Density ($\text{g}\cdot\text{cm}^{-3}$)	Active volume of one element (cm^3)	Number of elements	Total mass of the active elements (g)	Heat exchange fluid	ΔE ($\text{kV}\cdot\text{cm}^{-1}$)	ΔT_{span} (K)	f (Hz)	Energy (J)	Power (W)	Ref
PZST – (bulk)	250	7.6	0.14	24	26	Silicone oil (100 cP)	28	33	0.13	0.3	40×10^{-3}	[28]
PZST – (bulk)	250	7.6	0.24	175	319	Silicone oil (50 cP)	28	38	0.26	6.23	1.64**	[116]
73/27 P(VDF-TrFE) (polymer thin film)	50	1.9	25×10^{-3}	100	4.8	Silicone oil (200 cP)	330	44	0.08 – 0.5	0.75×10^{-3}	-	[96]
60/40 P(VDF-TrFE) (polymer thin film)	46	1.9	4.6×10^{-3}	38	330×10^{-3}	Silicone oil (50 cP)	177	17	0.06	0.6×10^{-3}	-	[125]

PST (multilayer capacitor)	38 (thickness per layer; total 19 active layers)	8.7	35×10^{-3}	28	8.7	Silicone oil (5 cP)	195	115	-	3.1	-	[30]
PST (multilayer capacitor)	38 (thickness per layer; total 9 active layers)	8.7	17×10^{-3}	280	42	Silicone oil (5 cP)	195	87	-	11.2	-	[30]

PZST= $\text{Pb}_{0.99}\text{Nb}_{0.02}(\text{Zr}_{0.68},\text{Sn}_{0.25},\text{Ti}_{0.07})_{0.98}\text{O}_3$, P(VDF-TrFE) = poly(vinylidene fluoride-trifluoroethylene), PST = $\text{Pb}(\text{Sc}_{1/2}\text{Ta}_{1/2})\text{O}_3$.

** This value was obtained only once, meaning that there was only one cycle performed.

2.4.3 Role of thermal control devices

To date, nearly all demonstrated macroscopic pyroelectric energy harvesters have employed fluid-based regenerators, typically arranging the active material in a parallel plate configuration. This design is advantageous due to its low flow resistance, high heat transfer coefficients, and easy access to electrical terminals. However, a major drawback of this approach is the large volume of inactive fluid, which lowers thermal efficiency and requires additional pumping power. Moreover, high cycle frequencies are difficult to implement because they demand high fluid flow rates. Among the few studies reporting power output, Olsen et al. [116] claimed a peak of 1.64 W, though this was calculated from energy harvested during a single cycle, not sustained power generation. Similarly, Lheritier et al. [30] reported 11.2 J of energy from a multilayer PST-based harvester over a 200-second cycle, corresponding to an average power of only 50 mW. Additionally, their numerical simulations suggested that power densities up to $2 \text{ W}\cdot\text{cm}^{-3}$ could be achieved by reducing the thickness of the material to 200 μm and using water as the heat transfer fluid (provided that appropriate electrical insulation is implemented). These factors represent key pillars for advancing pyroelectric power generation in fluid based pyroelectric harvesters.

Another promising route to increase power output is through thermal control devices, which exploit anisotropic thermal conductivity to modulate heat flow directionally. These devices vary the thermal resistance between the pyroelectric material and the heat reservoirs, enabling higher-frequency operation. They fall into three categories: fluidic, mechanical, and solid-state. Passive components like thermal diodes and regulators operate without external input, while thermal switches require external stimuli such as pressure, electric or magnetic fields. These components are characterized by a transfer function that relates the heat flow rate (Q) to the imposed temperature difference (ΔT). This section focuses on the application of thermal diodes and switches for electrothermal energy harvesting.

To illustrate the mechanism, consider an Olsen cycle applied to a pyroelectric material coupled with two thermal control devices, TD1 and TD2, which connect to the hot and cold reservoirs, respectively (see Figure 2.19). During the isothermal charging stage at low temperature, TD2 is activated to allow heat flow from the cold side while TD1 remains inactive. Once the material reaches the cold reservoir temperature (T_{cold}), it is electrically charged. Subsequently, TD2 is deactivated and TD1 is engaged to initiate isoelectric heating by transferring heat from the hot reservoir, while preventing backflow. Upon reaching the hot reservoir temperature (T_{hot}), the material is discharged. The cycle concludes with TD1 switching off and TD2 switching back on, allowing the system to return to its initial temperature and begin the next cycle. The

performance of a thermal diode is assessed through its rectification ratio (γ), which quantifies the asymmetry in forward and reverse heat flux:

$$\gamma = (|Q_{fwd}| - |Q_{rev}|) / |Q_{rev}|$$

Here, Q_{fwd} and Q_{rev} are the forward and reverse heat fluxes at a given temperature difference. It must be noted that Q_{fwd} is always greater than Q_{rev} at the same ΔT . Heat pipes serve as effective thermal diodes due to their ability to direct heat preferentially in one direction, resulting in a high rectification ratio. They are particularly relevant for electrothermal energy harvesting because they utilize the latent heat of vaporization and condensation of the working fluid, thereby achieving high heat transfer coefficients. This mechanism enables rapid thermal cycling and supports high-frequency operation with substantial power output. Active heat pipes are currently being explored for caloric cooling applications, with reports indicating enhanced cooling capabilities of approximately $12.5 \text{ W}\cdot\text{g}^{-1}$ at operational frequencies up to 20 Hz [127].

Likewise, thermal switches offer a method for dynamically modulating the thermal conductivity of a system. Their performance is commonly quantified by the switching ratio (SR), which measures the contrast between thermal conductivities in the ON (high) and OFF (low) states:

$$SR = \frac{\dot{Q}_{on}}{\dot{Q}_{off}}$$

where \dot{Q}_{on} and \dot{Q}_{off} are the heat fluxes during the ON and OFF states of the switch. For effective high-frequency operation, both a high switching ratio and rapid response times are essential [128–130]. In one study, Epstein and Malloy [131] demonstrated thin-film heat switches based on liquid crystals for thermal energy harvesting and caloric refrigeration. Their devices exhibited switching times on the order of milliseconds and achieved efficiencies up to 66% of the Carnot limit, attributed to substantial differences in thermal conductivity between states. In another investigation, Jia and Ju [132] evaluated liquid-based thermal interfaces using BTO multilayer capacitors and achieved a switching ratio exceeding 100 at 0.3 Hz, delivering a specific cooling power of $500 \text{ W}\cdot\text{m}^{-1}$. More recently, Cha et al. [133] applied a liquid-based thermal interface in a nonlinear pyroelectric energy conversion system using P(VDF-TrFE). Operating near 1 Hz over a temperature range of 40°C to 100°C with a field of $300 \text{ kV}\cdot\text{cm}^{-1}$, they reported an active power density of $110 \text{ mW}\cdot\text{cm}^{-3}$.

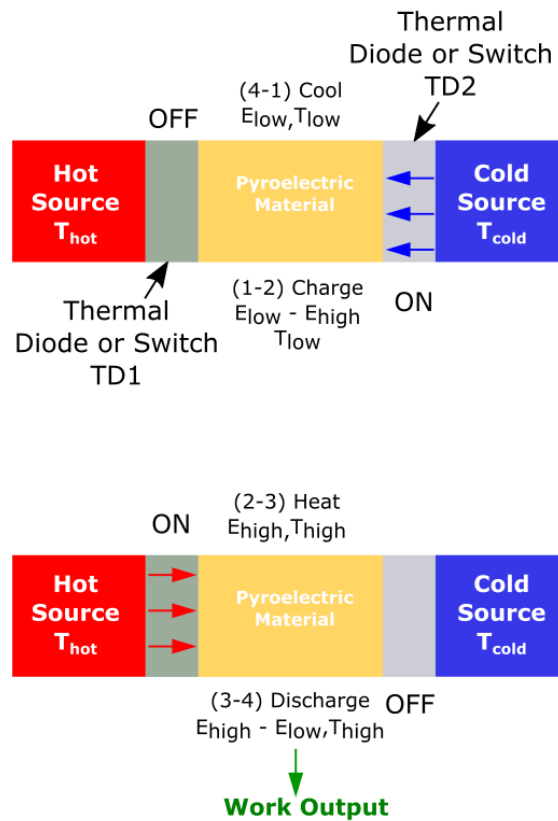


Figure 2.19 Working principle of thermal diode/switch under Olsen pyroelectric cycle.

2.4.4 Significance of power interface systems

Despite considerable progress in material development and thermal management, the overall performance of nonlinear pyroelectric devices remains limited at the system level, primarily due to energy losses in external power electronics. Although most energy recovery circuits have been tailored for electrocaloric systems, many of these architectures can be adapted for pyroelectric energy harvesting.

The most widely implemented recovery method in electrocaloric applications relies on resonant circuits, where energy is transferred between two capacitors through an inductor [134,135]. Defay et al. [134] demonstrated that using such a setup with antiphase operation between two BaTiO_3 MLCs enabled the recovery of up to 80% of the input energy. However, this approach is constrained by the inductor's charge transfer time constant [136]. In addition, high current levels during charging introduce conduction losses in both diodes and inductors, further limiting circuit efficiency. According to Mönch et al. [137], achieving system-level efficiencies as high as 50% of the Carnot limit requires minimizing both intrinsic material losses and external circuit dissipation.

To overcome the inherent limitations of resonant topologies, alternative solutions like switched-mode power converters have been proposed to improve overall efficiency [30,138,139]. One such approach, originally developed for piezoelectric harvesters, is

synchronized switch harvesting on inductor (SSHI). Guyomar et al. [38] evaluated this technique for thermal energy harvesting. In the SSHI architecture, the pyroelectric element is linked to a switchable inductor placed in parallel with the AC side of a rectifier bridge, while a storage capacitor is connected to the DC side (see Figure 2.20). The switch remains open during most of the thermal cycle and is momentarily closed at the temperature extrema, initiating a brief resonant oscillation. It is closed for a duration of $\pi\sqrt{L\cdot C}$, corresponding to half of the LC oscillation period, and is opened once the voltage polarity across the pyroelectric element inverts. As the material heats under open-circuit conditions, its voltage rises. Once the voltage reaches the DC bus level, the rectifier conducts, allowing charge to flow into the storage capacitor. The subsequent cooling phase returns the system to its initial state, completing the cycle. In this way, the losses can be reduced, and significant amount of the harvested energy can be extracted from the material for performing useful work.

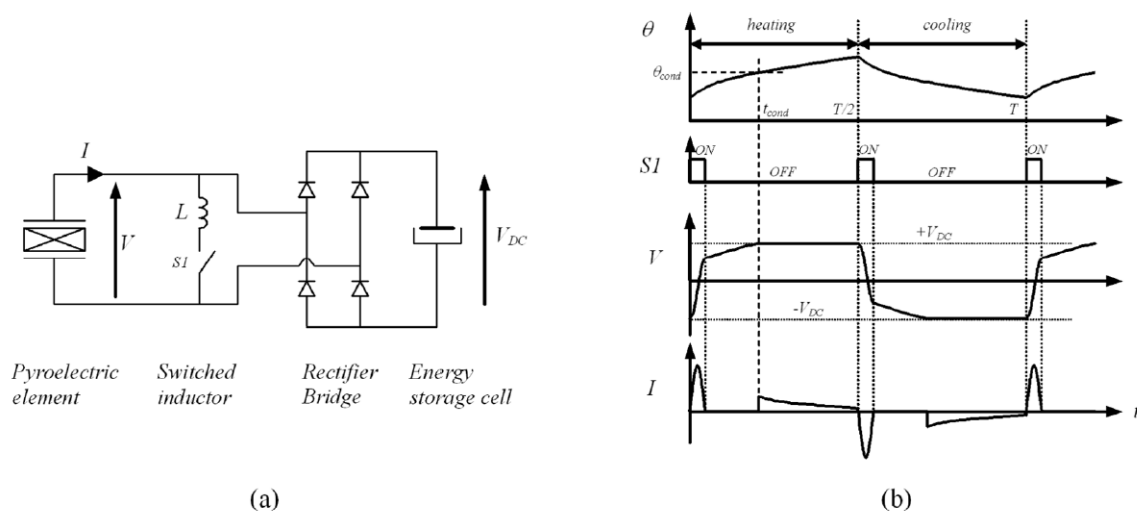


Figure 2.20 (a) Circuit diagram of parallel SSHI device and (b) typical waveform [36].

This chapter has established the theoretical and technological foundations of pyroelectric energy harvesting, beginning with the fundamental principles of polar materials and progressing through linear and nonlinear energy conversion mechanisms. A particular focus was given to advanced harvesting strategies, including regenerative cycle designs, macroscopic device architectures, and the critical roles of thermal control and power interface systems in enhancing overall performance. These discussions highlight the critical interplay between material properties, device geometry, and system-level components in determining the overall efficiency and applicability of pyroelectric energy harvesting technologies.

Chapter 3

Pyroelectric conversion potential of pure and doped $\text{Pb}(\text{Sc}_{1/2}\text{Ta}_{1/2})\text{O}_3$ thin films

3.1 Motivation

Lead scandium tantalate, $\text{Pb}(\text{Sc}_{1/2}\text{Ta}_{1/2})\text{O}_3$ (PST), has been widely investigated for electrocaloric (EC) and pyroelectric applications due to its peculiar order-disorder transition behaviour [140–144], high pyroelectric coefficient (p) [108,145,146] and large entropy variation (ΔS) close to its transition temperature [41,82,107], which occurs around room temperature. Earlier studies primarily focused on the EC response, demonstrating significant adiabatic temperature changes (ΔT_{ad}) in ordered PST ceramics [147–150]. More recent investigations have reported ΔT_{ad} values as high as 3.7 K at 40 kV/cm in highly ordered PST ceramics [151], and 5.5 K in PST multilayer capacitors (MLCs) at 290 kV/cm by driving the first-order transition using supercritical fields [82]. Despite advances in understanding PST's transition behaviour and their EC response, its potential for non-linear pyroelectric energy harvesting remains underexplored. Although a strong EC response directly correlates with a high p , this alone does not ensure high electrical work output under non-linear conditions, as external factors such as thermal conditions, charge–discharge rates, breakdown field, and hysteresis behaviour at elevated temperatures also substantially influence the performance. Recently, it was reported in our group that up to $4.4 \text{ J}\cdot\text{cm}^{-3}$ of energy density per cycle can be generated using the Olsen cycle in PST MLCs [30].

This raises the question of how to further enhance the energy harvesting performance of PST-based materials. One promising approach is utilizing thin films, as they allow the application of significantly higher electric fields, which directly scale with pyroelectric energy density. Additionally, thin films possess a smaller thermal time constant, enabling rapid heat exchange which could lead to high power densities. Recently, Pandya et al. [45] reported power densities as high as $500 \text{ W}\cdot\text{cm}^{-3}$ in relaxor thin films. Most importantly, thin films are compatible with standard microfabrication processes, making them ideal candidates for integration into microelectronic devices for energy harvesting and storage applications. However, despite extensive research on the processing of PST ceramics and thin films, no study has reported the non-linear

pyroelectric conversion potential of PST thin films, highlighting a critical gap in the literature.

This chapter aims to address this gap by investigating the non-linear pyroelectric response of PST thin films fabricated using the sol-gel technique. In addition to being a cost effective method, sol-gel deposition enables precise compositional control, which can be utilized to tailor the transition temperature of PST through doping. This also raises an important question: Is it possible to shift the transition temperature of sol-gel deposited PST thin films through doping? Previously, Shebanov et al. [147,149] reported that the transition temperature of PST bulk ceramics could be shifted with various dopants. While doping PST ceramics with 10 mol.% of Sb^{5+} , Y^{3+} , Ti^{4+} , or Nb^{5+} , a high ECE was reported due to the high ordering in these samples. However, the structural and dielectric characterizations of the doped samples were not provided in their study. Thus, the influence of these dopants on the structural and dielectric properties of PST, especially in thin film geometry, still remains an open question.

The main objectives of this chapter are as follows:

- 1) Prepare high-quality PST thin films using the sol-gel technique and investigate if their maximum harvestable pyroelectric energy density can surpass $4 \text{ J}\cdot\text{cm}^{-3}$.
- 2) Investigate the influence of Ti^{4+} doping on the transition temperature of PST and determine whether the transition can be shifted to higher temperatures, as reported by Shebanov et al. [12], through systematic variation of the dopant concentration.
- 3) Evaluate the pyroelectric conversion efficiency of undoped and Ti-doped PST thin films and indirectly estimate their performance in a multi-stage device through a conceptual study.

For clarity, this chapter begins with a background on PST and its physical properties (Section 3.2). This is followed by a section on the fabrication of PST thin films using the sol-gel technique (Section 3.3) and a detailed structural and electrical characterization to estimate their maximum harvestable energy density (Section 3.4). Subsequently, the Ti-doped PST system based on the existing literature is presented (Section 3.5). The synthesis of Ti-doped PST thin films is detailed in Section 3.6, followed by an estimation of the pyroelectric conversion efficiency of both pure and Ti-doped PST thin films based on electrical characterization in Section 3.7. This section also includes a conceptual study analysing the performance of Ti-doped PST thin films in a multistage device. Finally, Section 3.8 summarizes the key findings and conclusions of this study.

Among the several experimental results presented in this chapter, the dielectric measurements using Novocontrol Concept 40 dielectric spectrometer was performed by Dr. Torsten Granzow.

The results presented in the first part of this chapter focusing on the maximum harvestable energy density using PST thin films, are based on my first-author publication [152]: “*Large pyroelectric energy conversion in lead scandium tantalate thin films. Heliyon, 10(9), (2024)*”.

The second part of this chapter, which examines Ti-doped PST thin films for thermal energy conversion, is based on my research article, “*Ti-doped Pb(Sc_{0.5}Ta_{0.5})O₃ Thin Films for Non-linear Pyroelectric Energy Harvesting. Ceram Int, 51, (2025), 47264 – 47271*”.

3.2 Lead Scandium Tantalate – Pb(Sc_{1/2}Ta_{1/2})O₃ (PST)

PST has a perovskite structure of A(B_{1/2}B_{1/2})O₃, where the A-site is occupied by Pb²⁺ ions, while the octahedral B-site is occupied by Sc³⁺ and Ta⁵⁺ ions. Depending on the arrangement of B-site cation species, PST can exhibit different degrees of order, influencing its phase transition behaviour and physical properties [153,154]. If Sc³⁺ and Ta⁵⁺ ions alternate perfectly at adjacent B-sites (1:1 ordering), it leads to unit cell doubling, indicating perfect order. Ordered PST undergoes a sharp first order transition from ferroelectric to paraelectric phase around 290 – 300 K [145]. In disordered PST, Sc³⁺ and Ta⁵⁺ ions randomly occupy the B-site, resulting in a diffuse phase transition behaviour as shown in Figure 3.1.

The long-range order parameter (Ω) is quantified as $2n - 1$, where n denotes the fractional occupation number of either Sc or Ta ions in the alternating B-site. For a perfectly ordered sample, $\Omega \rightarrow 1$, and for a completely disordered sample, $\Omega \rightarrow 0$. Cation ordering in PST can be estimated using X-ray diffraction (XRD) [154], transmission electron microscopy (TEM) [155] or Raman spectroscopy [156]. Most commonly, Ω is quantified using XRD, as ordered samples give rise to superstructure peaks due to unit cell doubling [141,157]. By comparing the intensities of one of the superstructure peaks (111) to the base lattice (200) reflection of the sample with respect to the calculated ratio of intensities for perfect ordering, the value of Ω can be estimated using Equation (3.1) as follows:

$$\Omega^2 = \frac{\left(\frac{I_{111}}{I_{200}}\right)_{exp}}{\left(\frac{I_{111}}{I_{200}}\right)_{theory,\Omega=1}} \quad (3.1)$$

For an ordered PST sample, the (111) superstructure peak is observed at 18.8° and the calculated value of $\left(\frac{I_{111}}{I_{200}}\right)_{theory, \Omega=1}$ obtained using $\text{CuK}\alpha$ radiation is 1.33 [141]. It must be noted that this theoretical value slightly varies depending on the radiation source used, as peak intensity values change. For instance, $\left(\frac{I_{111}}{I_{200}}\right)_{theory, \Omega=1} = 1.4$ for $\text{CoK}\alpha$ radiation. Moreover, this value also varies upon the introduction of dopant species in the B-site, as it alters the structure factors for the (111) and (200) reflections [158].

The absence of superstructure peaks indicates that the material is disordered. Stenger et al.[140] were the first to investigate order – disorder transition behaviour in PST. They reported that a decrease in Ω led to a diffuse phase transition accompanied by an increase in the maximum dielectric constant (ϵ'_{max}). Disordered PST samples exhibit a relaxor behaviour with a broad transition temperature and a strong low frequency dielectric dispersion in the transition range. In contrast, ordered PST undergoes a sharp transition with a lower ϵ'_{max} , a higher Curie temperature (T_c) and a pronounced latent heat at the transition (see Figure 3.2). Subsequently, Setter et al. [154,157] reported that cation ordering can be induced in a disordered PST sample through suitable heat treatments. The main driving force responsible for ordering is the difference in ionic size and charge between the B-site cations. The larger the difference, the easier it is to induce ordering in the material. Since the Sc^{3+} (0.74 Å) and Ta^{5+} (0.64 Å) ions possess intermediate size and charge differences, PST is close to the limit of stability between ordered and disordered states. In other words, their diffusion kinetics is sluggish. Hence, to promote the ordering process, PST should be processed and annealed at high temperatures, typically around 1000°C for extended durations followed by a slow cooling rate [157].

Due to the challenges associated with high processing temperatures, the development of PST thin films only began to attract interest in the late 1980s, after Patel et al.[159] and Liu et al. [160] successfully fabricated them using the sol-gel technique at low temperatures. Later, a series of publications by R.W. Whatmore and colleagues reported on the different processing routes of PST thin films and the kinetics of their transformation from amorphous to perovskite phase during annealing [159,161–164]. It was reported that sol-gel deposited PST thin films must be annealed at high temperatures ($> 700^\circ\text{C}$) to obtain the best electrical properties comparable to bulk PST ceramics [164]. Such films exhibited a high pyroelectric coefficient ($3.8 \times 10^{-3} \text{ C}\cdot\text{m}^{-2}\cdot\text{K}^{-1}$ induced at $5 \text{ V}\cdot\mu\text{m}^{-1}$) at 30°C and a high material figure of merit ($11 \times 10^{-5} \text{ Pa}$) used for detector and sensing applications. However, due to the requirement of high annealing

temperatures, the impact of B site chemical ordering and kinetics of transformation in the ordered PST thin films were not studied thoroughly during this period.

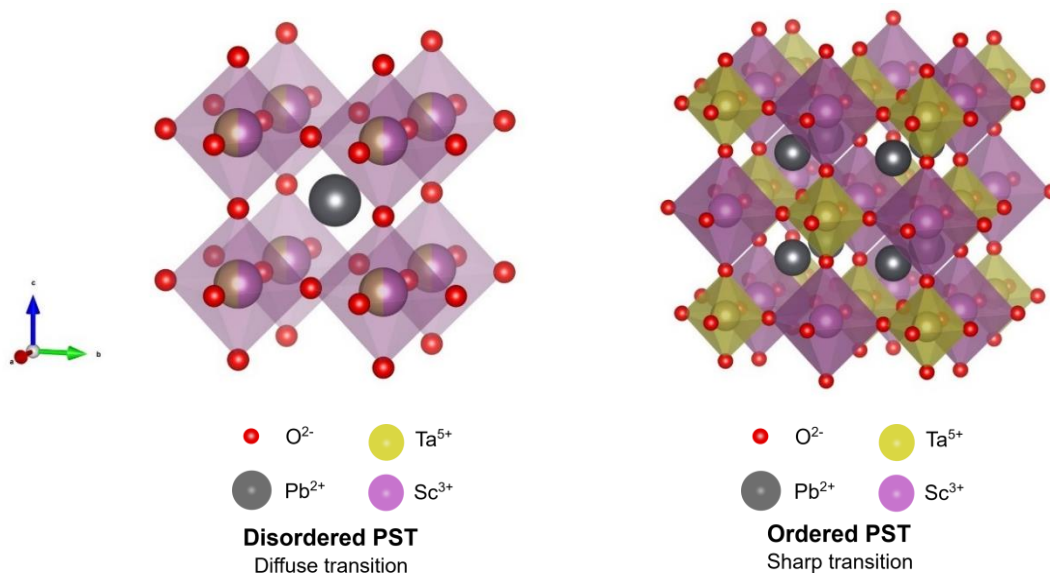


Figure 3.1 Perovskite structure $A(B'B'')O_3$ of disordered and ordered PST (drawn using VESTA software [165]).

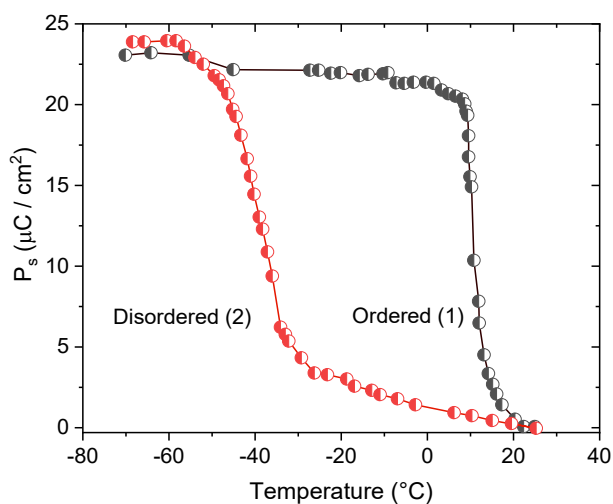


Figure 3.2 Spontaneous polarization change in disordered and ordered PST samples as a function of temperature (graph replotted from [154]).

In the early 2000s, Brinkmann et al.[166] investigated the processing parameters for achieving high cation order in sol-gel grown PST thin films. They reported the highest B-site order ($\Omega = 0.91$) in PST films grown on sapphire substrates after annealing them in a PbO saturated atmosphere for 35 h followed by a 5°C min^{-1} cooling rate. Additionally, they reported two important findings that deviate from the behaviour observed in bulk PST ceramics [167,168]:

- 1) The dielectric constant increased with an increase in B-site order in thin films, whereas it decreased with increasing order in bulk PST ceramics. However, in both cases, the T_c shifted to higher temperatures with increasing order.
- 2) The intrinsic nature of relaxor behaviour in disordered thin films was similar to that of ceramics/single crystals, although the nano-polar regions exhibited diluted quantitative responses due to low processing temperatures, and field-induced cooling did not induce long-range polar order in the disordered PST films.

Later, Correia et al.[169] investigated the EC properties of partially ordered ($\Omega = 0.32$) PST thin films on Pt-Si substrates. Using indirect techniques, they estimated a maximum $|\Delta T_{ad}|$ of 6.9 K when $\Delta E = 774 \text{ kV}\cdot\text{cm}^{-1}$ at $\sim 390 \text{ K}$. Most recently, Kovacova et al. [170] reported a high ECE of 15 K in relaxor PST thin films on c-sapphire substrate at 15°C when the field reached $1330 \text{ kV}\cdot\text{cm}^{-1}$. High ECE was observed due to the application of high electric field in-plane using interdigitated electrodes (IDEs). These studies encourage to investigate the non-linear pyroelectric conversion potential of PST thin films.

3.3 Preparation of PST solution and thin films

PST solution was prepared using the sol-gel technique² with lead(II) acetate trihydrate ($\geq 99.9\%$ purity), scandium(III) acetate hydrate ($\geq 99.9\%$ purity), tantalum(V) ethoxide metal precursors ($\geq 99.9\%$ purity) along with 2-methoxyethanol (2-MOE) as the solvent. All the reagents used in this work were purchased from *Merck, Germany*. Prior to the preparation of solution, lead and scandium precursors were freeze dried for 48 h to remove the water, as tantalum(V) ethoxide is highly moisture sensitive and hydrolyses rapidly. First, scandium (III) acetate and tantalum (V) ethoxide were mixed in 2-MOE and the mixture was refluxed for 24 h at 130°C under argon atmosphere. Since the 2-MOE solvent results in the structural modification of the Sc precursor, longer reaction times were necessary to obtain a homogeneous Sc/Ta complex. Nonetheless, the solutions prepared by this route were reported to be more stable and led to increased perovskite phase formation [171]. After completion of the reaction, a clear and transparent solution is obtained. Later, lead acetate (in 30 % excess) was mixed with the as-prepared Sc/Ta complex and an additional reflux step was carried out for 2 h. Excess lead content was used to compensate for any possible Pb loss during the heat treatment steps. Moreover, it was reported that a complete perovskite phase free of secondary pyrochlore phases could only be achieved with more than 20%

² Detailed background on the sol-gel technique can be found in Appendix A.1.

excess lead [57]. Finally, the prepared PST solution was distilled to remove the by-products from the reflux step, and it was diluted with 2-MOE solvent to obtain a final concentration of 0.3 M.

For film deposition, the PST solution was spin-coated onto c-sapphire substrates (purchased from Siegert Wafer) that had been coated with a 20 nm-thick HfO₂ buffer layer deposited using atomic layer deposition (ALD). The c-sapphire substrate was selected for two reasons: (1) its thermal expansion coefficient is close to that of PST, reducing thermal mismatch during annealing; and (2) previous studies have reported the highest B-site ordering in PST thin films deposited on sapphire substrates, as it can withstand high annealing temperatures. However, the use of a seed layer is often required on sapphire substrates to promote heterogeneous nucleation and initiate perovskite phase without any secondary pyrochlore phase [57]. Hence, PbTiO₃ (PT) was used as the seed layer to promote preferential orientation and facilitate perovskite phase formation. The PT solution was prepared via the sol-gel method using lead(II) acetate (in 30% excess) and titanium (IV) isopropoxide ($\geq 98\%$ purity) as metal precursors, with 1-methoxy 2-propanol (1M2P, $\geq 99.9\%$ purity) as the solvent. Acetylacetonate was added as a complexing agent to control the hydrolysis and polycondensation reaction of the PT solution [172]. The solution was refluxed at 130°C for 3 h under inert atmosphere followed by the distillation step to remove the remaining acetates and isopropanol byproducts. To obtain the final concentration of 0.1 M, the solution was diluted using 1M2P. Unlike the stable PST solution, the PT solution ages and degrades after approximately 30 days. However, PT films derived from 1M2P are known to yield better orientation and enhanced ferroelectric properties [172].

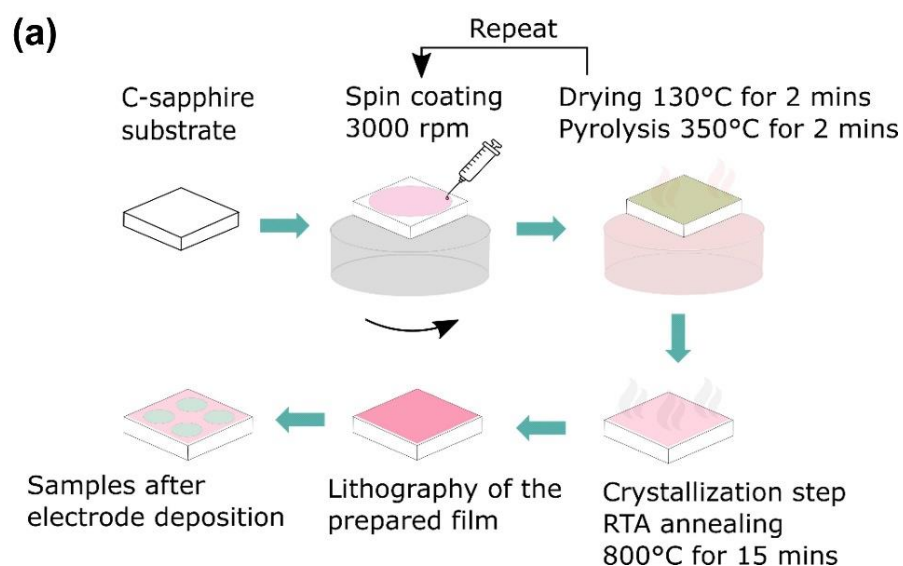
The PT solution was first spin coated onto the c-sapphire substrate at 3000 rpm for 30 s, followed by drying and pyrolysis at 130°C and 350°C for 2 mins each, respectively. The pyrolyzed film was crystallized at 700°C for 60 s in an 80% N₂ and 20% O₂ atmosphere using rapid thermal annealing (Annealsys AS-MASTER 2000) with a heating rate of 50°C s⁻¹. Following the seed layer deposition, the PST solution was spin-coated onto the substrate under similar deposition, drying and pyrolysis conditions. To achieve the desired film thickness, these steps were sequentially repeated four times. Finally, the film was annealed at 800°C for 15 min in the RTA chamber with the same heating rate, followed by furnace cooling, as shown in Figure 3.3 (a).

To characterize the in-plane electrical properties of the fabricated thin films, interdigitated (IDEs) electrodes were patterned using a lift-off photolithography

process with a maskless aligner MLA 150 (*Heidelberg Instruments, Germany*). A bi-layer resist approach was employed to define the electrode geometry. First, a polydimethylglutarimide-based lift-off resist (LOR3A, Microchem) was spin-coated onto the PST thin film followed by a layer of positive photoresist (S1813, Rohm and Haas). The electrode patterns were exposed using a maskless lithography tool (MLA 150, Heidelberg Instruments), with exposure parameters optimized through a dose test. After exposure, the pattern was developed by rinsing with MF-319 developer (Microposit, DOW), which dissolved the positive photoresist in the exposed regions.

Subsequently, platinum was deposited by sputtering using a BALTEC MDE020 metallizer. The deposition was carried out under an argon pressure of 3.5×10^{-2} mbar at a power of 40 W, with a target-to-substrate distance of 6 cm for 100 seconds, resulting in an electrode thickness of approximately 100 nm. Later, the lift-off was carried out by immersing the sample in a resist remover (Remover PG, Microchem).

To encapsulate the IDEs and prevent electrical arcs between the electrode fingers, an epoxy based negative photoresist (SU-8 3005, Microchem) was spin coated over the patterned samples. This encapsulation layer was then exposed, developed, and thermally cured to electrically isolate the devices. A schematic of the device is shown Figure 3.3 (b). Each IDE consists of 50 pair of fingers, with an effective length of 370 μm , a finger width of 5 μm and a 3 μm gap between adjacent fingers.



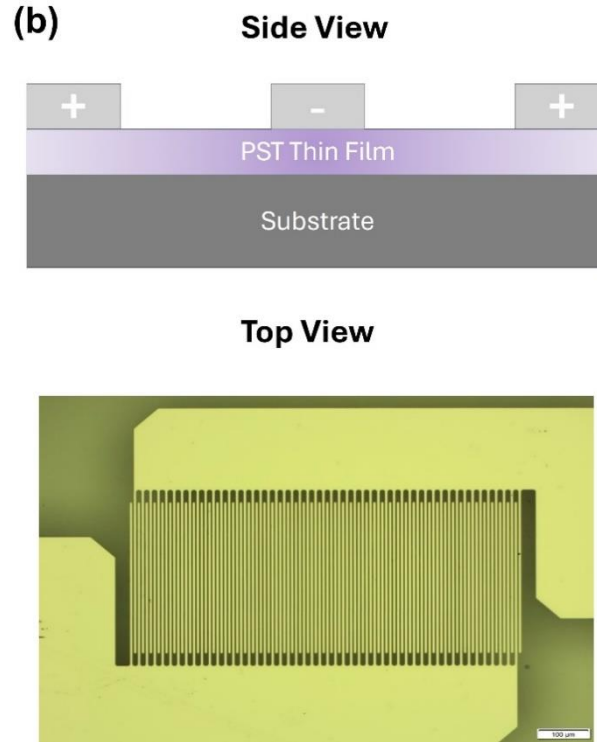


Figure 3.3 (a) Spin coating process flow for fabricating PST thin films. (b) Schematic of an IDE configuration along with the optical microscopy image of a PST thin film patterned with platinum IDEs.

3.4 Results and discussion

3.4.1 XRD analysis

To investigate the phase and texture of deposited PST thin films on c-sapphire substrates, a $\theta - 2\theta$ scan was performed from 10 to 70° with a step size of 0.02° and a 2 s time interval per step. The resulting XRD pattern indicates the presence of a single phase perovskite structure with a strong (200) orientation alongside a weak (220) peak [PDF card 01-074-2635] as shown in Figure 3.4 (a). No secondary pyrochlore phases were observed. The pronounced (200) orientation is attributed to the PbTiO_3 seed layer. Due to the preferential orientation of the film, the superstructure peaks might not be observed in the $\theta - 2\theta$ scan, which primarily provides information about the film's out-of-plane orientation.

Hence, to specifically investigate the presence of (111) superstructure peak relative to the (200) plane, the sample was tilted along the pseudo-cubic [111] direction to $\chi = 54.7^\circ$ (angle at which (111) peak would exhibit maximum intensity if B-site ordering were present), and a $\theta - 2\theta$ scan was carried out between 16 to 21° with a step size of 0.02° and a 20 s time interval per step using a collimated beam (see Appendix A.2 for more details about this technique). Since the main texture of the film is already known

and the sole interest is to detect the presence of (111) superstructure peak, comprehensive pole figure measurements were not performed. The absence of (111) peak at 18.8° when χ angle was fixed at 54.7° confirms that these films lack B-site ordering, as shown in Figure 3.4 (b).

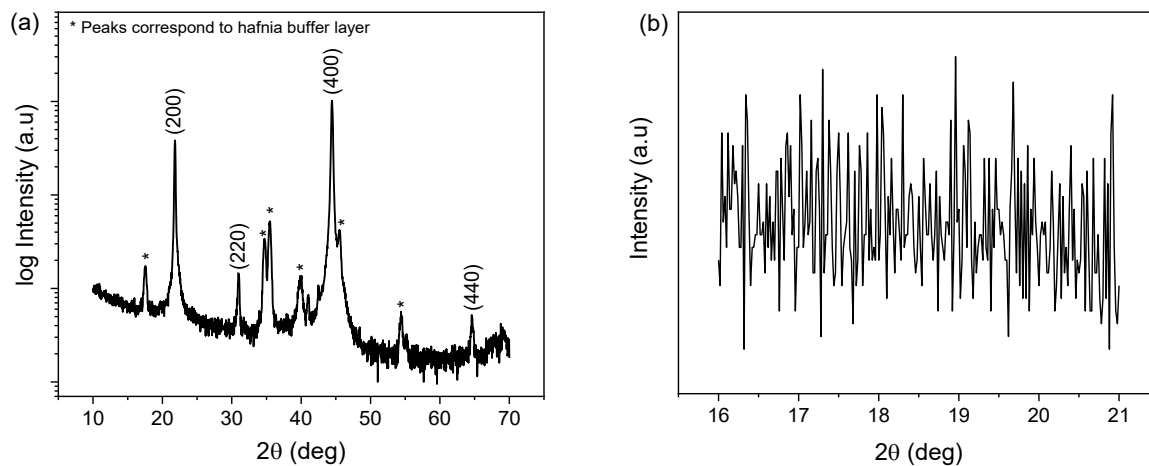


Figure 3.4 XRD pattern of sol-gel deposited PST thin film (a) $\theta - 2\theta$ scan at $\chi = 0^\circ$; (b) $\theta - 2\theta$ scan at $\chi = 54.7^\circ$.

3.4.2 Microstructure analysis

The morphology and cross section of the PST thin film were examined using a Helios Nanolab 650 SEM (details about the technique and the instrument can be found in Appendix A.3). The top-view SEM image revealed a dense and homogeneous microstructure with an average grain size of approximately 180 nm (see Figure 3.5 (a)). No secondary pyrochlore phases were observed. Although minor porosity was present, it accounted for less than 2% of the film area. Both the average grain size and porosity were estimated using ImageJ software. Additionally, the cross-section image indicated a film thickness of around 165 nm, exhibiting a dense uniform film growth, as shown in Figure 3.5 (b). For comparison, Brinkmann et al. [57] reported significantly larger grains ($\sim 5 \mu\text{m}$) in PST thin films fabricated on sapphire substrates. This considerable difference in grain size may be attributed to enhanced surface diffusion processes, driven by higher annealing temperatures and slower cooling rates, both of which are known to promote grain growth.

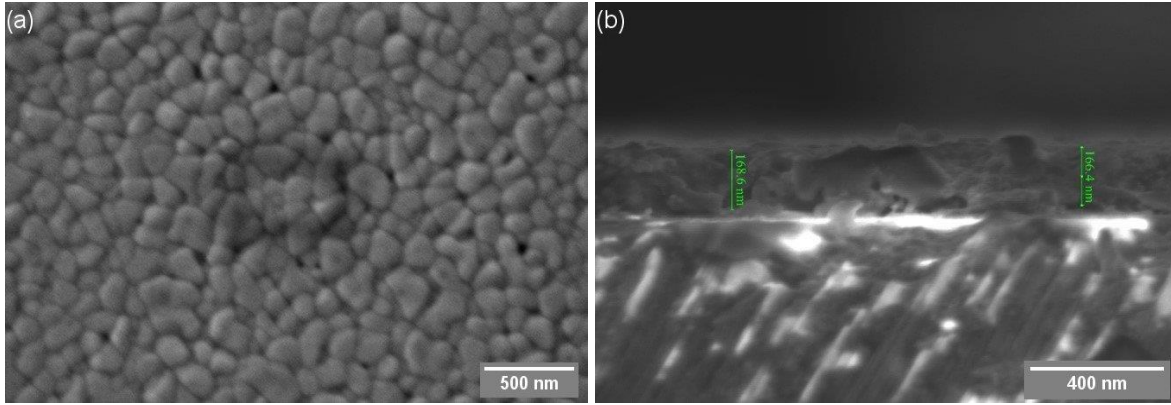


Figure 3.5 SEM images of the PST thin film (a) Top-view; (b) Cross-section.

3.4.3 Dielectric measurements and analysis

The dielectric constant (ϵ) and loss tangent ($\tan \delta$) of PST thin films were measured from -50 to 120°C at different frequencies using Novocontrol Concept 40 dielectric spectrometer. Under zero bias field conditions, ϵ reached a maximum of 3590 at 1 kHz, occurring at 40°C . Additionally, the broad peak observed in both ϵ and $\tan \delta$ suggests a diffuse phase transition, indicating the absence of B-site ordering, as shown in Figures 3.6 (a) and (b). These findings align with the XRD analysis. Moreover, the strong frequency dispersion, where T_m increases with frequency, confirms the relaxor behaviour of these films.

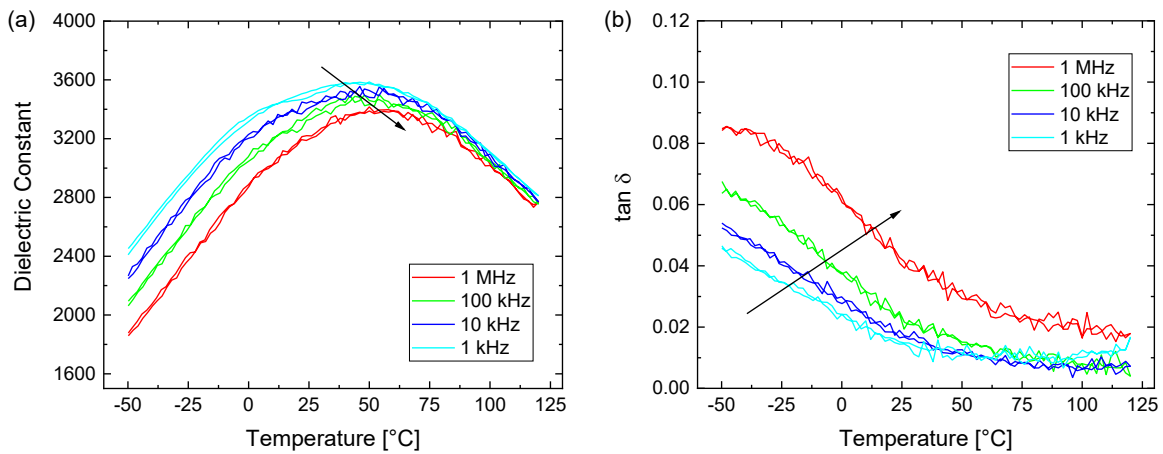


Figure 3.6 Temperature and frequency dependence of PST thin films (a) dielectric constant; (b) loss tangent.

The measured ϵ values for the disordered PST thin films are consistent with the previous reports from Brinkman and colleagues [173]. They also reported that ϵ value increased with B-site ordering in PST thin films, which was not the case in PST bulk ceramics and single crystals. However, a detailed explanation for this behaviour was not provided. Furthermore, they reported that applying a DC field during cooling

failed to induce long-range ordering in disordered PST thin films. To verify this claim, dielectric measurements were carried out under different bias fields while cooling through T_m (see Figure 3.7). While increasing the bias field, the value of ϵ decreased approximately by 8 %, which can be attributed to the polar region alignment [173]. The absence of significant shift in T_m and $\tan \delta$ profiles indicate the lack of field-induced phase transition.

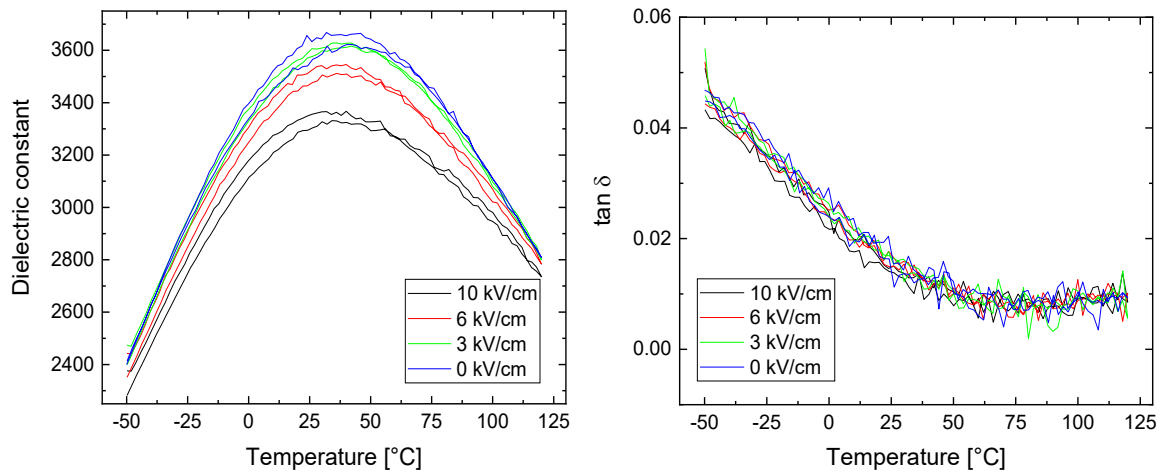


Figure 3.7 Dielectric constant and loss tangent behaviour of PST thin films under different bias fields across various temperatures.

3.4.4 Maximum harvestable energy density

To indirectly estimate the maximum harvestable energy density of PST thin films when subjected to Olsen cycle, bipolar $D - E$ loops were measured at different temperatures while varying the electric field and frequency using aixACCT TF 2000 analyser (check Appendix A.4 for more information about the measurement procedure and instrument specifications). Initially, to evaluate the breakdown limit of the film, $D - E$ loops were measured at room temperature under high electric fields. At 21°C, PST thin films were able to withstand fields exceeding $2000 \text{ kV}\cdot\text{cm}^{-1}$ at 100 Hz, yielding a P_{\max} value of $96 \text{ }\mu\text{C}\cdot\text{cm}^{-2}$, as shown in Figure 3.8. The slim loops with nearly zero remanence indicate relaxor behaviour, aligning with the frequency-dependent dielectric measurements. However, as the temperature increased, the hysteresis loops broadened, ultimately leading to the electrical breakdown of the capacitors at high fields.

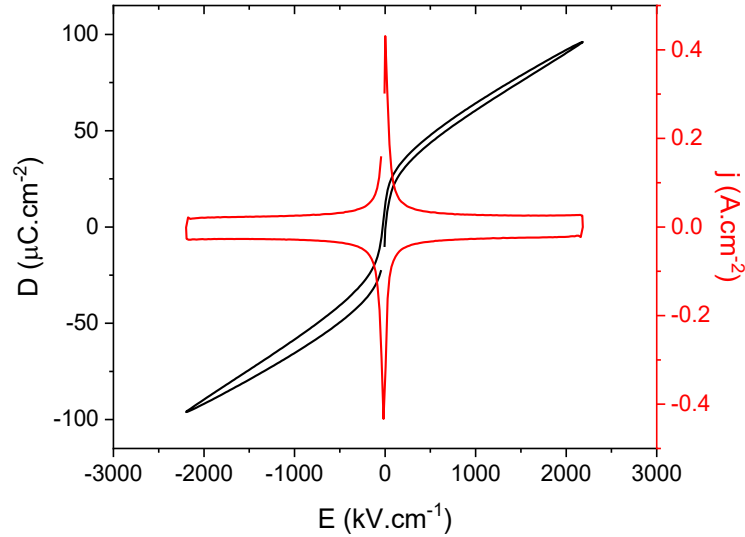


Figure 3.8 $D - E$ loop (in black) and $j - E$ loop (in red) of PST thin films.

Due to this reason, the maximum applied field was restricted to 1500 kV/cm. Additionally, the films were tested at different frequencies between 0 and 100°C, with the highest energy density of 6.5 J·cm⁻³ per cycle observed at 100 Hz. Figure 3.9 shows the first quadrant of the bipolar $D - E$ loops measured at different frequencies. As expected, at higher frequencies, the hysteresis loops broaden, reducing the harvestable energy density area, which is calculated using $\oint E dD$. Based on these results, all subsequent measurements were conducted at 100 Hz. Since thin films facilitate rapid heat exchange due to their small thermal time constant, this frequency would be suitable for the practical implementation of Olsen cycle in thin and thick films [71]. By enlarging the temperature span, a maximum harvestable energy density of 9.1 J·cm⁻³ per cycle was deduced when the Olsen cycle was implemented between 0 and 150°C, with the electric field varying from 50 to 1500 kV·cm⁻¹. To verify the reproducibility of the results, additional measurements were conducted on four different electrodes under identical conditions, yielding an average energy density of 8.8 J·cm⁻³ per cycle as shown in Figure 3.10. Despite the lower ΔP values, higher energy densities were achieved, as these high quality films were able to sustain large electric fields. Table 3.1 compares the pyroelectric energy densities of various materials from the literature.

Further improvement in energy density could be realized by enhancing both ΔP and ΔE . A large ΔP is observed in highly ordered PST samples, which could be attained by annealing them for longer durations or through doping which could result in the high degree of structural rearrangement to obtain 1:1 ordering, as suggested by Shebanov et al. [147].

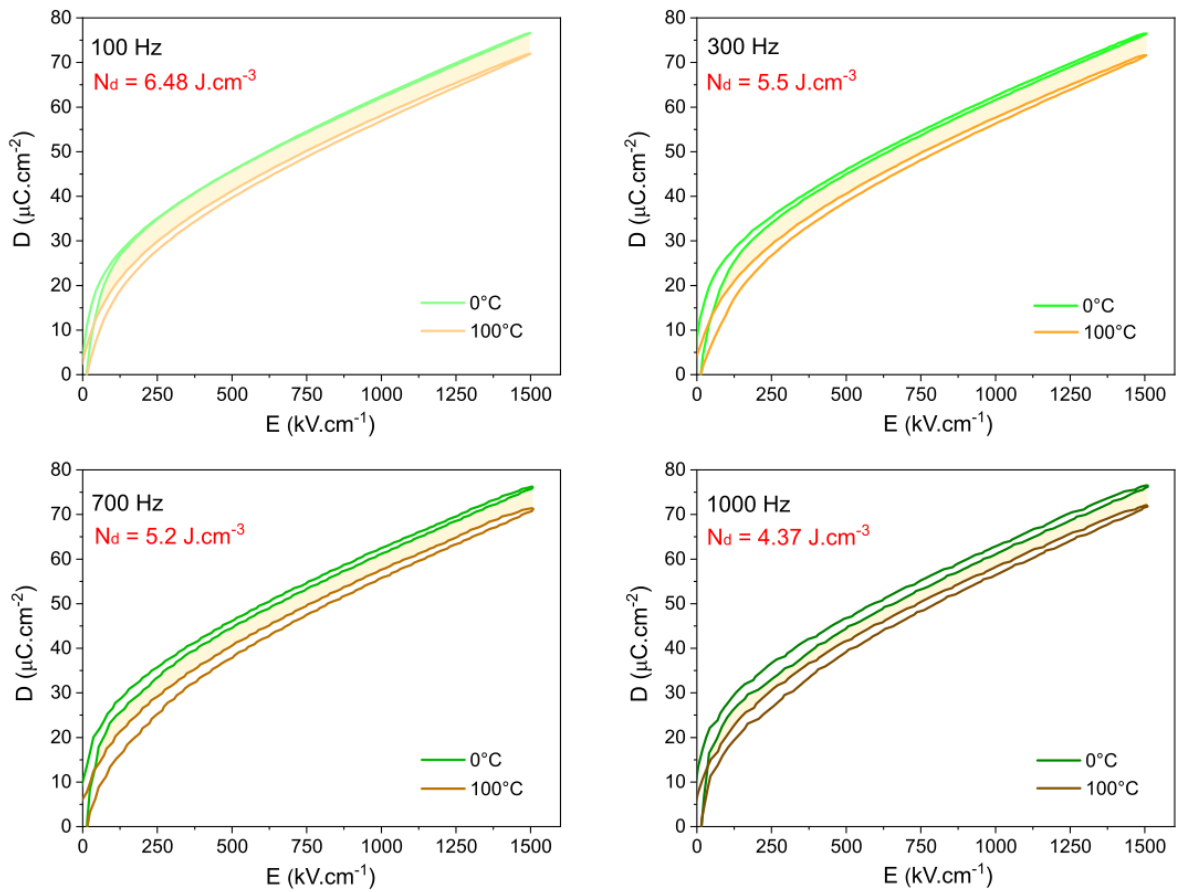


Figure 3.9 Indirect estimation of energy density using Olsen cycle between 0°C and 100°C at different frequencies.

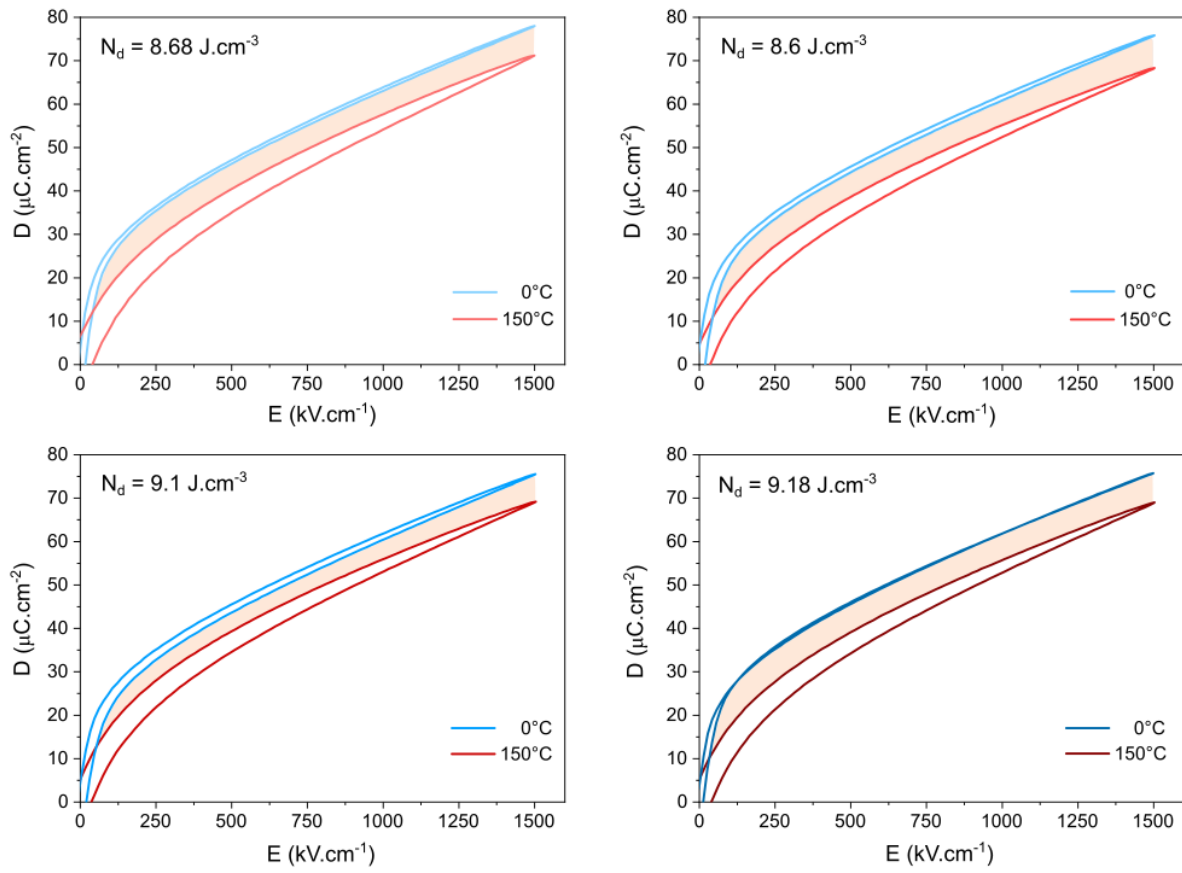


Figure 3.10 Maximum pyroelectric energy density in PST thin films using Olsen cycle between 0°C and 150°C .

Table 3.1 Pyroelectric energy densities of various materials using the Olsen cycle

Material	Type Thickness (μm)	ΔT (K)	T_i ($^{\circ}\text{C}$)	Energy density (J/cm^3)	ΔE (kV/cm)	Ref.
BaTiO_3	Thin film (0.1)	100	20	0.01	25	[44]
* $\text{Pb}_{0.99}\text{Nb}_{0.02}(\text{Zr}_{0.68}\text{Sn}_{0.25}\text{Ti}_{0.07})_{0.98}\text{O}_3$	Ceramic (250)	33	145	0.13	20	[35]
* $0.90\text{Pb}(\text{Mg}_{1/3}\text{Nb}_{2/3})\text{O}_3-0.10\text{PbTiO}_3$	Ceramic (1000)	50	35	0.18	30	[72]
* $\text{Pb}(\text{Zn}_{1/3}\text{Nb}_{2/3})_{0.955}\text{Ti}_{0.045}\text{O}_3$	Single crystal (1000)	60	100	0.24	20	[26]
*60PVDF-40TrFE	Thick film (50)	75	25	0.52	500	[80]
*8/65/35 (Pb, La)(Zr,Ti) O_3	Thick film (290)	135	25	0.88	73	[75]
* $(\text{Pb}_{0.86}\text{La}_{0.02}\text{Ba}_{0.11})(\text{Zr}_{0.58}\text{Sn}_{0.29}\text{Ti}_{0.13})\text{O}_3$	Ceramic (500)	122	28	0.89	55	[174]
* $0.68\text{Pb}(\text{Mg}_{1/3}\text{Nb}_{2/3})-0.32\text{PbTiO}_3$	Thin film (0.15)	90	25	1.06	267	[45]
* $\text{Pb}(\text{Sc}_{0.5}\text{Ta}_{0.5})\text{O}_3$	MLC – 9 layers of 38 μm each	175	5	4.43	195	[30]
$\text{Pb}_{0.99}\text{Nb}_{0.02}(\text{Zr}_{0.55}\text{Sn}_{0.40}\text{Ti}_{0.05})_{0.98}\text{O}_3$	Thin film (0.5)	200	25	7.3	873	[175]
$\text{Pb}_{0.97}\text{La}_{0.02}(\text{Zr}_{0.75}\text{Sn}_{0.18}\text{Ti}_{0.07})\text{O}_3$	Thick film (2)	260	25	7.8	600	[176]
$\text{Pb}(\text{Sc}_{0.5}\text{Ta}_{0.5})\text{O}_3$	Thin film (0.16)	150	0	9.1	1450	This Work

Direct implementation and measurement of energy density using the Olsen cycle is indicated with (*) sign.

3.5 Ti-doped PST thin films

The primary aim of this study is to investigate whether specific dopants can shift the transition temperature and promote cation ordering in sol-gel deposited PST thin films. To maintain optimal pyroelectric properties, particularly a high p , the selected dopant must exhibit high electronic polarizability while maintaining charge neutrality and structural stability of the perovskite phase [147]. Typically, dopant species and concentrations are chosen based on their ionic radii, size and valence state to avoid destabilizing the perovskite structure and to prevent the formation of non-ferroelectric pyrochlore phases.

Among various candidates, Ti^{4+} is of particular interest due to its high dielectric polarizability (2.93 \AA^3) and smaller ionic radius (0.605 \AA). In the early 1990s, Shebanov et al.[147–149,177] investigated how various dopants affect the T_c , the nature of the phase transition, and ECE in PST bulk ceramics. They reported a high ECE due to a pronounced first-order transition in PST when doped with Ti^{4+} (10 mol.%). Moreover, they observed a shift in T_c from 20°C to 30°C . However, detailed structural, dielectric, and EC characterizations were not provided for this composition in their work.

Further insights were provided by Giniewicz et al.[178,179] who investigated the structural and dielectric properties of $(1-x)\text{PST} - (x)\text{PT}$ solid solution. They reported an increase in both ϵ and T_m up to $x = 0.4$, attributing this behaviour to the presence of a morphotropic phase boundary (MPB) between $x = 0.35 - 0.45$. Additionally, they identified several distinct phases at room temperature depending on the composition: (1) a pseudo-cubic region of variable order – disorder (VOD) ($x = 0 - 0.1$), (2) a structurally invariable rhombohedral region ($x = 0.1 - 0.4$), and (3) a tetragonal region extending from $x = 0.4$ to $x = 1$. These low symmetry phases are separated by the VOD boundary ($x = 0.05 - 0.1$) and the MPB as shown in Figure 3.11. Beyond $x = 0.1$, no long range cation ordering was observed. Furthermore, the dielectric response became less diffuse and dispersive with increasing PT concentration, indicating a decrease in relaxor behaviour.

Building on these findings, Lin et al.[180] investigated the dielectric properties of $\text{Pb}(\text{Sc}_{1/2}\text{Ta}_{1/2})_{1-x}\text{Ti}_x\text{O}_3$ thin films prepared using the metal-organic chemical vapour deposition (MOCVD) technique. They also observed a shift in T_m to higher temperatures with increasing Ti content. However, no cation ordering was observed in these films. From the above mentioned references, it is clear that Ti^{4+} shift the T_m of PST to higher temperature. However, the structural and dielectric properties of Ti-doped PST thin films derived from sol-gel technique remain unexplored, especially in the context of electro-thermal energy conversion. This study aims to address this

question on the electro-thermal conversion potential of $\text{Pb}(\text{Sc}_{1/2}\text{Ta}_{1/2})_{1-x}\text{Ti}_x\text{O}_3$ thin films developed using the sol-gel technique.

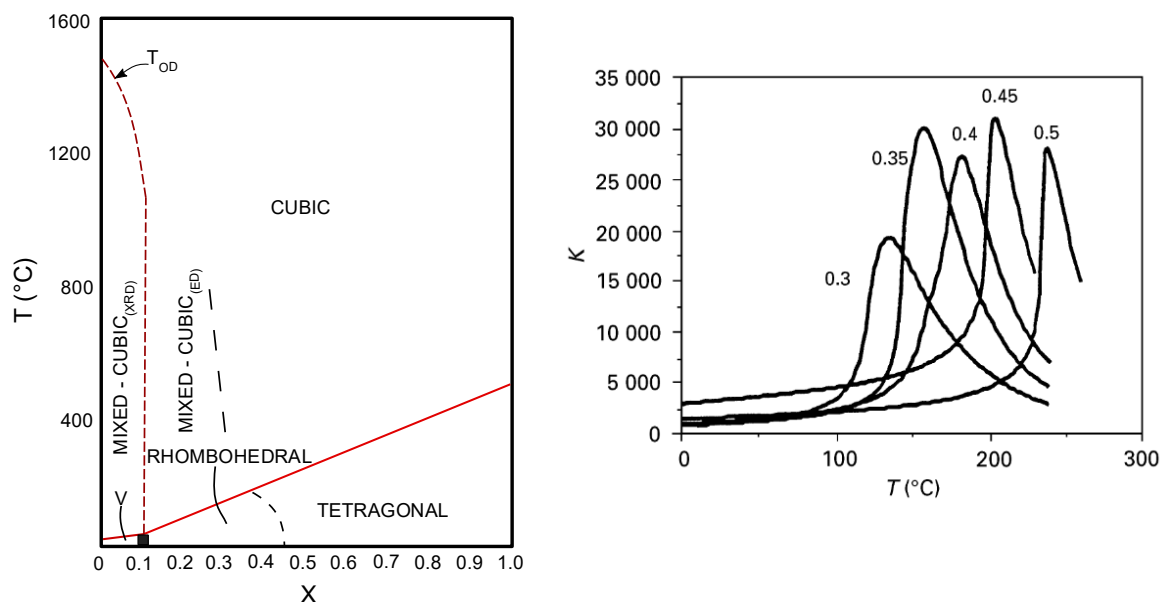


Figure 3.11 (a) Schematic depicting the $(1-x)\text{PST} - (x)\text{PT}$ solid solution system [x : mole fraction of PT]; (b) Dielectric constant of poled $(1-x)\text{PST} - (x)\text{PT}$ specimens for $x = 0.3 - 0.5$ at 1 kHz. Adapted from [181].

3.6 Synthesis of Ti-doped PST thin films

$\text{Pb}(\text{Sc}_{1/2}\text{Ta}_{1/2})_{1-x}\text{Ti}_x\text{O}_3$ ($x = 0, 0.05$ and 0.1) solutions were prepared similar to that of PST solution using lead (II) acetate trihydrate (99.9%), scandium (III) acetate trihydrate (99.9%), tantalum (V) ethoxide (99.9%), and titanium (IV) isopropoxide (97%) metal precursors, along with acetylacetone (99.5%, 2 mol equiv.), which served as a complexing agent, and 2-MOE as the solvent. First, scandium (III) acetate (which is obtained after freeze drying) and tantalum (V) ethoxide precursors were refluxed along with 2-MOE solvent at 130°C for 24 h under inert atmosphere. After obtaining a colourless Sc/Ta complex mixture, lead and titanium precursors were prepared separately before combining with the prepared Sc/Ta mixture. To prevent rapid hydrolysis reactions, titanium (IV) isopropoxide was dissolved in 2-MOE solution followed by the addition of acetylacetone. Later, the weighed amount of lead (II) acetate (in 30% excess) was added to this solution. Subsequently, the prepared Pb/Ti solution was combined with the Sc/Ta complex mixture, followed by an additional reflux step at 130°C for 2 h. Excess solvent and by-products were distilled to obtain a final solution concentration of 0.3 M. Subsequently, PSTT thin films ($x = 0, 0.05$ and 0.1) were fabricated on c-sapphire substrates using the spin coating technique. Prior

to the development of PSTT thin films, a Pt seed layer was deposited to initiate the formation of the perovskite phase. All the processing parameters for the seed layer and PSTT thin films were identical to those outlined in Section 3.3.

3.7 Results and discussion

3.7.1 XRD analysis

XRD patterns of the PSTT thin films ($x = 0, 0.05, \text{ and } 0.1$) indicate the presence of a single phase perovskite structure without any secondary phases [PDF card 01-074-2635]. Here, $\theta - 2\theta$ scan was performed between 15 and 55° with a step size of 0.02° and 2 s time interval per step. Note that for $x = 0$, XRD patterns were collected before the electrode deposition resulting in the absence of Pt peaks. The difference in the intensity of the Pt peaks between $x = 0.05$ and $x = 0.1$ is likely due to slight sample misalignment. This misalignment does not significantly influence the PSTT films, given their high mosaicity resulting from the sol-gel deposition process. All the films were preferentially oriented along (200). On increasing the Ti doping levels, the peak positions were slightly shifted towards higher 2θ angle attributing to the smaller ionic radii of Ti^{4+} (0.605 \AA) compared to Sc^{3+} (0.745 \AA) and Ta^{5+} (0.64 \AA) ions, as shown in Figure 3.12. Moreover, the peak intensity of $x = 0.1$ sample is relatively higher than that of the other two compositions, suggesting enhanced crystallinity and larger grain size, as later confirmed by SEM analysis.

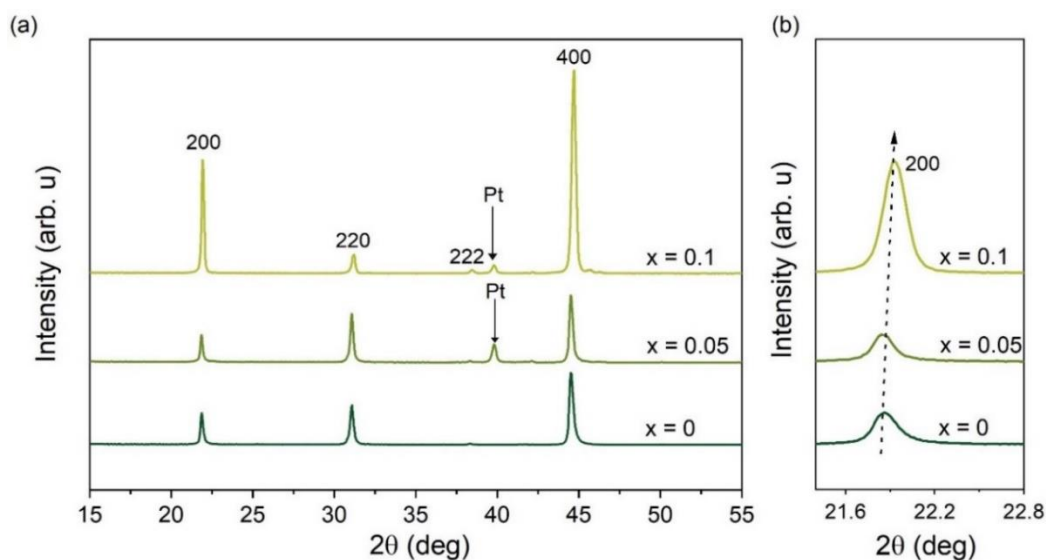


Figure 3.12 (a) XRD pattern of PSTT thin films ($x = 0, 0.05, \text{ and } 0.1$) on c-sapphire substrate; (b) magnified image of (200) peak.

To investigate the existence of B-site ordering in PSTT thin films, an adapted approach was carried out by tilting the sample to a fixed χ angle with respect to the main (200) texture of the film and the $\theta - 2\theta$ scan was carried out between 18 and 20° with a step

size of 0.02 and 10s time interval per step. In a similar manner to the experimental procedure outlined in Section 4.4, $\theta - 2\theta$ scan was performed by fixing $\chi = 54.7^\circ$ with a collimated beam but no (111) superstructure peak was observed in the doped films. It is worth noting that the sol-gel derived PSTT films possess a texture with large mosaicity. Hence, a small deviation in angle due to sample misalignment does not significantly affect diffraction peak intensity. Nonetheless, additional $\theta - 2\theta$ scans were also performed at different χ angles to ensure no deviations were overlooked, as shown in Figure 3.13. However, the absence of superstructure peak confirm that these films do not possess long range ordering.

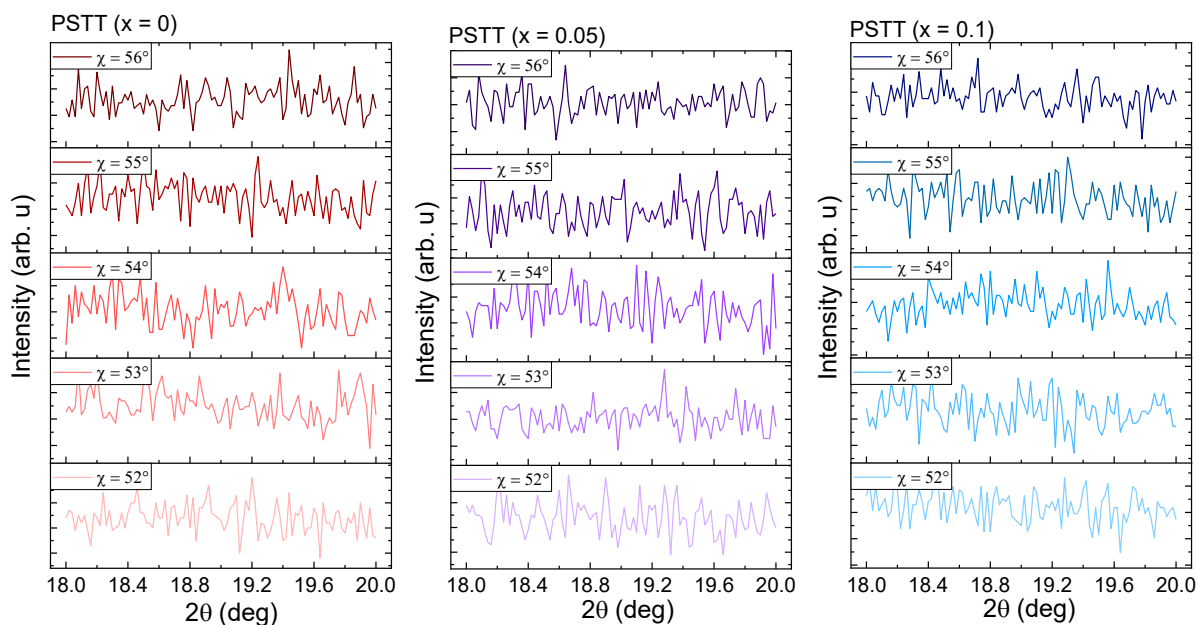


Figure 3.13 $\theta - 2\theta$ scans of PSTT thin films ($x = 0, 0.05,$ and 0.1) performed at different χ angles.

3.7.2 SEM analysis

The surface and cross-section of the PSTT thin films ($x = 0, 0.05,$ and 0.1) were analysed using SEM (see Figure 3.14). For $x = 0$, a dense microstructure without the presence of pyrochlore phases were observed. The cross-section images revealed a columnar film growth, and the thickness of the films was around 160 – 170 nm. With increasing Ti doping levels, the films exhibited a denser, columnar microstructure, along with a slight increase in film thickness compared to $x = 0$ sample. This densification suggests that Ti^{4+} incorporation enhances surface diffusion during film growth, leading to improved microstructural uniformity. The $x = 0.05$ sample showed a grain size distribution between 180 and 300 nm, with no visible porosity. The cross section revealed that the thickness of the film was around 172 nm. In the case of $x = 0.1$, the grains were significantly larger, ranging from 300 to 500 nm, which was estimated

using the ImageJ software. The increase in grain size for $x = 0.1$ suggests improved crystallinity, which is further supported by the enhanced peak intensity observed in the corresponding XRD patterns. Moreover, the film thickness was observed to be between 175 and 180 nm in the cross-sectional image. Although minor porosity was present along the columnar direction of the film, it did not have a detrimental effect on the electrical properties as shown in the subsequent sections.

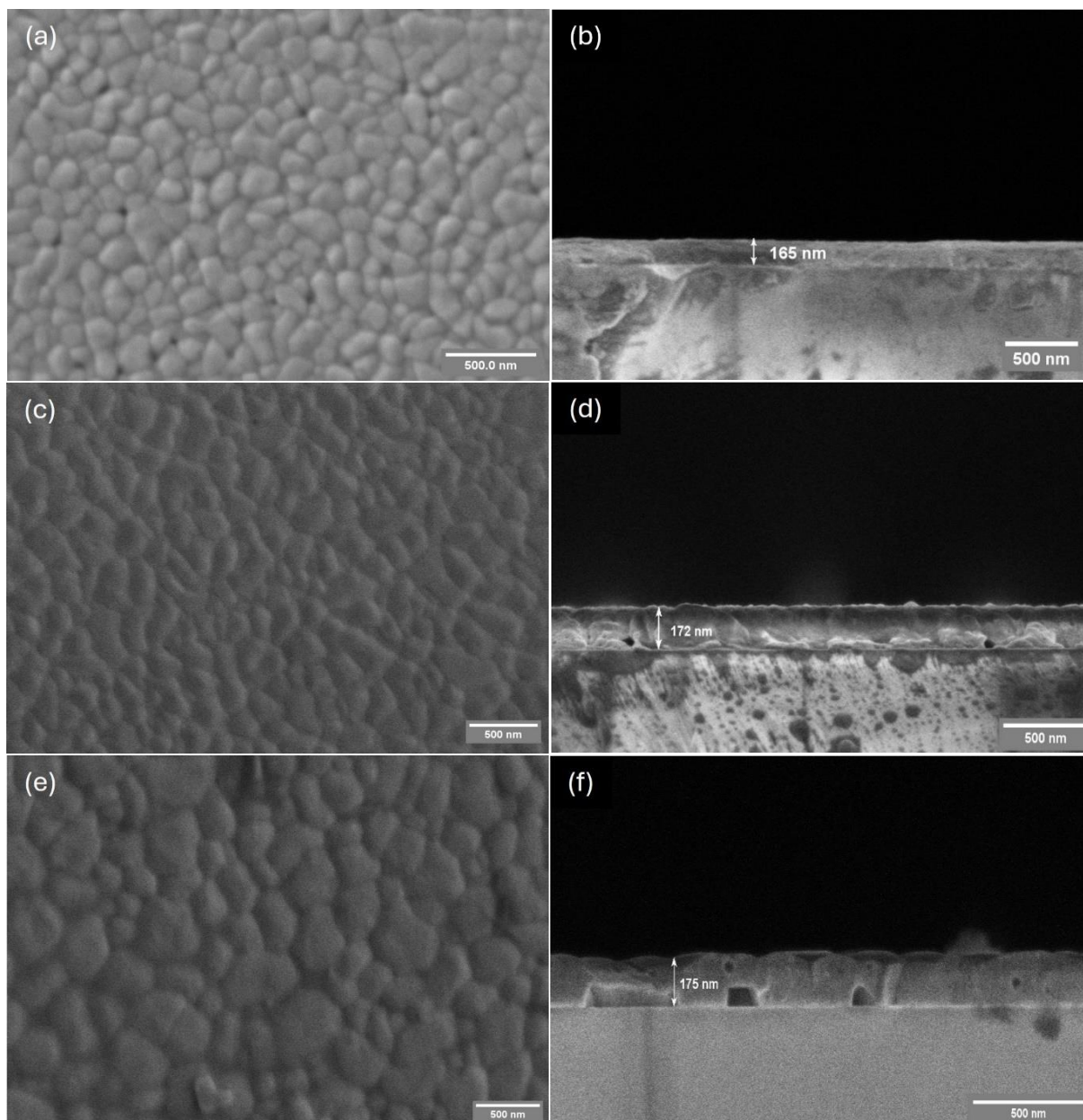


Figure 3.14 SEM images showing the top-view and cross section of PSTT thin films (a, b) $x = 0$; (c, d) $= 0.05$; (e, f) $= 0.1$.

3.7.3 Dielectric measurement

To investigate the T_m of PSTT thin films, dielectric measurements were carried out at 1 kHz from 0 to 120°C without applying a bias field using aixACCT TF 2000 analyser, as shown in Figure 3.15. For the undoped concentration ($x = 0$), a maximum ϵ of 4200 was obtained at 32°C. As the Ti^{4+} concentration increased, T_m shifted progressively to higher temperatures, reaching 60°C for $x = 0.05$ and approximately to 85°C for $x = 0.1$ at 1 kHz. Along with this shift, ϵ also increased, with the $x = 0.1$ composition exhibiting the highest value of around 5250 at 1 kHz. In addition, the Ti-doped films exhibited a lower dielectric loss compared to the undoped composition.

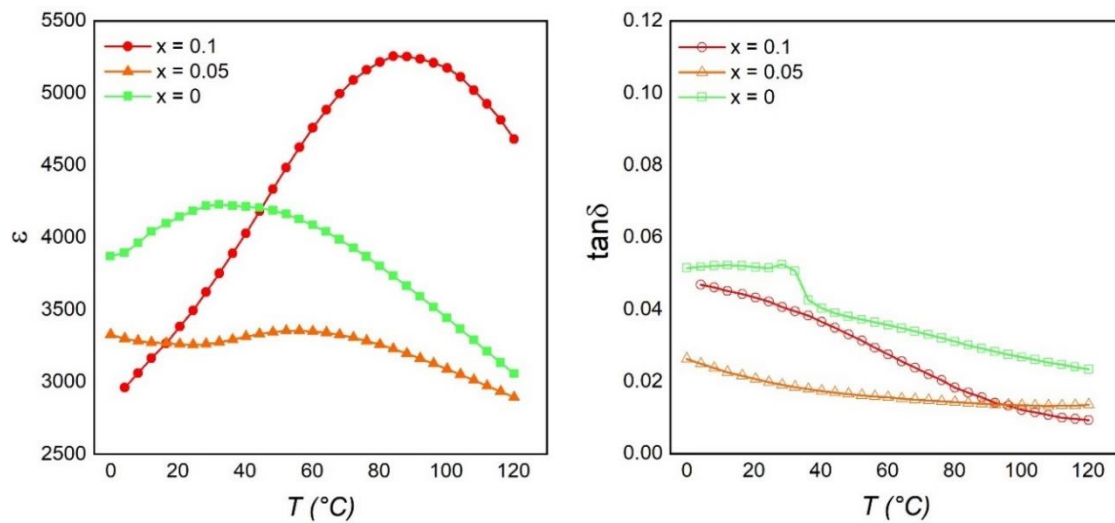


Figure 3.15 Temperature dependent permittivity measurements of PSTT thin films at 1 kHz.

Frequency dependent dielectric measurements at various temperatures, carried out using a Novocontrol Concept 40 dielectric spectrometer (refer Appendix A.5 for more information), revealed a diffuse dispersive response, further confirming the relaxor nature of these films, as shown in Figure 3.16. Additionally, T_m exhibited a clear upward trend with increasing Ti concentration, while the dielectric permittivity showed a slight decrease for $x = 0.05$, followed by a marked increase at $x = 0.1$, similar to the trend observed in measurements performed using the aixACCT system. It is worth noting that the discrepancy in dielectric permittivity values between the aixACCT system and the Novocontrol Concept 40 dielectric spectrometer is likely due to parasitic capacitance effects from the sample holder in the latter. Since the main objective was to investigate the trend in T_m , these differences in absolute permittivity values are not critical to the findings.

A similar increase in T_m with Ti doping has been reported by Lin et al.[180] and Giniewicz et al.[182] in PSTT thin films grown using MOCVD technique and $(1-x)PST - (x)PT$ ceramics respectively. This could be due to the reduced charge randomness in

the B-site, as the hetero-valent charge imbalance between Sc^{3+} and Ta^{5+} is reduced by substituting Ti^{4+} ions. Moreover, it has been reported that the material transitions from relaxor to normal ferroelectric state beyond a certain doping concentration [183]. This transition has been primarily associated with strong orbital hybridization between the Ti $3d$ and O $2p$ states, resulting in off-center ionic displacements within the TiO_6 octahedra and a directional shift of these displacements from (111) toward (001) with increased Ti concentration [183]. Based on these observations, it is reasonable to suggest that at lower doping levels, such as in our PSTT thin films, the overall structure remains disordered at the macroscopic scale, while the Ti-induced local distortions stabilize polar nanoregions and alter the dynamics of the relaxor state. This scenario would lead to a coexistence of ordered and disordered polar regions, potentially explaining the less diffuse dielectric peak observed for the $x = 0.1$ composition (see Figure 3.16 (c)) and clarifying the significant variation observed in the temperature-dependent dielectric constant.

In addition to the temperature and frequency dependent dielectric measurements, the diffuseness parameter of PSTT thin films was also evaluated using the modified Curie–Weiss law [184]. The diffuseness of the relaxor materials can be quantified by their diffuseness parameter, which is given by Equation (3.2):

$$1/\varepsilon - 1/\varepsilon_m = C^{-1}(T - T_m)^\gamma \quad (3.2)$$

where ε is the permittivity, ε_m is the maximum permittivity and T_m is its corresponding temperature, C is the Curie-like constant. The critical exponent of the permittivity (γ) gives a characteristic of the phase transition in a material. If the γ is 2, it corresponds to the relaxor behaviour and if it is close to 1, it corresponds to the normal ferroelectric transition. If the value of γ is between these limits ($1 < \gamma < 2$), the material exhibits a degree of diffuseness, which could correspond to the incomplete diffuse transition. For $x = 0$ and 0.05 composition, γ is around 2, indicating a perfectly relaxor characteristic, as shown in Figure 3.17 (a) and (b). With $x = 0.1$, γ is 1.67 (Figure 3.17 (c)) which could indicate their less diffuse transition close to their T_m as shown in Figure 3.16 (c).

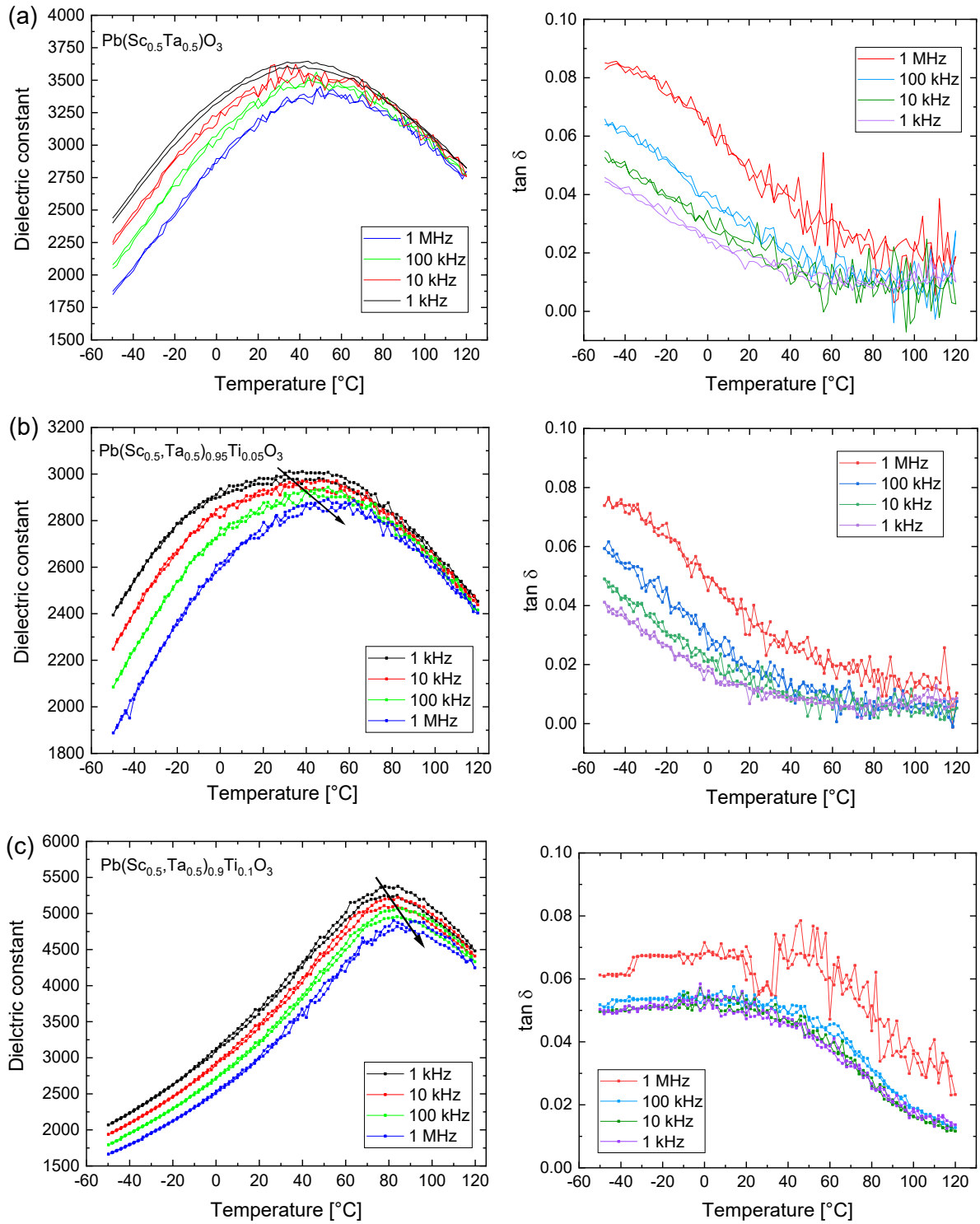


Figure 3.16 Dielectric constant (ϵ) and loss tangent ($\tan \delta$) values of PSTT thin films (a) $x = 0$, (b) $x = 0.05$, (c) $x = 0.1$, at different frequencies and temperatures.

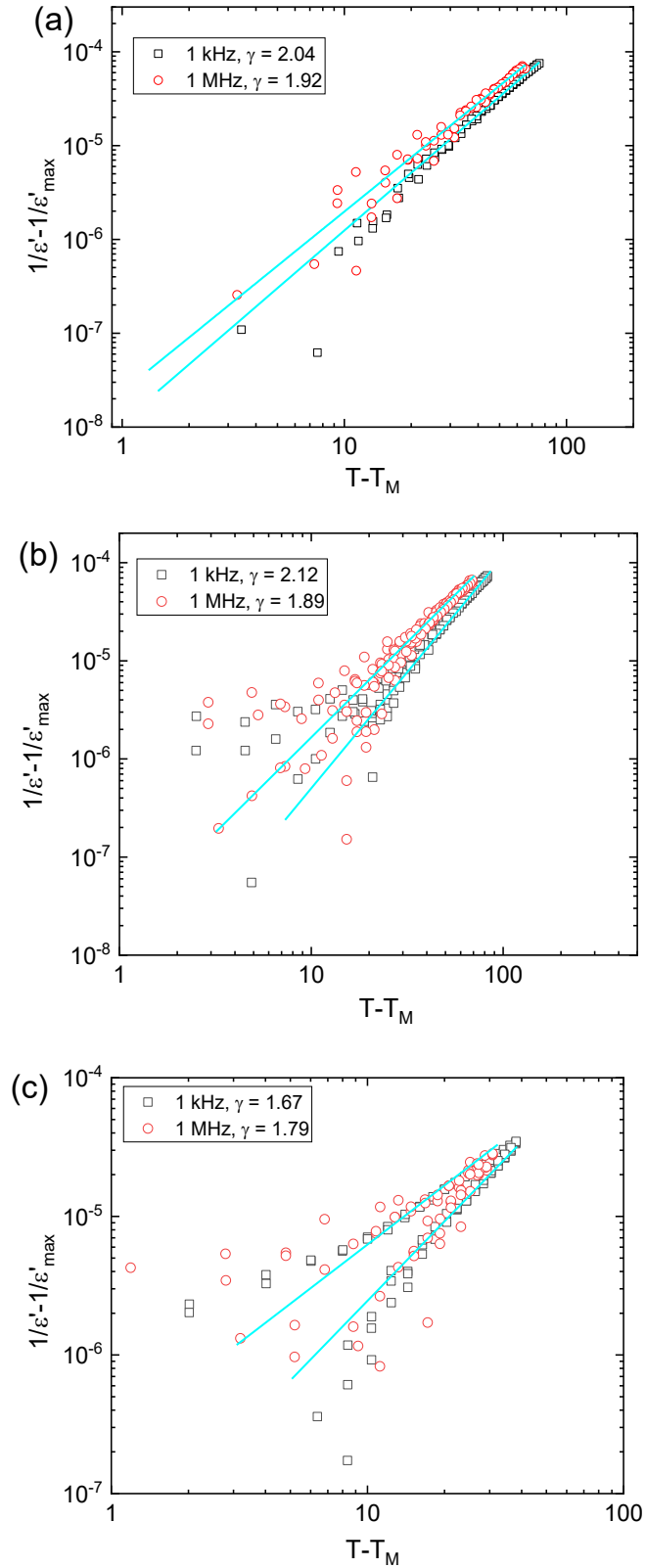


Figure 3.17 Logarithmic plots of the reciprocal permittivity ($1/\epsilon - 1/\epsilon_m$) vs. temperature ($T - T_m$) at 1 kHz and 1 MHz of PSTT thin films (a) $x = 0$, (b) $x = 0.05$, and (c) $x = 0.1$.

3.7.4 Pyroelectric energy density

Like the undoped films, the pyroelectric energy densities of PSTT thin films were deduced from the bipolar $D - E$ loops. By constructing an Olsen cycle using $D - E$ loops measured at different temperatures, the harvestable energy densities were estimated from $\oint E dD$. Figures 3.18 (a), (c), and (e) show magnified views of the first quadrant of the bipolar $D(E)$ loops measured at various temperatures, while Figures 3.18 (b), (d), and (f) display the corresponding pyroelectric energy densities across different temperature spans and initial temperatures. Maximum harvestable energy densities of 2.6 and 2.5 $\text{J}\cdot\text{cm}^{-3}$ were obtained for compositions $x = 0$ and $x = 0.05$, respectively, when the Olsen cycle was implemented between 0 and 80°C at a ΔE of 560 $\text{kV}\cdot\text{cm}^{-1}$. For the $x = 0.1$ sample, a maximum energy density of 3.06 $\text{J}\cdot\text{cm}^{-3}$ was achieved between 0 and 100 °C for the same ΔE . Since the T_m of the $x = 0.1$ composition is around 85°C, a notable increase in energy density was observed from 90 to 100°C. Beyond this temperature range, the energy density decreased by 10 to 15% due to broadened hysteresis loops, resulting from increased hysteretic losses. It is important to note that the pyroelectric energy density scales directly with ΔE and ΔT . The lower absolute values reported here compared to our previous results [152] on undoped thin films (where energy densities up to 9 $\text{J}\cdot\text{cm}^{-3}$ were obtained), arise from the reduced ΔE and ΔT conditions. Nevertheless, under comparable ΔT conditions, the doped films achieve a maximum energy density of 2.5 $\text{J}\cdot\text{cm}^{-3}$ for a ΔE of 560 $\text{kV}\cdot\text{cm}^{-1}$, which is comparable to the 2.0 $\text{J}\cdot\text{cm}^{-3}$ achieved by the undoped film for a slightly lower ΔE of 520 $\text{kV}\cdot\text{cm}^{-1}$ in our previous work [152], indicating the minimal impact of doping on energy density under these conditions.

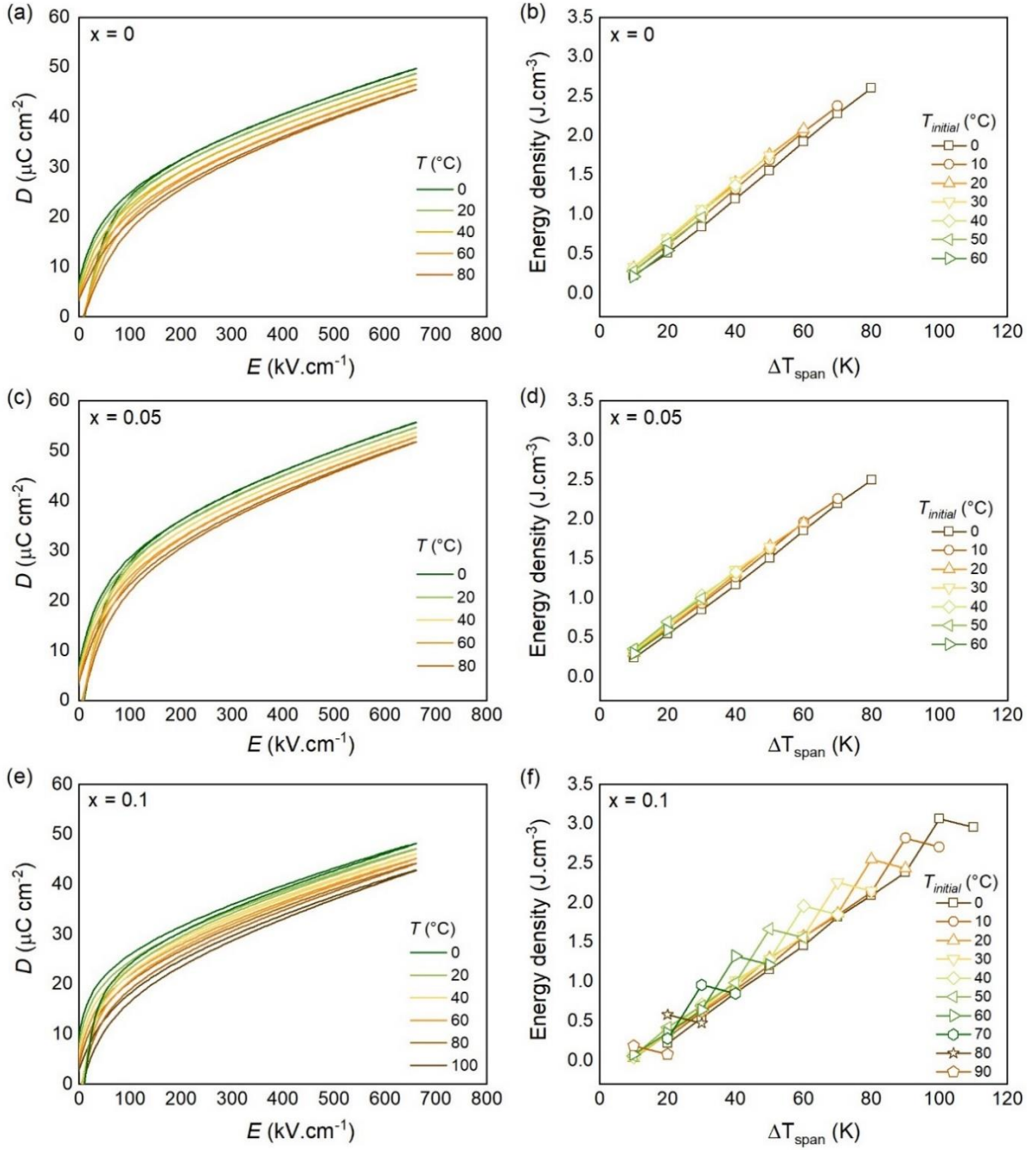


Figure 3.18 Bipolar $D - E$ loops (magnified) and energy densities of PSTT thin films: (a, b) $x = 0$, (c, d) $x = 0.05$, and (e, f) $x = 0.1$, at various initial temperatures and temperature spans for a ΔE of $560 \text{ kV}\cdot\text{cm}^{-1}$.

3.7.5 Electrocaloric effect

The electrocaloric effect (ECE) of PSTT thin films ($x = 0, 0.05$, and 0.1) was indirectly estimated using the Maxwell's relation $\left[\left(\frac{\partial D}{\partial T}\right)_E = \left(\frac{\partial S}{\partial E}\right)_T\right]$, as detailed in Section 2.1.3.

The total entropy differential of the sample is given by:

$$dS(T, E) = \left(\frac{\partial S}{\partial T}\right)_E + \left(\frac{\partial S}{\partial E}\right)_T \quad (3.3)$$

Under adiabatic conditions ($dS = 0$), we can express $\left(\frac{\partial S}{\partial T}\right)_E = \frac{C_E}{T}$, where C_E is the specific heat under at a constant electric field. Therefore, the adiabatic temperature variation of the sample can be estimated as:

$$\Delta T = - \int_{E1}^{E2} \frac{T}{C_E} \left(\frac{\partial P}{\partial T}\right)_E dE \quad (3.4)$$

Equation (3.4) explicitly shows the direct correlation between the adiabatic temperature variation of the sample (i.e., the electrocaloric effect) and the pyroelectric coefficient. By substituting the theoretical density value of $9070 \text{ kg}\cdot\text{m}^{-3}$ and specific heat capacity of $300 \text{ J}\cdot\text{kg}^{-1}\cdot\text{K}^{-1}$ for PST into Maxwell's relation, a maximum ΔT_{ad} of 4.3 K was obtained for the pure PST thin film at 50°C , which is slightly away from its T_m , for an electric field variation (ΔE) of $667 \text{ kV}\cdot\text{cm}^{-1}$ (see Figure 3.19).

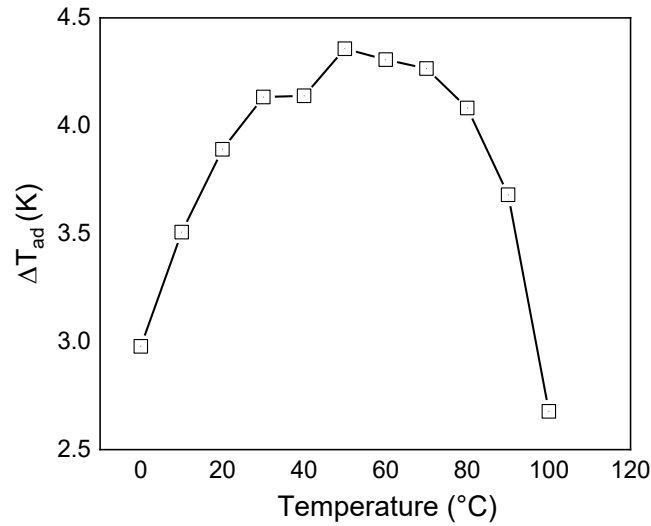


Figure 3.19 ΔT_{ad} versus temperature of PST thin film for a ΔE of $667 \text{ kV}\cdot\text{cm}^{-1}$.

By assuming the same theoretical density and specific heat capacity values, the ECE of the Ti-doped PST films was also estimated using the Maxwell's equation, as shown in Figure 3.20. A maximum ΔT_{ad} of 4.07 K was obtained for $x = 0.05$ composition at 60°C , corresponding to its T_m , under the same field conditions. Similarly, for $x = 0.1$ sample, the highest ECE of 5.17 K was estimated near its T_m at 90°C , for a ΔE of $667 \text{ kV}\cdot\text{cm}^{-1}$. Since, the ECE has been extracted at large electric fields, ΔT_{ad} is relatively large compared to the literature on bulk PST ceramic samples, which typically report ΔT_{ad} in the range of 1 to 3 K using the direct techniques.

Currently, the 3ω method is the only available technique for direct measurement of ECE in thin films [45,185]. However, this method presents several experimental challenges, including thermal losses to the substrate, difficulty in resolving small temperature changes, and sensitivity to interface quality. Owing to these experimental constraints, the indirect Maxwell's relation approach emerges as a more consistent

alternative for ergodic relaxor systems such as PSTT as the indirect measurements agree well with the direct techniques.

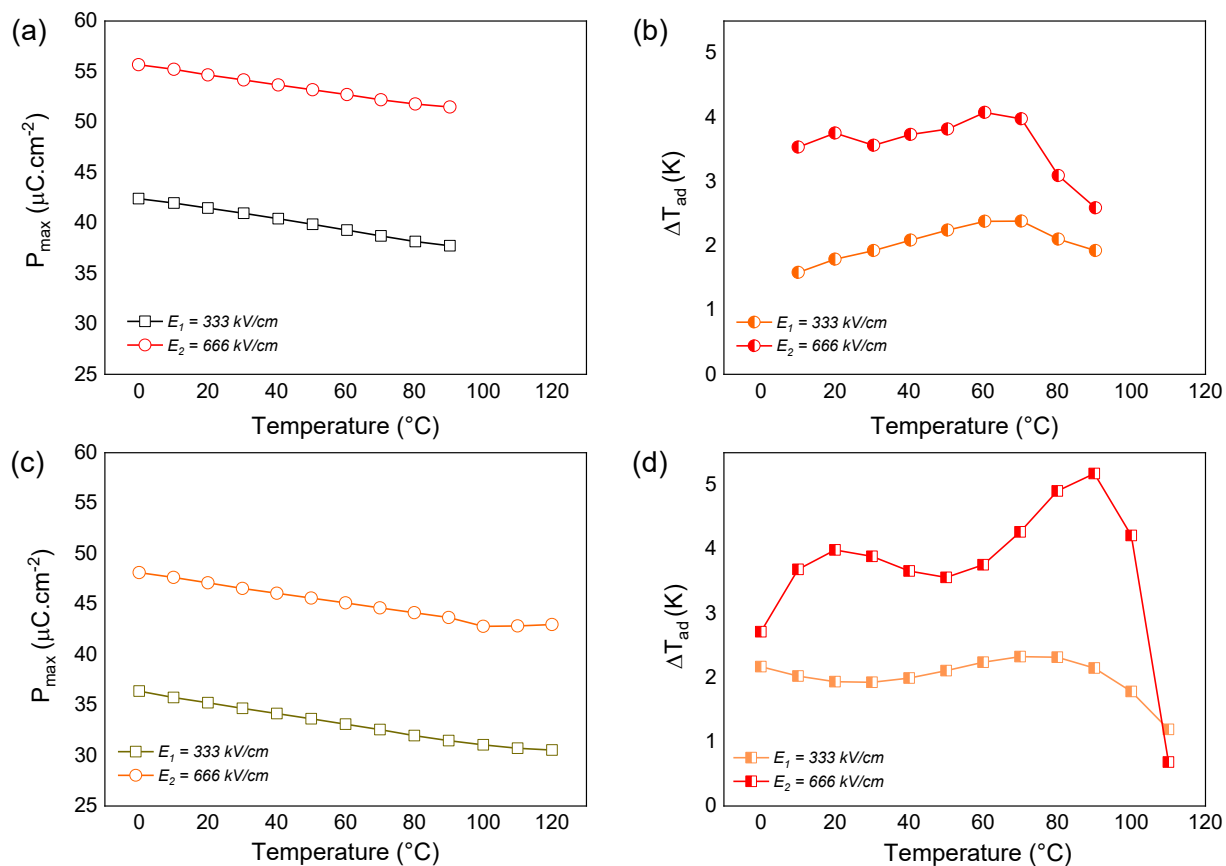


Figure 3.20 Maximum polarization (P_{max}) and adiabatic temperature change (ΔT_{ad}) of PSTT thin films (a, b) $x = 0.05$; (c, d) $x = 0.1$ as a function of temperature.

3.7.6 Pyroelectric conversion efficiency

Figure 3.21 (a – f) show the efficiency and relative efficiency of PSTT thin films as functions of both temperature span and initial temperature under an applied field of $\Delta E = 560 \text{ kV}\cdot\text{cm}^{-1}$. The pyroelectric conversion efficiency was evaluated using the Olsen cycle by calculating the ratio of harvested energy density to the total heat input. It is important to recognize that the total heat input constitutes of two parts: (1) the heat required to raise the material's temperature from the initial to the final temperature, and (2) the heat exchanged due to the intrinsic entropy change of the material during the high-temperature discharge stage of the Olsen cycle. To account for this additional heat, the ECE of the PSTT thin films estimated indirectly using the Maxwell's relation at different temperatures was considered.

By applying the efficiency equations mentioned in section 2.4.1, the PSTT thin films achieved a maximum conversion efficiency of approximately 1.1%, as shown in Figure 3.21 (a), (c), and (e). The efficiency curves for the $x = 0$ and 0.05 samples exhibited

similar trends, whereas the $x = 0.1$ sample deviated notably near its T_m . This deviation is attributed to the sharp increase in energy density observed near 85°C . Given the relatively small temperature spans in this study, the available thermal energy (exergy potential) is limited, resulting in modest absolute efficiency values. Consequently, relative efficiency provides a more meaningful metric for comparing the performance of these films. The $x = 0$ and $x = 0.05$ compositions reach a maximum of 27 and 30% Carnot efficiencies for a ΔT of 10 K near their T_m at 30 and 50°C respectively. Likewise, $x = 0.1$ composition yields a maximum relative efficiency of 18% of Carnot efficiency between 90 and 100°C as illustrated in Figure 3.21 (f). As expected, these results indicate that the PSTT films are most efficient close to their T_m . Due to their distinct transition temperatures, these compositions are promising candidates for multi-stage device configurations, where each stage can be optimized for a specific temperature window. The next section presents a conceptual analysis investigating the potential performance of such a multi-stage device composed of PSTT thin films based on the indirectly obtained results.

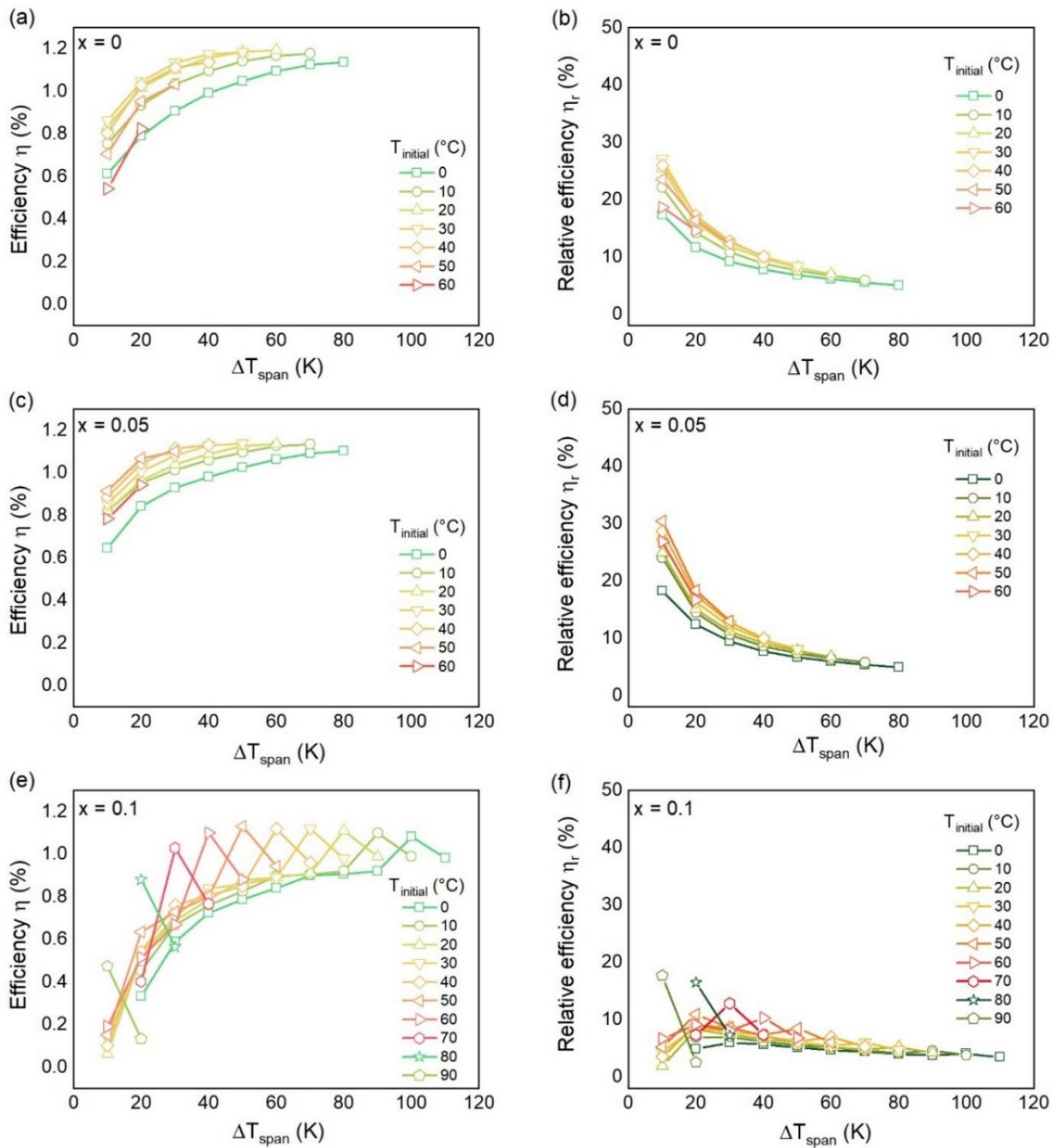


Figure 3.21 Efficiency and relative efficiency of PSTT thin films: (a, b) $x = 0$, (c, d) $x = 0.05$, and (e, f) $x = 0.1$, as a function of different temperature spans and initial temperature for a ΔE of $560 \text{ kV}\cdot\text{cm}^{-1}$.

3.7.7 Multistage device using PSTT thin films: A conceptual study

To illustrate the concept on multi-staging, the energy densities of PSTT thin films ($x = 0, 0.05$, and 0.1) were compared using the Olsen cycle over a 20 K temperature interval at different initial temperatures, as shown in Figure 3.22. Since the PSTT thin films have identical active volumes, energy density was chosen as the comparative metric, and it was estimated from the $D - E$ loops. For the undoped composition ($x = 0$), the peak energy output was observed when the Olsen cycle is implemented between 40

and 60°C, with diminishing energy densities beyond this range. In contrast, the doped samples ($x = 0.05$ and 0.1) exhibit significant energy output only above 40°C owing to their higher transition temperature. Energy densities greater than $0.6 \text{ J}\cdot\text{cm}^{-3}$ were achieved for the $x = 0.05$ sample only when the initial temperature of the Olsen cycle was between 40 and 60°C. On the other hand, the $x = 0.1$ sample produced enhanced energy output only when the Olsen cycle was implemented at 80 °C.

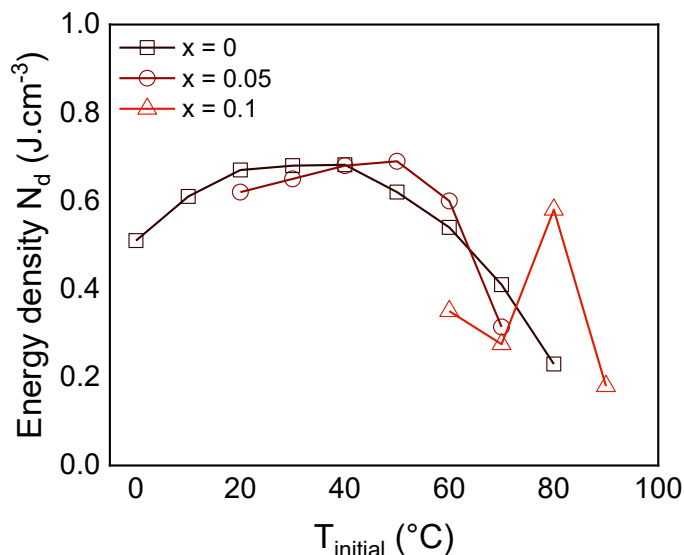


Figure 3.22 Energy densities of PSTT thin films ($x = 0, 0.05,$ and 0.1) calculated using the Olsen cycle, as a function of the starting temperature for a ΔT_{span} of 20 K.

Based on these results, one could envision a three-stage device consisting of PSTT thin films with different compositions ($x = 0, 0.05,$ and 0.1), leveraging their distinct energy output profiles across different temperature ranges. In this way, the operating temperature range of the device can be extended, resulting in enhanced energy harvesting efficiency compared to a three-stage system utilizing only the undoped composition ($x = 0$), which exhibits peak energy output within a narrower temperature window. Figure 3.23 shows the schematic of a three-stage device composed entirely of PST thin films against a three stage device consisting of PSTT thin films ($x = 0, 0.05,$ and 0.1), operating between 40 and 100°C. To estimate the total energy output of the three-stage devices, the energy densities of the individual compositions were summed over sequential 20 K temperature intervals: 40–60 °C, 60–80 °C, and 80–100 °C. For the three stage device composed solely of PST thin films, a total energy density of $1.45 \text{ J}\cdot\text{cm}^{-3}$ was obtained. Meanwhile, the three stage device composed of PSTT thin films exhibit a total energy density of $1.85 \text{ J}\cdot\text{cm}^{-3}$, showing a 27% increase over the same temperature range. This increase is due to the incorporation of doped samples ($x = 0.05$ and $x = 0.1$), which have a higher T_m alongside the undoped film. For instance, the energy density of the $x = 0.05$ sample is approximately 12% greater than the undoped composition between 60 – 80°C range. Above this optimal temperature range, the

energy density decreased significantly due to increased hysteresis, ultimately reaching a point where no energy could be harvested. To address this, the $x = 0.1$ composition is used to effectively harvest energy between 80 and 100°C, as its T_m is close to 90°C, leading to a peak in the energy density, as shown in Figures 3.18 and 3.22. It must be noted that the heat losses were assumed to be inexistent in this conceptual study.

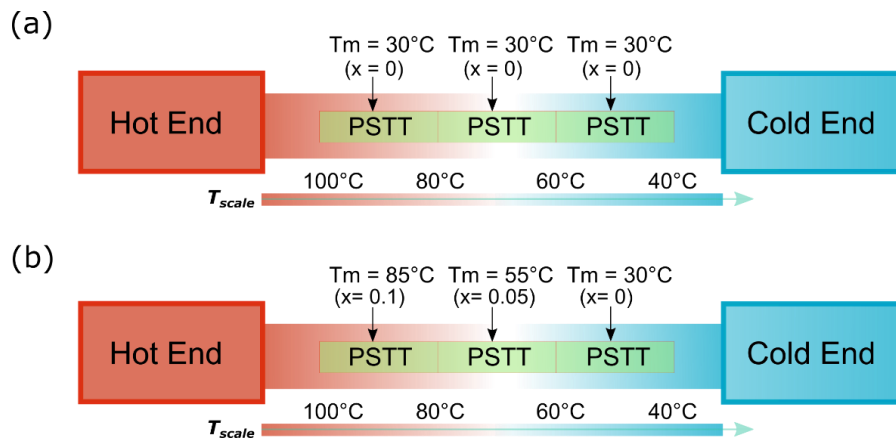


Figure 3.23 A three-stage device composed of (a) undoped sample ($x = 0$) and (b) with $x = 0, 0.05$, and 0.1 operating at different temperatures in stages.

Table 3.2 Energy density of PSTT thin films ($x = 0, 0.05$, and 0.1) when utilized as a three-stage pyroelectric converter across different temperature intervals (values taken from Figure 3.22).

Temperature intervals (°C)	Energy output of three-stage device composed entirely of undoped PSTT ($x = 0$) films (J·cm ⁻³)	Energy output of three-stage device composed of PSTT ($x = 0, 0.05$, and 0.1) films (J·cm ⁻³)
40 – 60	0.68	0.68
60 – 80	0.54	0.60
80 – 100	0.23	0.57

This conceptual study based on PSTT thin films indicate that the energy output of the device can be enhanced by combining materials with different transition temperatures. Further improvements in device efficiency can be achieved by (1) implementing heat regeneration techniques to reduce thermal losses, and (2) combining regeneration with multiple staging of materials with varying transition temperatures. A conceptual analysis addressing these strategies, based on the experimental results obtained from PSTT thin films, is presented in Appendix B.

3.8 Summary and conclusions

In this chapter, the non-linear pyroelectric conversion potential of sol-gel deposited PST thin films was first investigated. Structural and dielectric measurements confirmed that the PST thin films exhibit relaxor characteristics. A maximum pyroelectric energy density of $9.1 \text{ J}\cdot\text{cm}^{-3}$ was estimated using the Olsen cycle from the $D - E$ loops between 0 and 150°C for a ΔE of $1450 \text{ kV}\cdot\text{cm}^{-1}$.

Subsequently, the effect of Ti^{4+} doping on the structural, dielectric and non-linear pyroelectric conversion potential of sol-gel derived PST thin films was examined in detail. It was confirmed that by increasing the Ti^{4+} concentration, the transition temperature of $\text{Pb}(\text{Sc}_{0.5}\text{Ta}_{0.5})_{1-x}\text{Ti}_x\text{O}_3$ (PSTT) thin films can be shifted from 30°C ($x = 0$) to 90°C ($x = 0.1$). Similarly, the PSTT thin films exhibit diffuse transition behaviour, indicative of relaxor characteristics. Furthermore, PSTT thin films demonstrated pyroelectric conversion efficiencies of up to 30% of the Carnot efficiency near their transition temperatures. A maximum ECE of 5.2 K was also indirectly estimated using Maxwell's relation in PSTT thin films for a maximum field variation of $667 \text{ kV}\cdot\text{cm}^{-1}$.

Due to their distinct transition temperatures, these doped films were evaluated for use in a conceptual multi-stage device, resulting in a 27% increase in energy output compared to a device composed solely of undoped PST films. This study highlights the potential of PST and PSTT thin films for non-linear pyroelectric energy harvesting and underscores the promise of developing PSTT-based thin-film multilayer capacitors for future high-efficiency, multi-material cascade devices tailored for thermal energy harvesting.

Chapter 4

From thin films to bulk: Pyroelectric conversion efficiency of $\text{Pb}(\text{Sc}_{1/2}\text{Ta}_{1/2})\text{O}_3$ ceramics and multi-layer capacitors

4.1 Motivation

As established in the preceding chapters, nonlinear pyroelectric energy harvesters can be regarded as the electrical analogue of a classical heat engine, converting temporal temperature variations directly into electrical energy. The performance of a heat engine is primarily evaluated by its efficiency in converting heat into useful work. Similarly, assessing the thermal-to-electrical conversion efficiency of nonlinear pyroelectric materials is essential for determining their practical feasibility and for benchmarking them against alternative technologies such as thermoelectric generators.

While numerous studies have explored pyroelectric materials and their energy densities, the thermal-to-electrical conversion efficiency of these materials has not been widely investigated. To achieve high conversion efficiency, the pyroelectric materials must exhibit a substantial work output at a limited heat input as detailed in Section 2.4. High electrical work output, or pyroelectric energy density, depends critically on achieving large variations in both polarization (ΔP) and electric field (ΔE) in the material during electro-thermal conversion cycles. Meanwhile, the heat input can be reduced via heat regeneration, as discussed in Section 2.5.

In the previous chapter, the pyroelectric conversion efficiency of PST thin films was investigated in detail. Although PST thin films reached nearly 30% of the Carnot efficiency for a temperature span (ΔT) of 10 K near their transition, this was primarily attributed to the large ΔE , whereas ΔP remained modest due to their relaxor behaviour. While thin films are well suited for integration into microelectronic systems and show promise for low-power thermal energy harvesting, their use in large-scale applications is constrained by their inherently low active volume and the requirement of a supporting substrate.

To overcome the limitations associated with thin-film geometries and to achieve higher conversion efficiencies, this chapter investigates B-site ordered PST materials in two different geometries: (1) highly ordered bulk ceramic ($\Omega \approx 0.88$) with reduced

thickness ($\sim 90 \mu\text{m}$) and (2) multilayer capacitor (MLC) with an overall thickness of 0.5 mm consisting of 9 active layers (thickness of each layer = $38.6 \mu\text{m}$; $\Omega = 0.75$). The bulk ceramics exhibit strong B-site ordering, which results in a large ΔP . Additionally, their reduced thickness enables the application of high electric fields, making them well suited for evaluating the intrinsic material efficiency. In contrast, PST MLCs effectively combine the advantages of films and bulk ceramics by supporting high electric field application due to their thin dielectric layers, while also offering a larger active volume and a significant ΔP due to their B-site ordering. MLCs can thus be viewed as scaled-up architectures of stacked thick films, designed to increase thermal mass while preserving high electric field accessibility. This combination of properties makes MLCs particularly attractive for investigating high-efficiency pyroelectric conversion in scalable device architectures.

The primary objective of this chapter is to evaluate the nonlinear pyroelectric performance of PST ceramics and MLCs under the Olsen cycle, with particular emphasis on their thermal-to-electrical conversion efficiencies. While our previous work [30] demonstrated that PST MLCs can reach up to 40% of the Carnot efficiency for a ΔT of 10 K near their Curie temperature (T_c), the present study investigates whether reducing ΔT , while avoiding the thermal hysteresis region, can increase the efficiency beyond the 50% Carnot threshold. Furthermore, Olsen cycles were directly implemented to evaluate the nonlinear pyroelectric behaviour of PST across various temperature spans and electric fields. This chapter also discusses the influence of B-site cation ordering, the role of hysteresis, and the effects of electric field strength and operating frequency on the pyroelectric conversion efficiency of the material.

For clarity, this chapter begins with a brief note on the sample preparation and characterization techniques, presented in Section 4.2. This methods section also includes a description of the nonlinear measurement setup used to directly implement pyroelectric conversion cycles on PST. The experimental results on PST ceramics are discussed in Section 4.3, followed by the investigation of 0.5 mm thick PST MLC in Section 4.4. These results offer further insight into how variations in geometry and cation order affect energy conversion performance. Furthermore, Section 4.5 describes the influence of cycling frequency and highlights the pyroelectric performance of the 0.5 mm thick PST MLC under the Brayton cycle. Finally, the key findings are summarized in Section 4.6.

4.2 Methods

4.2.1 Sample preparation and characterization

PST bulk ceramic

PST ceramic was prepared via mechanochemical synthesis using stoichiometric amounts of PbO, Sc₂O₃, and Ta₂O₅ (Alfa Aesar, USA) precursors. The precursor powders were activated in a high energy planetary ball mill (PM 400, Retsch, Germany) using tungsten carbide balls at 300 rpm for 24 h. The milled powder was calcined at 1000 °C for 2 h in a closed alumina crucible. Subsequently, the powder was re-milled in isopropanol with zirconia balls at 200 rpm for 2 h to prevent agglomeration. The powder was compacted into cylindrical pellets using an isostatic press (Autoclave Engineers, USA) at 300 MPa and sintered at 1300 °C for 2 h. This was followed by annealing at 1000 °C for 48 h to enhance B-site cation ordering. Finally, gold electrodes (19 mm² area) were sputtered on both faces of the pellet. The detailed synthesis procedure and structural characterizations including XRD analysis for quantifying B-site order, SEM imaging for grain size evaluation, differential scanning calorimetry for estimating the T_c as well as the dielectric measurements of this sample can be found in the mentioned reference [186].

[These samples were provided by Jožef Stefan Institute, Ljubljana, Slovenia]

PST MLCs

PST MLCs were fabricated using solid-state reaction and tape casting method. To obtain a stoichiometric PST, Pb₃O₄, Sc₂O₃, and Ta₂O₅ starting precursors were ball-milled in distilled water with zirconia balls for 17 hours. The resulting slurry was dried, calcined at 850 °C for 4 hours, and then re-milled in an organic solvent with binder for 24 hours. PST green sheets were cast using a 300 μm doctor blade, and platinum paste was screen-printed to form internal electrodes. These sheets were stacked, pressed, and cut into chips. The binder was removed by heating at 500 °C for 4 hours, followed by sintering at 1400 °C for 4 hours. Finally, to enhance the B-site ordering in PST MLCs annealing was performed at 1000 °C for 100 – 1000 hours using a Pb₃O₄–ZrO₂ (1:1 molar ratio) packing powder. Silver paste was used to form the outer terminal electrodes. Further information regarding the preparation method can be found in [187] and the detailed structural characterizations of these samples are provided in our previous work [30].

[PST MLCs were prepared and fabricated by Tomoyasu Usui and Sakyō Hirose at Murata Manufacturing, Japan]

The dimensions and properties of PST ceramic and MLCs are provided in Table 4.1. For PST, the specific heat was measured and taken as $300 \text{ J kg}^{-1} \text{ K}^{-1}$ and the theoretical density of PST is 9.07 g cm^{-3} [188]. The measured density, active electrode area, dielectric layer thickness, zero-field T_c and their B-site cation order can also be found in this table.

Table 4.1 Properties and dimensions of PST ceramics and 0.5 mm thick PST MLC respectively.

Property	PST ceramic	0.5 mm PST MLC
Measured density (g cm^{-3})	8.76	8.57
Active area (mm^2)	19	48.7
# active layers	1	9
Layer thickness (μm)	86	38.6
Total # layers	1	11
Active volume (mm^3)	1.63	16.9
B-site order	0.88	0.75
Curie temperature T_c ($^{\circ}\text{C}$) [at zero applied field]	$\sim 20 - 23$	$\sim 18 - 20$

4.2.2 Nonlinear pyroelectric characterization setup

To directly implement the Olsen cycle and evaluate the performance of PST, a dedicated nonlinear pyroelectric characterization setup was employed in this work. As shown in Figure 4.1, the setup comprises a Linkam temperature stage, a Keithley 2410 source meter, and a FLIR X6580sc infrared camera. The entire cycle sequence was fully automated using a dedicated Python script, which controlled and monitored the temperature of the Linkam stage while simultaneously applying and recording the voltage and current profiles of the material in real time using the Keithley source meter.

The measurement sequence of the Olsen cycle began by cooling the sample with liquid nitrogen to initiate the charging step at low temperature. The sample was charged using Keithley 2410 source meter. In the following step, the sample was heated to high temperatures using the Linkam stage at a heating/cooling rate of $100^{\circ}\text{C min}^{-1}$ while maintaining the electric field using the source meter. This step corresponds to the isoelectric heating step of the Olsen cycle, which was followed by the discharge step at high temperature. Finally, the sample was cooled back to the starting temperature to commence the next cycle.

The same setup can be used to implement other pyroelectric conversion cycles by adjusting the applied electric field and its slew rate during the different steps of the cycle. For example, in the Olsen cycle, the field was applied and removed slowly to maintain quasi-isothermal conditions³. This was achieved by setting a low current compliance (< 0.2 mA) while operating the source meter in voltage-source mode. In contrast, implementing a Brayton cycle requires rapid charging and discharging to approach near adiabatic conditions, necessitating a high current compliance setting. Meanwhile, to implement a Stirling cycle, the current compliance of the device must be set to zero during the heating and cooling stages of the cycle to realize the isocharge steps, which will be discussed thoroughly in the next chapter.

Additionally, the infrared (IR) camera was used to monitor the temperature profile of the material by focusing on the active region of the sample surface, particularly during the application and removal of the electric field, to quantify the electrocaloric heat while implementing the cycle. Details about the IR thermography technique can be found in Appendix A.6.

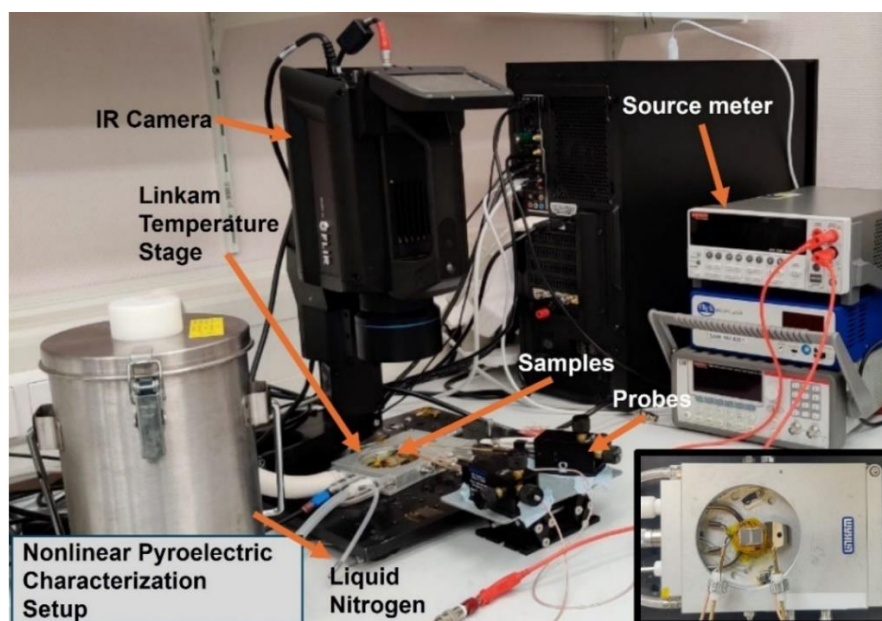


Figure 4.1 Picture of the nonlinear pyroelectric characterization experimental setup (Insert) Top-view image of the Linkam temperature stage used for thermally cycling the material.

³ As mentioned in Section 2.4.1, it is realistically not possible to reach perfect isothermal conditions as it takes infinite amount of time. Most of the system reach quasi-isothermal state. Likewise, it is also not possible to practically achieve true adiabatic conditions as there will be irreversible losses in the system in the form of hysteresis and the sample will exchange heat with the surroundings after a period of time. Hence, the system can reach near or quasi-adiabatic conditions making it extremely challenging to realize a Carnot like cycle for energy conversion.

4.3 Investigation of PST bulk ceramics

4.3.1 Characterization of $D - E$ loops

To quantify the nonlinear pyroelectric performance of PST bulk ceramic, unipolar $D - E$ loops were measured between 20 and 60°C in 5°C increments at a frequency of 1 Hz, under a maximum applied electric field of 130 kV·cm⁻¹. Since the primary aim of this chapter is evaluating conversion efficiency under bias field rather than pyroelectric energy density, the temperature range was limited to a 40 K interval around T_c , corresponding to the region where maximum conversion efficiency is expected due to the high pyroelectric coefficient of PST ceramics in this temperature window. The measurements were carried out using aixACCT TF 2000 analyser.

Due to the high degree of B-site ordering, the PST ceramic exhibits characteristics of a first-order ferroelectric, including significant remanent polarization when the electric field is applied and removed below its T_c . This residual polarization can distort the initial state of the sample, resulting in an offset in the polarization values, thus leading to a lower maximum polarization values in subsequent hysteresis loops. To eliminate the influence of remanent polarization, the sample was de-poled by heating well above T_c before each measurement.

Unipolar $D - E$ loops shown in Figure 4.2, were used to indirectly estimate the pyroelectric energy density of the sample. Similar to the measurement procedure described in the preceding chapter, the pyroelectric energy density was estimated by calculating the closed-loop integral $\oint E dD$, which corresponds to the area enclosed between the lower branch of the low-temperature $D - E$ loop (during field application) and the upper branch of the high-temperature $D - E$ loop (during field removal). A maximum energy density of 1.16 J·cm⁻³ was deduced between 20 and 60°C using the Olsen cycle at 130 kV·cm⁻¹ as shown in Figure 4.3. To avoid the electrical breakdown of the sample, the field was restricted to 130 kV·cm⁻¹. When the initial temperature of the cycle was below T_c , particularly for small temperature spans ($\Delta T = 5$ K), the change in electric displacement (ΔD) was minimal, resulting in negligible or in some cases negative energy densities due to overlapping $D - E$ loops. These values were omitted in Figure 4.3. However, a distinct variation in the maximum polarization is observed between 30 and 40°C. Indeed, this is attributed to the field induced shift of T_c to higher temperatures, as discussed in [186].

To validate the indirectly estimated energy densities, direct implementation of the Olsen cycle was also attempted on this sample using the nonlinear pyroelectric characterization setup. However, due to the small active area of this sample, the

generated current remained below the detection limit of the Keithley 2410 source meter, making it difficult to reliably track the current profile during the different stages of the cycle. As a result, direct measurements were not pursued further, and it was assumed that direct and indirect methods yield consistent results. This assumption is supported by previous experimental validation reported in our earlier study [30], and as will be shown in the following section, it also holds for PST MLCs.

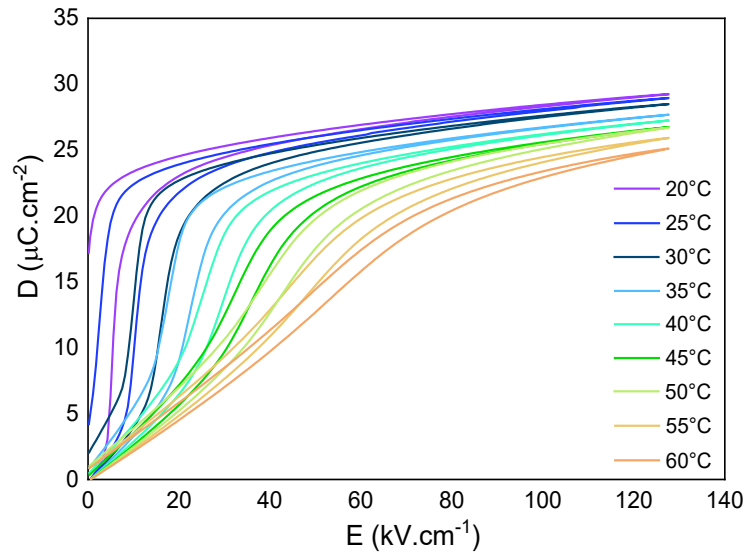


Figure 4.2 $D - E$ loops of PST ceramic at 1 Hz measured from 20 to 60°C for a maximum ΔE of 130 $\text{kV}\cdot\text{cm}^{-1}$.

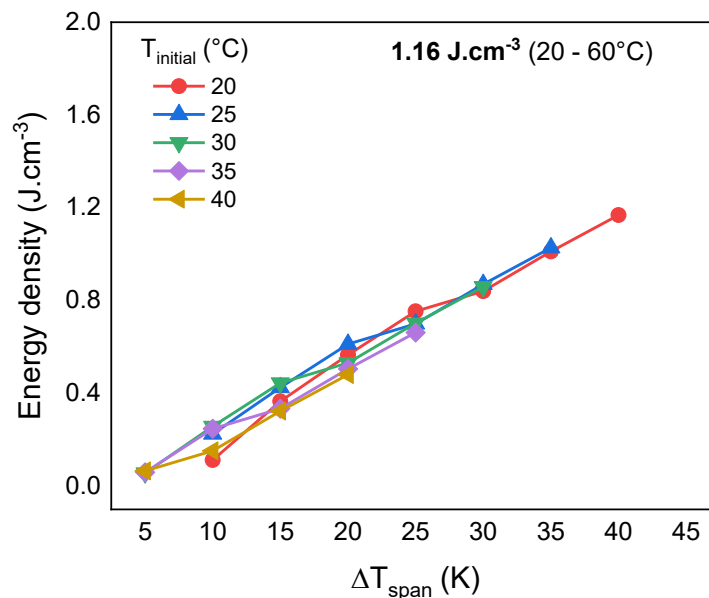


Figure 4.3 Indirect estimation of pyroelectric energy density at 1 Hz for a ΔE of 130 $\text{kV}\cdot\text{cm}^{-1}$.

4.3.2 Electrocaloric measurements

Following the $D - E$ loops measurement, the electrocaloric effect (ECE) of the PST ceramic was also directly measured using FLIR X6580sc IR camera (see Appendix A for device specifications). As mentioned in the previous chapter, quantifying the ECE of the material serves two key purposes: 1) Due to the thermodynamic converse relationship between the electrocaloric and pyroelectric effects, a strong ECE response implies a high potential for pyroelectric energy conversion; 2) The electrocaloric heat provides an upper bound estimate of the additional heat absorbed by the material during a thermodynamic cycle, particularly during field removal at elevated temperatures, thereby enabling quantification of the associated dipolar entropy change [41]. This additional heat must be taken into consideration while estimating the pyroelectric conversion efficiency of the material, which is detailed in the following section.

To ensure accurate temperature measurements, the sample surface was coated with black paint (Colorjelt Noir Mat, emissivity ~ 0.97) to approximate a perfect black body behaviour. In this way, external artefacts and spurious IR radiations from the surroundings were avoided. The electric field was applied systematically using Keithley 2410 source meter at 30°C . The measured adiabatic temperature variations (ΔT_{ad}) of the sample during both the heating and cooling phase of ECE is presented in Figure 4.4. A maximum ΔT_{ad} of 4.1 K was measured during the application of field to $150 \text{ kV}\cdot\text{cm}^{-1}$.

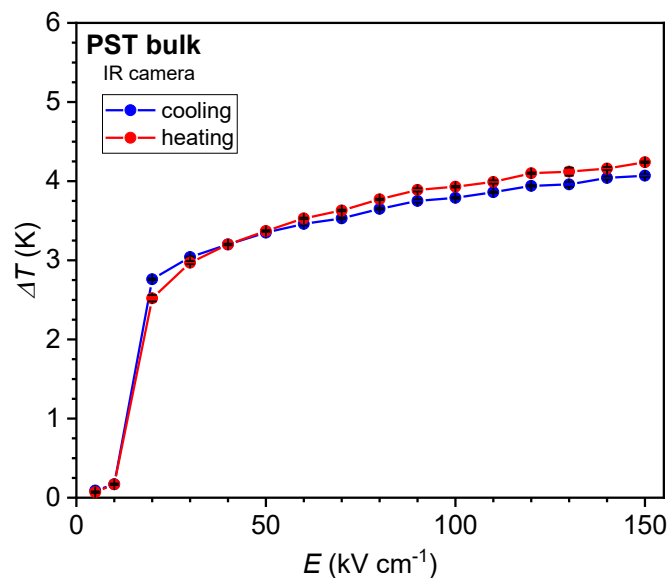


Figure 4.4 Adiabatic temperature variation of PST bulk ceramic at 30°C as a function of different electric field. [This measurement was performed by Dr. Uros Prah]

4.3.3 Pyroelectric efficiency of PST ceramic

The pyroelectric efficiency of this sample was estimated using the isothermal D – E loops for a ΔE of $130 \text{ kV}\cdot\text{cm}^{-1}$ at 1 Hz. As detailed in Section 2.4, the efficiency of the material is defined as the ratio of the harvested energy to the total heat input. For clarity, the equation for estimating the efficiency of the material when subjected to an Olsen cycle is restated below:

$$\eta_{Olsen} = \frac{\oint E dD}{\int_{T_{cold}}^{T_{hot}} C_p dT + Q_{hot}} \quad (4.1)$$

Here, the Q_{hot} corresponds to the additional heat input when the sample is discharged isothermally at high temperature during the Olsen cycle. To account for this contribution, the EC heat of the material discussed in the previous section was considered, as it has been reported that $C_p \Delta T_{EC}$ provides a good approximation of $T_h \Delta S_{E \rightarrow discharge}$ [41].

Accordingly, a maximum ΔT_{EC} of 4 K at $130 \text{ kV}\cdot\text{cm}^{-1}$ was considered in the analysis (see Figure 4.4) to maintain an upper bound for the heat input, thereby providing a lower bound for the efficiency (η) values, consistent with the methodology reported in our previous work [30]. Here, a maximum efficiency of 0.97 % was obtained between 20 and 60°C as shown in Figure 4.5 (a). While the measured pyroelectric conversion efficiency of the PST ceramic is relatively low ($\sim 1\%$), this outcome is a direct result of the limited exergy potential⁴ associated with small temperature spans ($\Delta T = 40 \text{ K}$). In other words, the amount of available thermal energy that can be converted into useful work (i.e., Carnot's potential) is limited for smaller temperature spans. Due to this reason, the absolute efficiency may appear low; however, this does not reflect the true performance of the material. Instead, evaluating the efficiency with respect to the Carnot limit provides a more meaningful comparison metric against existing technologies such as thermoelectric harvesters.

⁴ Exergy is defined as the maximum useful work that can be obtained from the system at a specified state with respect to its environment. The exergy content can be calculated by applying the Carnot equation, which indicates that the work potential is low for smaller temperature spans [216].

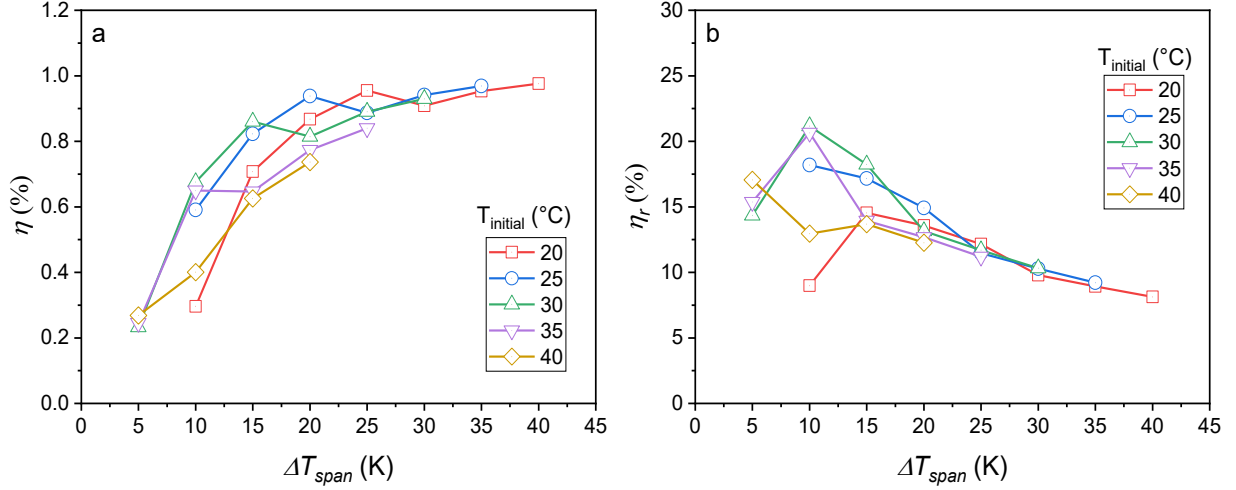


Figure 4.5 (a) Efficiency and (b) relative efficiency of PST ceramic using the Olsen cycle as a function of different temperature spans and initial temperatures.

The relative or second law efficiency (η_r) is defined as the ratio of the achieved efficiency to the Carnot efficiency, which is as follows:

$$\eta_{Olsen,r} = \frac{\eta_{Olsen}}{\eta_{Carnot}} = \frac{\oint E dD}{\int_{T_{cold}}^{T_{hot}} c_p dT + Q_{hot}} \left(\frac{T_{hot}}{\Delta T} \right) \quad (4.2)$$

A maximum η_r of 21% was obtained for the PST ceramic between 30 and 40°C (see Figure 4.5 (b)). The application of a high electric field ($\sim 130 \text{ kV}\cdot\text{cm}^{-1}$) shifted the T_c of PST ceramic to higher temperatures, resulting in the observed peak η_r at 30 °C. However, further enhancement of η_r at lower ΔT_{span} was limited by the pronounced electrical hysteresis exhibited by the sample at 1 Hz (see Figure 4.2).

Apart from the electrical hysteresis, thermal hysteresis of the sample might also affect the η_r of the cycle [103]. This PST ceramic exhibited a thermal hysteresis of approximately 4 K under zero bias, as estimated using differential scanning calorimetry and reported in [186]. As a result, for small temperature spans ($\Delta T_{span} \sim 5$ K) near the T_c , the cycle may not fully traverse the ferroelectric–paraelectric phase transition. In such cases, the material undergoes only a partial phase transformation, leading to an incomplete change in polarization (ΔP) and limiting the net energy harvested per cycle. Such incomplete transitions, due to the thermal lag between heating and cooling branches, can reduce the effective entropy change and subsequently the conversion efficiency, especially at lower temperature spans (i.e., ≤ 5 K close to the T_c of PST ceramic) where the cycle is confined within the hysteretic window [103,189]. While incomplete phase transitions have also been reported to limit electrocaloric cooling efficiencies [189,190], detailed characterization of thermal hysteresis under varying electric fields is essential to identify the minimum temperature span at which a fully reversible pyroelectric cycles can be implemented.

4.4 Nonlinear pyroelectric performance of PST MLC

While the PST ceramic exhibited a η_r of 21%, the conversion efficiency remained limited due to the hysteresis of the sample at narrow temperature intervals. Moreover, direct implementation of the Olsen cycle was not feasible because of the small active area and weak current signal. Following this, the PST MLCs were investigated due to their larger active area, improved thermal exchange characteristics, better scalability and most importantly for their large breakdown field. This section provides a detailed evaluation of the electrothermal behaviour and nonlinear pyroelectric response of 0.5 mm thick PST MLC.

4.4.1 Permittivity measurements

The relative permittivity (ϵ) of 0.5 mm thick PST MLCs was estimated using the aixACCT TF 2000 analyser at 1 kHz from -4 to 120 °C and back to -4 °C using a thermal loop function. The permittivity peak was observed at 20 °C for the 0.5 mm thick PST MLC as shown in Figure 4.6. These results agree well with the T_c measured using the DSC in [188].

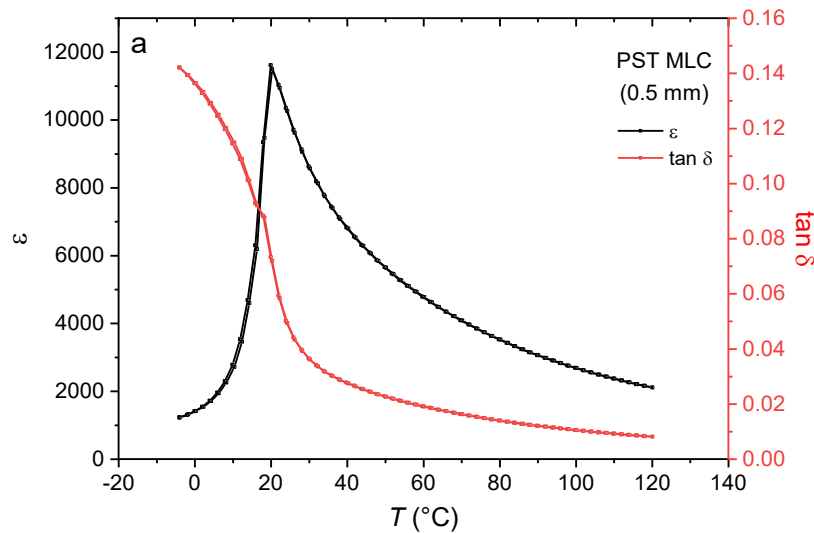


Figure 4.6 Relative permittivity and loss tangent measurements of 0.5 mm thick PST MLC performed at 1 kHz under a zero bias field condition. [This measurement was performed by Dr. Uros Prah]

4.4.2 Measurement of $D - E$ loops

To compare the nonlinear pyroelectric performance with that of PST ceramics, the 0.5 mm thick PST MLC was studied. In contrast to PST bulk ceramic, its B-site order was slightly lower ($\Omega = 0.75$). This comparison also allows for an investigation into how variations in B-site order influence thermal-to-electrical conversion efficiency under the same operating conditions.

Likewise, unipolar D - E loops were first measured from 20 to 60°C. To draw similar comparison with PST ceramics, the applied electric field was initially restricted to 130 $\text{kV}\cdot\text{cm}^{-1}$ and the frequency was also kept at 1 Hz, as shown in Figure 4.7. Here, the PST MLC exhibited significantly reduced electrical hysteresis compared to the bulk ceramic.

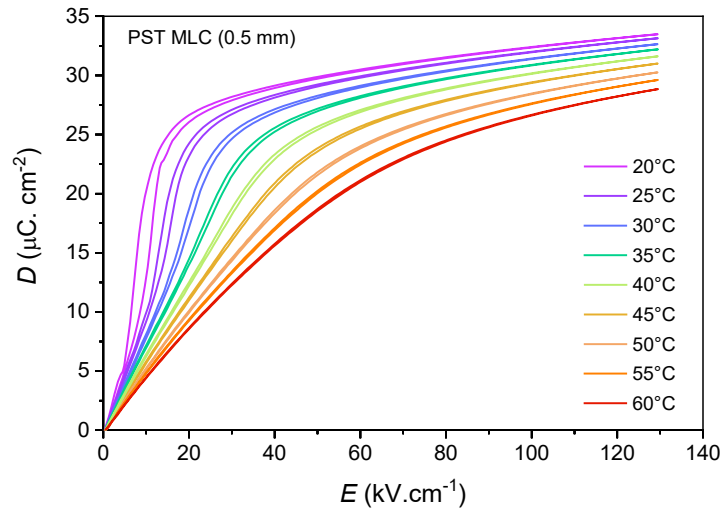


Figure 4.7 D - E loops of 0.5 mm thick PST MLC for a ΔE of 130 $\text{kV}\cdot\text{cm}^{-1}$ at 1 Hz.

The calculated energy density using $\oint E dD$ from the D - E loops is shown in Figure 4.8. A maximum energy density of 1.15 $\text{J}\cdot\text{cm}^{-3}$ was observed between 20 and 60°C at 1 Hz for a ΔE of 130 $\text{kV}\cdot\text{cm}^{-1}$. Due to the reduced hysteresis, higher energy densities were observed in narrow temperature spans ($\Delta T_{span} = 5$ K).

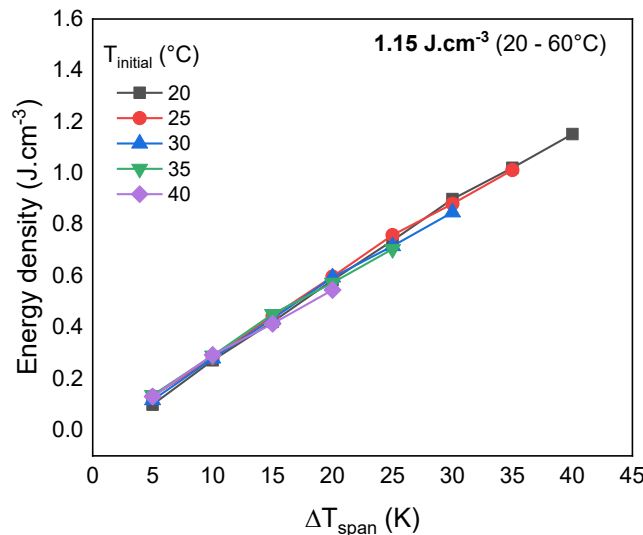


Figure 4.8 Energy density estimation from the isothermal D - E loops.

4.4.3 Direct implementation of the Olsen cycle

To validate the indirectly estimated energy density values and establish correlation with direct measurements, the Olsen cycle was implemented on the 0.5 mm thick PST MLC using the nonlinear pyroelectric characterization setup described in Section 4.2. As outlined in Section 2.4.1, the Olsen cycle consists of four stages: (1–2) isothermal charging, (2–3) isoelectric heating (i.e., heating under constant electric field), (3–4) isothermal discharging, and (4–1) isoelectric cooling of the material. These steps are clearly indicated in Figure 4.9 (a) and (b), which illustrate the recorded voltage and current profile of the material during the direct Olsen cycle and its corresponding energy profile as a function of time, respectively.

For this measurement, the sample was charged to 500 V ($130 \text{ kV}\cdot\text{cm}^{-1}$) at 20°C under a compliance current of $100 \mu\text{A}$. The charging process was completed within approximately 1.5 s. Given the relatively short duration, this step cannot be considered strictly isothermal or adiabatic. As discussed previously, achieving near-isothermal conditions would necessitate extremely slow charging rates, substantially extending the overall cycle duration and thereby making the process impractical for energy harvesting applications. Nevertheless, despite these shortcomings, the execution of an Olsen cycle under such conditions remains feasible, thus demonstrating the practical viability of this cycle over other pyroelectric conversion cycles.

Following the charging step, the sample was heated to 60°C while maintaining a constant electric field. The evolution of the pyroelectric current during the isoelectric heating step marks the onset of the energy harvesting process. Specifically, the observed negative current arises from the pyroelectric effect. As the polarization of PST decreases with increasing temperature, the pyroelectric coefficient becomes negative leading to a negative current, as shown in the insert. This behaviour, described by the relation $(I = Ap \frac{dT}{dt})$, indicates that the energy injected into the material during the initial charging step was being effectively recovered. This is further reflected in the energy profile of the material, which approaches zero at step (3), indicating that the injected energy was almost fully recovered.

Following this, the sample was discharged at 60°C by removing the applied voltage while maintaining a compliance current of $100 \mu\text{A}$. During this step, 19.42 mJ of energy was harvested by the material. Subsequently, the sample was cooled down to 20°C under zero applied voltage. This energy corresponds to a pyroelectric energy density of $1.14 \text{ J}\cdot\text{cm}^{-3}$ as the active volume of the material was 0.017 cm^3 (refer Table 4.1), indicating a very good agreement with the indirect measurements. Moreover,

including the cooling duration (assumed equal to the heating phase duration), the Olsen cycle was executed at a frequency of 0.015 Hz.

Despite the longer cycle duration, the charging and discharging rates were neither fast enough to approximate adiabatic conditions nor slow enough to ensure true isothermal behaviour. This was not explicitly mentioned in our previous work [30]. To evaluate this, additional measurements with slower electric field ramps were performed to approximate near-isothermal conditions (see Appendix C). The harvested energy showed no significant deviation, suggesting that the above mentioned cycle in Figure 4.9, closely represents an ideal Olsen cycle, despite the relatively faster charging and discharging steps. This characteristic is one of the key reasons why the Olsen cycle is favoured over other pyroelectric conversion cycles.

Similarly, direct Olsen cycles were implemented for different temperature spans by keeping the initial temperature constant at 20°C. Figure 4.10 shows the correlation between direct and indirect measurements across various temperature spans. Since the indirect measurements agree well with the direct measurements, the unipolar D - E loops were used to quantify the efficiency of this material.

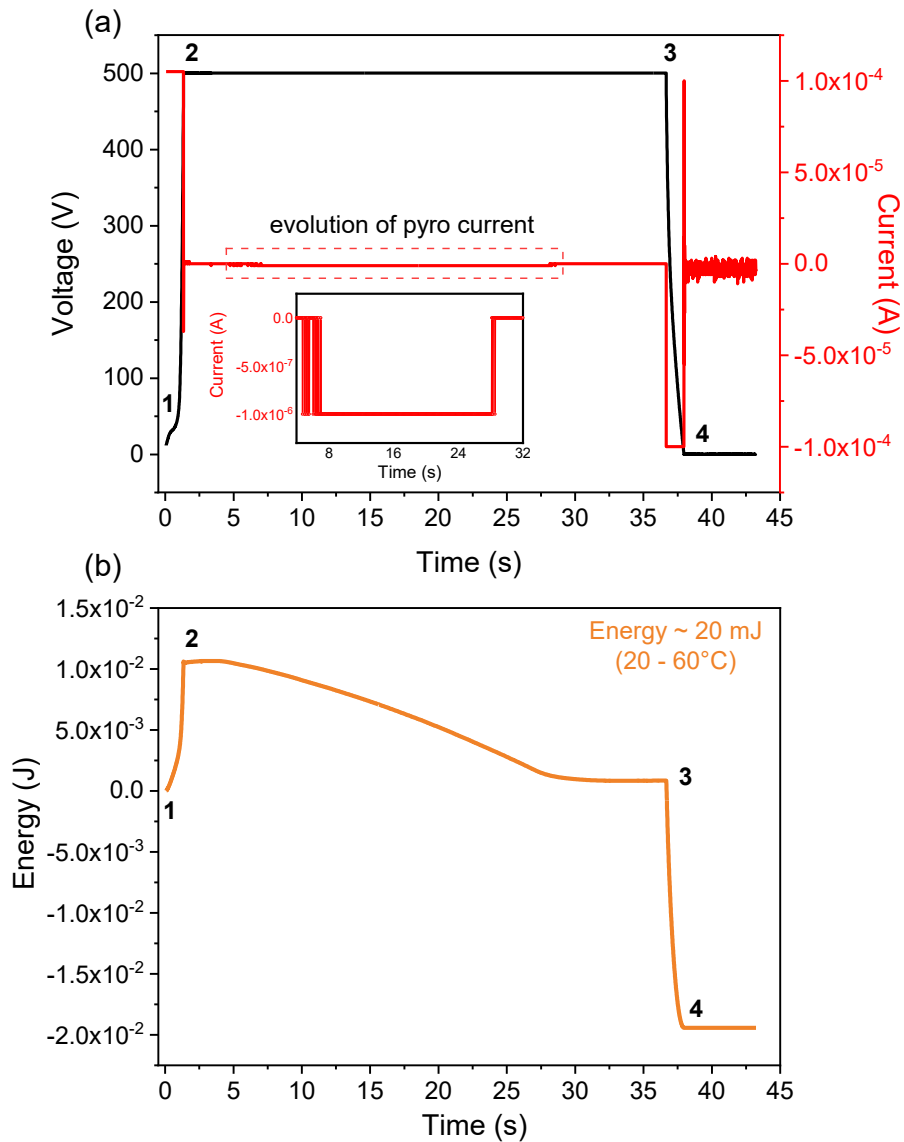


Figure 4.9 (a) Voltage (in black) and current (in red) temporal profiles of the 0.5 mm thick PST MLC subjected to an Olsen cycle; (Insert) Zoomed in view of current vs time profile during the isoelectric heating phase. (b) Corresponding energy profile (in maroon) of the material as a function of time. The inserted numbers (1,2,3 and 4) correspond to the different steps of the Olsen cycle. Negative energy represents the harvested energy.

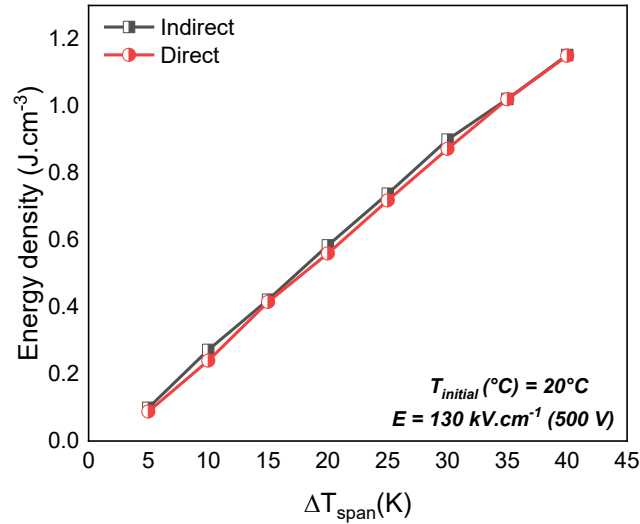


Figure 4.10 Correlation between indirect and direct Olsen cycle measurements on 0.5 mm thick PST MLC.

4.4.4 Evaluation of the pyroelectric conversion efficiency

To account for the additional heat contributions during the isothermal discharge step of the Olsen cycle, the ECE of the sample was considered for the efficiency calculation (i.e., $C_p \Delta T_{EC} \cong T_h \Delta S_{E \rightarrow \text{discharge}}$), as mentioned earlier. The adiabatic temperature variation of this sample was directly measured from its active area through the IR camera. A maximum ECE of 2.6 K was observed at 500 V (130 kV.cm⁻¹) on this 0.5 mm thick PST MLC at 30°C as shown in Figure 4.11. These results were taken from our previous work [30].

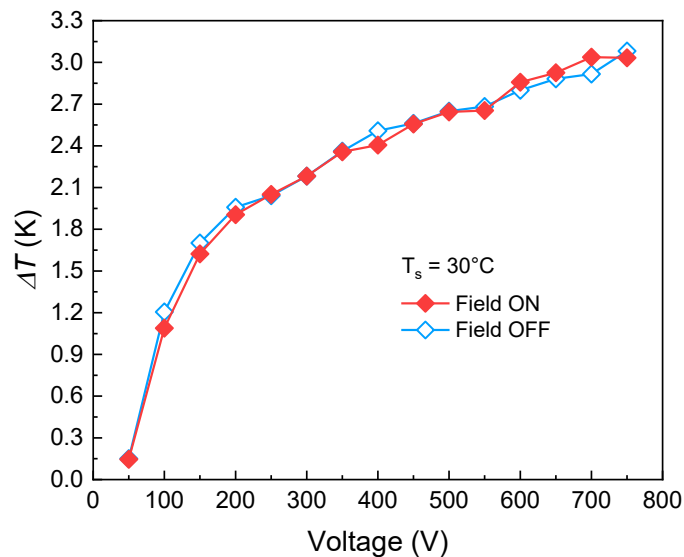


Figure 4.11 ECE of 0.5 mm thick PST MLC at a starting temperature of 30°C for different electric fields. [This result is adapted from the supplementary information (Figure 12.2) of reference [30]].

To calculate efficiency, the measured density and heat capacity values for the PST MLCs were taken from Table 4.1. Using equations (4.1) and (4.2) a maximum η of 1.07 % was obtained for a ΔT of 30 K starting at 20°C as shown in Figure 4.12 (a). Moreover, a maximum η_r of 43 % was achieved between 35 and 40°C, which is twice that of PST ceramic (see Figure 4.12 (b)). In contrast to the bulk ceramic, the 0.5 mm thick PST MLC exhibited a larger area between consecutive D - E loops even at smaller ΔT values, indicating a higher energy density under reduced temperature spans. This improvement can be attributed to the reduced thermal and electrical hysteresis of the MLC sample. Previous studies have confirmed minimal thermal hysteresis in ordered PST MLCs [187,191], which allows the material to undergo more complete and reversible ferroelectric to paraelectric transformations. This reversibility reduces energy losses associated with partial or incomplete transitions and metastable states, thereby enhancing the achievable energy density during the pyroelectric conversion cycle, especially under smaller ΔT_{span} .

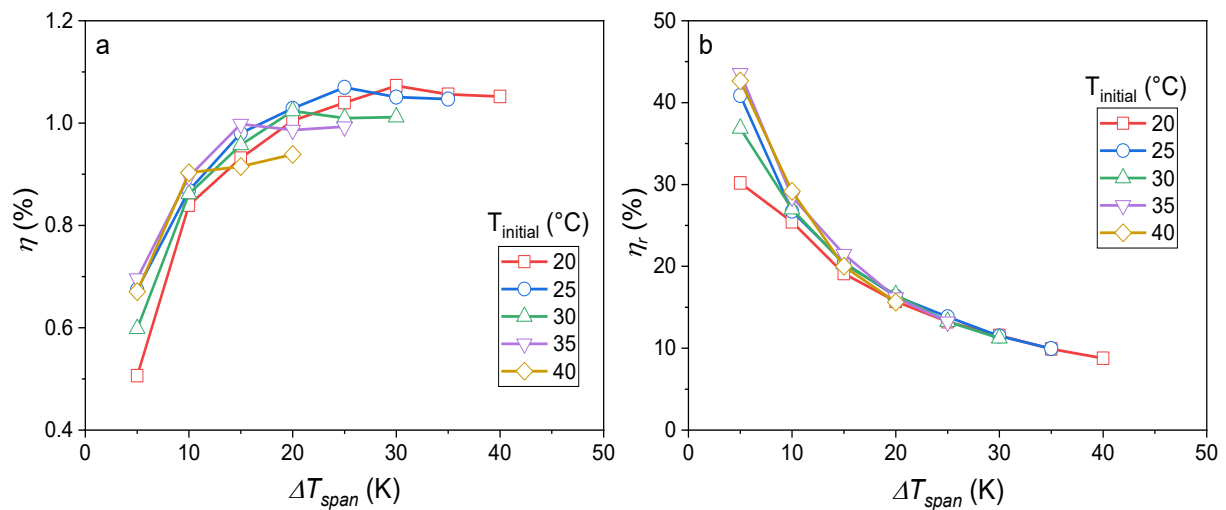


Figure 4.12 (a) Efficiency and (b) relative efficiency of a 0.5 mm thick PST MLC under the Olsen cycle for different temperature spans and starting temperatures at $130 \text{ kV}\cdot\text{cm}^{-1}$ and 1 Hz.

4.4.5 Pyroelectric efficiency of PST MLC at high electric fields

Additionally, the pyroelectric efficiency of the material was investigated under the application of extremely high electric fields. By applying a maximum electric field of $205 \text{ kV}\cdot\text{cm}^{-1}$, close to the breakdown limit of the sample, a pyroelectric energy density of $1.65 \text{ J}\cdot\text{cm}^{-3}$ was estimated from the D - E loops measured at 1 Hz using the Olsen cycle, between 20 and 70°C (Figure 4.13 (a) and (b)).

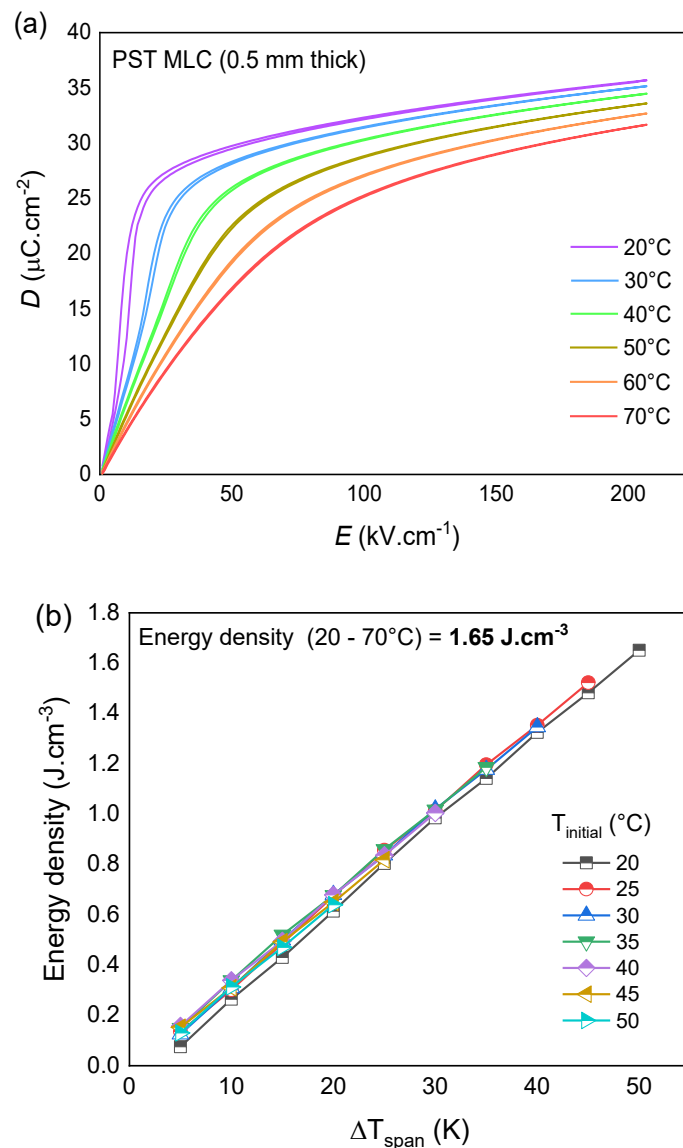


Figure 4.13 (a) Unipolar $D - E$ loops of 0.5 mm thick PST MLC between 20 and 70°C for a ΔE of $205 \text{ kV}\cdot\text{cm}^{-1}$ at 1 Hz. (b) Estimated energy density across different temperature spans and initial temperatures.

Next, direct Olsen cycles were implemented on this sample to validate the indirect measurements. The results are shown in Figures 4.14 and 4.15, respectively. In addition to monitoring the current, voltage, and energy profile of the material over time, the surface temperature was continuously recorded throughout the cycle using

an IR camera (see Figure 4.14 (a)). For this measurement, the compliance current was limited to 70 μA , and the sample was charged to 800 V ($\sim 205 \text{ kV}\cdot\text{cm}^{-1}$) at 20 $^{\circ}\text{C}$. The reduced compliance current setting on the Keithley source meter was intended to increase the charging duration. Despite this adjustment, the sample reached 800 V within approximately 2 seconds. Similar to the previous case, this charging step cannot be considered strictly isothermal or adiabatic. As a result, a discernible electrocaloric effect ($\Delta T_{\text{EC}} \sim 2 \text{ K}$) was still observed through the IR camera while charging the material. Subsequently, the sample was heated to 70 $^{\circ}\text{C}$ via Linkam stage at a heating rate of 100 $^{\circ}\text{C}$ per minute, followed by the discharge step at 70 $^{\circ}\text{C}$, as illustrated in Figure 4.14 (b). Likewise, the electrocaloric cooling effect was observed while discharging the sample. This corresponds to a harvested energy of 27 mJ, which is equivalent to 1.60 $\text{J}\cdot\text{cm}^{-3}$ (Figure 4.14 (c)). Later, the sample was cooled to 20 $^{\circ}\text{C}$ at zero voltage. During this cooling phase, the voltage and current were not monitored, as no energy contribution was expected in the absence of an external field.

Subsequently, the Olsen cycle was implemented for different temperature spans (ΔT_{span}) by keeping the starting temperature and applied voltage constant at 20 $^{\circ}\text{C}$ and 800 V, respectively. The experimentally obtained energy densities were then compared with those derived from indirect estimations, as shown in Figure 4.15.

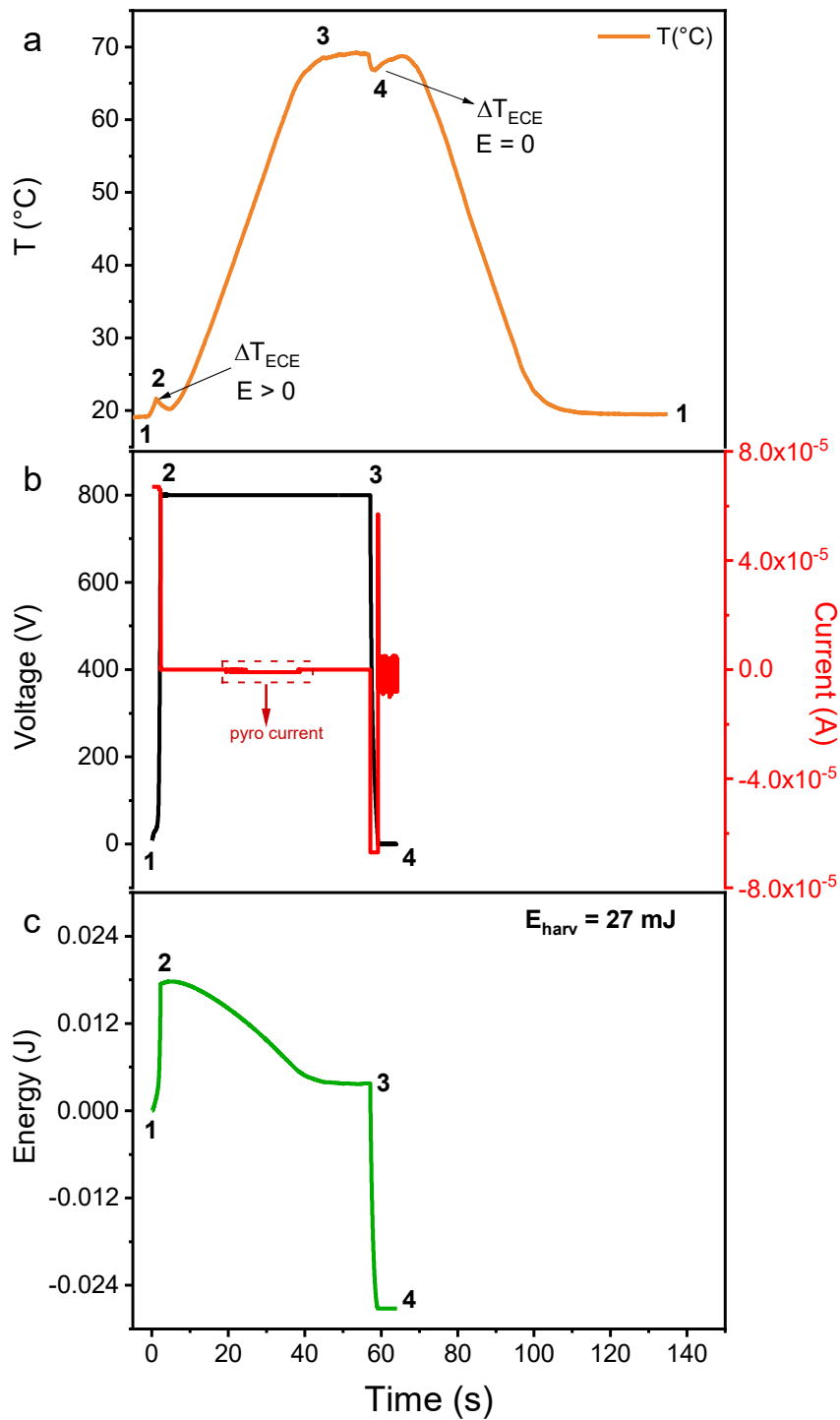


Figure 4.14 (a) Temperature profile of the PST MLC undergoing Olsen cycle between 20 and 70°C; (b) Corresponding voltage and current profile of the sample during different stages of the Olsen cycle; (c) Energy profile of the sample throughout the cycle as a function of time.

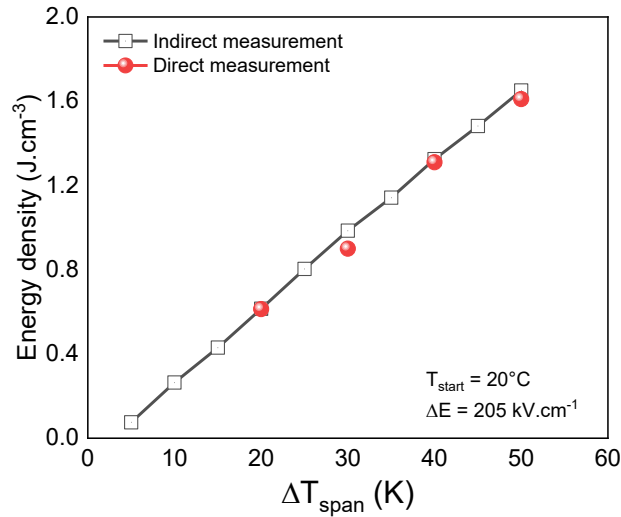


Figure 4.15 Comparison between directly implemented and indirectly estimated Olsen cycles for a 0.5 mm thick PST MLC at an initial temperature of 20 °C across different temperature spans (ΔT_{span}).

Similarly, the η and η_r values were calculated from the hysteresis loops and plotted in Figure 4.16 (a) and (b) respectively. A maximum η_r of 48% was observed between 40 and 45°C under the Olsen cycle at 1 Hz and 205 kV·cm⁻¹. Increasing the electric field from 130 kV·cm⁻¹ to 205 kV·cm⁻¹ shifted the temperature corresponding to peak η_r from 35 to 40 °C, indicating an electric field-induced upward shift in T_c [30,188]. To verify this trend, additional measurements at lower fields were conducted (see Appendix C), which further support that the observed shift in the relative efficiency peak from lower to higher temperatures with increasing field arises from electric field-induced transition behaviour of the material. Moreover, previous studies have reported that the application of strong electric fields can completely suppress thermal hysteresis in PST MLCs [103], which may further contribute to the enhanced efficiency observed at elevated fields within a narrow temperature span.

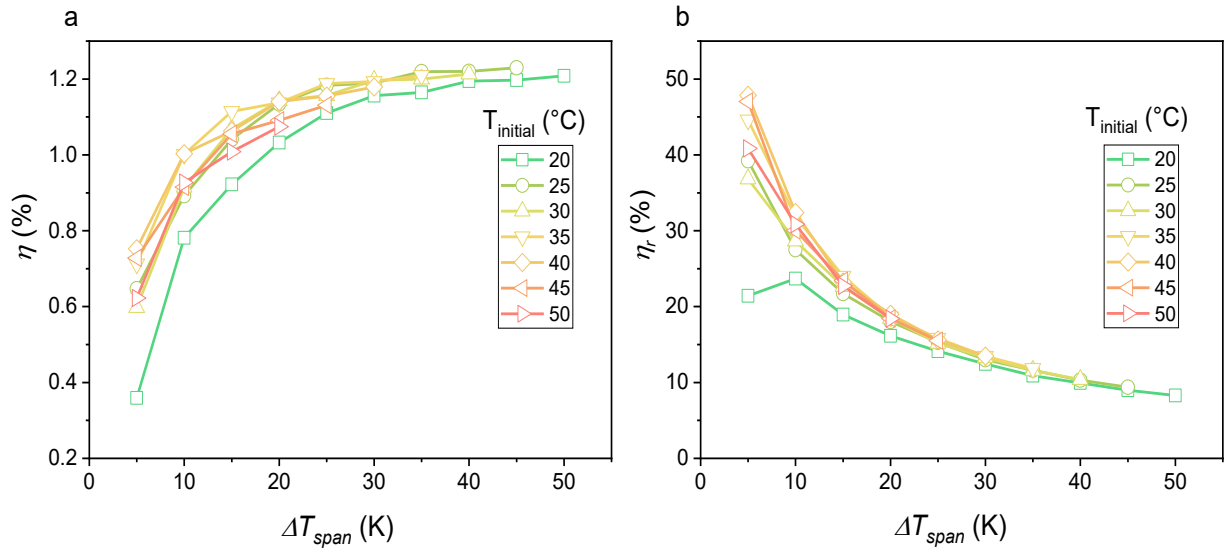


Figure 4.16 Estimated (a) η and (b) η_r of the 0.5 mm thick PST MLC under Olsen cycle at 1 Hz for a ΔE of $205 \text{ kV}\cdot\text{cm}^{-1}$.

4.5 Influence of frequency on the performance of PST MLC

In addition to examining the role of electric field strength, this section investigates how operating frequency impacts the pyroelectric conversion efficiency of a 0.5 mm thick PST MLC. In the earlier sections, energy densities and relative efficiencies were estimated using unipolar D - E loops measured at a low frequency of 1 Hz. Furthermore, a very good correlation between the indirect and direct Olsen cycle measurements was observed.

This naturally raises two questions: (1) How does increasing the cycling frequency affect the nonlinear pyroelectric response and relative efficiency of PST MLC? (2) More specifically, can higher frequencies drive the system toward near-adiabatic conditions, thereby enabling the implementation of Brayton cycles? Moreover, operating in the near-adiabatic regime provides a direct means to compare the efficiency and energy output of Brayton and Olsen cycles under identical field and temperature conditions.

For the system to reach near-adiabatic conditions, the timescale for electric field application must be comparable to or shorter than the material's thermal time constant [192,193]. In other words, the electric field must be applied much faster than the rate at which heat can diffuse through the material, thereby minimizing thermal exchange with the surroundings. A practical estimate of the thermal response time, also referred to as the thermal diffusion time constant, can be obtained using the classical one dimensional heat conduction model [194]. The thermal time constant (τ_{th}) of PST MLC can be estimated using equation (4.3) as follows,

$$\tau_{th} = L^2/\alpha \quad (4.3)$$

where L is total thickness of the sample, and α is thermal diffusivity of the sample, which is defined as

$$\alpha = \frac{k}{\rho C_p} \quad (4.4)$$

For this calculation, thermal conductivity k of PST was taken as $2.1 \text{ W m}^{-1} \text{ K}^{-1}$, density ρ as 9070 kg m^{-3} , and specific heat capacity C_p of $300 \text{ J kg}^{-1} \text{ K}^{-1}$ [195]. Substituting these values into equation (4.4) yields a thermal diffusivity α of $0.78 \text{ mm}^2 \text{ s}^{-1}$. Given that the PST MLC consists of eleven layers in total, including nine active layers each $38.6 \text{ }\mu\text{m}$ thick, the overall sample thickness accounting for both dielectric and electrode layers is approximately $420 \text{ }\mu\text{m}$ as reported in our previous work [30]. Using this value and α in Equation (4.3), τ_{th} is estimated to be approximately 0.25 s . This estimate is consistent with previously reported thermal time constant values for PST MLCs [188]. It should be noted that this is an approximation and several factors such as the contact resistance, and thermal resistance between the layers and electrodes were not considered for this calculation [196].

Therefore, to approximate near-adiabatic conditions in PST MLCs, $D - E$ loops were measured at 10 Hz across various temperatures. Figure 4.17 (a) and (b) shows the unipolar and bipolar adiabatic $D - E$ loops for a ΔE of $205 \text{ kV}\cdot\text{cm}^{-1}$. In contrast to previous measurements, the unipolar $D - E$ loops measured at 10 Hz between 20 and 40°C (see Figure 4.17 (a)) exhibited incomplete depolarization, resulting in open $D - E$ loops. This effect is more pronounced at lower temperatures where polarization switching is slower. This discrepancy arises due to current delivery limitations of the aixACCT TF Analyzer 2000, which can only supply a maximum of 20 mA . As a result, while applying high voltages at high frequency, the instrument cannot precisely follow the triangular voltage waveform at the very beginning and end of the measurements, resulting in incomplete discharge of the sample and leading to open $D - E$ loops. Hence, indirect estimation of energy densities from these unipolar loops will result in incorrect values.

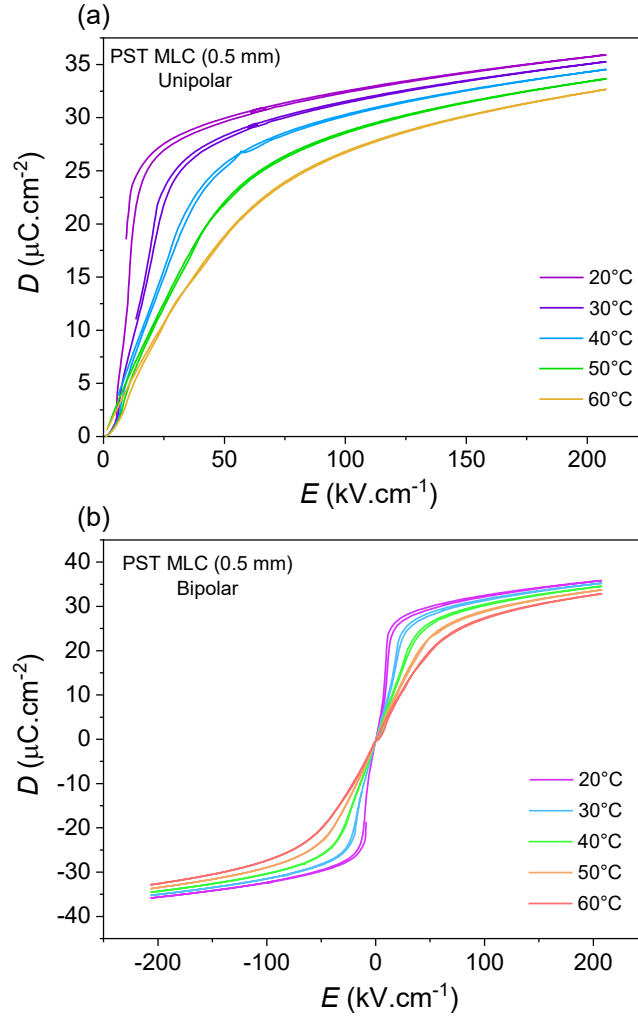


Figure 4.17 Adiabatic $D - E$ loops (a) unipolar , (b) bipolar of 0.5 mm thick PST MLC measured at 10 Hz for a ΔE of $205 \text{ kV}\cdot\text{cm}^{-1}$.

To mitigate these issues, bipolar $D - E$ loops were employed for the estimation of energy density and pyroelectric conversion efficiency. Although the aforementioned limitations are also present in bipolar measurements, the application of an alternating electric field forces the sample to depolarize. For consistency and to avoid the influence of distorted reverse-field behaviour, energy density calculations were performed using only the first quadrant of the bipolar loop. This approach enables reliable numerical integration of the $\int_0^{E_{max}} EdD$ term while minimizing artifacts. It should be noted that bipolar loops typically exhibit greater hysteresis compared to unipolar loops, which results in a smaller enclosed area between the polarization and electric field curves, thereby yielding a comparatively lower calculated energy density, as reported by Olsen et al. [35]. As shown in Figure 4.18, a maximum harvestable energy density of $1.26 \text{ J}\cdot\text{cm}^{-3}$ was achieved between 20 and 60°C for a ΔE of $205 \text{ kV}\cdot\text{cm}^{-1}$. Following this, a preliminary attempt was made to directly implement

and characterize this sample under a Brayton cycle within the same temperature range. Although the experiment was not successful, the details of this experiment and its outcomes are provided in Appendix C.

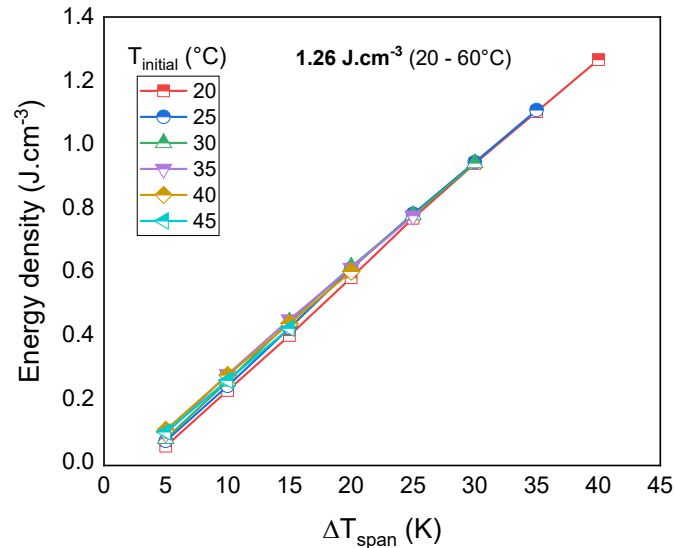


Figure 4.18 Pyroelectric energy density across different temperature spans and initial temperatures estimated from the bipolar $D - E$ loops at 10 Hz and $\Delta E = 205 \text{ kV}\cdot\text{cm}^{-1}$.

Consistent with the methodology outlined in the previous section, the efficiency (η) and relative efficiency (η_r) of PST MLC under Brayton cycle were estimated using the corresponding bipolar $D - E$ loops. The η of the Brayton cycle is expressed in equation (4.5):

$$\eta_{Brayton} = \frac{\oint E dD}{\int_{T_2}^{T_3} c_p \rho dT} \quad (4.5)$$

Since the electric field is applied and removed rapidly in the Brayton cycle, the system briefly attains a near adiabatic condition, during which heat exchange with the surroundings is negligible. As a result, additional heat contributions such as the electrocaloric heat, which was considered in the Olsen cycle can be neglected in this case. In other words, no additional heat input is required during the near adiabatic charging and discharging states of the Brayton cycle, potentially enhancing the overall conversion efficiency. Figure 4.19 (a) and (b) shows the η and η_r of PST MLC under Brayton cycle. A maximum η of 1.2% was obtained between 20 and 60°C, and a maximum η_r of 50 % was obtained between 40 and 45°C. These results indicate that it is possible to achieve slightly higher η_r using the Brayton cycle compared to the Olsen cycle without considering any heat regeneration.

However, it should be noted that at higher operating frequencies, the material may not reach its maximum polarization value within the short field application time. Consequently, the energy density obtained under the Brayton cycle is slightly lower than that of the Olsen cycle. This reduction in energy density represents a trade-off, as the Brayton cycle does not require additional heat input. This observation is consistent with previous reports on Brayton and Ericsson cycles in the context of electrocaloric refrigeration, where high efficiencies were similarly observed under rapid cycling conditions when no heat regeneration was implemented [134,136].

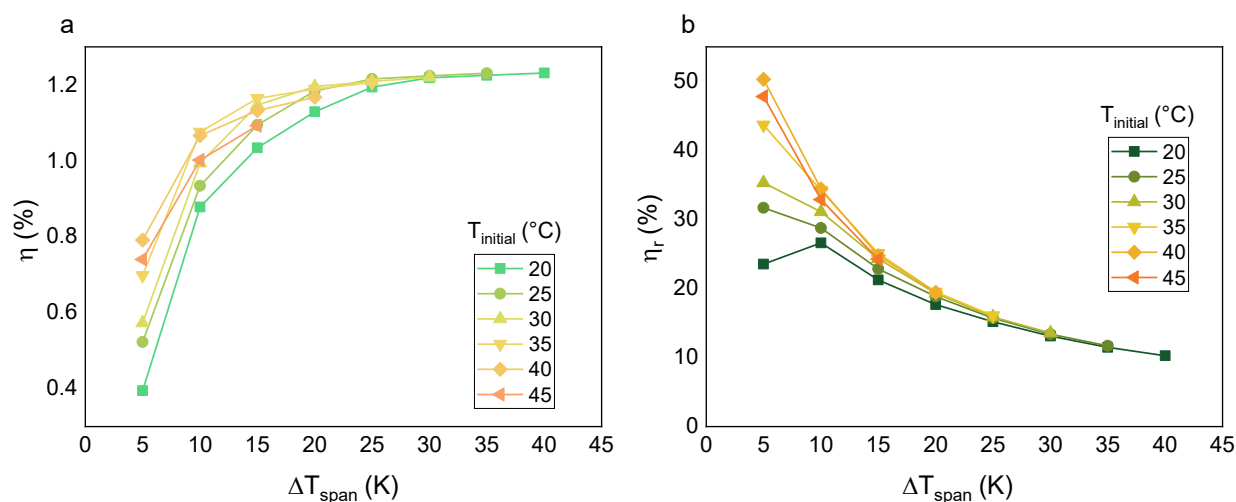


Figure 4.19 (a) η and (b) η_r of the 0.5 mm thick PST MLC under Brayton cycle at 10 Hz for a ΔE of $205 \text{ kV}\cdot\text{cm}^{-1}$.

4.6 Summary and conclusions

This chapter investigated the nonlinear pyroelectric performance of PST bulk ceramics and PST MLCs under the Olsen cycle. These samples were selected to examine the influence of high B-site cation ordering, the impact of device geometry, and their practical feasibility for macroscopic applications. The key findings are summarized below:

- PST bulk ceramics exhibited a maximum relative efficiency (η_r) of 21% under the Olsen cycle between 30 and 40°C at $130 \text{ kV}\cdot\text{cm}^{-1}$.
- PST MLCs (0.5 mm thick) demonstrated improved performance with a maximum η_r of 43% under the same Olsen cycle conditions, primarily due to reduced hysteresis.
- Under high electric fields ($205 \text{ kV}\cdot\text{cm}^{-1}$), PST MLCs achieved an η_r of 48% under the Olsen cycle between 40 and 45°C, indicating field-enhanced efficiency through a shift in the T_c .

- Direct implementation of the Olsen cycle validated the energy output and efficiency estimations derived from isothermal D – E loops of PST MLC.
- A preliminary study on the relative efficiency of PST MLCs operating under the Brayton cycle was conducted. At a cycling frequency of 10 Hz and an applied electric field of 205 kV/cm, the devices achieved a maximum relative efficiency (η_r) of 50%, which is comparable to, or slightly higher than, that observed for the Olsen cycle. Nonetheless, further experimental validation through direct implementation of the Brayton cycle remains necessary.

In summary, this chapter has explored the influence of B-site ordering, device geometry, hysteresis behaviour, electric field strength, and cycling frequency on nonlinear pyroelectric energy harvesting using the PST material system. Among the configurations investigated, the multilayer capacitor (MLC) geometry exhibited the highest pyroelectric conversion efficiency and was therefore examined in greater detail. Notably, PST MLCs demonstrated a maximum relative efficiency of 50%, confirmed through both indirect and direct implementations of pyroelectric conversion cycles. These results further indicate that it is indeed possible to surpass the 50% material efficiency threshold even without incorporating heat regeneration. Collectively, these findings underscore the strong potential of PST MLCs for practical, macroscopic energy harvesting applications.

Chapter 5

Proof-of-concept: Pyroelectric energy harvesting devices using $\text{Pb}(\text{Sc}_{1/2}\text{Ta}_{1/2})\text{O}_3$ multi-layer capacitors

5.1 Motivation

Hitherto, the majority of research has focused on improving the pyroelectric properties of materials, especially the pyroelectric coefficient p and figure of merit (FOM), while comparatively little attention has been given to their practical implementation in macroscopic energy harvesting devices. This limited progress at the system level is due to the challenges associated with (1) establishing a proper temperature-varying heat source, (2) direct implementation of electro-thermodynamic cycles and (3) the lack of efficient electronic systems to convert the harvested energy into useful work from the non-linear pyroelectric energy harvesting devices.

Olsen et al.[34] were among the first to investigate the practical implementation of macroscopic pyroelectric energy harvesting devices by subjecting materials to electro-thermodynamic cycles. They also demonstrated that a spatial temperature gradient can be transformed into temperature fluctuations over time using a caloric fluid oscillating between hot and cold reservoirs, as detailed in Section 2.5. Following the pioneering work of Olsen and colleagues [116], Sebald et al.[7] revisited the concept of nonlinear pyroelectric energy harvesting and compared its performance with that of thermoelectric energy conversion. They reported that higher efficiencies can be achieved in the former, especially when the operating temperature range is limited [197]. Furthermore, they emphasized that power interface circuits must be optimized to limit the conversion losses and maximize the energy extracted from the pyroelectric harvester. To achieve this, they investigated various nonlinear energy processing techniques and reported that switched-mode power converters offer a highly efficient solution [36]. They also demonstrated that the nonlinear switching process can boost the voltage of the pyroelectric material intermittently and emphasized that this technique is simple enough to be self-powered [38], as discussed in Section 2.4.4. Their primary motivation was to pursue the development of self-powered energy harvesters for integration into microelectronic systems, aiming to harness ambient energy sources such as vibrations or waste heat to supplement or replace batteries and enable long lasting device operation.

Based on these insights, the main objective of this chapter is to design, implement, and experimentally validate a self-powered pyroelectric energy harvester operating under the Stirling cycle, using PST MLCs as the active material. This proof-of-concept system aims to demonstrate the feasibility of autonomous operation without relying on external power sources. To achieve this, the system incorporates a dedicated microcontroller, low-voltage converter and a switched-mode power converter for efficient energy conditioning and system control. Furthermore, this chapter seeks to extend the concept to a macroscopic scale by developing a harvester capable of sustaining its own operation while continuously powering an external electronic device. This chapter comprehensively details the design, implementation, and experimental validation of the proposed system, thereby addressing the broader question of whether continuous, stand-alone operation of a macroscopic pyroelectric energy harvester is practically achievable.

For clarity, this chapter is organized into three main sections. Section 5.2 explores the direct implementation and characterization of Stirling cycles on PST MLCs. Section 5.3 details the design and implementation of a fully autonomous pyroelectric energy harvester using only two PST MLCs as the active material. Section 5.4 presents a scaled-up self-powered harvester comprising 60 PST MLCs, capable of operating for several hours without external energy sources while continuously powering an external electronic device. This section also details the prototype, including the circuit, which builds upon the system introduced in Section 5.3, along with the integration of the external device. Finally, Section 5.5 summarizes the key findings presented in this chapter.

Since this work required expertise in electrical and electronic engineering in addition to thermal engineering, prototyping using PST MLCs, and implementation of pyroelectric Stirling cycles, it was carried out in collaboration with some of my colleagues. Their contributions are duly acknowledged here:

- The autonomous circuit (including the Arduino code for the microcontroller) discussed in Section 5.3 was developed by Mr. Olivier Bouton with valuable inputs from Dr. Emmanuel Defay and Dr. Jérôme Polesel.
- LTSpice simulations were performed by Mr. Olivier Bouton.
- LTC 3588-1 board was evaluated with the help of Mr. Olivier Bouton, Dr. Veronika Kovacova and Dr. Alvar Torello.
- The macroscopic pyroelectric energy harvester was designed and constructed by the author. Valuable insights and technical discussions with Dr. Longfei Song and Dr. Junning Li supported the development and refinement of the system.

- The electronics for the self-powered macroscopic pyroelectric prototype discussed in Section 5.4 was developed by Mr. Nouredine Bousri. He was also responsible for programming the microcontrollers used in this work.
- The inductor used in the macroscopic system in Section 5.4 was selected by Dr. Longfei Song and Mr. Nouredine Bousri.
- The pump and valve controller system was designed by Dr. Omar Ramirez Sanchez.
- The external Bluetooth communication device, based on the XIAO BLE sensor, along with the custom-built application for recording the transmitted data, was developed by Mr. Nouredine Bousri with the aid of Dr. Jérôme Polesel and Mr. Olivier Bouton.
- All the components were mechanically assembled together with the help of Mr. Mathieu Gerard.

The first part of the results on the autonomous pyroelectric energy harvester using two PST MLCs, as presented in Section 5.3 of this chapter, is based on my contributions to the publication: *Lheritier P, Torelló A, Usui T, Nouchokgwe Y, Aravindhana A, Li J, Prah U, Kovacova V, Bouton O, Hirose S, Defay E. "Large harvested energy with non-linear pyroelectric modules, Nature. 609(7928): (2022), 718–21"*.

The second part of this chapter on self-powered macroscopic pyroelectric energy harvester detailed in Section 5.4 is based on my contributions to the article "*One-watt pyroelectric generator*", which is currently under peer-review.

5.2 Stirling cycle

The Stirling thermodynamic cycle can be adapted for pyroelectric energy harvesting and this conversion cycle consists of four steps: (1) isothermal polarization, (2) isocharge heating, (3) isothermal depolarization, and (4) isocharge cooling, as detailed in Section 2.4.1. Among the various pyroelectric conversion cycles, the pyroelectric Stirling cycle stands out for its simplicity and ease of implementation. Unlike the Olsen or Brayton cycle, which require the application of high fields throughout the cycle to achieve large work outputs, the Stirling cycle can deliver a considerably high energy output with low field input. This is due to the isocharge heating step, which amplifies the input energy without continuous field control. These characteristics make the Stirling cycle more practical for device implementations as the electrical and electronic circuit complexities can be avoided.

To directly implement and evaluate the performance of 0.5 mm thick PST MLCs under the Stirling cycle, the same experimental setup used to perform the Olsen cycle, as detailed in Section 4.2.2, comprising the Linkam stage and the Keithley 2410 source

meter, was employed. Likewise, this experiment was also completely automated using a Python script to apply and continuously monitor the voltage, current and energy as a function of time throughout the cycle. More details about the dimensions such as the active and inactive volume of the 0.5 mm thick PST MLC can be found in the previous chapter (see Table 4.1).

Figure 5.1 shows the direct analysis of the Stirling cycle on a 0.5 mm-thick PST MLC ($10.4 \times 7.2 \times 0.5 \text{ mm}^3$) cycled from 5 to 95°C at an input voltage of 25 V. The different stages of the cycle are marked in the graph. Due to the open circuit heating step, the output voltage reached 650 V, which is 26 times that of the input voltage (see Figure 5.1 (a)). At the end of this cycle, 25 mJ of energy was harvested by this sample (see Figure 5.1 (b)), corresponding to an active energy density of $1.47 \text{ J}\cdot\text{cm}^{-3}$ per cycle, given its active volume of 17 mm^3 .

To draw a proper comparison between the direct and indirect methods, isothermal $D - E$ loops were also collected on this sample at different temperatures using aixACCT TF 2000 analyser and Trek 609E-6 high voltage amplifier. Since the amplified output voltage from the direct analysis was observed at 650 V, the unipolar $D - E$ loops were measured under 1 Hz at 5 and 95°C at 650 V, corresponding to $170 \text{ kV}\cdot\text{cm}^{-1}$ (see Figure 5.2). The blue shaded region represents the isothermal charging step at 25 V ($\sim 7 \text{ kV}\cdot\text{cm}^{-1}$), indicative of the input energy. The orange area represents the energy harvested by the material under the Stirling cycle, as this area was integrated by keeping the displacement D constant. The deduced active energy density was around $1.64 \text{ J}\cdot\text{cm}^{-3}$ per cycle, equivalent to an absolute energy of 28 mJ. These results indicate good correlation between the two methods.

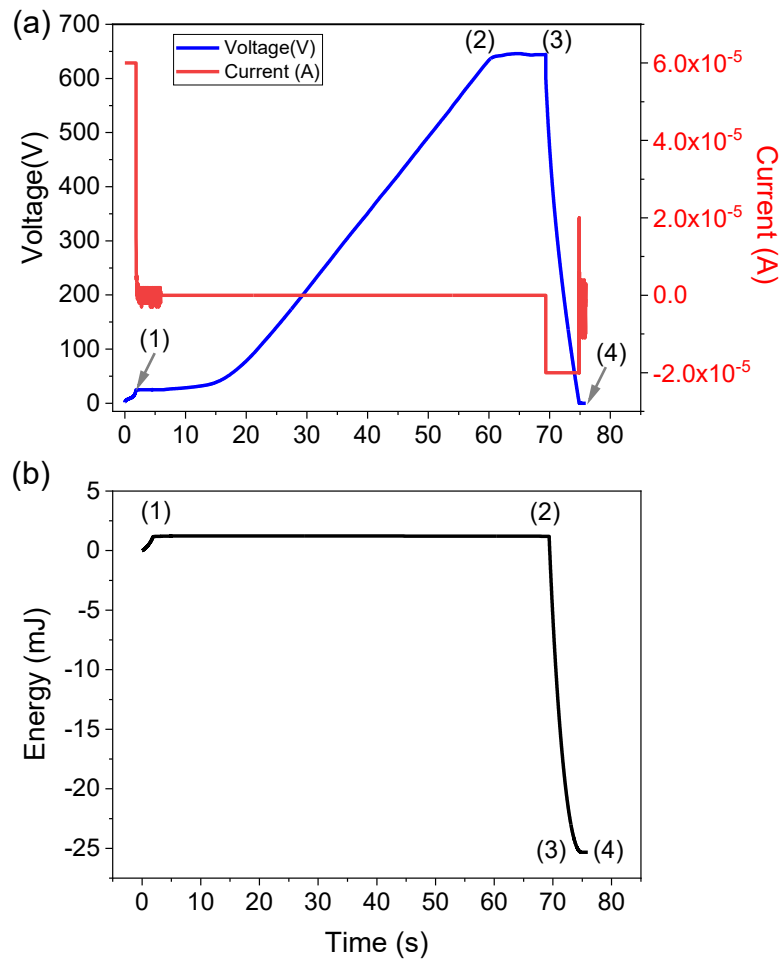


Figure 5.1 Direct implementation of the Stirling cycle on 0.5 mm thick PST MLC between 5 and 95°C. (a) Voltage and current profile as a function of time (b) Energy profile as a function of time.

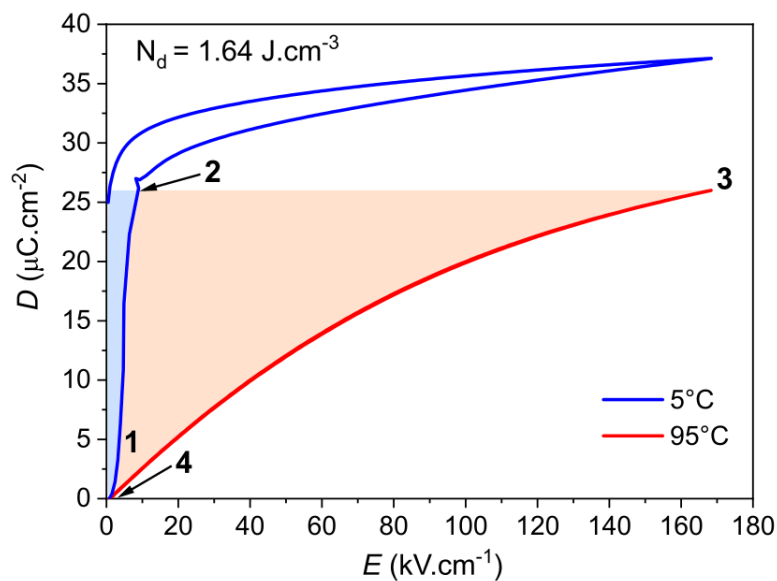


Figure 5.2 Isothermal unipolar $D - E$ loops of 0.5 mm thick PST MLC measured at 5 and 95°C for an applied field of $170 \text{ kV}\cdot\text{cm}^{-1}$. The blue region corresponds to the input

energy. The blue and orange regions corresponds to the total energy output of the material and the orange area alone corresponds to the amount of harvested energy from heat.

From these observations, it can be inferred that the key advantage of the Stirling cycle lies in its ability to amplify the supplied energy due to the isocharge (open circuit) heating step. This characteristic makes it particularly attractive for further investigation of electrical energy gain, which is defined as the ratio of harvested energy to the input energy supplied during charging.

$$Gain = \frac{\text{Energy harvested}}{\text{Energy supplied}}$$

In the context of Figure 5.2, this corresponds to the ratio of the orange area to the blue area. Previous studies have shown that the Stirling cycle yields higher electrical gain at low electric fields compared to the Olsen cycle for the same temperature span (ΔT), provided that the material's phase transition lies within this range [37]. These results were obtained in $\text{Pb}(\text{Zn}_{1/3}\text{Nb}_{2/3})_{0.955}\text{Ti}_{0.045}\text{O}_3$ single crystals, focusing primarily on the field induced ferroelectric to ferroelectric ($FE - FE$) phase transition.

To verify if similar behaviour is observed in PST MLC, the electrical gain under the Stirling and Olsen cycles was directly measured on one single 0.5 mm thick PST MLC and reported in Figure 5.3 (a). In this study, the ΔT was fixed between 20 and 70 °C, and the operating frequency was kept at 0.01 Hz, while the input voltage was varied accordingly. This temperature range was selected to encompass the T_c of PST (~ 20 °C) and to avoid voltage overshoot during the Stirling cycle, as the field is not controlled during the open circuit heating step. These results indicate that the gain is higher for Stirling cycle at low fields, and it starts to decrease with increasing fields. Measurements of the Stirling cycle beyond a starting field of 70 $\text{kV}\cdot\text{cm}^{-1}$ were not performed due to the risk of electrical breakdown. In contrast, for the Olsen cycle, the electrical energy gain reaches a maximum at a certain field and then remains steady. At high electric fields, the injected energy increases but the harvested energy shows limited improvement due to the polarization saturation, resulting in smaller ΔP and hence lower electrical energy gain.

Hence the relative efficiency, which is known as the efficiency with respect to Carnot efficiency will also be higher for the Stirling cycle at lower applied fields compared to the Olsen cycle (see Figure 5.3 (b)) due to the higher electrical gain. This scenario changes at higher electric fields, where only the Olsen cycle can be reliably implemented, as the voltage amplification during the Stirling cycle may lead to sample breakdown. Additionally, the electric field is actively controlled throughout the Olsen cycle, making it more suitable for operation at high fields, as reported in our previous

work [30]. Using the Stirling cycle, a maximum Carnot efficiency of 6.22 % was achieved at an applied field of 78 $\text{kV}\cdot\text{cm}^{-1}$, compared to 5.20 % for the Olsen cycle under the same field. The reported efficiency value increased to 8.60 % of Carnot efficiency at 205 $\text{kV}\cdot\text{cm}^{-1}$ for the Olsen cycle.

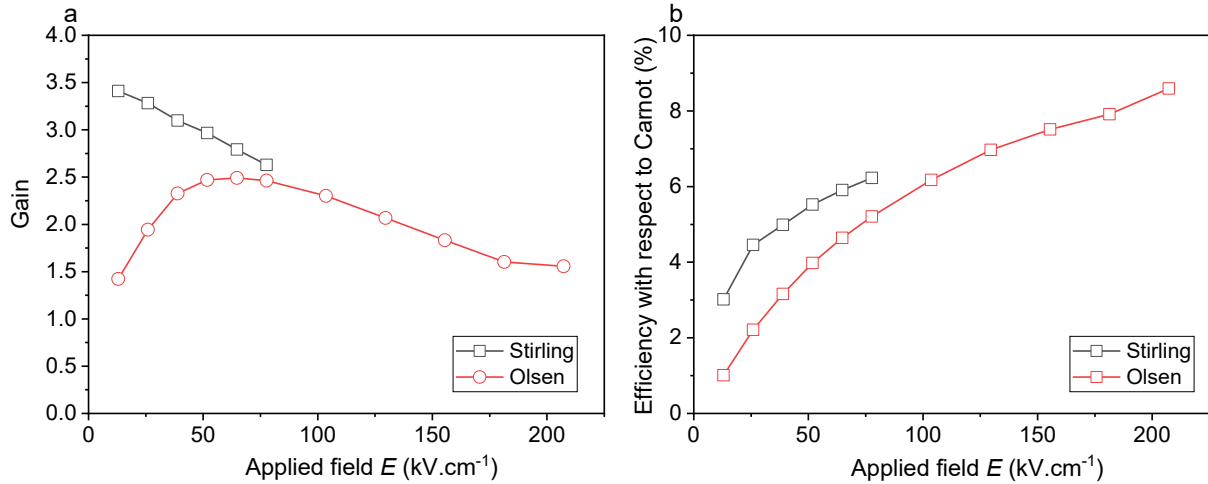


Figure 5.3 (a) Electrical gain in 0.5 mm thick PST MLC under Stirling (in black) and Olsen (in red) cycle. (b) Estimated efficiency with respect to Carnot for the Stirling (in black) and Olsen (in red), as a function of the applied field.

Unlike in the previous chapter, the electrical energy gain and relative efficiency in this study were calculated directly from the measured results rather than being derived from the $D-E$ loops, as these measurements were performed for only one temperature range. It is also important to note that the additional heat contributions arising from dipolar entropy changes during the discharge step, typically represented by electrocaloric (EC) heat, as discussed in earlier chapters were not included in the efficiency comparison presented here. This simplification was made to streamline the analysis and because the EC contribution is negligible at the lower electric fields of interest. While high-field results of the Olsen cycle were presented for completeness, the primary focus of the comparison between the Olsen and Stirling cycles is on the electrical energy gain at low-field operation. Accordingly, the relative efficiency (η_r) was calculated using:

$$\eta_r = \frac{\eta}{\eta_{Carnot}} = \frac{\oint E dD}{\int_{T_{cold}}^{T_{hot}} C_p dT} \left(\frac{T_{hot}}{\Delta T} \right)$$

These findings highlight the potential of the Stirling cycle for practical applications that demand low input energy and high energy output. Given these advantages, the Stirling cycle was chosen as the basis for developing the autonomous energy harvesting system described in the following section.

5.3 Autonomous pyroelectric energy harvester

The objective of this work is to develop an autonomous pyroelectric energy harvester capable of spontaneously operating across a defined temperature interval. The energy extracted from the pyroelectric material is utilized both to drive successive Stirling cycles and to power the electronics required for system operation, thereby eliminating the need for any external energy source.

To realize such an autonomous system, three key aspects must be addressed. First, the maximum harvestable energy from PST MLCs at different temperatures and applied electric fields must be characterized. Second, the high output voltage generated during the Stirling cycle must be effectively stepped down and stored, necessitating a highly efficient low-voltage converter. Finally, a microcontroller capable of making real-time decisions based on sensor input is required to autonomously manage energy extraction and system operation.

Hence, the autonomous harvester can be divided into three blocks:

- (1) the harvester block, composed of the pyroelectric materials
- (2) the converter part, consisting of the low-voltage converter, a DC/DC converter, and storage capacitors
- (3) the controller block, embedding the microcontroller, temperature sensor, and boost converter

To address the first requirement, the energy harvested by a single 0.5 mm thick PST MLC under the Stirling cycle was evaluated at a starting temperature of 5 °C across different temperature spans (ΔT) and applied voltages, as shown in Figure 5.4. The results show that the harvested energy increases with both the final temperature and the applied voltage. Larger temperature spans lead to higher output voltages (> 500 V) and greater energy extraction, with the maximum harvested energy (~18 mJ) achieved between 5 °C and 105 °C at an applied voltage of 20 V.

It is also important to note that the harvested energy is influenced by both intrinsic and extrinsic factors. Intrinsic parameters such as the applied voltage and temperature span naturally impact the energy output, as expected. However, extrinsic including slight fluctuations in the final temperature, variations in the duration the sample is held at elevated temperature, or non-ideal discharge conditions may also contribute to variability in the measured energy. While some of these effects are unavoidable in practice, efforts were made to minimize them for these measurements.

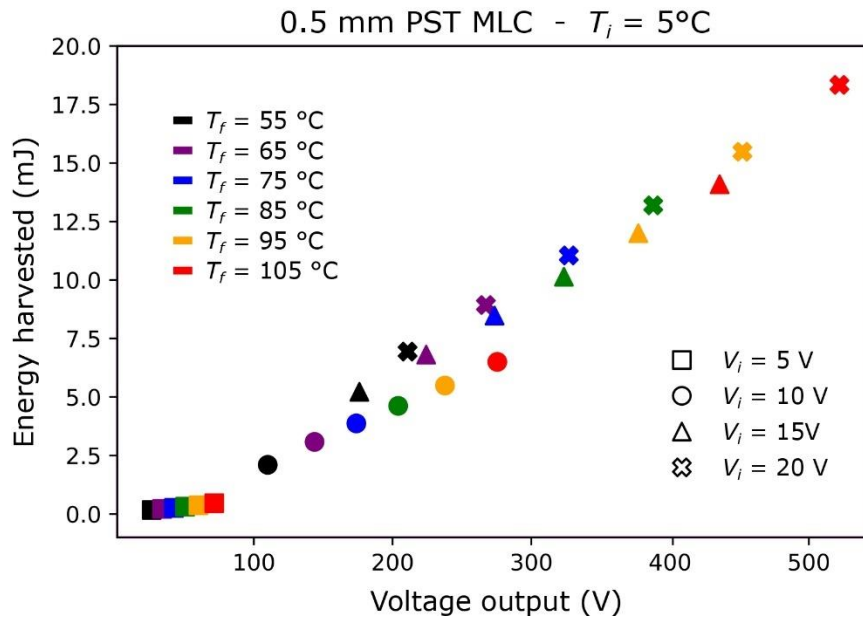


Figure 5.4 Energy harvested by 0.5 mm thick PST MLC under Stirling cycle across various temperature spans as a function of output voltage. The initial temperature was kept at 5°C and the input voltage was varied from 5 to 20 V, which are annotated with different symbols. The final temperature for each cycle is indicated by different colour legends.

5.3.1 Low-voltage converter

To practically implement the Stirling cycle in a functional system, the high output voltage of the PST MLC must be efficiently stepped down to a usable level. To achieve this, a low-voltage converter composed of a reed relay (S2-05EU), an inductor (1140-122K-RC, 1.2 mH, 5.5 A, $0.23\ \Omega$), and two diodes (BYW56-TR, breakdown $\sim 600 - 1000\ \text{V}$) was designed. Its operation is analogous to a buck converter, as shown in Figure 5.5.

During operation, when the switch is closed (ON-state) to discharge the PST MLC (after the isocharge heating step of the Stirling cycle), the current from the material flows through the circuit. In this phase, diode D1 is forward biased, resulting in an increase in current through the inductor. The inductor stores the energy in the form of magnetic field, inducing a voltage polarity across its terminals. This voltage drop across its terminals counteracts the source voltage, leading to a reduction in the output voltage. As the current continues to flow through the circuit, it simultaneously transfers the energy into the storage capacitor. It is important to note that during this phase, diode D2 remains reverse biased and prevents any current flow through its path.

When the switch is opened (OFF-state), the voltage source (i.e., PST MLC for this case) is disconnected and the current in the circuit begins to decrease. This reduction in current causes the magnetic field stored in the inductor to collapse, resulting in a

reversal of the voltage polarity across its terminals. As a result, the diode D2 becomes forward biased, allowing the inductor to discharge its stored energy into the storage capacitor. In this phase, the inductor effectively acts as a current source, maintaining the flow of current and delivering energy to the output. Through this controlled process, the high voltage from the PST MLC is efficiently stepped down and stored in the capacitor as a lower, usable voltage.

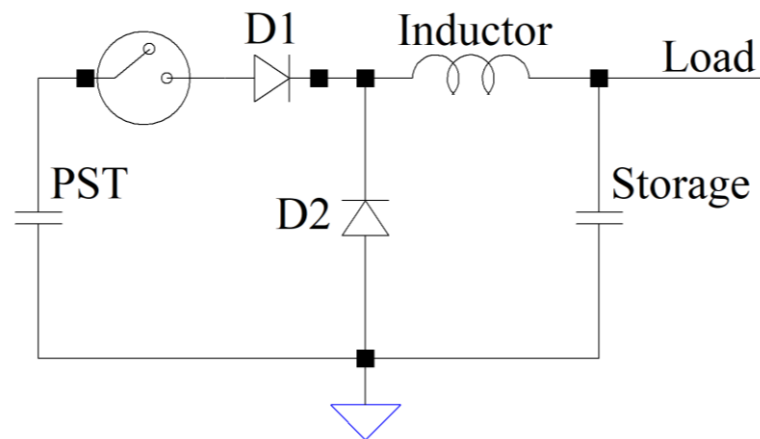


Figure 5.5 Schematic of the low-voltage converter circuit drawn using LTspice software.

To evaluate the performance of the low-voltage converter, the energy transferred from the PST MLC into the storage capacitor was measured. Several passive components including the inductors, diodes, and relays were initially evaluated through LTspice simulations and subsequently tested experimentally. Final component selection was based on their measured power consumption and overall efficiency. Real-time voltage monitoring of both the PST MLC and the storage capacitor was carried out using a Keithley 2410 and a Keithley 2400 source meter, automated through a Python-based data acquisition script. For initial testing, tantalum electrolytic capacitors (capacitance of each is $10.5 \mu\text{F}$ with a rating of 16 V) were used as storage elements, as their stored energy can be estimated using the relation $E = \frac{1}{2} CV^2$.

Figure 5.6 presents the harvested energy, and the energy stored (left Y – axis) in the capacitor as a function of the output voltage of a single 0.5 mm thick PST MLC subjected to the Stirling cycle for five different temperature spans from 55 to 95°C. The initial temperature was maintained at 5°C, and the input voltage was kept constant at 20 V. Depending on the temperature span of the cycle, the final output voltage of the PST MLC varied between 240 and 510 V. The energy harvested by PST MLC was directly obtained using the Keithley 2410 source meter, which continuously recorded the voltage and current of the sample over time throughout the Stirling cycle. In contrast, the energy stored in the output capacitor was measured after discharging the

PST MLC through the low-voltage converter circuit. In this case, the stored energy was estimated using $E = \frac{1}{2}CV^2$ as mentioned earlier. Additionally, the percentage of transmitted energy (right Y – axis) from the PST MLC into the storage capacitor is plotted in red as a function of the output voltage, which is based on the final temperature.

It must be noted that the final voltage and the transmitted energy developed across the storage capacitor depends directly on its capacitance. To ensure maximum energy transfer from each conversion cycle while preventing the voltage from exceeding the capacitor’s rated limit (i.e., the maximum voltage it can withstand without electrical breakdown, which was 16 V in this case), the total capacitance was adjusted according to the temperature span of the Stirling cycle. This was accomplished by connecting multiple capacitors in parallel to vary the total storage capacity. For instance, a storage capacitance of 84 μF was used when the cycle operated between 5°C and 55°C, while 126 μF was employed for a wider span of 5°C to 95°C. The transmitted energy percentage was calculated by comparing the energy in the storage capacitor to the total energy harvested by the material. Using this low-voltage converter, 75 – 80% of the harvested energy⁵ was successfully transferred into the storage capacitors.

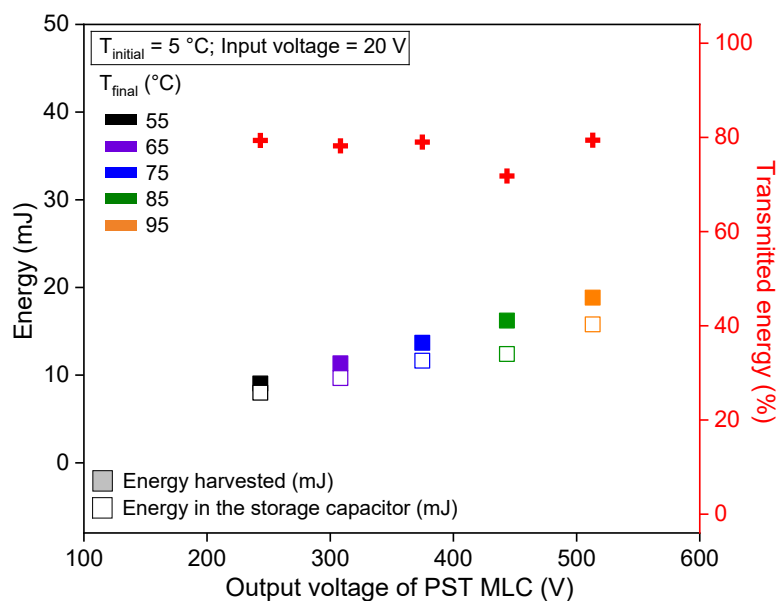


Figure 5.6 Energy harvested by 0.5 mm-PST MLC (filled squares) and the energy stored in the capacitors (open squares) as a function of the output voltage during Stirling cycle operation at different temperature spans. The corresponding final

⁵ However, it must be emphasized that this observed efficiency is due to the Stirling cycle. A preliminary measurement without the Stirling cycle, in which the charged PST MLC was directly discharged into the storage capacitor, reveals a significantly lower efficiency. This comparison highlights that the Stirling cycle plays a crucial compensatory role, and therefore, the present low voltage converter design, while effective, is not yet fully optimized.

temperatures for each cycle are indicated in the colour legend. The right Y-axis represents the percentage of transmitted energy from the PST MLC to the storage capacitor as a function of the final output voltage for each temperature span.

Following the optimization of the low-voltage converter, the next step involved evaluating the LTC 3588-1 board. This DC-DC converter is essential for providing a steady and regulated DC voltage (~ 3.6 V) to power the microcontroller. This board consists of an internal capacitor, a full wave bridge rectifier and a buck converter that regulate the power flow. The board also features an undervoltage lockout (UVLO) mechanism with ultralow standby current (< 90 nA) and a wide hysteresis window, allowing the input capacitor in the LTC board to accumulate charge before efficiently delivering it to the output storage device. Using the voltage regulator, the voltage from its internal capacitor is effectively stepped down and it delivers an output of 3.6 V. Once regulation is achieved, the system enters a low-power sleep mode, minimizing energy consumption. The buck converter in the board activates only as needed to maintain output stability. More information about the detailed functioning of this converter board can be found elsewhere [198].

To evaluate its performance, the storage capacitor was directly connected to the LTC 3588-1 board, which served as the power source. The energy from storage capacitors is transferred to the internal capacitor of the LTC 3588-1 board, where it was stepped down to supply a regulated DC output voltage. The input and output voltage of the LTC board was monitored using the National Instruments Data Acquisition device (NI-DAQ) with the help of LabView software. For this test, the Stirling cycle was performed over a temperature range of 5 to 25 °C on a 0.5 mm thick PST MLC, with an input voltage of 25 V. The same low-voltage converter setup was retained, while the storage capacitor's capacitance was set to 60 μ F. Although the LTC board can handle a maximum input of 20 V, the temperature span was limited to keep the internal capacitor voltage below the 10 V detection threshold of the NI-DAQ device. Figure 5.7 shows the internal capacitor's voltage and the output voltage of LTC 3588-1 board as a function of time.

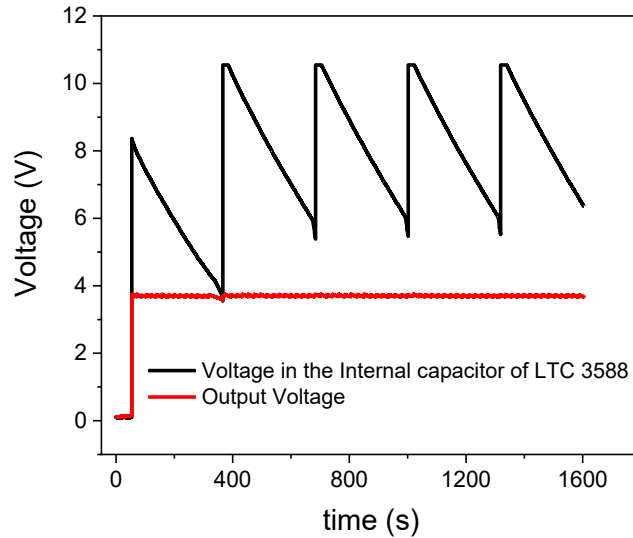


Figure 5.7 Voltage profile of LTC 3588-1 DC/DC converter board monitored using the LabView software. The black line corresponds to the voltage of LTC board’s internal capacitor while the red line indicates the output voltage from the LTC board, which is at 3.6 V.

5.3.2 Description of the autonomous system

The autonomous harvester integrates several key electronic components to enable energy extraction, voltage conversion, and autonomous operation. Two 0.5 mm thick PST MLCs (electrically connected in parallel) were used as the pyroelectric energy harvester. For the low-voltage converter, the same components as mentioned in the previous sub-section were employed with the only exception on the storage capacitors. For this system, a multilayer storage capacitor (KTD250B107M80A0B00, $C = 500 \mu\text{F}$) was used instead of the linear capacitors. For energy management and regulation, the system includes a DC/DC converter (LTC3588-1), a boost converter (LT8410; $V_{\text{out}} = 16 \text{ V}$), a microcontroller (ATtiny45), and a temperature sensor (TMP36FSZ).

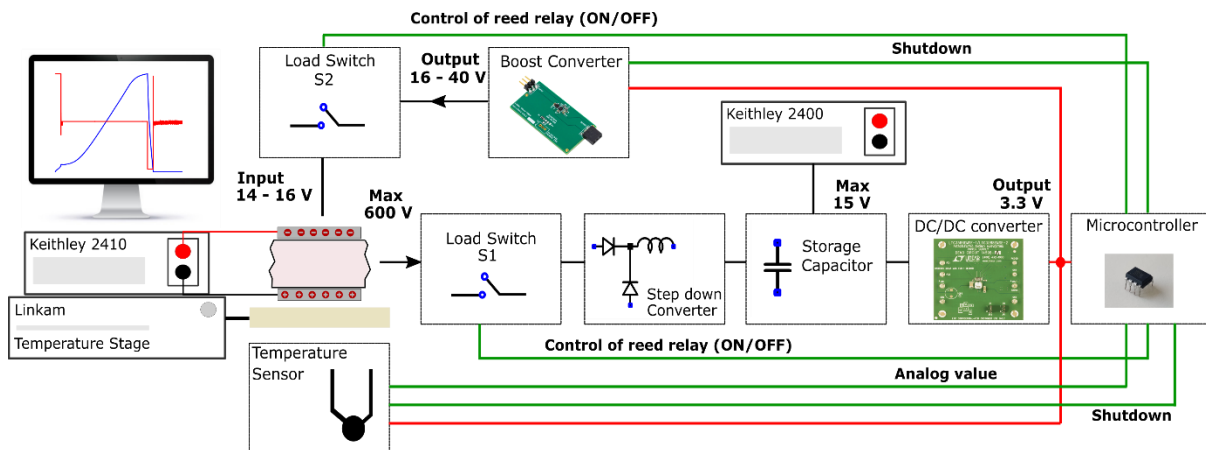


Figure 5.8 Overall schematic of the autonomous pyroelectric energy harvester.

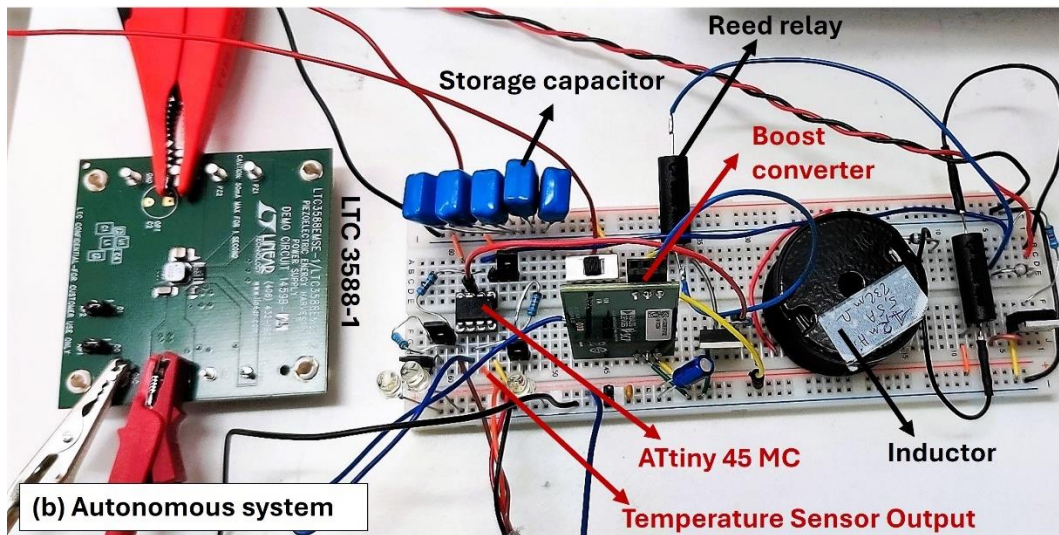
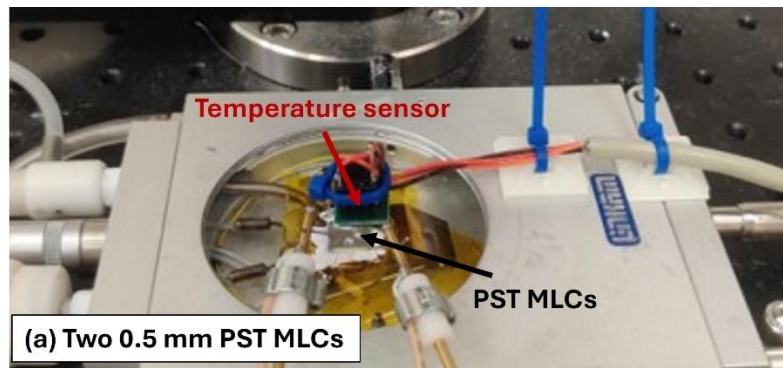


Figure 5.9 Experimental set-up of the autonomous pyroelectric energy harvester: (a) the harvester block comprising of two 0.5 mm thick PST MLCs, (b) the autonomous control circuit with all components clearly labelled.

Operating principle

Figure 5.8 shows the complete design of the autonomous pyroelectric energy harvesting system, while Figure 5.9 displays the experimental setup with the key components of the autonomous board clearly labelled. For continuous operation, the storage capacitor must first be charged to supply the initial energy required to activate all electronic components. This initial charge was provided using a Keithley 2400 source meter, which also continuously monitors the capacitor voltage. After this initial charging step, the system operates autonomously without any external energy input.

The energy stored in the capacitor is regulated through an LTC 3588-1 board, which provides a stable 3.6 V DC output. This regulated voltage powers the ATtiny 45 microcontroller (MC). It is important to note that the LTC 3588-1 requires a minimum input voltage of 4 V to remain operational. If the voltage drops below this threshold, the system will automatically shut down. Therefore, the voltage across the storage capacitor must consistently remain above this value to ensure uninterrupted system operation. Once the microcontroller is activated, the voltage across the storage

capacitor slightly decreases. The microcontroller is programmed using the Arduino IDE and optimized for low-power operation. It communicates digitally with the passive components in the system and makes real-time decisions such as switching, activating the boost converter, or entering sleep mode based on temperature inputs from the sensor. The microcontroller samples temperature data every 4 seconds.

To perform thermal cycling of the pyroelectric material, a Linkam temperature controller was employed. When the temperature of the stage reaches the predefined threshold set in the microcontroller, the system initiates the boost event. During this phase, switch S2 is closed, allowing the boost converter to draw energy from the storage capacitor (via the LTC 3588-1 regulator) and deliver a stepped-up DC voltage to charge the material. This step corresponds to the isothermal polarization phase of the Stirling cycle. After charging, switch S2 is opened, and the temperature of the stage is increased, initiating the open-circuit heating step of the Stirling cycle. All operations, including temperature cycling using the Linkam stage and real time monitoring of voltages across the material and the storage capacitor were automated using a Python script. Once the temperature of the material reaches the upper limit of the predefined interval set in the microcontroller, the system automatically initiates the discharge process. This is accomplished by closing the load switch S1, allowing the energy converted by the material during the Stirling cycle to pass through the low-voltage converter and be stored in the capacitor. Sustained system operation is possible only if the energy extracted from the material after each cycle exceeds the energy required to power the system components.

Power consumption of the system

The overall energy consumption of the autonomous system was evaluated using the Oti Arc Energy Meter. This instrument was employed in place of the LTC board, which delivers a 3.6 V DC, to initiate all electronic components and to continuously monitor their power usage. Since the microcontroller was programmed with specific temperature thresholds to autonomously trigger the boost and discharge events, the temperature values were set to 30 and 50 °C for this specific experiment. To simulate these thermal conditions, the sensor was manually heated using a heat gun. The microcontroller sampled temperature every 4 seconds and initiated the boost event when the temperature fell below the lower threshold, and the discharge event when it exceeded the upper threshold. This setup allowed precise measurement of the energy consumed by the electronic components in the system during each stage of operation without external intervention.

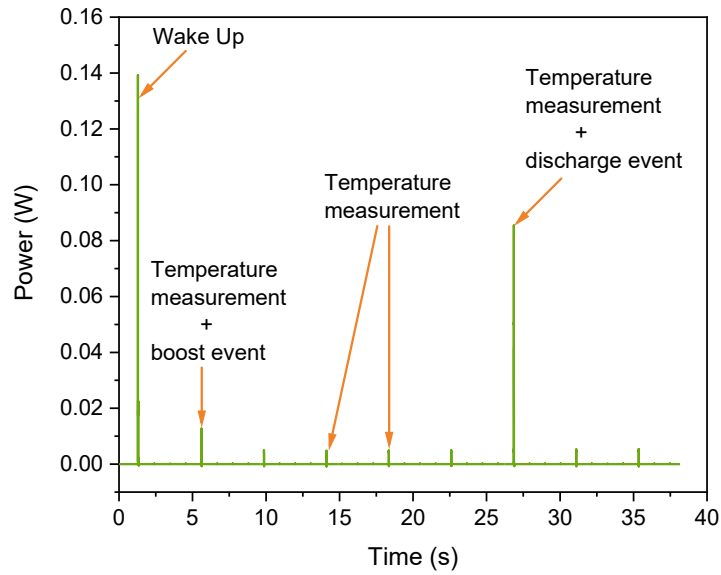


Figure 5.10 Power consumption of the autonomous system at different stages of the Stirling cycle.

Figure 5.10 illustrates the overall power consumption of the autonomous system during different stages of the Stirling cycle, as annotated in the graph. During the wake-up phase, the system consumes approximately 0.14 W of power for 3 ms, corresponding to 0.43 mJ of energy. When the measured temperature falls below the predefined threshold in the microcontroller, the system initiates a boost event, consuming about 0.17 mJ of energy. This step corresponds to the isothermal charging leg of the Stirling cycle. Additionally, temperature monitoring by the sensor consumes 0.03 mJ of energy every four seconds. Once the temperature exceeds the upper threshold, the system triggers the discharge event, which consumes approximately 0.67 mJ of energy. During sleep mode, the system consumes a very minimal energy of 17 μ J every second.

Having detailed the operational principles and power requirements of the autonomous harvester, the next section presents the experimental results obtained from the fully integrated system and provides a comprehensive discussion of its performance and feasibility for practical applications.

5.3.3 Results and discussion

Figure 5.11 shows the voltage profile across both the storage capacitor (in blue) and PST MLCs (in red) as a function of time. Initially, the 500 μ F storage capacitor was pre-charged to 9 V at 15 $^{\circ}$ C to supply the energy required to activate the autonomous system. The slight drop in capacitor voltage corresponds to the initial power consumed by the microcontroller and other passive components during system startup. Following this, the two 0.5 mm thick PST MLCs were cooled to -5 $^{\circ}$ C using

the Linkam temperature stage for a dwell time of 8 s, which is below the lower temperature threshold of 5 °C programmed into the microcontroller. Once this temperature was detected by the sensor probe, the data was relayed to the microcontroller, which then triggered the boost event. As a result, the storage capacitor voltage dropped from 8 V to approximately 5 V, while the boost converter charged the PST MLCs to 15 V. This was followed by the open circuit heating step of the Stirling cycle to 85°C for a dwell time of 13 s, during which the voltage across the PST MLCs was amplified to approximately 400 V. This step corresponds to the isocharge heating step of the Stirling cycle. Since the cycle's final temperature is higher than the upper temperature limit of 70°C programmed into the microcontroller, it will automatically discharge the PST MLCs through the reed relay. The energy harvested from the sample is passed through the low-voltage converter which steps down the voltage and stores the energy in the storage capacitor. As a result, the voltage of the storage capacitor increases from 4.3 V to 11 V. With each successive Stirling cycle lasting 160 s, the voltage across the storage capacitor progressively increased, reaching 13 V after four cycles. This corresponds to a 40% increase from the initial voltage and a net energy gain of 22 mJ.

To further verify the reproducibility and robustness of the autonomous system, an additional experiment was conducted using two 1 mm thick PST MLCs ($10.4 \times 7.2 \times 1$ mm³, consists of 19 active layers each 38 µm thick & 2 capping layers; electrically connected in parallel) under the same thermal conditions for the Stirling cycle. In this case, a slightly higher initial input voltage of 14 V was required, as the system was unable to maintain stable operation at 9 V, as shown in Figure 5.12. This experiment was conducted over an extended duration (~ 40 min) comprising of 16 consecutive Stirling cycles, with each cycle lasting for about 150 s, during which a consistent stepwise increase in the storage capacitor voltage was observed, thereby confirming the repeatability and reliability of the system's performance.

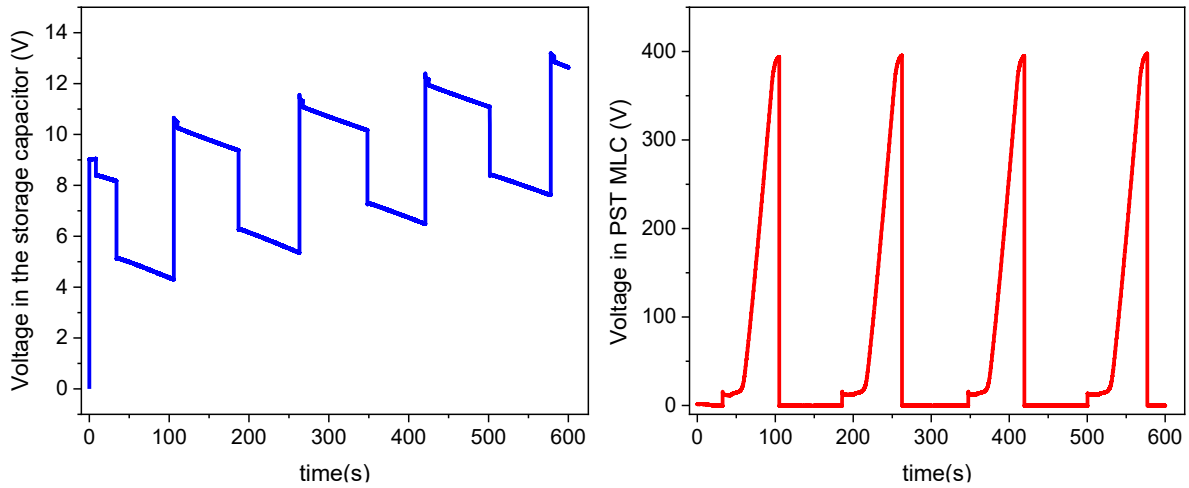


Figure 5.11 Voltage profile of the storage capacitors (left – in blue) and two PST MLCs of 0.5 mm thickness (right – in red) as a function of time.

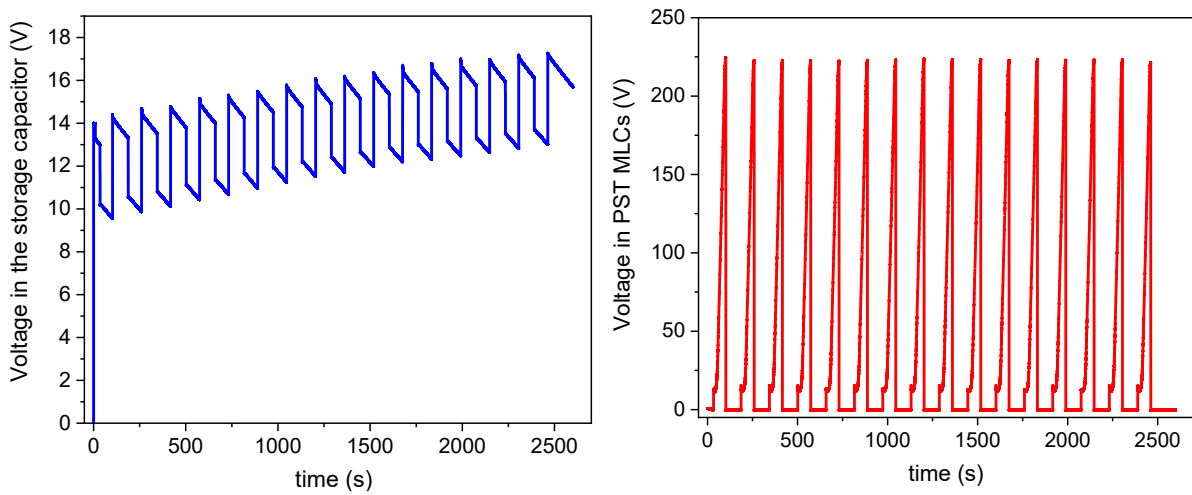


Figure 5.12 Voltage profile of the storage capacitors (left – in blue) and two PST MLCs of 1 mm thickness (right – in red) as a function of time.

5.4 Self-powered macroscopic pyroelectric energy harvester – GEN 1

Following the validation of the autonomous system in the preceding section, the concept scaled up to a macroscopic device configuration. To implement this macroscopic approach, a prototype designated GEN 1 was developed using PST MLCs. The device design employs the parallel-plate heat exchanger configuration based on earlier electrocaloric and pyroelectric prototypes developed in our group [30,57,126]. The primary goal of this implementation was to demonstrate that the energy extracted from GEN 1 is sufficient not only to sustain autonomous operation of the Stirling cycle by powering the system’s electronic components, but also to continuously power an external electronic device, without relying on any external energy source.

However, transitioning from the previous small-scale implementation to a macroscopic prototype presents several additional complexities. Firstly, establishing a time-varying heat source capable of delivering a uniform temperature swing across all PST MLCs within the device is essential. The Linkam heating stage, employed previously, is unsuitable due to geometric constraints posed by the larger macroscopic structure. Consequently, a heat transfer fluid was introduced, which flows through the porous structure of the prototype, thereby facilitating improved heat exchange. This requirement also influenced the decision to adopt a parallel-plate heat exchanger configuration (see Figure 5.13), as this arrangement inherently facilitates efficient fluid flow and proper heat exchange. Secondly, precise synchronization between the heating and cooling phases of the Stirling cycle and the circulation of hot and cold fluids must be maintained.

For a self-sustaining pyroelectric energy harvester device, the charge and discharge sequences must align accurately with the thermal cycling events to properly execute a Stirling cycle. Moreover, scaling the device necessitates replacing many electronic components used previously in smaller-scale implementations such as step-down converters, switches, and other passive elements, as significantly higher charge and discharge currents are encountered at macroscopic scales. The subsequent sections provide a detailed discussion on the design, integration, and autonomous operation of GEN 1.

5.4.1 Design of GEN 1

GEN 1 consists of 60 PST MLCs (arranged in 6 rows \times 10 columns), each 0.5 mm thick, assembled in a parallel plate heat exchanger configuration using strips of double-sided adhesive tape on both sides, as shown in Figure 5.13 (a) and (b). The slit width was set to 8 mm, and the spacing between the stacks was maintained at 0.42 mm, enabling the heat transfer fluid to flow through the structure for effective heat exchange. Electrical connection was ensured by applying conductive silver epoxy paste along the terminals of the MLCs, while copper wires were used on both sides to connect all units in parallel. The copper wires connected to the PST MLC terminals were extended outside the prototype, allowing a direct application of the electric field using a source meter, as detailed in our previous works [30,57].

To prevent structural deformation and ensure mechanical stability, the assembly was housed in a protective wooden casing and enclosed in a transparent polyolefin tube, chosen for its favourable thermal insulation properties. This polyolefin tube was shrunk using a heat gun to conform tightly to the prototype's geometry, thereby minimizing air gaps and enhancing thermal insulation around the device. Additionally, two K-type thermocouples were positioned at the inlet and outlet of the prototype to monitor the heat transfer fluid's temperature.

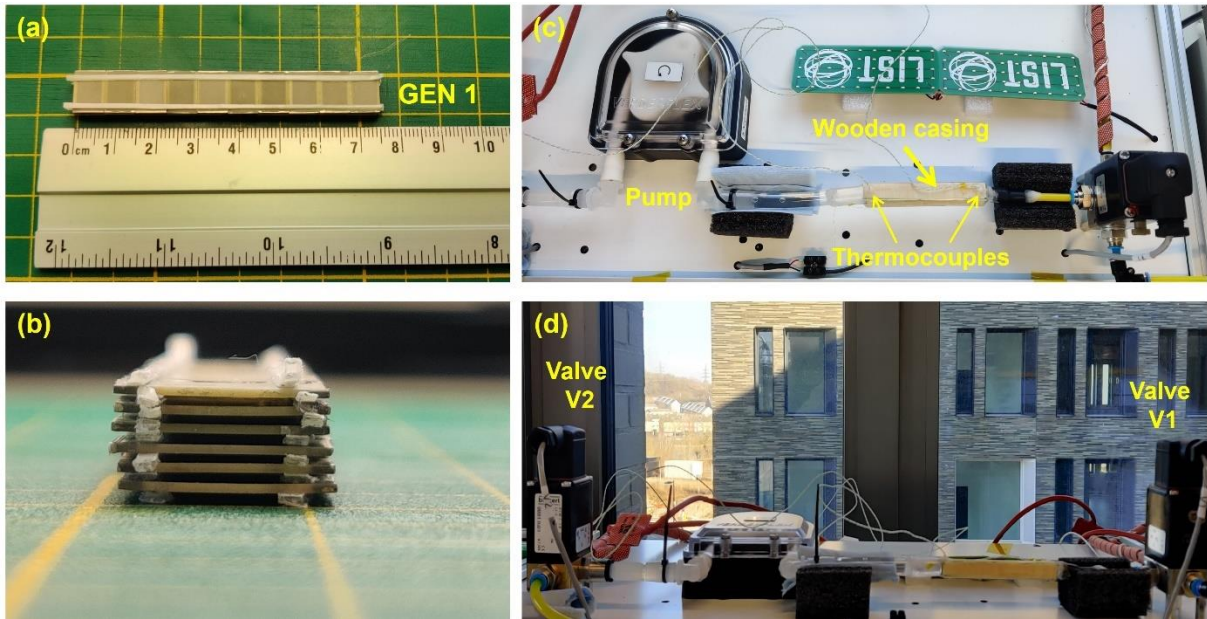


Figure 5.13 Pictures of self-powered pyroelectric energy harvester. (a) Top view image of GEN 1, (b) Side view showing the stacked structure and spacing between MLCs (c, d) Experimental setup showing the enclosed prototype, peristaltic pump and solenoid valves.

To induce periodic thermal variation across the prototype, silicone oil (5 cSt at 25°C, Sigma Aldrich) was used as the heat transfer fluid. To establish the cold and hot sources, two reservoirs of silicone oil were maintained at different temperatures by immersing them into two separate chillers (Lauda Eco RE 415) – one set to a high temperature and the other kept at low temperature. A peristaltic pump was used to circulate the silicone oil through GEN 1, while two three-way solenoid valves alternated the flow between the hot and cold reservoirs (see Figure 5.13 (c) and (d)). The fluid was transported using flexible silicone tubing, selected for its chemical compatibility. The operation of both the pump and valves required an input of 24 V DC, which was provided by an external power supply.

For automated thermal cycling, an Arduino Nano board was programmed to control the switching of valves. This ensured synchronized operation with the heating and cooling steps of the Stirling cycle. The Arduino Nano was triggered by a control pulse from the master microcontroller of the autonomous system, which manages the complete device operation, as detailed in the next sub-section. A key innovation of this setup is its closed-loop fluid circulation system, which allows the silicone oil to recirculate back to its original reservoir after each cycle. This recirculation enables long-term autonomous operation of the device using a limited volume of fluid by steadily maintaining its temperature, as shown in Figure 5.14. While the focus of this section is on the self-powered operation of the macroscopic pyroelectric device, a

detailed characterization of the thermal cycling behaviour in this configuration is discussed separately in related work [30].

5.4.2 Autonomous system implementation

To spontaneously charge and discharge the macroscopic pyroelectric energy harvester without drawing external energy, an autonomous system similar to one described in Section 6.3 was developed. In contrast to the previous setup, the energy extracted from GEN 1 is used not only to execute the Stirling cycle and sustain the system but also to continuously power an external Bluetooth low energy (BLE) communication module device. Figure 5.14 presents the complete schematic of the self-powered pyroelectric energy harvester, illustrating the interaction between GEN 1, the fluidic control unit, autonomous system, and the connected external device based on a Bluetooth Low Energy (BLE) communication module.

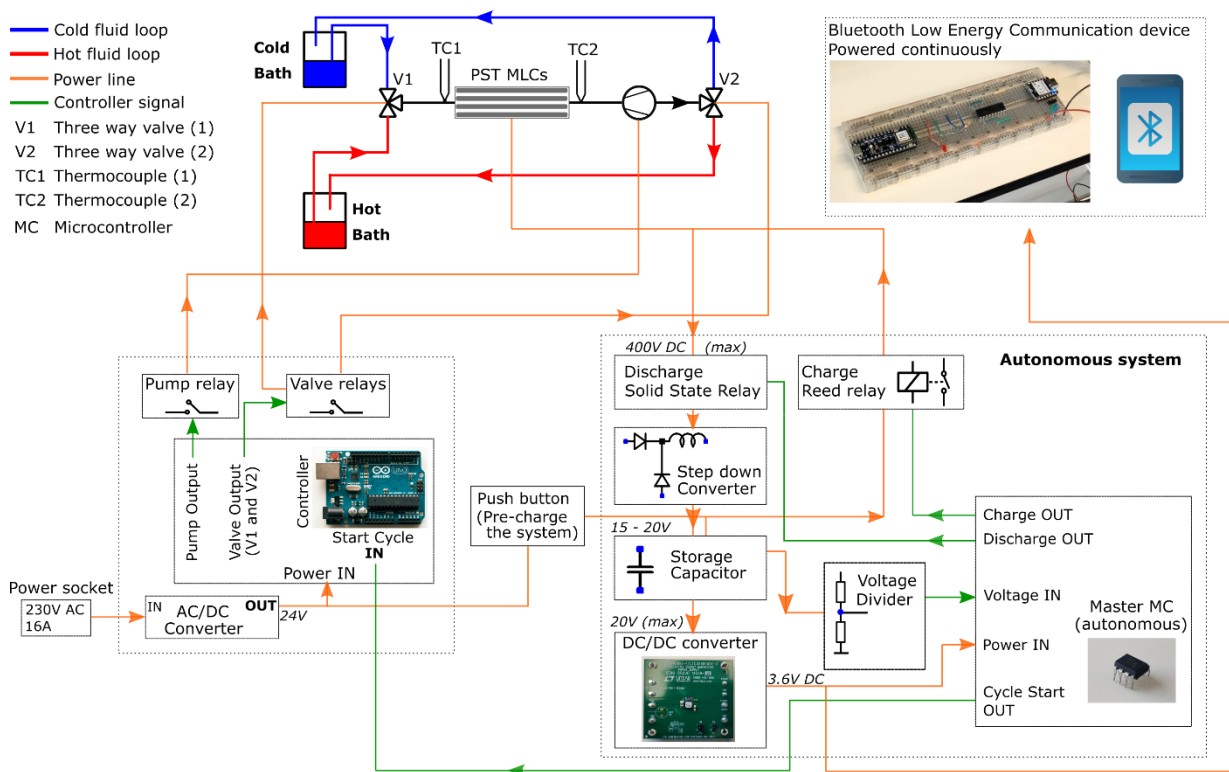


Figure 5.14 Schematic of the self-powered macroscopic pyroelectric energy harvester system.

The autonomous system integrates several functional components: a low power consuming microcontroller (Master MC), a step down converter (composed of two diodes – BYW56-TR, and a 5 mH inductor – Hammond 195G10) with storage capacitors, a DC/DC converter (LTC 3588-1), a voltage divider, and relays for fast switching (a reed relay for the charging phase and a solid-state relay, selected for its capability to handle higher currents, for the discharging phase), as shown in Figure

5.15. These components collectively manage the energy harvesting, power conditioning, and switching events required to sustain the device in a self-powered mode. The operational details of each component are provided in Section 5.4.5.

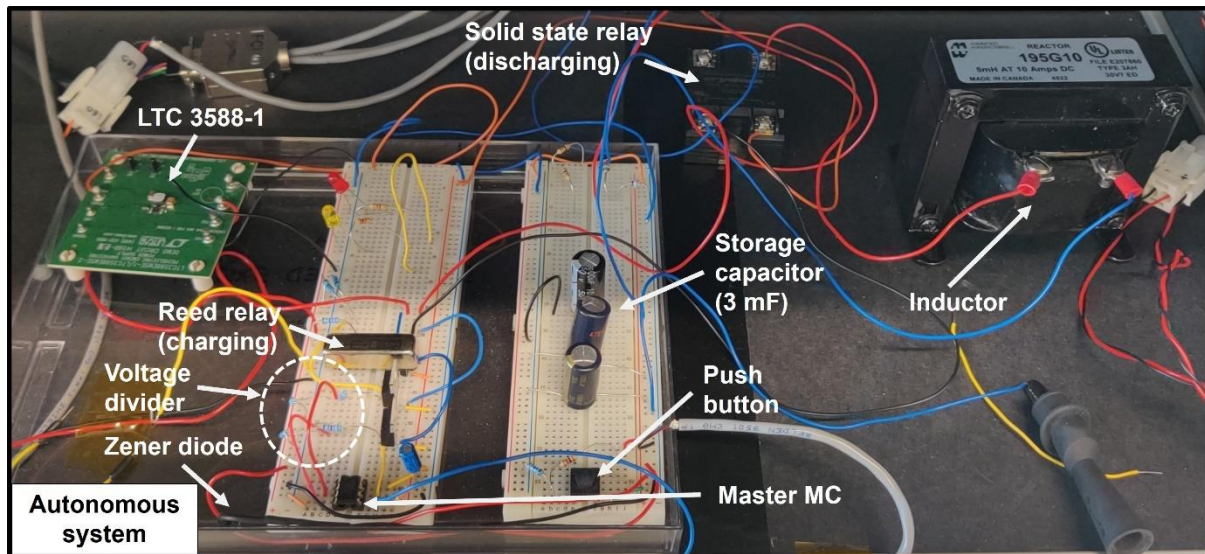


Figure 5.15 Experimental setup of the autonomous system board.

Unlike the system detailed in Section 5.3, the initiation of Stirling cycle in this system is governed by the voltage level across the storage capacitor. When this voltage reaches a predefined threshold programmed into the master MC, the system initiates the charging of the harvester. During this phase, the peristaltic pump is switched ON to circulate cold silicone oil through the prototype, ensuring that the device is at the required low temperature. Upon completion of the charging step, the master MC sends a control signal to the Arduino Nano board, which switches the control valves to stop the cold fluid flow and begin the circulation of hot fluid through GEN 1. This corresponds to the isocharge heating step of the Stirling cycle. After a fixed heating duration, the system automatically triggers the discharge step at high temperature and transfers the harvested energy through the step down converter and into the storage capacitor. Before initiating the next cycle, the master MC reverts the direction of control valves such that the cold fluid is once again circulated through the prototype to restore the initial low temperature condition. Thus, the Stirling cycle is sequentially implemented on GEN 1: 1) charge at low temperature, (2) isocharge heating by passing the hot fluid, (3) high temperature discharge step, and (4) cool down to lower temperature by passing the cold fluid under open circuit condition.

However, ensuring the sustained operation of this macroscopic pyroelectric energy harvester required the resolution of three key technical challenges:

I. Stable temperature span

Since the harvested energy in a pyroelectric system is directly related to the temperature difference experienced by the multilayer capacitors, it was essential to maintain stable thermal conditions in both the hot and cold fluid reservoirs. Earlier systems and macroscopic pyroelectric prototype designs [30] employed an open loop fluidic configuration, where the heat transfer fluid, after flowing through the prototype during the heating or cooling phase, was not returned to its original reservoir. Instead, it was collected in a separate container. This arrangement limited the number of thermal cycles that could be executed, as the available volume of fluid became progressively depleted, thereby restricting long duration operation.

To address this limitation, the present work introduces a closed loop fluidic circuit that enables the silicone oil to be recirculated back to its respective reservoir following each cycle. This configuration allows the same volume of fluid to be reused across multiple cycles, providing sufficient time for thermal stabilization before re-entering the system. Maintaining a consistent temperature difference during each cycle was critical, as any reduction in this difference directly decreased the amount of energy harvested and could compromise the overall stability and performance of the autonomous system. To support this function, the timing of the valve switching was carefully coordinated with the control signals from the master microcontroller, ensuring that charging and discharging events occurred precisely during the cold and hot fluid phases, respectively. In addition, the cold side fluidic tubes were thermally insulated using Superwool fibre to minimize heat loss and preserve the temperature gradient necessary for efficient energy conversion.

II. Power management

For the self-maintained operation of the device, the power extracted from the prototype must be carefully managed to sustain both the system and the connected external electronic device. To achieve this, all electronic components, including the external module, were carefully selected with an emphasis on minimizing power consumption. A key approach involved optimizing the wake-up and sleep intervals of the master MC, thereby significantly reducing unnecessary energy usage. Additionally, particular attention was given to the durations of the charging and discharging stages within each cycle, as these events represent periods of maximum power consumption. More details about the overall power consumption of the system is provided in Section 5.4.4.

III. Step down converter

Another critical component of the autonomous system is the step down (or low-voltage) converter. Similar to the design described previously in Section 5.3, this component reduces the high output voltage generated during the Stirling cycle and transfers the energy into the storage capacitor. The converted voltage was regulated carefully to remain below 20 V, corresponding to the maximum allowable input for the LTC 3588-1 DC/DC converter. However, unlike the previous configuration, GEN 1 comprises 60 PST MLCs connected in parallel, resulting in peak discharge currents that can reach several amperes for brief intervals (milliseconds). Therefore, the inductor and capacitor used in the low-voltage converter circuit were specifically selected to effectively manage these higher currents, ensuring reliable voltage regulation, safe operation, and stable long-term performance of the system. It is worth mentioning that for this experiment no efforts were taken to optimize the efficiency of the step down converter, which still needs to be investigated for future works.

5.4.3 External communication module device

To demonstrate the practical application of the self-maintained pyroelectric energy harvester, we implemented an external communication module, which was continuously powered by the harvested energy. This external module was based on the XIAO BLE nRF52840 sensor board. A Bluetooth Low Energy (BLE) protocol was employed to transmit data wirelessly to a smartphone, where a dedicated custom-developed application received and recorded the transmitted data, as shown in Figure 5.16. This device is similar to the self-powered communication module previously developed by Glinsek et al. [199].

For demonstration purposes, the built-in temperature sensor and inertial measurement unit on the sensor board were utilized, alongside monitoring the Received Signal Strength Indicator (RSSI) values, which reflects the power level of the received RF signal after accounting for antenna and cable losses. These parameters were transmitted to a smartphone via Bluetooth periodically at one-second intervals, enabling continuous, real-time monitoring of the device's performance.

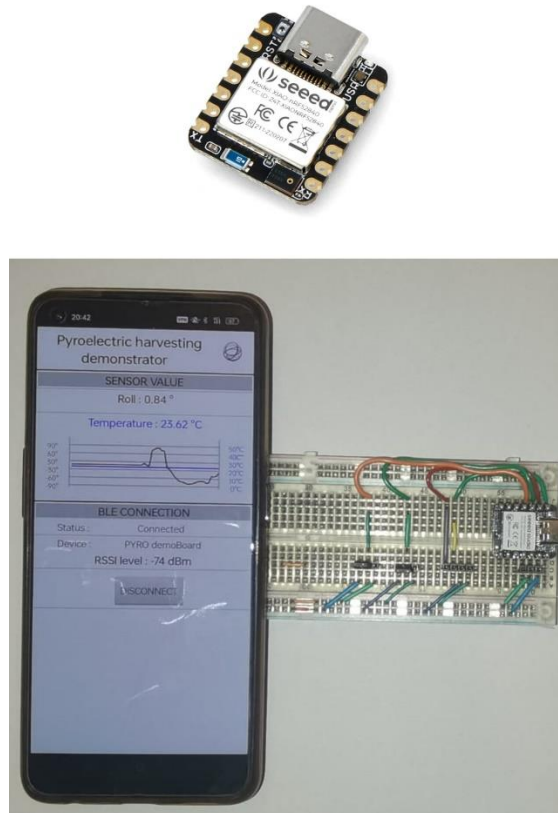


Figure 5.16 Photograph of the XIAO BLE-based communication module used as the external device, along with the custom-built application in the mobile to retrieve the data transmitted via Bluetooth by the device.

5.4.4 Overall power consumption of the demonstrator

To ensure continuous and sustained operation of GEN 1, the power harvested during each Stirling cycle must consistently exceed the cumulative power consumption of both the autonomous system and the external device. Therefore, a detailed characterization of the system's power requirement was carried out to determine the optimal charge voltage and temperature span of the Stirling cycle, both of which directly influence the harvested energy. It should be noted that the power consumption of the Arduino Nano board, which was used solely for controlling the solenoid valves, was not measured in this study, as it operates independently of the autonomous system.

The power consumption of the autonomous system and the external device was evaluated using an Otii Arc energy meter, which temporarily replaced the LTC 3588-1 converter to directly supply power to all electronic components in the system. This measurement procedure was similar to the one described previously in Section 6.3, and the corresponding experimental schematic is shown in Figure 5.17.

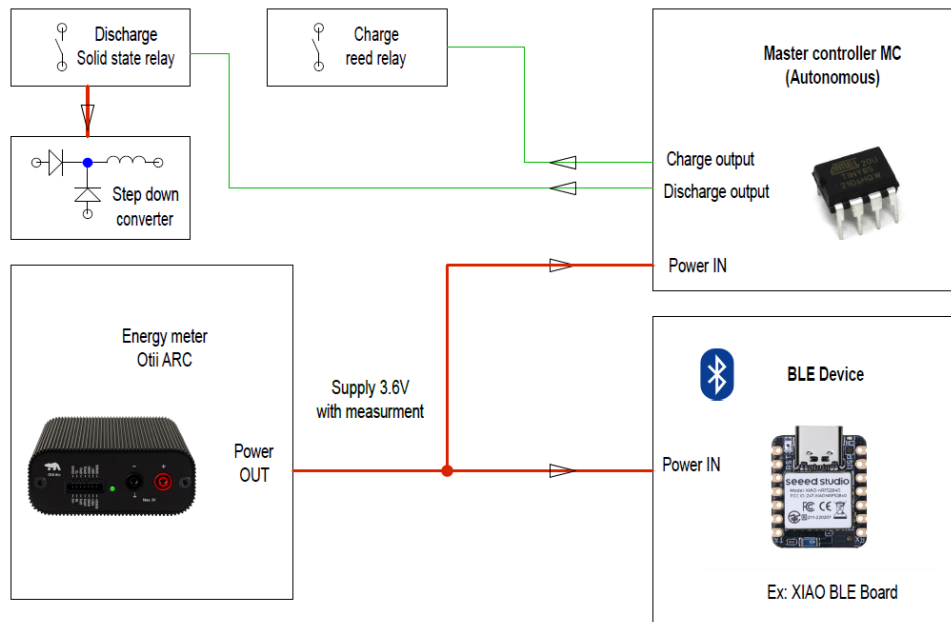


Figure 5.17 Schematic of the power measurement setup used to evaluate the power consumption of both the autonomous system and the external BLE device.

Under these test conditions, the master microcontroller continuously executed the Stirling cycle, allowing precise measurement of its power consumption during both the active phase and the low power sleep mode. The overall power consumption of the autonomous system used to sustain GEN 1 is shown in Figure 5.18 (a). The transient power peaks indicate the power consumed by the charge and discharge relays during their respective switching events, which are annotated in the graph. Additionally, the power consumption of the external device was monitored throughout the experiment. Once activated, the Bluetooth module continuously transmitted sensor data via wireless communication. The combined power consumption of the full system is illustrated in Figure 5.18 (b).

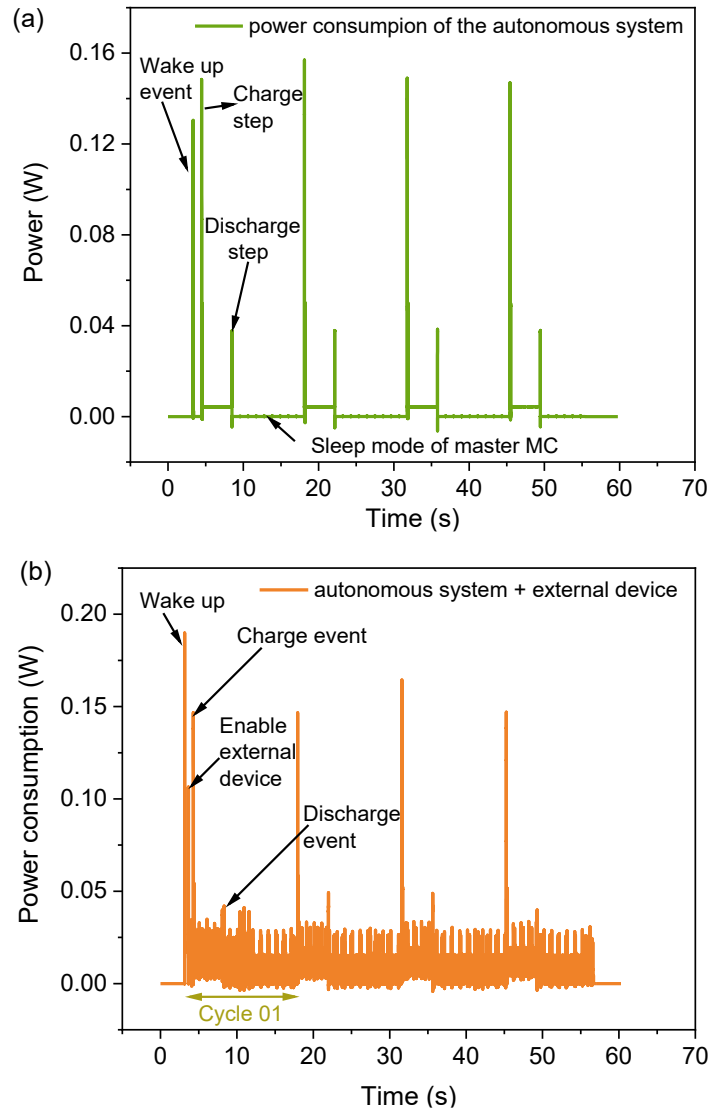


Figure 5.18 Measured power consumption values of (a) the autonomous system and (b) both the autonomous system and external BLE device as a function of time. Different events such as the wake up, charge and discharge steps are marked in the figure. The presence of smaller peaks in 5.18 (b) correspond to the communication bursts of the Bluetooth communication module.

The autonomous system consumed an average power of 4.3 mW during the charging, heating and discharging stages of the Stirling cycle. During the cooling phase, the master MC transitioned to a low power sleep mode, reducing the power consumption to approximately 0.1 mW. As a result, the average power required by the autonomous system over one complete cycle was significantly reduced to approximately 1.5 mW. Notably, the charging events showed higher transient power peaks than the discharging phases (see Figure 5.18 (a)). This is because additional power is required to operate the charging relay, along with the energy needed to charge GEN 1.

Figure 5.18 (b) shows the average power consumption of both the Bluetooth communication module and the autonomous system. During the first three stages of the cycle (charging, heating and discharging), the combined average power consumption increased to approximately 9.5 mW. However, when accounting for the full cycle, including the cooling phase where the master microcontroller remains in sleep mode, the average combined power requirement decreased to about 6 mW. In terms of energy, this corresponds to roughly 80 mJ per cycle, which includes the energy required to charge GEN 1 for the subsequent cycle. To maintain uninterrupted operation, the energy harvested from GEN 1 must consistently exceed this 80 mJ threshold per cycle.

Due to the usage of LTC 3588-1 board, GEN 1 is limited by the input charge voltage to less than 20 V. Hence, the only variable parameter is the temperature span of the Stirling cycle. It must be noted that very high ΔT can result in significant voltage amplification and the discharge current can reach several amperes for few milliseconds, which can potentially result in the electrical breakdown of GEN 1. To tackle these challenges, several parameters such as the temperature span, cycle duration, charge voltage, and the selection of passive components, particularly the reed and solid state relays, were carefully selected and optimized to ensure safe, and reliable operation of the system.

5.4.5 Functioning of the self-powered pyroelectric energy harvester

The experimental setup of the self-powered pyroelectric energy harvester is shown in Figure 5.19. For clarity, readers are encouraged to revisit Figure 5.14, which outlines order of operation and interaction between components, including the flow of power and control signals. A detailed explanation of the system's operation and the corresponding results are discussed in this section.

To activate the electronic components of the self-powered pyroelectric energy harvester, the storage capacitor within the autonomous system must first be charged, as it provides the initial energy required for initiating the system. Therefore, the storage capacitor (3 mF, rated at 35 V) was directly charged from an electrical outlet via an AC/DC converter (marked as the electrical box in Figure 5.19) by manually pressing the push-button. The voltage of the storage capacitor must exceed the predefined threshold value programmed in the master microcontroller, which was approximately 18 V. The capacitor voltage was continuously monitored using an oscilloscope (PicoScope 3000). Once it reached around 20 V, the external power supply was disconnected, ensuring that the system functioned solely on the harvested energy.

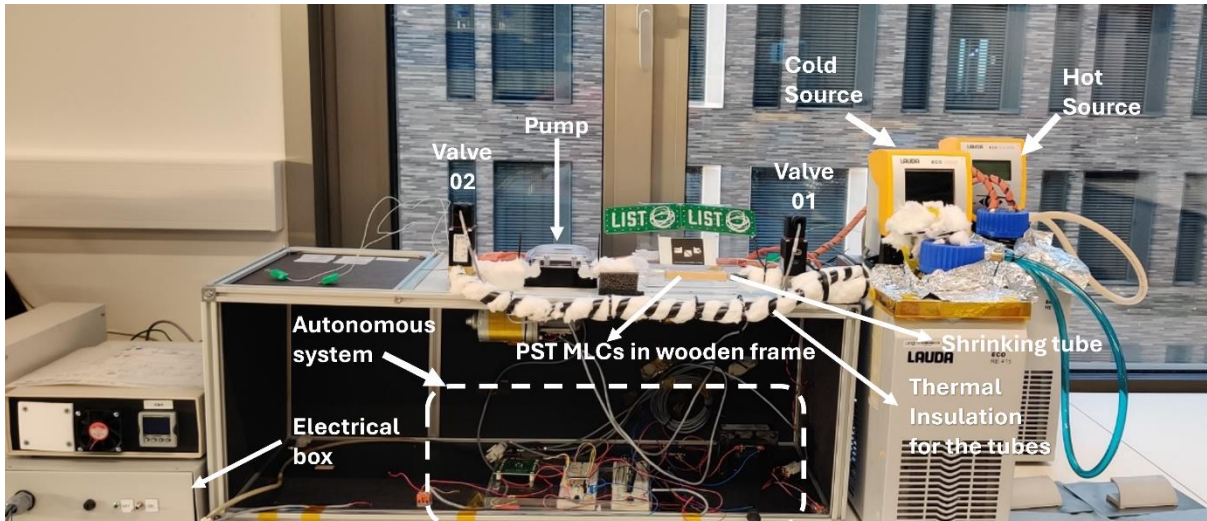


Figure 5.19 Experimental setup of the self-powered macroscopic pyroelectric energy harvester.

The stored energy in the capacitor is routed through the LTC 3588-1 DC/DC converter, which delivers a regulated 3.6 V DC output. This output is used to power both the master MC and the external BLE communication module. At this stage, the master MC also begins monitoring the storage capacitor's voltage through its analog-to-digital converter (ADC) pin. To protect from overvoltage, a voltage divider was used. This arrangement allows the microcontroller to track the capacitor level accurately while avoiding unnecessary power consumption. Simultaneously, the XIAO BLE sensor module draws power directly from the storage capacitor via the LTC board. Once activated, this device will start transmitting the data recorded by its onboard temperature and orientation sensors to a smartphone through Bluetooth (BLE 5 module). A dedicated mobile application was developed for real-time data logging and visualization. Since the device transmits data every second, the voltage across the storage capacitor gradually decreases.

Following this, the peristaltic pump is activated, and cold silicone oil begins circulating through the prototype, initiating the cooling phase of the cycle. The inlet and outlet temperatures of GEN 1 are monitored using K-type thermocouples. For this experiment, the cold reservoir was maintained at -5°C using a chiller.

As the energy consumption of the system and the external device causes the storage capacitor voltage to drop to the predefined threshold (approximately 18 V), the master MC initiates the next phase by charging GEN 1 using the energy from the storage capacitor via the reed relay. After this step, a control signal is sent from the master microcontroller to the Arduino Nano, prompting valve V1 to redirect flow from the cold reservoir to the hot reservoir, maintained at 85°C . This transition marks the isocharge heating step of the Stirling cycle, during which the voltage across the MLCs

rises from about 15 V to nearly 200 V. A delay between valve actuation sequences was introduced to minimize the mixing of hot and cold silicone oil. This delay is essential for maintaining a stable ΔT .

Next, the system executes the high-temperature discharge step through a solid-state relay, chosen for its rapid switching capability and high current tolerance. The harvested energy is routed through a step down converter and stored back into the storage capacitor. The resulting harvested energy is directed through a step down converter and stored back into the storage capacitor. During this step, the voltage rise across the capacitor is monitored, and the voltage across GEN 1 is recorded using the PicoScope 3000. The system is then allowed to cool for approximately 8 seconds before initiating the next cycle. This delay enables the silicone oil to fully re-thermalize with its respective reservoir, maintaining a consistent ΔT across cycles. With stable thermal conditions, the macroscopic pyroelectric energy harvester sustained autonomous operation for several minutes.

During operation, key system parameters, including the inlet and outlet fluid temperatures of GEN 1, the voltage across the storage capacitor, and the voltage generated by the PST MLCs were continuously monitored over a period exceeding 30 minutes. Additionally, data transmitted by the external Bluetooth communication module were also recorded using the custom application. These results are shown in Figures 5.20 (a–c) and 5.21, respectively.

From the storage capacitor voltage data, the net energy gain per cycle was calculated using:

$$Net\ energy\ per\ cycle = 0.5 * C * V_{final}^2 - 0.5 * C * V_{initial}^2 \quad (5.1)$$

By taking the first two consecutive Stirling cycles into consideration:

$$Net\ energy\ gain = 0.5 * 3 * 10^{-3} * [(20.20)^2 - (18.50)^2] \quad (5.2)$$

This leads to:

$$Net\ energy\ gain \approx 100\ mJ \quad (5.3)$$

This value corresponds to the energy extracted from the PST MLCs and stored in the capacitor. It is particularly relevant as it reflects the energy available to power system components, rather than total harvested energy. Notably, this value exceeds the 80 mJ threshold required for continuous self-powered operation.

It should be noted that the harvested energy was not measured directly as the current profile could not be continuously monitored during the charge and discharge events. Although a clamp meter (PicoScope 60A AC/DC) was used to obtain a rough estimate of the current values, its limited sampling resolution resulted in insufficient data for

reliable data analysis. Therefore, the harvested energy and the efficiency of the low-voltage converter were not extensively investigated as the primary focus was towards the extracted energy, which is the available energy for doing useful work.

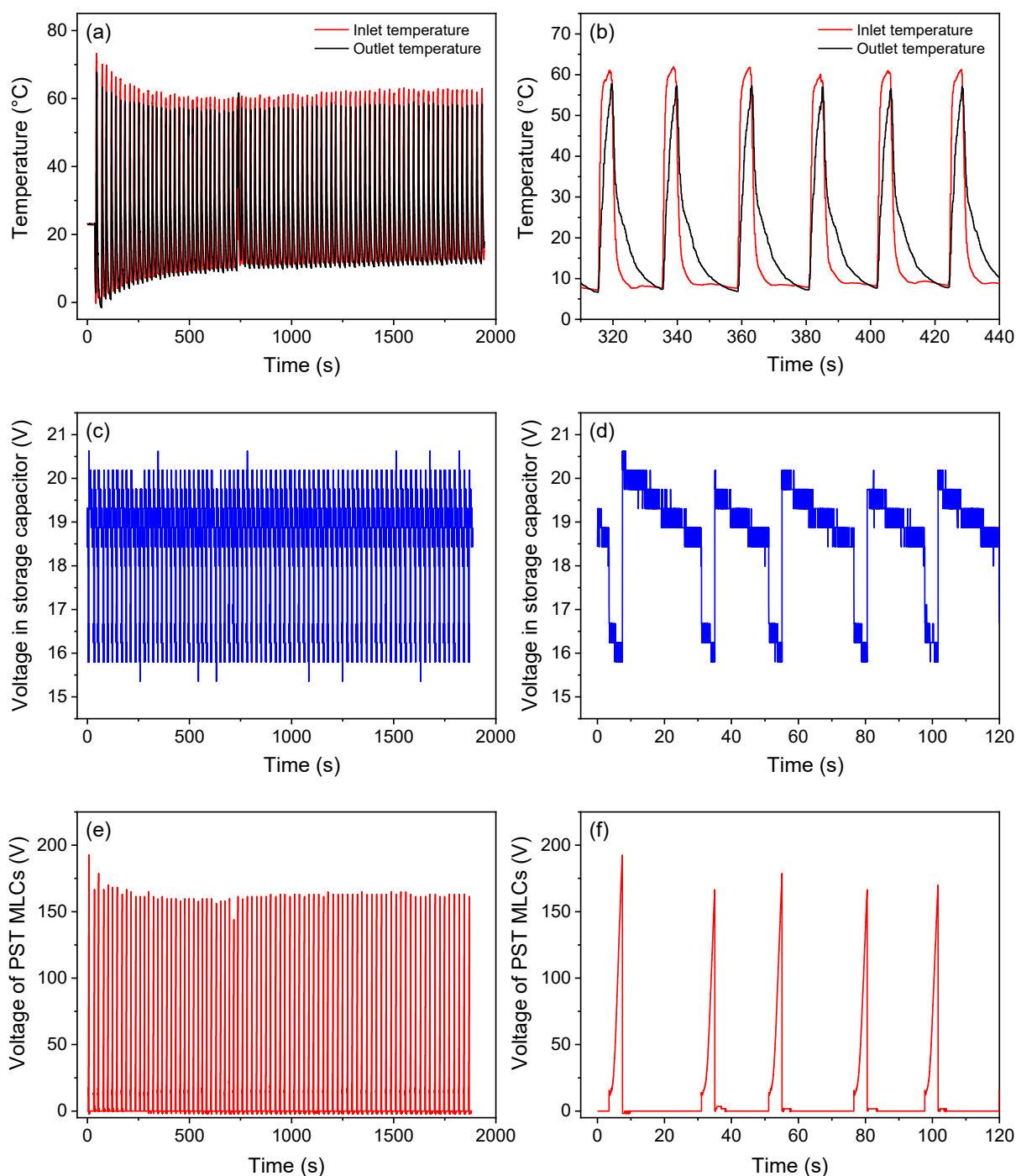


Figure 5.20 (a) Inlet and outlet temperature profiles of GEN 1, (b) Magnified view on the right. (c) Voltage evolution of the storage capacitor, (d) Zoomed-in view of the voltage profile. (e) Voltage response of GEN 1 and (f) a magnified image, as a function of operating time.

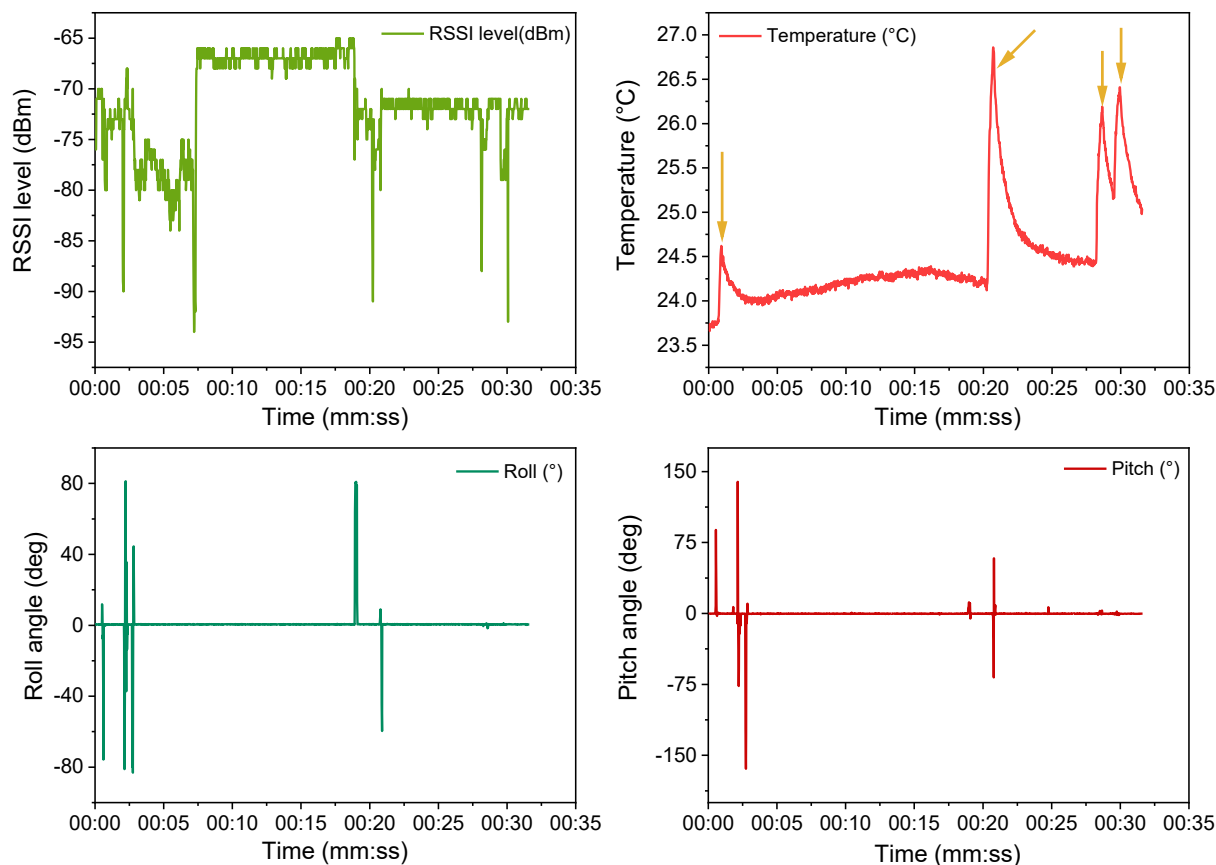


Figure 5.21 Data transmitted by the low power consumption BLE communication module to the custom-built mobile application as a function of time.

The sensor data, acquired from the onboard XIAO BLE module, includes pitch and roll angles (bottom plots – Figure 5.21), as well as the received signal strength indicator (RSSI) and temperature values (top plots – Figure 5.21). To observe the variations in the roll and pitch angles, the XIAO BLE sensor board was occasionally rotated. Similarly, to modulate the RSSI levels, the distance between the BLE device and the smartphone was randomly varied within an approximate range of less than 5 meters. Likewise, to record the temperature changes, the sensor was pressed and released with a finger (as indicated by arrows in Figure 5.20), resulting in the temperature peaks.

5.5 Summary and conclusions

This chapter demonstrates the practical feasibility of nonlinear pyroelectric energy harvesters through the design and implementation of a self-powered system capable of converting low-grade thermal energy into usable electrical energy. The major contributions and findings presented are outlined below:

- A self-powered autonomous pyroelectric energy harvester operating under the Stirling cycle was developed using two PST MLCs. With only 0.3 g of active

material, the system sustained prolonged operation, and the energy extracted from the material is effectively managed to power the control circuitry and trigger subsequent Stirling cycles, without the need of an external power supply.

- For the first time, a macroscopic self-powered pyroelectric energy harvester composed of 60 PST MLCs operating under the Stirling cycle was developed and experimentally validated. This system not only sustained its own operation but also continuously powered an external electronic device (based on BLE communication module), demonstrating its feasibility as a stand-alone energy source even when operated within a modest temperature span of 50 K.
- To enable long-duration operation with minimal resources, a closed-loop fluid circulation system was implemented. By recirculating a limited volume of silicone oil between hot and cold reservoirs, a stable temperature differential (ΔT) was maintained across the prototype, allowing uninterrupted operation for over 30 minutes and potentially much longer under steady conditions.
- The prototype effectively addressed three critical challenges in realizing practical macroscopic pyroelectric harvesters: (1) generating a reliable temperature-varying heat source, (2) synchronizing the thermodynamic cycle steps with controlled fluidic switching, and (3) developing an efficient power interface to manage and utilize the energy extracted from the active pyroelectric material.

In summary, the results presented in this chapter strongly support the potential of nonlinear pyroelectric systems for practical energy harvesting applications. The successful demonstration of a self-powered macroscopic pyroelectric prototype, capable of autonomously sustaining its operation and continuously powering an external device, represents a meaningful step forward in the field. The integration of autonomous control, external load support, and thermal cycling through a compact closed-loop system represents a major step toward real-world implementation of this technology in microelectronics and low-power sensor networks. Additionally, these experiments also indicate that it is possible to realise a macroscopic device which operates for a long duration without implementing any heat regeneration strategies. Furthermore, the findings suggest that with appropriate scaling of the active material and energy interface circuitry, the system could be scaled to deliver tens of watts for higher power applications, thus extending its relevance to a broader range of energy harvesting scenarios.

Chapter 6

Conclusion and perspectives

This chapter summarizes the key findings presented throughout this dissertation and outlines future perspectives for advancing this topic into a viable technology with significant market potential, particularly in the context of waste heat energy recovery.

Chapter 1 highlights the need for waste heat recovery techniques along with the market demand and potential. Moreover, this chapter underscores the significance of nonlinear pyroelectric energy harvesting in efficiently transforming low grade waste heat into electrical energy over other conventional technologies such as thermoelectric generators. The main objectives of this doctoral dissertation along with the structure of this thesis are provided in this chapter.

Chapter 2 provides a background on nonlinear pyroelectric energy harvesting using ferroelectric materials. Although the concept of implementing closed pyroelectric conversion cycles, analogous to those in conventional heat engines, has been recognized for nearly seven decades, the available literature remains limited. In particular, there is a lack of detailed discussion on several critical topics, including the advantages and limitations of different thermodynamic cycles, the role of phase transitions in enhancing energy conversion, the development of suitable figures of merit for nonlinear pyroelectric materials, and the system-level performance of nonlinear pyroelectric energy harvesting devices. Therefore, the primary aim of this chapter is to address these gaps by providing detailed discussions on each of these aspects.

Chapter 3 explores the pyroelectric conversion potential of lead scandium tantalate (PST) in thin film form. Although PST is known for its excellent electrocaloric and pyroelectric properties, its nonlinear pyroelectric conversion potential in thin film geometry has not yet been investigated. The main motivation of this work is to investigate the pyroelectric energy density and conversion efficiency in PST thin films and to understand the influence of chemical modification on their structural and functional properties. The main findings of this chapter are summarized below:

- PST thin films exhibit a maximum harvestable energy density of $9.1 \text{ J}\cdot\text{cm}^{-3}$ between 0 and 150°C at 100 Hz, under an electric field variation (ΔE) of $1450 \text{ kV}\cdot\text{cm}^{-1}$ following the Olsen pyroelectric cycle.

- By doping PST thin films with Ti^{4+} in different concentrations, the temperature of the dielectric constant maximum (T_m) was systematically shifted from 30°C to 90°C .
- Ti-doped PST thin films yield a maximum electrocaloric temperature variation of 5.2 K at 90°C for a ΔE of $667 \text{ kV}\cdot\text{cm}^{-1}$, estimated using the Maxwell relation.
- A maximum of 30% Carnot efficiency was achieved in Ti-doped PST thin films using the Olsen cycle for a 10 K temperature span from its transition temperature.
- By integrating Ti-doped PST thin films across different working temperatures, the electrical work output can be enhanced. A conceptual analysis based on the energy density values of Ti-doped PST thin films indicates a 27% improvement in the energy output over the same temperature range when compared to a device employing undoped PST thin films.

Chapter 4 investigates the pyroelectric conversion efficiency of PST bulk ceramics and multilayer capacitors (MLCs) under the Olsen cycle. Moreover, direct implementation of the Olsen cycle was performed on these samples, which agree well with the indirect measurements. The primary objective of this chapter is to evaluate the influence of intrinsic material characteristics, including B-site cation ordering and geometric configuration, as well as the effect of external parameters on the conversion efficiency of the material. Key findings of this chapter are listed below:

- PST ceramics exhibit a maximum of 21% Carnot efficiency between 30 and 40°C for a ΔE of $130 \text{ kV}\cdot\text{cm}^{-1}$, under the Olsen cycle.
- PST MLCs yield a maximum pyroelectric energy density of $1.65 \text{ J}\cdot\text{cm}^{-3}$ between 20 and 70°C for a maximum field of $205 \text{ kV}\cdot\text{cm}^{-1}$. This was also experimentally verified through direct implementation of the Olsen cycle under identical conditions.
- PST MLCs reach nearly 50% Carnot efficiency under the Olsen cycle between 40 and 45°C for a maximum field of $205 \text{ kV}\cdot\text{cm}^{-1}$.
- Under non-regenerative conditions, Brayton cycle yields a slightly higher relative efficiency compared to the Olsen cycle under similar experimental conditions.

Chapter 5 demonstrates the practical feasibility of nonlinear pyroelectric energy harvesting using PST MLCs based on the Stirling cycle. The central objective of this chapter, and of the thesis as a whole, is to develop a self-powered device based on the non-linear pyroelectric modules operating under a Stirling cycle. The key findings are summarized below:

- An autonomous pyroelectric energy harvesting device operating under the Stirling cycle was developed using only two PST MLCs. The device is capable of sustained operation, provided the material periodically reaches the defined lower and upper temperature thresholds. In this study, the autonomous functioning of the device was deliberately terminated after 40 minutes of continuous operation.

- A macroscopic pyroelectric energy harvester operating under the Stirling cycle is demonstrated for the first time. A key innovation is the integration of a closed loop fluidic control system that circulates hot and cold fluids from their respective thermal reservoirs, maintaining the temperature gradient through continuous recirculation.
- A self-powered macroscopic pyroelectric energy harvester consisting of 60 PST MLCs can function effectively for extended durations without any external power supply while continuously powering a Bluetooth Low Energy (BLE) communication module. The BLE module functioned autonomously by drawing energy from a storage capacitor, which was replenished after each Stirling cycle. Sensor data from the device was continuously transmitted to a mobile device and recorded using a custom built application.
- The self-powered macroscopic prototype functioned uninterrupted for over 30 minutes under the Stirling cycle between 5 and 60°C, after which the operation was manually terminated.

In summary, this work highlights the nonlinear pyroelectric conversion potential of PST in different forms and the significance of this technology through a proof of concept demonstration.

Future perspectives

An outlook on advancing nonlinear pyroelectric energy harvesting toward various market applications is provided below:

- **Pyroelectric thin films**

In the current era of rapid advancements in artificial intelligence (AI), the need for high-performance and energy-efficient microelectronic devices is expected to accelerate further, driving the integration of even more densely packed transistors following the Moore's law. This trend could also lead to significant energy losses in the form of waste heat. Pyroelectric thin films offer a promising solution by converting a portion of this low-grade waste heat into electricity, potentially serving as an auxiliary source of energy. Owing to their compatibility with standard microfabrication techniques, these materials can be directly integrated into existing device architectures. However, to advance this field, several key challenges must be addressed:

1. Direct implementation of pyroelectric conversion cycles on thin films and implementing efficient power management circuits to quantify their performance.
2. Investigate the material degradation behaviour in pyroelectric thin films subjected to direct pyroelectric conversion cycles to improve the device reliability.

3. Fabricate high quality ferroelectric pyroelectric thin films without the need for rigid substrates

One viable solution is to develop thin film multilayer capacitor based on ferroelectric materials that do not require extremely high processing conditions, such as HfO₂ based ferroelectrics, which is CMOS compatible. Moreover, the material and pyroelectric conversion cycle should be selected based on the trade-off between pyroelectric coefficient, breakdown strength, specific heat and their conversion efficiency.

- **Thermal control elements to enhance power output**

Nonlinear pyroelectric materials require rapid cycling of both electric field and temperature to achieve high electrical power output. However, naturally occurring time-varying temperature sources are rare and difficult to harness. To address this limitation, thermal control elements—such as thermal switches, diodes, or regulators can be employed to efficiently manage the heat flow into and out of the material. These components can improve cycle frequency and ultimately increase the overall power output. In addition, the use of thermal control devices serves as an alternative to the reliance on inactive dielectric heat transfer fluids, which can also reduce the size of the system drastically.

- **Solid-state pyroelectric energy harvesters based on ferroelectric polymers**

Ferroelectric polymers based on PVDF-TrFE are highly promising for nonlinear pyroelectric energy harvesting due to their significant entropy change and favourable power-to-weight ratio. Additionally, these materials are mechanically flexible and can be fabricated on bendable substrates or as free-standing films, offering considerable design versatility. Their low mass also makes them suitable for scaled-up device implementations, particularly in applications such as data centres, where they could be employed to convert waste heat into usable electrical energy. However, several challenges must be addressed to realize efficient macroscopic devices. First, the intrinsic leakage current of these materials must be reduced to minimize energy loss. Second, the inherently low thermal conductivity of these polymers limits effective heat exchange, necessitating improved thermal management strategies to enhance overall device performance.

- **Conversion efficiency of pyroelectric devices**

To improve the conversion efficiency, heat management techniques such as heat regeneration must be implemented. Another strategy as discussed in Chapter 2, corresponds to the implementation of cascaded systems consisting of active pyroelectric materials with varying transitions that work over a broad range of

temperature and the heat released by one serve as the input heat for the next material stage, thereby improving the efficiency. However, such configurations must be practically implemented, and their performance thoroughly evaluated under realistic operating conditions to validate their effectiveness and reliability.

- **Advanced power electronic systems for enhancing the extracted energy**

An important yet underexplored area in pyroelectric energy harvesting is the development of advanced power interface circuits. These circuits are essential for the efficient extraction, conditioning, and management of the energy generated by pyroelectric devices, and are critical for maximizing overall system performance. To this end, highly efficient power electronic systems are required to minimize energy losses and improve switching performance. Furthermore, such electronic systems can enable the implementation of alternative thermodynamic conversion cycles, such as the Brayton cycle, which require adiabatic charging and discharging conditions.

Finally, the realization of a highly efficient macroscopic nonlinear pyroelectric energy harvester requires a holistic optimization of material properties, thermal management strategies, and electrical as well as electronic system design, ensuring that all components function synergistically to maximize energy conversion performance in practical applications.

Appendix A

This section presents an overview of the experimental and characterization techniques used throughout this thesis. It begins with a background on the chemical solution synthesis, especially the sol-gel synthesis method. The subsequent part discusses the structural and electrical characterization techniques, including the instruments used for performing these measurements. Finally, the infrared (IR) thermography setup is described, with particular attention to the FLIR X6580sc IR camera used for thermal characterization of the PST bulk samples.

A.1 Chemical solution deposition

Chemical solution deposition (CSD) is widely utilized for synthesizing perovskite thin films due to its high compositional control, low cost, good homogeneity, and uniform film thickness over large areas [200]. Thin film fabrication via CSD consists of four basic steps: (i) solution preparation by dissolving the metal precursors into a suitable solvent; (ii) solution deposition onto a substrate using an appropriate coating technique such as spin coating; (iii) low temperature heat treatment for the removal of organic solvents followed by a pyrolysis step (typically 300 – 400°C) for the formation of an amorphous film; and (iv) high temperature annealing (> 500 °C) for the densification and crystallization of the amorphous film into the desired phase. It is important to note that deposition parameters and thermal processing conditions vary significantly based on the solution chemistry.

Depending on precursor type and the chemical reactions occurring during processing, CSD approaches can be categorized into three groups: sol-gel processes, metal-organic decomposition, and hybrid routes [201]. In this thesis, all films were prepared via the sol-gel method, which employs alkoxide precursors and 2-methoxyethanol (2-MOE) as solvent. The fundamental chemical reactions in the sol-gel process include hydrolysis and condensation (with elimination of water or alcohol) reactions. An overview of the sol-gel process and its related fabrication techniques is illustrated in Figure A1.

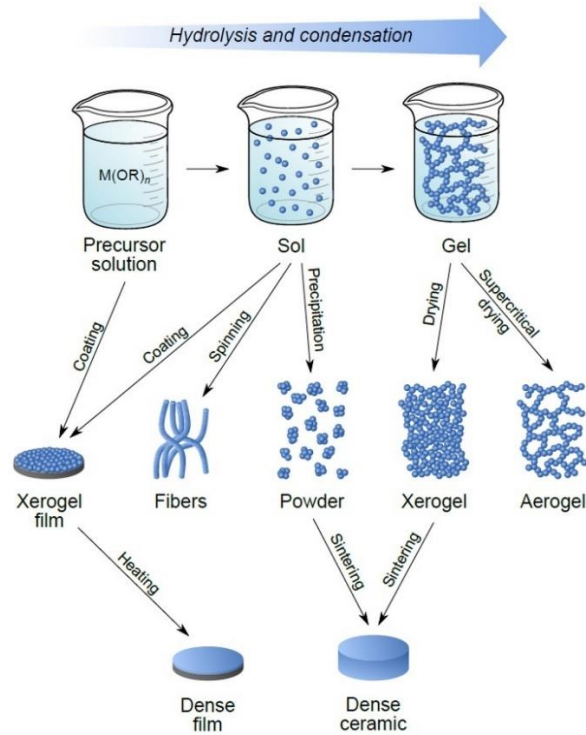
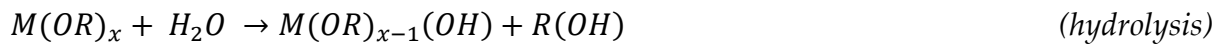
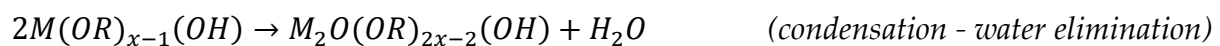


Figure A1 Overview of the sol-gel process and related fabrication techniques. Adapted from [202].

Initially, hydrolysis occurs when metal alkoxides ($M(OR)_x$, where M denotes metal and R an organic moiety) react with water, forming hydroxyl-containing metal alkoxides [202]. These reactions are presented below [203]:



Subsequently, condensation reactions take place between the hydroxylated species, creating metal-oxygen-metal (M–O–M) linkages accompanied by elimination of alcohol or water:



Additionally, the use of 2-MOE solvent induces an alcohol exchange reaction, reducing the hydrolysis sensitivity of the metal precursors:



where OR represents the reactive alkoxy group and OR' is the less reactive 2-methoxyethanol group. Through precise control of these reactions, the reactivity of the precursors can be effectively tailored, ensuring the development of thin films with uniform composition and structure.

For instance, the sol-gel synthesis of $\text{Pb}(\text{Sc}_{1/2}\text{Ta}_{1/2})\text{O}_3$ (PST) requires the use of multiple alkoxide precursors, and the final composition is influenced by factors such as the choice of starting materials, reflux duration, and the sequence of mixing these precursors. In this work, the B-site starting precursors were first combined and refluxed in 2-MOE to promote compositional homogeneity and solution stability, followed by the addition of the lead precursor. This approach minimizes premature hydrolysis and phase separation, ensuring a uniform and stable precursor solution as reported also by Brinkman et al.[204]. After the reflux and distillation steps, additional 2-MOE was added to dilute the solution to the desired concentration. This was followed by the fabrication of PST thin films via spin coating, along with appropriate thermal treatments to achieve the desired crystalline phase. Further details on PST solution preparation and thin film processing on single crystal substrates can be found in Chapter 4. The subsequent fabrication of electrodes for electrical measurements using conventional photolithography is described in the following section.

A.2 X-ray techniques

To analyse the crystal structure and texture of the thin films presented in this dissertation, θ - 2θ scans were performed using a Bruker D8 Diffractometer (Bruker, USA) with $\text{Cu K}\alpha$ radiation ($\lambda = 1.54 \text{ \AA}$). This configuration is particularly effective for assessing out-of-plane crystallographic orientations in films, as it probes diffraction from lattice planes parallel to the film surface. During a θ - 2θ scan, the X-ray source and detector move synchronously: the incident angle θ increases incrementally while the detector angle moves to 2θ , dynamically satisfying Bragg's law for constructive interference. The relationship is expressed as: $n\lambda = 2 d_{hkl} \sin\theta$, where n is an integer representing the diffraction order, λ is the X-ray wavelength, θ is the Bragg angle, and d_{hkl} is the interplanar spacing corresponding to the crystallographic plane with Miller indices (hkl) . The interplanar spacing d_{hkl} , determined by the crystal structure, dictates the angular positions of diffraction peaks observed in the scan. This θ - 2θ or *lock-coupled* scan provides information primarily about the crystal structure and preferential orientation of the film.

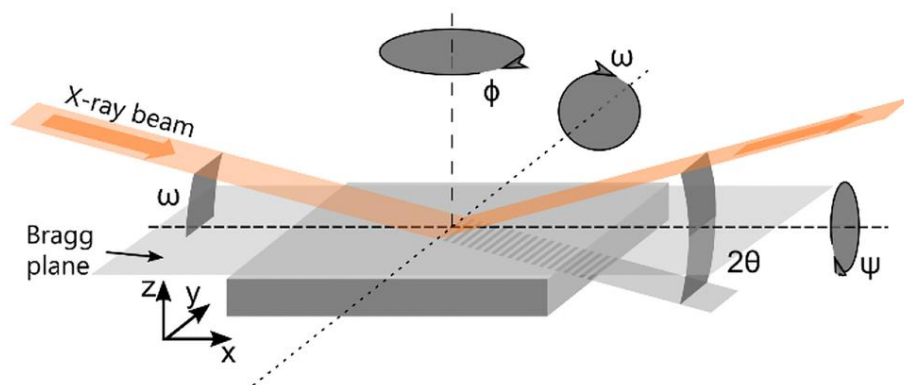


Figure A2 Schematic showing the various angles and degrees of freedom in a typical diffractometer used for thin film measurements. Adapted from [205].

To detect superstructure reflections arising from long-range cation ordering in preferentially oriented films such as PST thin films, an adapted θ - 2θ measurement was employed. In such materials, superstructure peaks often arise from planes inclined relative to the film normal and therefore do not satisfy the Bragg condition in standard lock-coupled scans. To bring these planes into the diffraction condition, the sample was tilted by a fixed χ angle corresponding to the orientation of the superstructure planes [206,207]. Since these peaks typically exhibit low intensity, extended acquisition times were used to improve detection sensitivity. Additionally, a parallel-beam setup incorporating Soller slits and collimators was used to reduce beam divergence, enhance angular resolution, and suppress background scatter, thereby improving the signal-to-noise ratio for identifying superstructure peaks relative to the main texture of the film. More details about this adapted approach can be found in following chapter on PST thin films.

A.3 Scanning electron microscopy

Scanning electron microscopy (SEM) employs a focused electron beam to systematically scan the surface of a specimen, enabling the visualization of microstructural features beyond the resolution limits of optical microscopy. As the incident electrons interact with the sample, various signals are generated, including secondary electrons, backscattered electrons, Auger electrons, characteristic X-rays, and cathodoluminescence through elastic and inelastic scattering processes [208]. These signals can be utilized for high-resolution imaging and elemental analysis.

Secondary electron imaging was used to examine surface topography and cross-sectional features of the thin films. A Helios NanoLab 650 SEM (FEI, USA) operated at 3 kV with a through-lens detector enabled high-resolution imaging in this work.

A.4 Electrical characterization

Field correction in interdigitated electrodes

The main challenge in characterizing the ferroelectric properties of the thin films using IDEs lies in the inhomogeneous and curved field distribution within the material, which can compromise the accuracy of the extracted electrical properties. Therefore, appropriate field corrections are necessary to estimate the effective field distribution and penetration depth. A simplified geometrical model, as described in [209], was used to approximate the electric field by considering the IDE structure as an array of parallel plate capacitors extending along the film thickness. In this approach, the equivalent area and effective electrode spacing are determined based on the assumption that the electrodes span the entire film thickness, as illustrated in Figure A3.

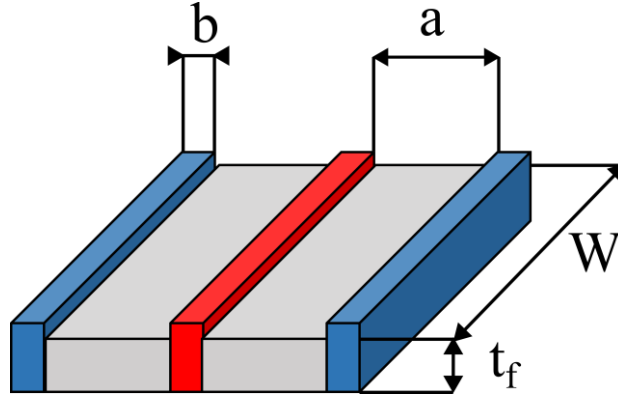


Figure A3 Schematic of the IDE geometry based on the simple model, which assumes the structure behaves as an equivalent network of $(2N - 1)$ parallel plate capacitors in parallel. Adapted from [210].

This approximation is valid when the electrode gap a , and finger width b are each at least one order of magnitude greater than the film thickness t_f . Furthermore, to avoid significant contributions from stray fields at IDE finger tips, the finger length W must be at least two orders of magnitude larger than the electrode gap a [210]. Under these conditions, the equivalent active area of the IDE capacitor is calculated as $(2N - 1)Wt_f$, where N is the number of electrode pairs. To account for the curvature of the electric field between adjacent fingers, a correction factor Δa is applied to the electrode spacing, where $\Delta a \approx 1.324 t_f$. Consequently, the effective electrode distance becomes $a + \Delta a$, and the IDE capacitance is expressed as:

$$C = \epsilon_0 \epsilon_r \frac{(2N - 1)Wt_f}{a + \Delta a} \quad (\text{A.1})$$

where ϵ_0 is the vacuum permittivity and ϵ_r is the relative permittivity of the dielectric material. A more detailed comparison of IDE field models and correction techniques can be found in [211].

Ferroelectric characterization

To investigate the electrical properties of the ferroelectric materials, particularly their polarization behaviour and zero-field permittivity response across various temperatures and frequencies up to 5 kHz, an aixACCT TF 2000 Ferroelectric Analyzer was used. To ensure reproducibility of measurements, ferroelectric characterizations were performed multiple times on the samples.

Polarization – Electric Field measurements

Ferroelectric polarization can be measured using several methods, most of which are based on monitoring the current response of a ferroelectric capacitor when subjected to an electric field. A common approach involves applying a triangular voltage waveform and measuring the resulting switching current, as illustrated in Figure A4.

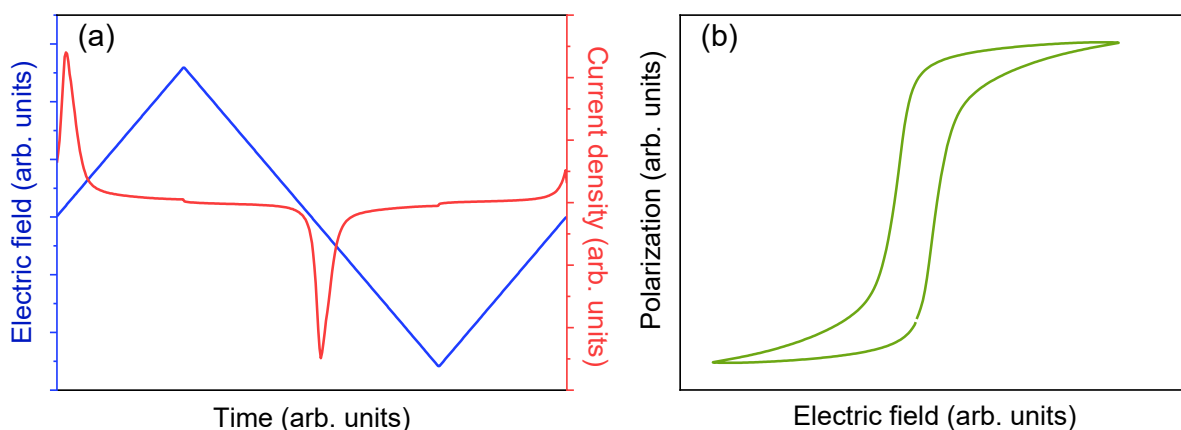


Figure A4 (a) Graph of the applied electric field and current density response of a PST bulk ceramic capacitor used for measuring the polarization hysteresis loops. (b) Measured polarization hysteresis loop.

For an ideal, non-leaky capacitor, the change in polarization ΔP over a time interval Δt is given by:

$$\Delta P = P(\Delta t) - P(0) = \int_0^{\Delta t} j(t) dt \quad (\text{A.2})$$

where $j(t)$ is the current density due to domain switching.

Figure A4 (a) shows a typical triangular field waveform and the corresponding current density response. The resulting polarization-electric field loop is obtained by integrating the current signal, as shown in Figure A4 (b).

In practice, the measured current includes unwanted contributions such as parasitic capacitance and other setup-specific artifacts. To minimize these effects, particularly when measuring small-area capacitors, this work employed the virtual ground method using the aixACCT TF Analyzer 2000 system. In this method, an operational amplifier is used with its inverting input connected to the output of a current-to-voltage converter through a feedback resistor, and also to ground. The voltage is measured as the difference between the amplifier's output and ground. Ideally, the voltage difference between the inverting and non-inverting inputs remains zero or negligible, allowing the capacitor under test to be connected to a virtual ground.

Small signal capacitance measurements

The zero-field permittivity measurements were obtained from the capacitance values, which is derived from the AC small signal current response upon the application of an electric field. For all the measurements, the small signal amplitude was maintained at 0.25 V and the permittivity values were derived using the model described in the previous section [211]. Since the aixACCT TF 2000 analyser is limited to 5 kHz frequency range, detailed frequency and temperature dependent dielectric measurements were performed using a dielectric spectrometer system.

A.5 Dielectric spectroscopy

Dielectric spectroscopy involves measuring the dielectric properties, such as permittivity and dielectric losses of a material when subjected to an electric field at a given frequency. In practice, these measurements are performed by superimposing a small-amplitude AC signal onto a DC bias field and subsequently measuring the capacitance from the resulting AC small-signal current response, as shown in Figure A5. This arrangement can be modelled as a simple parallel RC circuit, where the resistance represents the dielectric losses. Here the conduction current across the capacitor is assumed to be negligible.

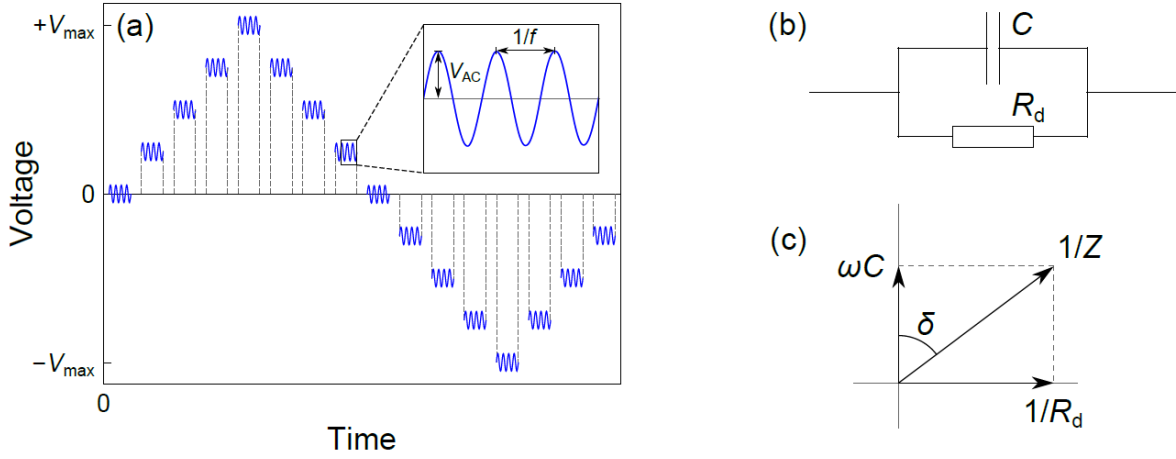


Figure A5 Measurement principle of ϵ - E loops. (a) AC signal superimposed on a staircase DC bias (b) Equivalent RC circuit model (c) Complex plane representation showing the inverse impedance components and their phase relationship. Adapted from [202].

The dielectric permittivity (ϵ_r) is typically represented as a complex quantity, where the real part (ϵ') indicates the capacity of the material to store electrical energy, and the imaginary part (ϵ'') quantifies the energy dissipation through dielectric losses.

$$\epsilon_r = \epsilon' - j\epsilon'' \quad (\text{A.3})$$

Dielectric losses are commonly expressed using the loss tangent:

$$\tan\delta = \frac{\epsilon''}{\epsilon'} = \frac{1}{\omega CR_d} \quad (\text{A.4})$$

Here, δ is the phase angle between the reactive (capacitive) and resistive components in the complex impedance plane, R_d is the resistance and ω is the angular frequency of the AC signal (see Figure A5). Since the capacitance is defined as $\left(\frac{\partial Q}{\partial V}\right)$, the relative permittivity of the material can be obtained using:

$$\epsilon_r \cong \frac{Cd}{A\epsilon_0} \quad (\text{A.5})$$

where d is the thickness of the dielectric layer, A is the electrode area, and ϵ_0 is the vacuum permittivity for a parallel-plate capacitor. Typically, the capacitance value is taken at zero bias field to derive the relative permittivity of the material. In the case of IDE geometry, the relative permittivity of the material can be derived using Equation (A.1) and (A.5), as they are modelled as parallel-plate capacitors.

In this work, the dielectric measurements of PST thin films at high frequencies was performed using Novocontrol Concept 40 dielectric spectrometer system. Measurements were carried out between -50 to 120°C , at frequencies ranging from 1 kHz to 1 MHz. The AC amplitude was kept at 0.2 V. Dielectric measurements were performed both without and with a maximum bias field of $10\text{ kV}\cdot\text{cm}^{-1}$ to assess if field induced phase transition was present. Further details regarding specific measurement conditions are provided in the following chapter.

A.6 Infrared thermography

Infrared (IR) thermography is a non-contact technique that transforms the thermal energy (heat) emitted by the objects in the IR band of the electromagnetic spectrum into a visible image, representing the surface temperature distribution of the measured object [212]. This can be achieved using an IR sensor or camera. An IR camera consists of an optical lens system that focuses incoming IR radiation onto a detector sensor. The detector consists of thousands of pixels arranged in a grid, which converts the infrared energy into electronic signals. Each pixel generates a signal proportional to the intensity of received radiation. These raw signals are then processed through onboard electronics to produce temperature-calibrated thermal images, including colour maps that represent the real-time surface temperature of the object.

One of the key advantages of an IR camera is its ability to deliver both high spatial and temporal resolution, allowing precise tracking of rapid and localized thermal changes. In this work, IR thermography was used to monitor the electrocaloric heat of PST bulk samples as well as its temperature under pyroelectric conversion cycles.

To ensure the reliability of these temperature measurements, the emissivity of the sample surfaces was carefully controlled. Emissivity is a surface-dependent property that defines how efficiently a material emits infrared radiation relative to an ideal black body (emissivity $\varepsilon = 1$). Most metals and ceramics exhibit low or variable emissivity and may also reflect ambient infrared radiation, resulting in errors in recorded temperatures. To mitigate this, all samples were coated with Colorjelt Noir Mat, a high-emissivity matte black paint that raises the surface emissivity to approximately 0.97 . This coating ensures that the radiation detected by the camera originates almost entirely from the sample itself, rather than from surrounding reflections.

All thermal measurements in this study were performed using a FLIR X6580sc infrared camera, which features a cooled InSb detector with a spectral sensitivity

range of 1.5–5.1 μm , suitable for detecting mid-wave IR radiation. The camera provides a spatial resolution of 640×512 pixels, allowing detailed thermal imaging over a wide field of view. Its thermal sensitivity, or noise equivalent temperature difference (NETD), is approximately 20 mK, enabling detection of subtle temperature changes. The frame rate is adjustable from 100 Hz up to 2 kHz [213].

A key parameter in thermal imaging is the integration time, which defines how long the sensor collects infrared radiation for each frame. Longer integration times can increase signal strength and improve temperature accuracy but may risk sensor saturation at higher temperatures. Conversely, shorter integration times reduce exposure and allow for higher frame rates but may compromise temperature precision due to lower signal levels. Data were analysed using FLIR ResearchIR 4 software, which enabled selection of regions of interest (ROI), temporal tracking of average surface temperatures, and export of data for quantitative analysis. More details about the IR thermography can be found in [103].

Appendix B

This section presents the significance of cascading based on the results obtained from PSTT thin films. Moreover, this simple conceptual study will underscore the significance of heat regeneration and multistaging in the context of pyroelectric energy harvesting.

(1) Efficiency Analysis of a Three-Stage Device with Heat Regeneration

The efficiency of the material is as follows:

$$\eta_{mat} = \frac{W_{mat}}{Q_{mat}} \quad (\text{B.1})$$

where W_{mat} is the electrical work output, estimated using $\oint E dD$ and Q_{mat} is the total heat input, given by:

$$Q_{mat} = mC_p\Delta T + Q_{EC} \quad (\text{B.2})$$

where m denotes the mass, C_p is the specific heat capacity of the material, and ΔT is the temperature range and Q_{EC} represents the additional heat due to the electrocaloric effect.

For a single stage device operating over a ΔT of 60 K without regeneration and assuming Q_{EC} is negligible, the heat input simplifies to $Q_{mat} = mC_p(60)$. This scenario corresponds to Figure B1 (a), where the temperature ranges from 313 K to 373 K. The efficiency of such a single-stage device can be defined as:

$$\eta_{SS} = \frac{W_{tot}}{Q_{tot}} \quad (\text{B.3})$$

where the total work output and heat input simplifies to $W_{tot} = W_{mat}$ and $Q_{tot} = Q_{mat}$ respectively, for a single stage ($n = 1$) device. This leads to:

$$\eta_{SS} = \frac{W_{mat}}{Q_{mat}} = \eta_{mat} \quad (\text{B.4})$$

The total efficiency of the device is limited to the efficiency of the single material, which typically leads to a limited work output with a large heat input. To overcome this limitation, the same material can be used in multiple stages with ideal heat regeneration such that the heat rejected from a higher-temperature stage serves as the input heat for the subsequent stages.

In the case of a three-stage device operating between 313 K to 373 K, the temperature span is divided into three smaller intervals (eg., 20 K per stage), as shown in Figure B1 (b). Hence, the heat input per stage is minimized and the external heat must be provided only for the high temperature stage.

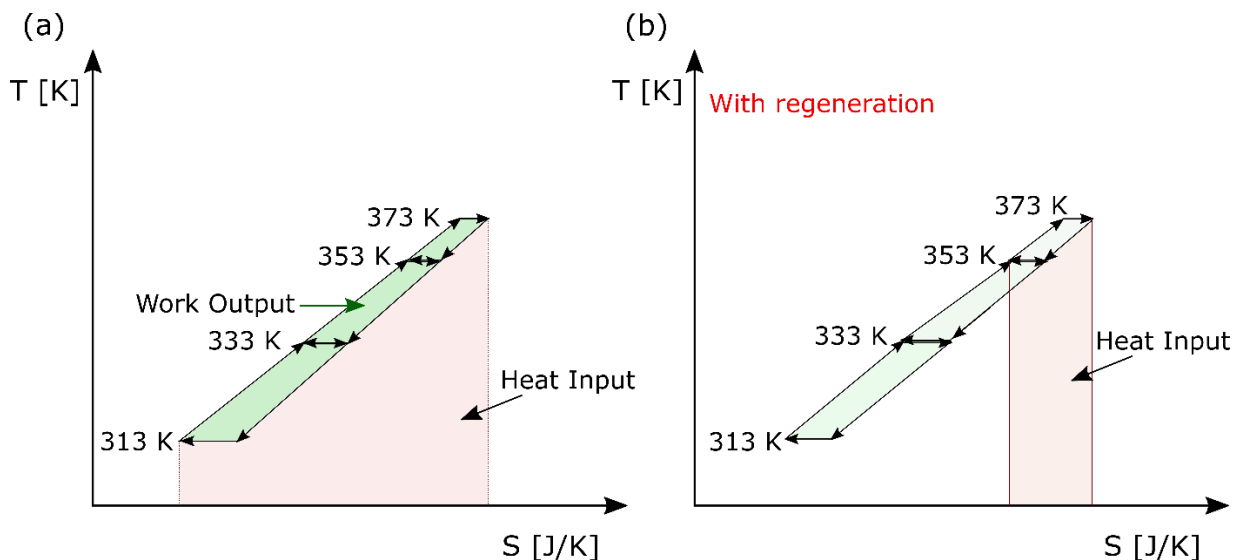


Figure B1 (a) Schematic of a single material subjected to pyroelectric Olsen cycle without any heat regeneration (b) Implementation of multiple stages utilizing the same material with regeneration to limit the heat input.

The efficiency of a three-stage device using the same material with ideal heat regeneration is given by:

$$\eta_{TS} = \frac{W_{TS}}{Q_{TS}} \quad (\text{B.7})$$

where the total work output W_{TS} is:

$$W_{TS} = 3 \cdot W_{stage} = 3 \cdot \eta_{stage} \cdot Q_{stage} \quad (\text{B.8})$$

By assuming a negligible Q_{EC} , the total external heat input is:

$$Q_{TS} = Q_{stage} = mC_p(20) \quad (\text{B.9})$$

For the sake of simplifying the calculation, we suppose that the pyroelectric material has a constant efficiency η over the entire range of temperatures. Hence, the overall efficiency of the three-stage device becomes:

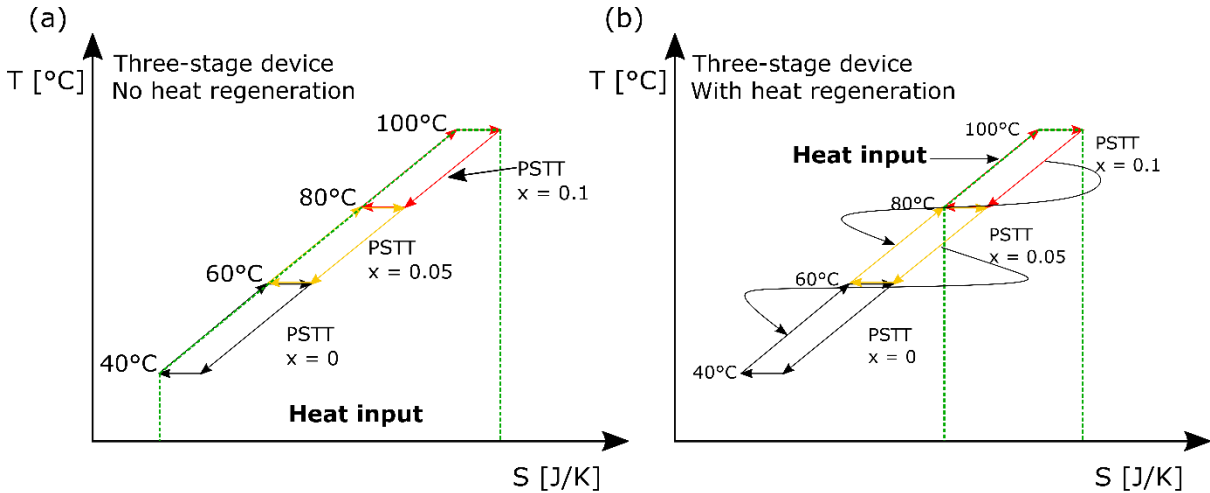
$$\eta_{TS} = \frac{3 \cdot \eta_{stage} \cdot Q_{stage}}{Q_{stage}} = \frac{3 \cdot \eta_{stage} \cdot mC_p(20)}{mC_p(20)} = 3 \cdot \eta_{stage} \quad (\text{B.10})$$

This conceptual study indicates that by implementing multiple stages and heat regeneration, the efficiency of the device can be increased by a factor of three using the same material.

(2) Conceptual analysis of a cascaded system with heat regeneration

To further improve conversion efficiency, cascaded systems can be employed. Instead of using the same material across all stages, cascaded configurations incorporate materials with different transition temperatures. This ensures that each stage operates near its optimal temperature window, maintaining high energy output throughout the device's full thermal span. Olsen et al.[214] have experimentally validated the concept of cascading and reported a 20% improvement in efficiency compared to conventional single-stage pyroelectric regenerators.

In the present study, the efficiency of a three-stage device composed of PSTT thin films ($x = 0, 0.05, \text{ and } 0.1$) was estimated using energy density values extracted from their respective $D - E$ loops, as illustrated in Figure 3.22. Two conceptual scenarios were considered: one without heat regeneration and one with ideal regeneration (heat losses were assumed to be inexistent) as shown in Figure B2.



Energy density of PSTT Thin films
 $(x = 0) : 0.68 \text{ J}\cdot\text{cm}^{-3}$; $(x = 0.05) : 0.60 \text{ J}\cdot\text{cm}^{-3}$ and $(x = 0.1) : 0.57 \text{ J}\cdot\text{cm}^{-3}$

Figure B2 (a) Three-stage device composed of PSTT thin films ($x = 0, 0.05, \text{ and } 0.1$) without heat regeneration, (b) With heat regeneration.

The efficiency of the three-stage PSTT device without regeneration is given by:

$$\eta = \frac{\text{Work Output}}{\text{Heat Input}} = \frac{\text{Energy density}}{C\rho\Delta T + Q_{ECE}} \quad (\text{B.11})$$

Using the same C and ρ values of $300 \text{ J}\cdot\text{kg}^{-1}\cdot\text{K}^{-1}$ and $9070 \text{ kg}\cdot\text{m}^{-3}$ for a ΔT of 60 K (from 40 to 100°C), the efficiency of the system becomes:

$$\eta = \frac{0.68+0.60+0.57}{300*9070*10^{-6}*(60+4.2)} = 1.05 \% \quad (\text{B.12})$$

Only the Q_{EC} contribution from the high temperature stage is considered for the calculation as the remaining electrocaloric heat from the other stages serves to pre-

cool or pre-heat the other stages and does not add to the external heat input. The dotted green lines represent the total heat input for the device.

The corresponding Carnot efficiency of this system is as follows:

$$\eta_{Carnot} = \frac{\Delta T}{T_{hot}} = \frac{60}{373} = 16.08 \% \quad (B.13)$$

The second law efficiency or the relative efficiency is:

$$\eta_r = \frac{\eta}{\eta_{Carnot}} = 6.50\% \quad (B.14)$$

When heat regeneration is implemented, the thermal energy rejected by the high-temperature stage is recycled and used to power the subsequent stages. Since the three stages are thermally connected in series, the heat released by the $x = 0.1$ composition serves as the input heat for the $x = 0.05$ stage. This thermal exchange allows the high-temperature stage to return to its initial temperature while transferring usable energy to the next stage. In this configuration, only the high-temperature stage requires external heating, while the remaining stages operate using the recuperated heat. As a result, the total external heat input is significantly reduced, directly contributing to enhanced overall efficiency. The dotted green line in Figure B2 (b) represents this minimal external input required exclusively for the $x = 0.1$ stage.

Assuming ideal regeneration conditions and negligible electrocaloric losses from the lower stages, the efficiency of the multi-stage system is calculated using the same C and ρ values over the temperature range of 40 to 100 °C:

$$\eta = \frac{0.68+0.60+0.57}{300*9070*10^{-6}*(20+4.2)} = 2.80 \% \quad (B.15)$$

The corresponding relative (second-law) efficiency is:

$$\eta_r = \frac{\eta}{\eta_{Carnot}} = \frac{2.8}{16.08} = 17.4 \% \quad (B.16)$$

These results indicate a nearly threefold increase in energy conversion efficiency for the cascaded device with regeneration compared to the same system operating without regeneration. This conceptual analysis highlights the potential of combining heat regeneration and cascaded configurations to enhance overall conversion efficiency. It would be worthwhile to investigate the performance of these compositions either in thick film or thin-film multilayer capacitor form, that enable practical implementation of heat regeneration and multi-staging to validate these findings.

Appendix C

C.1 Indirect estimation of Olsen cycles at low electric fields

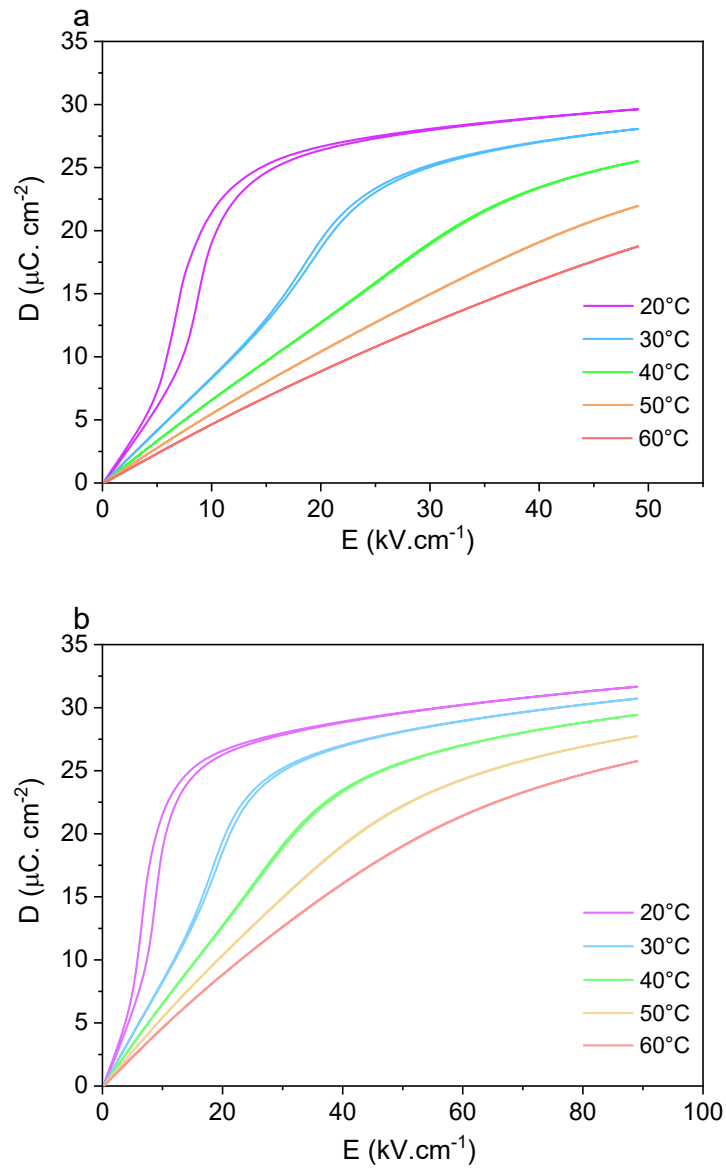


Figure C1 Unipolar $D - E$ loops measured at 1 Hz between 20 and 60°C at a maximum field of (a) 50 $\text{kV}\cdot\text{cm}^{-1}$ and (b) 90 $\text{kV}\cdot\text{cm}^{-1}$.

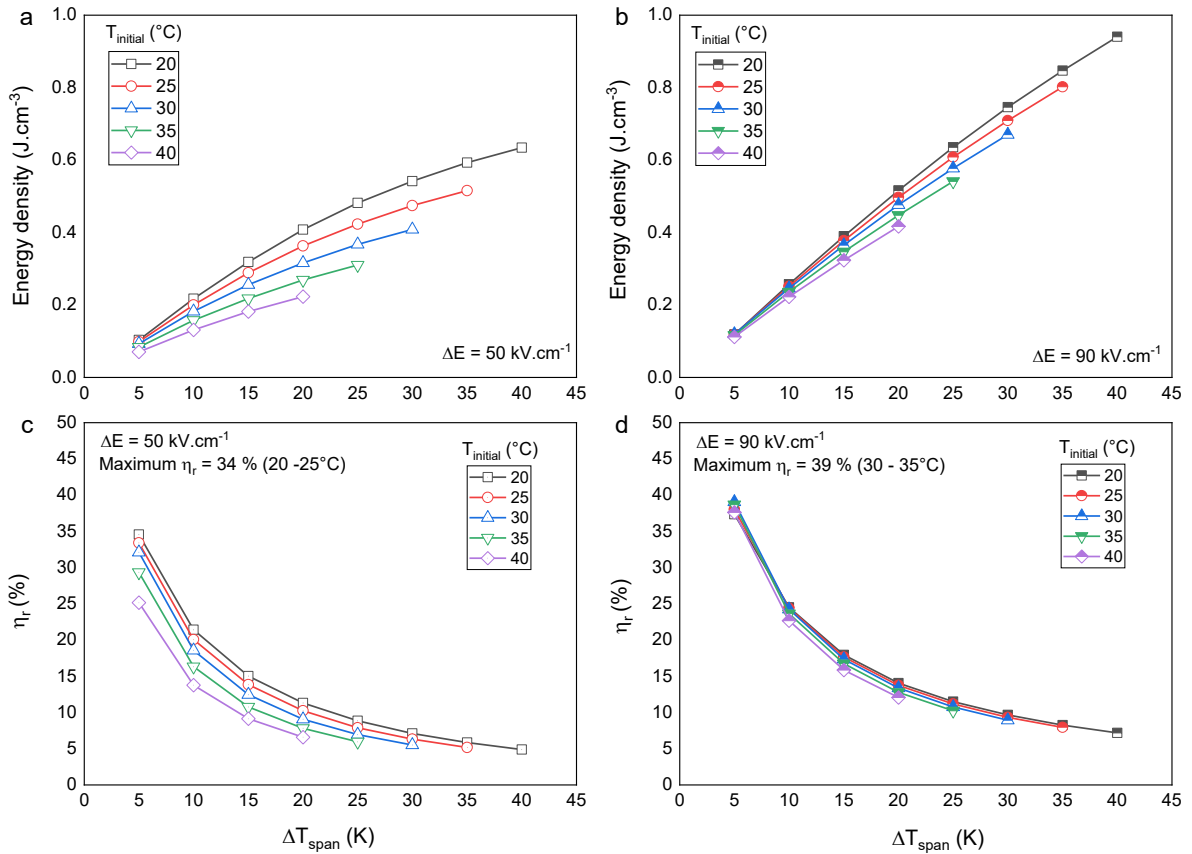


Figure C2 Estimated energy densities at (a) $50 \text{ kV}\cdot\text{cm}^{-1}$ and (b) $90 \text{ kV}\cdot\text{cm}^{-1}$, and relative efficiencies (η_r) from $D - E$ loops at (c) $50 \text{ kV}\cdot\text{cm}^{-1}$ and (d) $90 \text{ kV}\cdot\text{cm}^{-1}$ respectively.

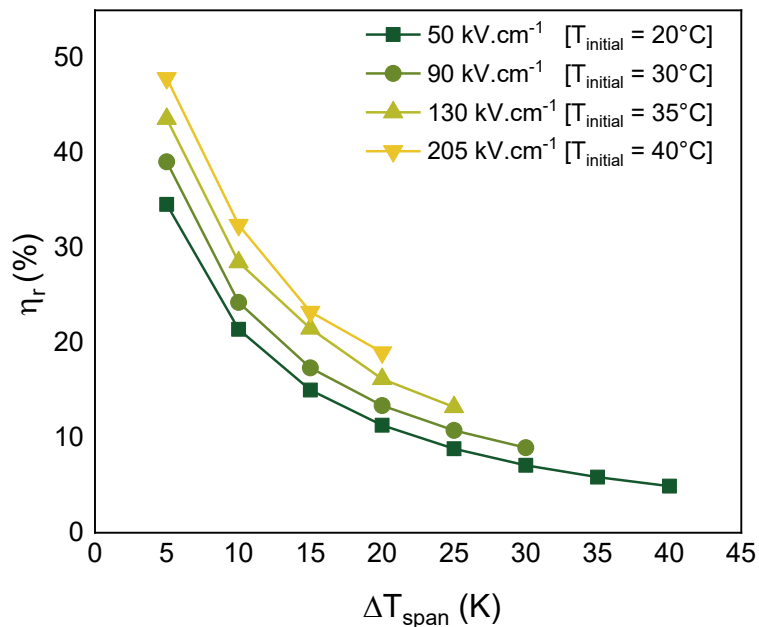


Figure C3 Maximum relative efficiencies obtained at different initial temperatures as a function of electric field and temperature span.

As the electric field was increased from 50 to 205 kV·cm⁻¹ (as detailed in Chapter 4), the initial temperature at which peak relative efficiency was observed shifted from 20°C to 40°C for a 5 K temperature span, as shown in Figure C3.

C.2 Direct Olsen cycle under slow charging and discharging conditions

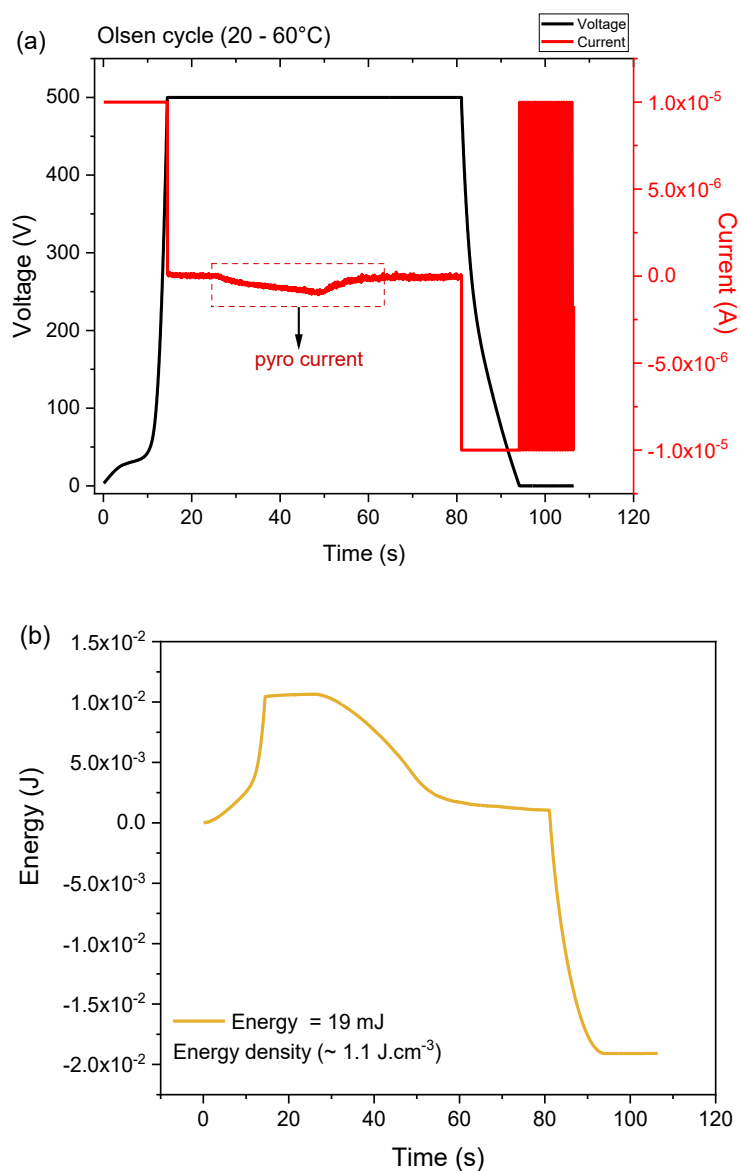


Figure C4 Direct Olsen cycle in a 0.5 mm thick PST MLC between 20 and 60°C under a maximum electric field of 130 kV·cm⁻¹ and slow charge – discharge rates (~ 16 s, respectively): (a) voltage and current profile, (b) harvested energy as a function of time.

Despite slow charge – discharge rates, the obtained energy density ($\sim 1.1 \text{ J}\cdot\text{cm}^{-3}$) is similar to Olsen cycle performed at a relatively faster charge – discharge rates ($\sim 2 \text{ s}$), which was around 20 mJ or approximately $1.2 \text{ J}\cdot\text{cm}^{-3}$.

Similarly, direct Olsen cycles were also performed under a maximum electric field of $205 \text{ kV}\cdot\text{cm}^{-1}$ by slowly charging and discharging the sample. Figure C5 shows the comparison of energy densities obtained from indirect D – E loops (at 1 Hz and 0.1 Hz) and direct Olsen cycle measurements conducted at an initial temperature of 20°C with an input voltage of 800 V . The results correspond to fast ($\sim 2 \text{ s}$) and slow ($\sim 15 \text{ s}$) charge–discharge rates, as indicated by different current compliance settings.

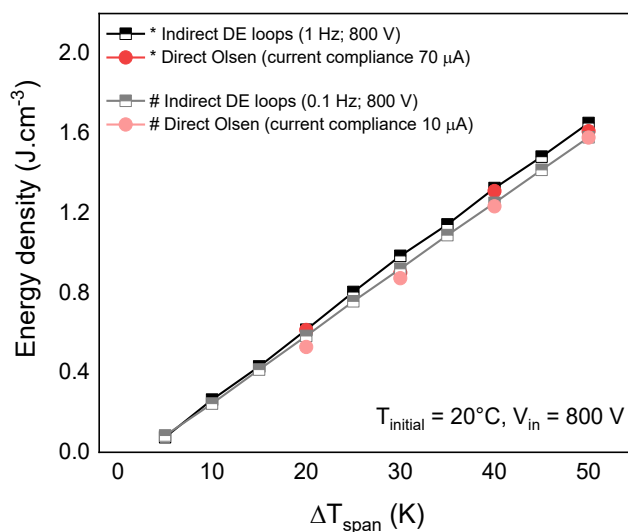


Figure C5 Comparison of energy densities obtained from indirect (at 1 Hz and 0.1 Hz) and direct Olsen cycle measurements conducted under fast and slow charge – discharge conditions at an initial temperature of 20°C with an input voltage of 800 V . The results presented in the main text of Chapter 4 are indicated with (*), while additional measurements are denoted with (#).

C.3 Direct Brayton cycle

Unlike the Olsen cycle, the Brayton cycle consists of two adiabatic (charging and discharging) and two isoelectric field (heating and cooling) steps, as discussed in Section 2.3.1. Direct Brayton cycle implementation was performed between 20 and 60°C using the nonlinear pyroelectric characterization setup. Figure C6 presents the voltage, current, and energy profiles of the 0.5 mm thick PST MLC as functions of time. To approximate near-adiabatic conditions, the sample was charged to 800 V within 0.2 s under a compliance current limit of 1 mA . This was followed by isoelectric heating to 60°C and discharging the sample to zero volts at 60°C within 0.25 s using a compliance current of 0.7 mA . Subsequently, the sample was cooled to 20°C . However, the maximum harvested energy obtained from this preliminary cycle was

only 15 mJ, corresponding to an energy density of $0.9 \text{ J}\cdot\text{cm}^{-3}$, which is significantly lower than the value estimated from the corresponding $D - E$ loops ($\sim 1.26 \text{ J}\cdot\text{cm}^{-3}$).

This discrepancy is attributed to a known artifact of the Keithley 2410 source meter. When the sample is discharged rapidly, the instrument may fail to collect a sufficient number of data points (the partially filled symbols in Figure C5 correspond to the data points), especially during transient current spikes, leading to an underestimation of the actual harvested energy. The author acknowledges this measurement artefact and recognizes that a more systematic and carefully controlled evaluation of the Brayton cycle is still required. The current measurement is therefore considered only a preliminary demonstration. Nevertheless, this initial result highlights the experimental challenges associated with accurately executing Brayton cycles at high fields and frequencies in bulk systems such as MLCs, and these measurements further highlight why the Olsen cycle is preferred over other pyroelectric conversion cycles.

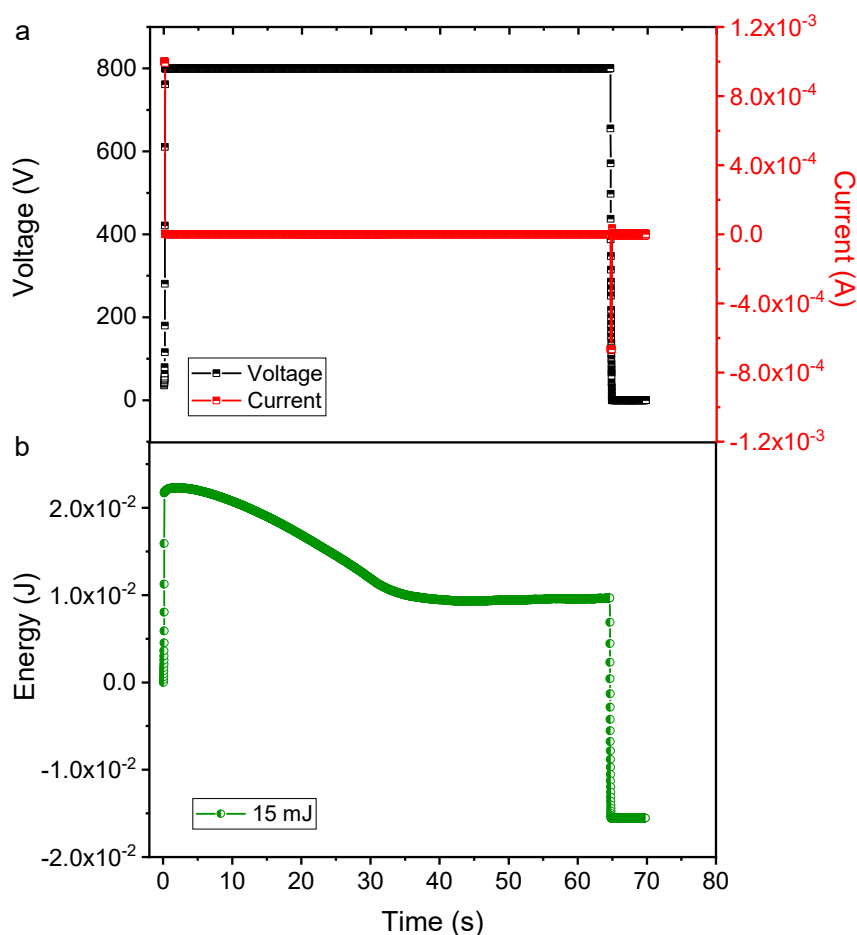


Figure C6 Direct measurement of voltage, current and energy profile of the PST MLC as a function of time.

PhD Output

Publications

1. **A. Aravindhan**, S. Glinsek, S. Girod, A.B. Martinez, T. Granzow, V. Kovacova, E. Defay, “Large pyroelectric energy conversion in lead scandium tantalate thin films”, *Heliyon*, 10(9), 2024.
2. **A. Aravindhan**, V. Kovacova, E. Defay, “Converting heat to electricity with non-linear pyroelectrics: A review”, *International Materials Reviews*, 2025. (Accepted)
3. **A. Aravindhan**, S. Glinsek, T. Granzow, L. Song, Y. Nouchokgwe, V. Kovacova, E. Defay, “Ti-doped $Pb(Sc_{0.5}Ta_{0.5})O_3$ Thin Films for Non-linear Pyroelectric Energy Harvesting”, *Ceramics International*, 51, 47264-47271, 2025.
4. **A. Aravindhan**, Y. Nouchokgwe, T. Granzow, T. Usui, S. Hirose, V. Kovacova, E. Defay, “Pyroelectric conversion efficiency of $Pb(Sc_{0.5}Ta_{0.5})O_3$ multilayer capacitors”, 2025. (In-preparation)

Co-author publications

5. P. Lheritier, A. Torelló, T. Usui, Y. Nouchokgwe, **A. Aravindhan**, J. Li, U. Prah, V. Kovacova, O. Bouton, S. Hirose, E. Defay, “Large harvested energy with non-linear pyroelectric modules”, *Nature*, 609(7928), 718-721, 2022.
6. T. Granzow, **A. Aravindhan**, Y. Nouchokgwe, V. Kovacova, S. Glinsek, S. Hirose, T. Usui, H. Uršič, I. Goričan, W. Jo, C.H. Hong, E. Defay, “Quantitative correlation between structural (dis-) order and diffuseness of phase transition in lead scandium tantalate”, *arXiv preprint arXiv:2506.17126*, 2025. (Under Review)
7. L. Song, **A. Aravindhan**, J. Li, Y. Nouchokgwe, M. Khalil, F. Ni, N. Bousri, O. Ramirez, J. Polesel-Maris, M. Gerard, S. Glinsek, U. Prah, O. Bouton, T. Usui, S. Hirose, V. Kovacova, E. Defay, “Non-linear pyroelectric generators in the watt range for autonomous systems”, 2025. (Under Review)

During the course of my doctoral studies, I also contributed to two research publications in the field of the electrocaloric cooling. While not directly part of this dissertation, these works are closely related and complementary to the core objectives of my research.

8. **A. Aravindhhan**, P. Lheritier, A. Torelló, U. Prah, Y. Nouchokgwe, A. El Moul, X. Chevalier, F.D. Dos Santos, E. Defay, V. Kovacova, *“Direct measurement of electrocaloric effect in P (VDF-TrFE-CFE) film using infrared imaging”*, Journal of Materiomics, 9(2), 256-260, 2023.
9. J. Li, A. Torelló, V. Kovacova, U. Prah, **A. Aravindhhan**, T. Granzow, T. Usui, S. Hirose, E. Defay, *“High cooling performance in a double-loop electrocaloric heat pump”*, Science, 382(6672), 801-805, 2023.

Conferences

1. *“Direct measurement of electrocaloric effect in P(VDF-TrFE-CFE) film using infrared imaging”*(Oral Presentation) at International Symposium of Applications of Ferroelectrics (ISAF), Tours, France (2022).
2. *“From electrocaloric cooling to pyroelectric energy harvesting using lead scandium tantalate multilayer capacitors”* (Oral Presentation) at Material Research Society (MRS) Spring Meeting, San Francisco, USA (2023).
3. *“Non-linear pyroelectric materials for electro-thermal energy harvesting”* (Poster) at International School of Oxide Electronics (ISOE), Cargese, France (2023).

References

- [1] N. Abas, A. Kalair, N. Khan, Review of fossil fuels and future energy technologies, *Futures*. 69 (2015) 31–49. <https://doi.org/10.1016/j.futures.2015.03.003>.
- [2] C. Forman, I.K. Muritala, R. Pardemann, B. Meyer, Estimating the global waste heat potential, *Renew. Sustain. Energy Rev.* 57 (2016) 1568–1579. <https://doi.org/10.1016/j.rser.2015.12.192>.
- [3] E. Garofalo, M. Bevione, L. Cecchini, F. Mattiussi, A. Chiolerio, Waste Heat to Power: Technologies, Current Applications, and Future Potential, *Energy Technol.* 8 (2020) 1–22. <https://doi.org/10.1002/ente.202000413>.
- [4] L.E. Bell, Cooling, heating, generating power, and recovering waste heat with thermoelectric systems, *Science* (80-.). 321 (2008) 1457–1461. <https://doi.org/10.1126/science.1158899>.
- [5] X. Zhang, L.D. Zhao, Thermoelectric materials: Energy conversion between heat and electricity, *J. Mater.* 1 (2015) 92–105. <https://doi.org/10.1016/j.jmat.2015.01.001>.
- [6] G. Chen, M.S. Dresselhaus, G. Dresselhaus, J.P. Fleurial, T. Caillat, Recent developments in thermoelectric materials, *Int. Mater. Rev.* 48 (2003) 45–66. <https://doi.org/10.1179/095066003225010182>.
- [7] G. Sebald, D. Guyomar, A. Agbossou, On thermoelectric and pyroelectric energy harvesting, *Smart Mater. Struct.* 18 (2009). <https://doi.org/10.1088/0964-1726/18/12/125006>.
- [8] J. He, T.M. Tritt, Advances in thermoelectric materials research: Looking back and moving forward, *Science* (80-.). 357 (2017). <https://doi.org/10.1126/science.aak9997>.
- [9] S.P. Alpay, J. Mantese, S. Trolier-Mckinstry, Q. Zhang, R.W. Whatmore, Next-generation electrocaloric and pyroelectric materials for solid-state electrothermal energy interconversion, *MRS Bull.* 39 (2014) 1099–1109. <https://doi.org/10.1557/mrs.2014.256>.
- [10] D.A. Zabeck, Pyroelectric structures and devices for thermal energy harvesting, Doctoral dissertation, University of Bath (2016).
- [11] A.S. Mischenko, Q. Zhang, J.F. Scott, R.W. Whatmore, N.D. Mathur, Giant electrocaloric effect in thin-film $\text{PbZr}_{0.95}\text{Ti}_{0.05}\text{O}_3$, *Science* (80-.). 311 (2006) 1270–1271. <https://doi.org/10.1126/science.1123811>.

- [12] B. Neese, B. Chu, S.G. Lu, Y. Wang, E. Furman, Q.M. Zhang, Large electrocaloric effect in ferroelectric polymers near room temperature, *Science* (80-.). 321 (2008) 821–823. <https://doi.org/10.1126/science.1159655>.
- [13] P. Durcansky, R. Nosek, J. Jandacka, Use of stirling engine for waste heat recovery, *Energies*. 13 (2020). <https://doi.org/10.3390/en13164133>.
- [14] R.W. Whatmore, Y. You, R. Xiong, C. Eom, 100 years of ferroelectricity — A celebration, *APL Mater.* 9 (7), 070401 (2021) 1–7. <https://doi.org/10.1063/5.0059208>.
- [15] J. Valasek, The early history of ferroelectricity, *Ferroelectrics*, 2 (1971) 239–244. <https://doi.org/10.1080/00150197108234098>.
- [16] D. Damjanovic, Hysteresis in Piezoelectric and Ferroelectric Materials, *The Science of Hysteresis*, 3 (2006) 337–465. <https://doi.org/10.1016/B978-012480874-4/50022-1>.
- [17] C.R. Bowen, J. Taylor, E. Le Boulbar, D. Zabek, A. Chauhan, R. Vaish, Pyroelectric materials and devices for energy harvesting applications, *Energy Environ. Sci.* 7 (2014) 3836–3856. <https://doi.org/10.1039/c4ee01759e>.
- [18] H. Huang, J.F. Scott, *Ferroelectric Materials for Energy Applications*, John Wiley & Sons (2018).
- [19] A. Greco, C. Aprea, A. Maiorino, C. Masselli, A review of the state of the art of solid-state caloric cooling processes at room-temperature before 2019, *Int. J. Refrig.* 106 (2019) 66–88. <https://doi.org/10.1016/j.ijrefrig.2019.06.034>.
- [20] G. Velarde, S. Pandya, J. Karthik, D. Pesquera, L.W. Martin, Pyroelectric thin films - Past, present, and future, *APL Mater.* 9, 010702 (2021). <https://doi.org/10.1063/5.0035735>.
- [21] L. Pilon, I.M. McKinley, Pyroelectric Energy Conversion, *Annu. Rev. Heat Transf.* (2016) 279–334. <https://doi.org/10.1615/AnnualRevHeatTransfer.2016015566>
- [22] R.W. Whatmore, S.B. Stringfellow, N.M. Shorrocks, Ferroelectric materials for uncooled thermal imaging, *Infrared Technol.* XIX. 2020 (1993) 391–402. <https://doi.org/10.1117/12.160576>.
- [23] R.W. Whatmore, S.J. Ward, Pyroelectric infrared detectors and materials - A critical perspective, *J. Appl. Phys.* 133, 080902 (2023). <https://doi.org/10.1063/5.0141044>.
- [24] S.B. Lang, Pyroelectricity: From ancient curiosity to modern imaging tool, *Phys. Today*. 58 (2005) 31–36. <https://doi.org/10.1063/1.2062916>.
- [25] L. V. Efimenko, M.A. Itskovskii, L.S. Kremenchugskii, Non-linear pyroelectric

- effect in the phase transition region of ferroelectric crystals, *Ferroelectrics*. 22 (1978) 713–715. <https://doi.org/10.1080/00150197808237377>.
- [26] A. Khodayari, S. Pruvost, G. Sebald, D. Guyomar, S. Mohammadi, Nonlinear pyroelectric energy harvesting from relaxor single crystals, *IEEE Trans. Ultrason. Ferroelectr. Freq. Control*. 56 (2009) 693–698. <https://doi.org/10.1109/TUFFC.2009.1092>.
- [27] D.G. Froom, A note on the use of titanates as thermoelectric transducers, *Can J Phys*. 32 (4) (1954) 313–317. <https://doi.org/https://doi.org/10.1139/p54-029>.
- [28] R.B. Olsen, J.M. Briscoe, D.A. Bruno, W.F. Butler, A Pyroelectric Energy Converter Which Employs Regeneration, *Ferroelectrics*. 38 (1981) 975–978. <https://doi.org/10.1080/00150198108209595>.
- [29] J.D. Childress, Application of a Ferroelectric Material in an Energy Conversion Device, *J. Appl. Phys*. 33 (1962) 1793–1798. <https://doi.org/10.1063/1.1728833>.
- [30] P. Lheritier, A. Torelló, T. Usui, Y. Nouchokgwe, A. Aravindhan, J. Li, U. Prah, V. Kovacova, O. Bouton, S. Hirose, E. Defay, Large harvested energy with non-linear pyroelectric modules, *Nature*. 609 (2022) 718–721. <https://doi.org/10.1038/s41586-022-05069-2>.
- [31] J. He, J. Chen, Y. Zhou, J.T. Wang, Regenerative characteristics of electrocaloric Stirling or Ericsson refrigeration cycles, *Energy Convers. Manag.* 43 (2002) 2319–2327. [https://doi.org/10.1016/S0196-8904\(01\)00183-2](https://doi.org/10.1016/S0196-8904(01)00183-2).
- [32] J. He, J. Chen, J.T. Wang, B. Hua, Inherent regenerative losses of a ferroelectric Ericsson refrigeration cycle, *Int. J. Therm. Sci.* 42 (2003) 169–175. [https://doi.org/10.1016/S1290-0729\(02\)00016-9](https://doi.org/10.1016/S1290-0729(02)00016-9).
- [33] B.M. Hanrahan, F. Sze, A.N. Smith, N.R. Jankowski, Thermodynamic cycle optimization for pyroelectric energy conversion in the thin film regime, *Int. J. Energy Res.* 41 (2017) 1880–1890. <https://doi.org/10.1002/er>.
- [34] R.B. Olsen, Ferroelectric Conversion of Heat To Electrical Energy - a Demonstration., *J. Energy*. 6 (1982) 91–95. <https://doi.org/10.2514/3.62580>.
- [35] R.B. Olsen, D. Evans, R.B. Olsen, D. Evans, Pyroelectric energy conversion : Hysteresis loss and temperature sensitivity of a ferroelectric material, *J. Appl. Phys*. 54 (1983) 5941–5944. <https://doi.org/10.1063/1.331769>.
- [36] G. Sebald, E. Lefeuvre, D. Guyomar, Pyroelectric energy conversion: Optimization principles, *IEEE Trans. Ultrason. Ferroelectr. Freq. Control*. 55 (2008) 538–551. <https://doi.org/10.1109/TUFFC.2008.680>.
- [37] D. Guyomar, S. Pruvost, G. Sebald, Energy Harvesting Based on FE-FE Transition in Ferroelectric Single Crystals, *IEEE Trans. Ultrason. Ferroelectr. Freq. Control*. 55 (2008) 279–285. <https://doi.org/10.1109/TUFFC.2008.646>.

- [38] D. Guyomar, G. Sebald, E. Lefeuvre, A. Khodayari, Toward heat energy harvesting using pyroelectric material, *J. Intell. Mater. Syst. Struct.* 20 (2009) 265–271. <https://doi.org/10.1177/1045389X08093564>.
- [39] G. Taxil, M. Lallart, B. Ducharne, T.T. Nguyen, H. Kuwano, T. Ono, G. Sebald, Modeling of Olsen cycle for pyroelectric energy harvesting and assessment of abnormal electrocaloric effect in ferroelectric single crystals, *J. Appl. Phys.* 132, 144101 (2022). <https://doi.org/10.1063/5.0107429>.
- [40] A.K. Tagantsev, V.O. Sherman, K.F. Astafiev, J. Venkatesh, N. Setter, Ferroelectric materials for microwave tunable applications, *J. Electroceram.* 11 (5) (2003) 5–66. <https://doi.org/10.1023/b:jecr.0000015661.81386.e6>.
- [41] Y. Nouchokgwe, P. Lheritier, C.H. Hong, A. Torelló, R. Faye, W. Jo, C.R.H. Bahl, E. Defay, Giant electrocaloric materials energy efficiency in highly ordered lead scandium tantalate, *Nat. Commun.* 12 (2021) 1–7. <https://doi.org/10.1038/s41467-021-23354-y>.
- [42] B. Hanrahan, Y. Espinal, S. Liu, Z. Zhang, A. Khaligh, A. Smith, S.P. Alpay, Combining inverse and conventional pyroelectricity in antiferroelectric thin films for energy conversion, *J. Mater. Chem. C.* 6 (2018) 9828–9834. <https://doi.org/10.1039/C8TC02686F>.
- [43] A. Aravindhana, P. Lheritier, A. Torelló, U. Prah, Y. Nouchokgwe, A. El Moul, X. Chevalier, F. Domingues Dos Santos, E. Defay, V. Kovacova, Direct measurement of electrocaloric effect in P(VDF-TrFE-CFE) film using infrared imaging, *J. Mater.* 9 (2023) 256–260. <https://doi.org/10.1016/j.jmat.2022.10.009>.
- [44] B. Bhatia, H. Cho, J. Karthik, J. Choi, D.G. Cahill, W. Lane, W.P. King, High Power Density Pyroelectric Energy Conversion in Nanometer-Thick BaTiO₃ Films, *Nanoscale Microsc. Thermophys. Eng.* 20 (2016) 137–146. <https://doi.org/10.1080/15567265.2016.1252820>.
- [45] S. Pandya, J. Wilbur, J. Kim, R. Gao, A. Dasgupta, C. Dames, L.W. Martin, Pyroelectric energy conversion with large energy and power density in relaxor ferroelectric thin films, *Nat. Mater.* 17 (2018) 432–438. <https://doi.org/10.1038/s41563-018-0059-8>.
- [46] Z. Zhang, B. Hanrahan, C. Shi, A. Khaligh, Management and storage of energy converted via a pyroelectric heat engine, *Appl. Energy.* 230 (2018) 1326–1331. <https://doi.org/10.1016/j.apenergy.2018.09.101>.
- [47] B. Bhatia, Nanometer-thick oxide films for pyroelectric energy conversion, Doctoral dissertation, University of Illinois at Urbana-Champaign, (2014).
- [48] M.C. Aprea C, Greco A, Maiorino A, Electrocaloric refrigeration: an innovative, emerging, eco-friendly refrigeration technique., in: *J. Phys. Conf. Ser.*, IOP Publishing, 796 (2017). <https://doi.org/https://doi.org/10.1088/1742->

6596/796/1/012019.

- [49] A. Torelló, E. Defay, Electrocaloric Coolers: A Review, *Adv. Electron. Mater.* 8 2101031 (2022). <https://doi.org/10.1002/aelm.202101031>.
- [50] K. Hong, T.H. Lee, J.M. Suh, S.H. Yoon, H.W. Jang, Perspectives and challenges in multilayer ceramic capacitors for next generation electronics, *J. Mater. Chem. C.* 7 (2019) 9782–9802. <https://doi.org/10.1039/c9tc02921d>.
- [51] Z. Fan, L. Li, X. Mei, F. Zhao, H. Li, X. Zhuo, X. Zhang, Y. Lu, L. Zhang, M. Liu, Multilayer ceramic film capacitors for high-performance energy storage: progress and outlook, *J. Mater. Chem. A.* 9 (2021) 9462–9480. <https://doi.org/10.1039/d0ta12332c>.
- [52] R. Faye, T. Usui, A. Torello, B. Dkhil, X. Moya, N.D. Mathur, S. Hirose, E. Defay, Heat flow in electrocaloric multilayer capacitors, *J. Alloys Compd.* 834 (2020). <https://doi.org/10.1016/j.jallcom.2020.155042>.
- [53] Y. Liu, B. Dkhil, E. Defay, Spatially Resolved Imaging of Electrocaloric Effect and the Resultant Heat Flux in Multilayer Capacitors, *ACS Energy Lett.* 1 (2016) 521–528. <https://doi.org/10.1021/acsenergylett.6b00232>.
- [54] S. Kar-Narayan, N.D. Mathur, Predicted cooling powers for multilayer capacitors based on various electrocaloric and electrode materials, *Appl. Phys. Lett.* 95, 242903 (2009). <https://doi.org/10.1063/1.3275013>.
- [55] S. Crossley, J.R. McGinnigle, S. Kar-Narayan, N.D. Mathur, Finite-element optimisation of electrocaloric multilayer capacitors, *Appl. Phys. Lett.* 104, 082909 (2014) 18–22. <https://doi.org/10.1063/1.4866256>.
- [56] R. Faye, H. Strozyk, B. Dkhil, E. Defay, Large heat flux in electrocaloric multilayer capacitors, *J. Phys. D: Appl. Phys.* 50, 464002 (2017). <https://doi.org/10.1088/1361-6463/aa8d0f>.
- [57] J. Li, A. Torelló, V. Kovacova, U. Prah, A. Aravindhana, T. Granzow, T. Usui, S. Hirose, E. Defay, High cooling performance in a double-loop electrocaloric heat pump, *Science (80-.)*. 382 (2023) 801–805. <https://doi.org/10.1126/science.adi5477>.
- [58] Q. Zhang, R.W. Whatmore, Sol-gel PZT and Mn-doped PZT thin films for pyroelectric applications, *J. Phys. D: Appl. Phys.* 34 (2001) 2296–2301. <https://doi.org/10.1088/0022-3727/34/15/308>.
- [59] X. Tan, J. Frederick, C. Ma, W. Jo, J. Rödel, Can an electric field induce an antiferroelectric phase out of a ferroelectric phase?, *Phys. Rev. Lett.* 105 (2010) 2–5. <https://doi.org/10.1103/PhysRevLett.105.255702>.
- [60] Z. Xu, Z. Fan, X. Liu, X. Tan, Impact of phase transition sequence on the electrocaloric effect in Pb(Nb,Zr,Sn,Ti)O₃ ceramics, *Appl. Phys. Lett.* 110,

- 082901 (2017). <https://doi.org/10.1063/1.4976827>.
- [61] X. Dai, A. Digiovanni, D. Viehland, Dielectric properties of tetragonal lanthanum modified lead zirconate titanate ceramics, *J. Appl. Phys.* 74 (1993) 3399–3405. <https://doi.org/10.1063/1.354567>.
- [62] G.H. Haertling, *Ferroelectric Ceramics: History and Technology*, *Ferroelectr. Fundam. Collect.* 818 (2007) 157–178. <https://doi.org/10.1002/9783527618002.ch6>.
- [63] T.K. Chin, F.Y. Lee, I.M. McKinley, S. Goljahi, C. Lynch, L. Pilon, Direct thermal to electrical energy conversion using 9.5/65/35 PLZT ceramics in the ergodic relaxor phase, *IEEE Trans. Ultrason. Ferroelectr. Freq. Control.* 59 (2012) 2373–2385. <https://doi.org/10.1109/TUFFC.2012.2470>.
- [64] F.Y. Lee, H.R. Jo, C.S. Lynch, L. Pilon, Pyroelectric energy conversion using PLZT ceramics and the ferroelectric – ergodic relaxor phase transition, *Smart Mater. Struct.* 22, 025038 (2013). <https://doi.org/10.1088/0964-1726/22/2/025038>.
- [65] R. Kandilian, A. Navid, L. Pilon, The pyroelectric energy harvesting capabilities of PMN-PT near the morphotropic phase boundary, *Smart Mater. Struct.* 20, 055020 (2011). <https://doi.org/10.1088/0964-1726/20/5/055020>.
- [66] L. Pilon, I.M. Mckinley, Pyroelectric Energy Conversion, *Annu. Rev. Heat Transf.* (2016) 279–334. <https://doi.org/10.1615/AnnualRevHeatTransfer.2016015566>.
- [67] Z.G. Ye, B. Noheda, M. Dong, D. Cox, G. Shirane, Monoclinic phase in the relaxor-based piezoelectric/ferroelectric $Pb(Mg_{1/3}Nb_{2/3})O_3-PbTiO_3$ system, *Phys Rev B.* 64, 184114 (2001). <https://doi.org/https://doi.org/10.1103/PhysRevB.64.184114>.
- [68] H. Uršič, M. Santo Zarnik, M. Kosec, $Pb(Mg_{1/3}Nb_{2/3})O_3-PbTiO_3$ (PMN-PT) Material for Actuator Applications, *Smart Mater. Res.*, 452901 (2011). <https://doi.org/10.1155/2011/452901>.
- [69] G. Sebald, L. Lebrun, B. Guiffard, D. Guyomar, Morphotropic PMN – PT system investigated by comparison between ceramics and crystal, *J. Eur. Ceram.* 25, (2005) 2509–2513. <https://doi.org/10.1016/j.jeurceramsoc.2005.03.092>.
- [70] M. Davis, D. Damjanovic, N. Setter, Electric-field-, temperature-, and stress-induced phase transitions in relaxor ferroelectric single crystals, *Phys. Rev. B - Condens. Matter Mater. Phys.* 73, 014115 (2006) 1–16. <https://doi.org/10.1103/PhysRevB.73.014115>.
- [71] S. Pandya, J. Wilbur, J. Kim, R. Gao, A. Dasgupta, C. Dames, L.W. Martin, Pyroelectric energy conversion with large energy and power density in relaxor ferroelectric thin films, *Nat. Mater.* 17 (2018) 432–438.

<https://doi.org/10.1038/s41563-018-0059-8>.

- [72] G. Sebald, S. Pruvost, D. Guyomar, Energy harvesting based on Ericsson pyroelectric cycles in a relaxor ferroelectric ceramic, *Smart Mater. Struct.* 17, 015012 (2008). <https://doi.org/10.1088/0964-1726/17/01/015012>.
- [73] I.M. McKinley, R. Kandilian, L. Pilon, Waste heat energy harvesting using the Olsen cycle on 0.945Pb(Zn 1/3Nb 2/3)O 3-0.055PbTiO 3 single crystals, *Smart Mater. Struct.* 21, 035015 (2012). <https://doi.org/10.1088/0964-1726/21/3/035015>.
- [74] J. Kim, S. Yamanaka, I. Murayama, T. Katou, T. Sakamoto, T. Kawasaki, T. Fukuda, T. Sekino, T. Nakayama, M. Takeda, M. Baba, H. Tanaka, K. Aizawa, H. Hashimoto, Y. Kim, Pyroelectric power generation from the waste heat of automotive exhaust gas, *Sustain. Energy Fuels.* 4 (2020) 1143–1149. <https://doi.org/10.1039/c9se00283a>.
- [75] F.Y. Lee, S. Goljahi, I.M. Mckinley, C.S. Lynch, L. Pilon, Pyroelectric waste heat energy harvesting using relaxor ferroelectric 8 / 65 / 35 PLZT and the Olsen cycle, *Smart Mater. Struct.* 21, 025021 (2012). <https://doi.org/10.1088/0964-1726/21/2/025021>.
- [76] A.S. Siao, I.M. McKinley, C.K. Chao, C.C. Hsiao, L. Pilon, Pyroelectric waste heat energy harvesting using the Olsen cycle on Pb(Zr, Ti)O₃-Pb(Ni, Nb)O₃ ceramics, *J. Appl. Phys.* 124, 174104 (2018). <https://doi.org/10.1063/1.5037112>.
- [77] I.M. McKinley, F.Y. Lee, L. Pilon, A novel thermomechanical energy conversion cycle, *Appl. Energy.* 126 (2014) 78–89. <https://doi.org/10.1016/j.apenergy.2014.03.069>.
- [78] B. Fan, G. Yang, M.Y. Li, P. Liu, S. Qiu, M. Shen, H. Liu, G. Zhang, Q. Wang, S. Jiang, Lead-free Ba(1-x)SrxTiO₃ ceramics for room-temperature pyroelectric energy conversion, *Ceram. Int.* 44 (2018) 8270–8276. <https://doi.org/10.1016/j.ceramint.2018.02.009>.
- [79] S. Patel, D. Sharma, A. Singh, R. Vaish, Enhanced thermal energy conversion and dynamic hysteresis behavior of Sr-added Ba_{0.85}Ca_{0.15}Ti_{0.9}Zr_{0.1}O₃ ferroelectric ceramics, *J. Mater.* 2 (2016) 75–86. <https://doi.org/10.1016/j.jmat.2016.01.002>.
- [80] A. Navid, L. Pilon, Pyroelectric energy harvesting using Olsen cycles in purified and porous poly(vinylidene fluoride-trifluoroethylene) [P(VDF-TrFE)] thin films, *Smart Mater. Struct.* 20, 025012 (2011). <https://doi.org/10.1088/0964-1726/20/2/025012>.
- [81] J. Li, A. Torelló, Y. Nouchokgwe, T. Granzow, V. Kovacova, S. Hirose, E. Defay, Electrocaloric effect in BaTiO₃ multilayer capacitors with first-order phase transitions, *J. Phys. Energy.* 2, 024017 (2023). <https://doi.org/10.1088/2515-7655/acc972>

- [82] B. Nair, T. Usui, S. Crossley, S. Kurdi, G.G. Guzmán-Verri, X. Moya, S. Hirose, N.D. Mathur, Large electrocaloric effects in oxide multilayer capacitors over a wide temperature range, *Nature*. 575 (2019) 468–472.
<https://doi.org/10.1038/s41586-019-1634-0>.
- [83] X.S. Qian, H.J. Ye, Y.T. Zhang, H. Gu, X. Li, C.A. Randall, Q.M. Zhang, Giant electrocaloric response over a broad temperature range in modified BaTiO₃ Ceramics, *Adv. Funct. Mater.* 24 (2014) 1300–1305.
<https://doi.org/10.1002/adfm.201302386>.
- [84] H. He, X. Lu, E. Hanc, C. Chen, H. Zhang, L. Lu, Advances in lead-free pyroelectric materials: A comprehensive review, *J. Mater. Chem. C*. 8 (2020) 1494–1516. <https://doi.org/10.1039/c9tc05222d>.
- [85] X.D. Jian, B. Lu, D.D. Li, Y.B. Yao, T. Tao, B. Liang, J.H. Guo, Y.J. Zeng, J. Le Chen, S.G. Lu, Direct Measurement of Large Electrocaloric Effect in Ba(Zr_xTi_{1-x})O₃ Ceramics, *ACS Appl. Mater. Interfaces*. 10 (2018) 4801–4807.
<https://doi.org/10.1021/acsami.7b15933>.
- [86] Z.K. Liu, X. Li, Q.M. Zhang, Maximizing the number of coexisting phases near invariant critical points for giant electrocaloric and electromechanical responses in ferroelectrics, *Appl. Phys. Lett.* 101, 082904 (2012) 8–12.
<https://doi.org/10.1063/1.4747275>.
- [87] G. Dai, S. Wang, G. Huang, G. Chen, B. Lu, D. Li, T. Tao, Y. Yao, B. Liang, S.G. Lu, Direct and indirect measurement of large electrocaloric effect in barium strontium titanate ceramics, *Int. J. Appl. Ceram. Technol.* 17 (2020) 1354–1361.
<https://doi.org/10.1111/ijac.13384>.
- [88] X. Niu, X. Jian, X. Chen, H. Li, W. Liang, Y. Yao, T. Tao, B. Liang, S.G. Lu, Enhanced electrocaloric effect at room temperature in Mn²⁺ doped lead-free (BaSr)TiO₃ ceramics via a direct measurement, *J. Adv. Ceram.* 10 (2021) 482–492. <https://doi.org/10.1007/s40145-020-0450-1>.
- [89] L. Yang, X. Li, E. Allahyarov, P.L. Taylor, Q.M. Zhang, L. Zhu, Novel polymer ferroelectric behavior via crystal isomorphism and the nanoconfinement effect, *Polymer*. 54 (2013) 1709–1728. <https://doi.org/10.1016/j.polymer.2013.01.035>.
- [90] X. Qian, D. Han, L. Zheng, J. Chen, M. Tyagi, Q. Li, F. Du, S. Zheng, X. Huang, S. Zhang, J. Shi, H. Huang, X. Shi, J. Chen, H. Qin, J. Bernholc, X. Chen, L.Q. Chen, L. Hong, Q.M. Zhang, High-entropy polymer produces a giant electrocaloric effect at low fields, *Nature*. 600 (2021) 664–669.
<https://doi.org/10.1038/s41586-021-04189-5>.
- [91] S.G. Lu, B. Rožič, Q.M. Zhang, Z. Kutnjak, R. Pirc, M. Lin, X. Li, L. Gorny, Comparison of directly and indirectly measured electrocaloric effect in relaxor ferroelectric polymers, *Appl. Phys. Lett.* 97, 202901 (2010) 1–4.

<https://doi.org/10.1063/1.3514255>.

- [92] Q.M. Li, X., Qian, X.S., Gu, H., Chen, X., Lu, S.G., Lin, M., Bateman, F., Zhang, Giant electrocaloric effect in ferroelectric poly (vinylidene fluoride-trifluoroethylene) copolymers near a first-order ferroelectric transition., *Appl Phys Lett.* 101, 132903 (2012). <https://doi.org/10.1063/1.4756697>.
- [93] R. Ma, Z. Zhang, K. Tong, D. Huber, R. Kornbluh, Y.S. Ju, Q. Pei, Highly efficient electrocaloric cooling with electrostatic actuation, *Science* (80-.). 357 (2017) 1130–1134. <https://doi.org/10.1126/science.aan5980>.
- [94] Y. Meng, Z. Zhang, H. Wu, R. Wu, J. Wu, H. Wang, Q. Pei, A cascade electrocaloric cooling device for large temperature lift, *Nat. Energy.* 5 (2020) 996–1002. <https://doi.org/10.1038/s41560-020-00715-3>.
- [95] H. Cui, Q. Zhang, Y. Bo, P. Bai, M. Wang, C. Zhang, X. Qian, R. Ma, Flexible microfluidic electrocaloric cooling capillary tube with giant specific device cooling power density, *Joule.* 6 (2022) 258–268. <https://doi.org/10.1016/j.joule.2021.12.010>.
- [96] R.B. Olsen, D.A. Bruno, J.M. Briscoe, E.W. Jacobs, Pyroelectric conversion cycle of vinylidene fluoride-trifluoroethylene copolymer, *J. Appl. Phys.* 57 (1985) 5036–5042. <https://doi.org/10.1063/1.335280>.
- [97] M. Ikura, Ferroelectrics Conversion of Low-Grade Heat to Electricity Using Pyroelectric Copolymer, *Ferroelectrics.* 267 (2010) 403–408. <https://doi.org/10.1080/713715909>.
- [98] L. Kouchachvili, M. Ikura, Improving the efficiency of pyroelectric conversion, (2008) 328–335. <https://doi.org/10.1002/er>.
- [99] R.W. Whatmore, Pyroelectric devices and materials, *Reports Prog. Phys.* 49 (1986) 1335–1386. <https://doi.org/10.1088/0034-4885/49/12/002>.
- [100] G. Sebald, L. Seveyrat, D. Guyomar, L. Lebrun, B. Guiffard, G. Sebald, L. Seveyrat, D. Guyomar, L. Lebrun, B. Guiffard, S. Pruvost, Electrocaloric and pyroelectric properties of 0.75Pb(Mg $_{1/3}$ Nb $_{2/3}$)O $_3$ –0.25PbTiO $_3$ single crystals, *J. Appl. Phys.* 100, 124112 (2006). <https://doi.org/10.1063/1.2407271>.
- [101] C.R. Bowen, J. Taylor, E. Le Boulbar, D. Zabek, V.Y. Topolov, A modified figure of merit for pyroelectric energy harvesting, *Mater. Lett.* 138 (2015) 243–246. <https://doi.org/10.1016/j.matlet.2014.10.004>.
- [102] B. Narayan, Q. Wang, J. Roscow, C. Wan, C. Bowen, New pyroelectric figures of merit for harvesting dynamic temperature fluctuations, *J. Mater. Chem. A.* (2025) 12977–12987. <https://doi.org/10.1039/d5ta00704f>.
- [103] B. Nair, Electrocaloric applications based on multilayer capacitors of PbSc $_{0.5}$ Ta $_{0.5}$ O $_3$, Doctoral dissertation, University of Cambridge, 2020.

- [104] Y. Kim, J. Kim, S. Yamanaka, A. Nakajima, T. Ogawa, T. Serizawa, H. Tanaka, M. Baba, T. Fukuda, K. Yoshii, M. Takeda, N. Yamada, T. Nakayama, K. Niihara, *Renewable Energy: Novel Electrothermodynamic Power Generation*, *Adv. Energy Mater.* 5, 1401942 (2015). <https://doi.org/10.1002/aenm.201570071>.
- [105] M.T. Tachibana M, Bourgès C, *Thermal conductivity of lead zirconate titanate $PbZr_{1-x}Ti_xO_3$* , *Appl. Phys. Express.* 16, 101002 (2023). <https://doi.org/10.35848/1882-0786/ad0359>
- [106] A. Negi, H.P. Kim, Z. Hua, A. Timofeeva, X. Zhang, Y. Zhu, K. Peters, D. Kumah, X. Jiang, J. Liu, *Ferroelectric Domain Wall Engineering Enables Thermal Modulation in PMN – PT Single Crystals*, *Adv. Mater.* 35, 2211286 (2023). <https://doi.org/10.1002/adma.202211286>.
- [107] P. Lhéritier, Y. Nouchokgwe, V. Kovacova, C.H. Hong, À. Torelló, W. Jo, E. Defay, *Measuring lead scandium tantalate phase transition entropy by infrared camera*, *J. Eur. Ceram. Soc.* 41 (2021) 7000–7004. <https://doi.org/10.1016/j.jeurceramsoc.2021.07.002>.
- [108] R. Watton, M.A. Todd, *Induced pyroelectricity in sputtered lead scandium tantalate films and their merit for ir detector arrays*, *Ferroelectrics.* 118 (1991) 279–295. <https://doi.org/10.1080/00150199108014766>.
- [109] Y. He, *Heat capacity, thermal conductivity, and thermal expansion of barium titanate-based ceramics*, *Thermochim. Acta.* 419 (2004) 135–141. <https://doi.org/10.1016/j.tca.2004.02.008>.
- [110] C. Mao, S. Yan, S. Cao, C. Yao, F. Cao, G. Wang, X. Dong, X. Hu, C. Yang, *Effect of grain size on phase transition, dielectric and pyroelectric properties of BST ceramics*, 34 (2014) 2933–2939. <https://doi.org/10.1016/j.jeurceramsoc.2014.04.005>.
- [111] M. Tihtih, J.E.F.M. Ibrahim, M.A. Basyooni, R. En-nadir, W. Belaid, M.M. Abdelfattah, I. Hussainova, G. Pszota, I. Kocserha, *Enhanced optical and thermal conductivity properties of barium titanate ceramic via strontium doping for thermo-optical applications*, *Opt. Quantum Electron.* 55, 226 (2023). <https://doi.org/10.1007/s11082-022-04516-8>.
- [112] C. Mart, S. Abdulazhanov, M. Czernohorsky, T. Kämpfe, D. Lehninger, K. Falidas, S. Eßlinger, K. Kühnel, S. Oehler, M. Rudolph, *Energy harvesting in the back-end of line with CMOS compatible ferroelectric hafnium oxide.*, in: *IEEE Int. Electron Devices Meet.*, (2020) 26.3.1– 26.3.4.
- [113] Y.A. Genenko, J. Glaum, M.J. Hoffmann, K. Albe, *Mechanisms of aging and fatigue in ferroelectrics*, *Mater. Sci. Eng. B.* 192 (2015) 52–82. <https://doi.org/10.1016/j.mseb.2014.10.003>.
- [114] X.J. Lou, *Polarization fatigue in ferroelectric thin films and related materials*, J.

- Appl. Phys. 105, 024101 (2012). <https://doi.org/10.1063/1.3056603>.
- [115] J. Glaum, M. Hoffman, Electric fatigue of lead-free piezoelectric materials, *J. Am. Ceram. Soc.* 97 (2014) 665–680. <https://doi.org/10.1111/jace.12811>.
- [116] R.B. Olsen, D.A. Bruno, J.M. Briscoe, J. Dullea, Cascaded pyroelectric energy converter, *Ferroelectrics*. 59 (1984) 205–219. <https://doi.org/10.1080/00150198408240091>.
- [117] A. Bradeško, L. Fulanović, M. Vrabelj, M. Otoničar, H. Uršič, A. Henriques, C.C. Chung, J.L. Jones, B. Malič, Z. Kutnjak, T. Rojac, Electrocaloric fatigue of lead magnesium niobate mediated by an electric-field-induced phase transformation, *Acta Mater.* 169 (2019) 275–283. <https://doi.org/10.1016/j.actamat.2019.03.017>.
- [118] L. Fulanović, J. Koruza, N. Novak, F. Weyland, B. Malič, V. Bobnar, Fatigueless electrocaloric effect in relaxor $\text{Pb}(\text{Mg}_{1/3}\text{Nb}_{2/3})\text{O}_3$ multilayer elements, *J. Eur. Ceram. Soc.* 37 (2017) 5105–5108. <https://doi.org/10.1016/j.jeurceramsoc.2017.06.011>.
- [119] H. Cao, A.G. Evans, Electric-Field-Induced Fatigue Crack Growth in Piezoelectrics, *J. Am. Ceram. Soc.* 77 (1994) 1783–1786. <https://doi.org/10.1111/j.1151-2916.1994.tb07051.x>.
- [120] S.R. Hoh, Conversion of Thermal to Electrical Energy with Ferroelectric Materials, *Proc. IEEE*. 51 (1963) 838–845. <https://doi.org/10.1109/PROC.1963.2277>.
- [121] R.C. Freiman, S.W., Pohanka, Review of mechanically related failures of ceramic capacitors and capacitor materials., *J Am Ceram Soc.* 72 (1989) 2258–2263. <https://doi.org/10.1111/j.1151-2916.1989.tb06070.x>.
- [122] A. Navid, D. Vanderpool, A. Bah, L. Pilon, Towards optimization of a pyroelectric energy converter for harvesting waste heat, *Int. J. Heat Mass Transf.* 53 (2010) 4060–4070. <https://doi.org/10.1016/j.ijheatmasstransfer.2010.05.025>.
- [123] Gonzalo JA, Ferroelectric materials as energy converters, *Ferroelectrics*. 11 (1976) 423–429. <https://doi.org/https://doi.org/10.1080/00150197608237774>.
- [124] D. Drummond, J.E., Fargo, V., Ream, J., Briscoe, J.M., Brown, Experimental demonstration of heat-to-electricity conversion within a dielectric., in: 14th Intersoc. Energy Convers. Eng. Conf., (1979) 1819-1824.
- [125] H. Nguyen, A. Navid, L. Pilon, Pyroelectric energy converter using copolymer P(VDF-TrFE) and Olsen cycle for waste heat energy harvesting, *Appl. Therm. Eng.* 30 (2010) 2127–2137. <https://doi.org/10.1016/j.applthermaleng.2010.05.022>.

- [126] A. Torelló, P. Lheritier, T. Usui, Y. Nouchokgwe, M. Gérard, O. Bouton, S. Hirose, E. Defay, Giant temperature span in electrocaloric regenerator, *Science* (80-.). 370 (2020) 125–129. <https://doi.org/10.1126/science.abb8045>.
- [127] L.M. Maier, P. Corhan, A. Barcza, H.A. Vieyra, C. Vogel, J.D. Koenig, O. Schäfer-Welsen, J. Wöllenstein, K. Bartholomé, Active magnetocaloric heat pipes provide enhanced specific power of caloric refrigeration, *Commun. Phys.* 3 (2020) 1–6. <https://doi.org/10.1038/s42005-020-00450-x>.
- [128] K. Klinar, T. Swoboda, M. Muñoz Rojo, A. Kitanovski, Fluidic and Mechanical Thermal Control Devices, *Adv. Electron. Mater.* 7, 2000623 (2021). <https://doi.org/10.1002/aelm.202000623>.
- [129] T. Swoboda, K. Klinar, A.S. Yalamarthy, A. Kitanovski, M. Muñoz Rojo, Solid-State Thermal Control Devices, *Adv. Electron. Mater.* 7, 2000625 (2021). <https://doi.org/10.1002/aelm.202000625>.
- [130] G. Wehmeyer, T. Yabuki, C. Monachon, J. Wu, C. Dames, Thermal diodes, regulators, and switches: Physical mechanisms and potential applications, *Appl. Phys. Rev.* 4, 041304 (2017). <https://doi.org/10.1063/1.5001072>.
- [131] R.I. Epstein, K.J. Malloy, Electrocaloric devices based on thin-film heat switches, *J. Appl. Phys.* 106, 064509 (2009) 1–8. <https://doi.org/10.1063/1.3190559>.
- [132] Y. Jia, Y. Sungtaek Ju, A solid-state refrigerator based on the electrocaloric effect, *Appl. Phys. Lett.* 100, 242901 (2012). <https://doi.org/10.1063/1.4729038>.
- [133] G. Cha, Y.S. Ju, Pyroelectric energy harvesting using liquid-based switchable thermal interfaces, *Sensors Actuators, A Phys.* 189 (2013) 100–107. <https://doi.org/10.1016/j.sna.2012.09.019>.
- [134] E. Defay, R. Faye, G. Despesse, H. Strozyk, D. Sette, S. Crossley, X. Moya, N.D. Mathur, Enhanced electrocaloric efficiency via energy recovery, *Nat. Commun.* 9, 1827 (2018). <https://doi.org/10.1038/s41467-018-04027-9>.
- [135] Y. Meng, Z. Zhang, H. Wu, R. Wu, J. Wu, H. Wang, Q. Pei, A cascade electrocaloric cooling device for large temperature lift, *Nat. Energy.* 5 (2020) 996–1002. <https://doi.org/10.1038/s41560-020-00715-3>.
- [136] D.E. Schwartz, Thermodynamic cycles and electrical charge recovery in high-efficiency electrocaloric cooling systems, *Int. J. Refrig.* 131 (2021) 970–979. <https://doi.org/10.1016/j.ijrefrig.2021.02.003>.
- [137] S. Mönch, R. Reiner, P. Waltereit, M. Basler, R. Quay, S. Gebhardt, C. Molin, D. Bach, R. Binniger, K. Bartholomé, How highly efficient power electronics transfers high electrocaloric material performance to heat pump systems, *MRS Adv.* 8 (2023) 787–796. <https://doi.org/10.1557/s43580-023-00670-7>.

- [138] S. Monch, R. Reiner, K. Mansour, P. Waltereit, M. Basler, R. Quay, C. Molin, S. Gebhardt, D. Bach, R. Binniger, K. Bartholome, A 99.74% Efficient Capacitor-Charging Converter Using Partial Power Processing for Electrocalorics, *IEEE J. Emerg. Sel. Top. Power Electron.* 11 (2023) 4491–4507. <https://doi.org/10.1109/JESTPE.2023.3270375>.
- [139] S. Moench, R. Reiner, P. Waltereit, C. Molin, S. Gebhardt, D. Bach, R. Binniger, K. Bartholome, Enhancing Electrocaloric Heat Pump Performance by Over 99% Efficient Power Converters and Offset Fields, *IEEE Access.* 10 (2022) 46571–46588. <https://doi.org/10.1109/ACCESS.2022.3170451>.
- [140] C.G.F. Stenger, F.L. Scholten, A.J. Burggraaf, Ordering and diffuse phase transitions in Pb (Sc_{0.5}Ta_{0.5})O₃ ceramics, *Solid State Commun.* 32 (1979) 989–992. [https://doi.org/10.1016/0038-1098\(79\)90812-3](https://doi.org/10.1016/0038-1098(79)90812-3).
- [141] H.C. Wang, W.A. Schulze, Order-Disorder Phenomenon in Lead Scandium Tantalate, *J. Am. Ceram. Soc.* 73 (1990) 1228–1234. <https://doi.org/10.1111/j.1151-2916.1990.tb05184.x>.
- [142] F. Chu, G.R. Fox, N. Setter, Dielectric properties of complex perovskite lead scandium tantalate under dc bias, *J. Am. Ceram. Soc.* 81 (1998) 1577–1582. <https://doi.org/10.1111/j.1151-2916.1998.tb02519.x>.
- [143] F. Chu, N. Setter, A.K. Tagantsev, The spontaneous relaxor-ferroelectric transition of Pb(Sc_{0.5}Ta_{0.5})O₃, *J. Appl. Phys.* 74 (1993) 5129–5134. <https://doi.org/10.1063/1.354300>.
- [144] K. Brinkman, Y. Wang, D. Su, A. Tagantsev, P. Muralt, N. Setter, The Impact of chemical ordering on the dielectric properties of lead scandium tantalate Pb (Sc₁₂Ta₁₂)O₃ thin films, *J. Appl. Phys.* 102, 044110 (2007). <https://doi.org/10.1063/1.2770834>.
- [145] N.M. Shorrocks, R.W. Whatmore, P.C. Osbond, Ferroelectrics Lead scandium tantalate for thermal detector applications, *Ferroelectrics.* 106 (2011) 387–392. <https://doi.org/10.1080/00150199008214614>.
- [146] W. Liu, G. Wang, S. Cao, C. Mao, F. Cao, X. Dong, The effect of excess PbO on dielectric and pyroelectric properties of lead scandium tantalate ceramics, *J. Am. Ceram. Soc.* 93 (2010) 2735–2742. <https://doi.org/10.1111/j.1551-2916.2010.03767.x>.
- [147] L. Shebanov, K. Borman, On lead-scandium tantalate solid solutions with high electrocaloric effect, *Ferroelectrics.* 127 (1992) 143–148. <https://doi.org/10.1080/00150199208223361>.
- [148] L.A. Shebanov, E. Birks, K.J. Borman, X-ray studies of electrocaloric lead-scandium tantalate ordered solid solutions, *Ferroelectrics.* 90 (1989) 165–172. <https://doi.org/10.1080/00150198908211286>.

- [149] L. Shebanovs, A. Sternberg, W.N. Lawless, K. Borman, Isomorphous ion substitutions and order-disorder phenomena in highly electrocaloric lead-scandium tantalate solid solutions, *Ferroelectrics*. 184 (1996) 239–242. <https://doi.org/10.1080/00150199608230266>.
- [150] A. Sternberg, L. Shebanovs, E. Birks, M. Ozolinsh, Structure ordering effects in lead containing ceramic perovskites, *J. Korean Phys. Soc.* 32, S981 (1998).
- [151] Y. Nouchokgwe, P. Lheritier, C.H. Hong, A. Torelló, R. Faye, W. Jo, C.R.H. Bahl, E. Defay, Giant electrocaloric materials energy efficiency in highly ordered lead scandium tantalate, *Nat. Commun.* 12, 3298 (2021) 1–21. <https://doi.org/10.1038/s41467-021-23354-y>.
- [152] A. Aravindhan, S. Glinsek, S. Girod, A.B. Martinez, T. Granzow, V. Kovacova, E. Defay, Large pyroelectric energy conversion in lead scandium tantalate thin films, *Heliyon*. 10 (9), e30430 (2024). <https://doi.org/10.1016/j.heliyon.2024.e30430>.
- [153] C.G.F. Stenger, A.J. Burggraaf, Order–disorder reactions in the ferroelectric perovskites $\text{Pb}(\text{Sc}_{1/2}\text{Nb}_{1/2})\text{O}_3$ and $\text{Pb}(\text{Sc}_{1/2}\text{Ta}_{1/2})\text{O}_3$. II. Relation between ordering and properties, *Phys. Status Solidi*. 61 (1980) 653–664. <https://doi.org/10.1002/pssa.2210610240>.
- [154] N. Setter, L.E. Cross, The role of B-site cation disorder in diffuse phase transition behavior of perovskite ferroelectrics, *J. Appl. Phys.* 51 (1980) 4356–4360. <https://doi.org/10.1063/1.328296>.
- [155] I.M. Reaney, D.J. Barber, Transmission electron microscopy of lead scandium tantalate thin-films, *J. Microsc.* 160 (1990) 213–224. <https://doi.org/10.1111/j.1365-2818.1990.tb03059.x>.
- [156] B. Mihailova, M. Bastjan, B. Schulz, M. Rübhausen, M. Gospodinov, R. Stosch, B. Güttler, T. Malcherek, U. Bismayer, Resonance Raman scattering of relaxors $\text{PbSc}_{0.5}\text{Ta}_{0.5}\text{O}_3$ and $\text{PbSc}_{0.5}\text{Nb}_{0.5}\text{O}_3$, *Appl. Phys. Lett.* 90 (2007) 88–91. <https://doi.org/10.1063/1.2433763>.
- [157] N. Setter, L.E. Cross, The contribution of structural disorder to diffuse phase transitions in ferroelectrics, *J. Mater. Sci.* 15 (1980) 2478–2482. <https://doi.org/10.1007/BF00550750>.
- [158] W. Liu, G. Wang, S. Cao, C. Mao, X. Dong, Structural, dielectric, and pyroelectric properties of $(1-x)\text{PbSc}_{0.5}\text{Ta}_{0.5}\text{O}_3$ - $(x)\text{PbHfO}_3$ ceramics, *J. Am. Ceram. Soc.* 93 (2010) 3023–3026. <https://doi.org/10.1111/j.1551-2916.2010.03996.x>.
- [159] A. Patel, N. Shorrocks, R. Whatmore, Tfp258. Physicochemical properties of sol-gel derived lead scandium tantalate $\text{Pb}(\text{Sc}_{0.5}\text{Ta}_{0.5})\text{O}_3$ thin films, *Ferroelectrics*. 134 (1992) 343–348. <https://doi.org/10.1080/00150199208015610>.

- [160] L. Donhang, M. Linqing, D.A. Payne, D.D. Viehland, Sol-gel synthesis of $\text{Pb}(\text{Sc}_{0.5}\text{Ta}_{0.5})\text{O}_3$ powders and thin layers, *Mater. Lett.* 17 (1993) 319–322. [https://doi.org/10.1016/0167-577X\(93\)90022-P](https://doi.org/10.1016/0167-577X(93)90022-P).
- [161] R.W. Whatmore, A. Patel, N.M. Shorrocks, F.W. Ainger, Ferroelectric Materials For Thermal IR Sensors State-Of-The-Art And Perspectives, *Ferroelectrics*. 104 (1990) 269–283. <https://doi.org/10.1080/00150199008223829>.
- [162] T. Takeishi, R.W. Whatmore, Low temperature sol gel deposition of PST ($\text{Pb}(\text{Sc}_{0.5}\text{Ta}_{0.5})\text{O}_3$) thin films, *Ferroelectrics*. 228 (1999) 53–60. <https://doi.org/10.1080/00150199908226125>.
- [163] J. Battat, Z. Huang, P.P. Donohue, M.A. Todd, R.W. Whatmore, Kinetics of phase transformations in lead scandium tantalate thin films, *Integr. Ferroelectr.* 60 (2004) 87–94. <https://doi.org/10.1080/10584580490441692>.
- [164] Z. Huang, P.P. Donohue, Q. Zhang, D.J. Williams, C.J. Anthony, R.W. Whatmore, M.A. Todd, Comparative microstructure and electrical property studies of lead scandium tantalate thin films as prepared by LDCVD, sol-gel and sputtering techniques, *J. Phys. D. Appl. Phys.* 36 (2003) 270–279. <https://doi.org/10.1088/0022-3727/36/3/309>.
- [165] K. Momma, F. Izumi, VESTA 3 for three-dimensional visualization of crystal, volumetric and morphology data, *J. Appl. Crystallogr.* 44 (2011) 1272–1276. <https://doi.org/10.1107/S0021889811038970>.
- [166] K. Brinkman, Positional Order in Lead Scandium Tantalate (PST) as a "tool" for the Investigation of Relaxor Ferroelectric Behavior in Thin Films, Doctoral dissertation, École Polytechnique Fédérale de Lausanne, (2004).
- [167] K. Brinkman, Y. Wang, D. Su, A. Tagantsev, P. Muralt, N. Setter, K. Brinkman, Y. Wang, D. Su, A. Tagantsev, P. Muralt, N. Setter, The Impact of chemical ordering on the dielectric properties of lead scandium tantalate $\text{Pb}(\text{Sc}_{1/2}\text{Ta}_{1/2})\text{O}_3$ thin films, *J. Appl. Phys.* 102, 044110 (2013). <https://doi.org/10.1063/1.2770834>.
- [168] K. Brinkman, A. Tagantsev, V. Cherman, Y. Wang, N. Setter, S. Kamba, J. Petzelt, Peculiar features of the dielectric response in lead scandium tantalate $\text{Pb}(\text{Sc}_{1/2}\text{Ta}_{1/2})\text{O}_3$ thin films, *MRS. Proc.* 966, 0966-T07-37 (2006). <https://doi.org/10.1557/proc-0966-t07-37>.
- [169] T.M. Correia, S. Kar-Narayan, J.S. Young, J.F. Scott, N.D. Mathur, R.W. Whatmore, Q. Zhang, PST thin films for electrocaloric coolers, *J. Phys. D. Appl. Phys.* 44, 165407 (2011). <https://doi.org/10.1088/0022-3727/44/16/165407>.
- [170] V. Kovacova, S. Glinsek, S. Girod, E. Defay, High Electrocaloric Effect in Lead Scandium Tantalate Thin Films with Interdigitated Electrodes, *Sensors*. 22, 4049 (2022). <https://doi.org/10.3390/s22114049>.

- [171] K. Brinkman, Y. Wang, M. Cantoni, D. Su, N. Setter, P.K. Petrov, Processing and properties of ferroelectric relaxor lead scandium tantalate $\text{Pb}(\text{Sc}_{1/2}\text{Ta}_{1/2})\text{O}_3$ thin films, *J. Mater. Res.* 22 (2007) 217–232. <https://doi.org/10.1557/jmr.2007.0023>.
- [172] N. Godard, P. Grysan, E. Defay, S. Glinšek, Growth of {100}-oriented lead zirconate titanate thin films mediated by a safe solvent, *J. Mater. Chem. C* 9 (2021) 281–287. <https://doi.org/10.1039/d0tc04066e>.
- [173] K. Brinkman, A. Tagantsev, V. Cherman, Y. Wang, N. Setter, S. Kamba, J. Petzelt, Peculiar features of the dielectric response in lead scandium tantalate $\text{Pb}(\text{SC}_{1/2}\text{Ta}_{1/2})\text{O}_3$ thin films, *MRS. Proc.* 966, 0966-T07-37 (2006). <https://doi.org/10.1557/proc-0966-t07-37>.
- [174] Z. Liu, T. Lu, S. Yan, Q. Liao, X. Dong, G. Wang, Y. Liu, Large electrocaloric and pyroelectric energy harvesting effect over a broad temperature range via modulating the relaxor behavior in non-relaxor, *J. Mater. Chem. A* 9 (2021) 22015–22024. <https://doi.org/10.1039/d1ta03894j>.
- [175] X. Wang, X. Hao, Q. Zhang, S. An, X. Chou, Energy-storage performance and pyroelectric energy harvesting effect of PNZST antiferroelectric thin films, *J. Mater. Sci.: Mater. Electron.* 28 (2017) 1438–1448. <https://doi.org/10.1007/s10854-016-5679-7>.
- [176] S.A. Xihong Hao, Ye Zhao, Giant Thermal–Electrical Energy Harvesting Effect of $\text{Pb}_{0.97}\text{La}_{0.02}(\text{Zr}_{0.75}\text{Sn}_{0.18}\text{Ti}_{0.07})\text{O}_3$ Antiferroelectric Thick Film, *J. Am. Ceram. Soc.* 98 (2015) 361–365. <https://doi.org/https://doi.org/10.1111/jace.13387>.
- [177] L. Shebanovs, K. Borman, W.N. Lawless, A. Kalvane, Electrocaloric Effect in Some Perovskite Ferroelectric Ceramics and Multilayer Capacitors, *Ferroelectrics*. 273 (2002) 37–41. <https://doi.org/10.1080/00150190211761>.
- [178] J.R. Giniewicz, A.S. Bhalla, L.E. Cross, An investigation of the structural and dielectric properties of the solid solution system $(1-x)\text{Pb}(\text{Sc}_{1/2}\text{Ta}_{1/2})\text{O}_3-(x)\text{PbTiO}_3$, *Ferroelectr. Lett. Sect.* 12 (1990) 37–41. <https://doi.org/10.1080/07315179008200855>.
- [179] J.R. Giniewicz, A.S. Bhalla, L.E. Cross, Variable structural ordering in lead scandium tantalate-lead titanate materials, *Ferroelectrics*. 211 (1998) 281–297. <https://doi.org/10.1080/00150199808232349>.
- [180] C.H. Lin, P.A. Friddle, C.H. Ma, H. Chen, Effect of composition and growth temperature on the dielectric properties of $\text{Pb}(\text{ScTa})_{1-x}\text{Ti}_x\text{O}_3$ (PSTT) thin films grown by MOCVD, *Ferroelectrics*. 259 (2001) 229–238. <https://doi.org/10.1080/00150190108008743>.
- [181] J.R. Giniewicz, A.S. Bhalla, L.E. Cross, Identification of the morphotropic

- phase boundary in the lead scandium tantalate-lead titanate solid solution system, *J. Mater. Sci.* 32 (1997) 2249–2253.
<https://doi.org/10.1023/A:1018516031468>.
- [182] J.R. Giniewicz, A.S. Bhalla, L.E. Cross, An investigation of the structural and dielectric properties of the solid solution system $(1-x)$ Pb(Sci/2Tal/2)O₃-(x) PbTiO₃, *Ferroelectr. Lett. Sect.* 12 (1990) 35–42.
<https://doi.org/10.1080/07315179008200855>.
- [183] A.I. Frenkel, D.M. Pease, J. Giniewicz, E.A. Stern, D.L. Brewster, M. Daniel, J. Budnick, Concentration-dependent short-range order in the relaxor ferroelectric $(1-x)$ Pb(Sc,Ta)O₃-xPbTiO₃, *Phys. Rev. B - Condens. Matter Mater. Phys.* 70, 014106 (2004). <https://doi.org/10.1103/PhysRevB.70.014106>.
- [184] K. Uchino, S. Nomura, Critical Exponents Of The Dielectric Constants In Diffused- Phase-Transition Crystals, *Ferroelectrics.* 44 (1982) 55–61.
<https://doi.org/10.1080/00150198208260644>.
- [185] S. Pandya, J.D. Wilbur, B. Bhatia, A.R. Damodaran, C. Monachon, A. Dasgupta, W.P. King, C. Dames, L.W. Martin, Direct Measurement of Pyroelectric and Electrocaloric Effects in Thin Films, *Phys. Rev. Appl.* 7, 034025 (2017) 1–13. <https://doi.org/10.1103/PhysRevApplied.7.034025>.
- [186] Y. Nouchokgwe, N.S. Fedorova, P. Biswas, I. Gorican, S. Drmovsek, B. Mukherjee, U. Prah, Stable antiferroelectric phase in calcium-doped lead scandium tantalate, arXiv preprint arXiv:2502.02402. (2025) 1–36.
<https://doi.org/https://doi.org/10.48550/arXiv.2502.02402>.
- [187] B. Nair, T. Usui, S. Crossley, S. Kurdi, G.G. Guzmán-Verri, X. Moya, S. Hirose, N.D. Mathur, Large electrocaloric effects in oxide multilayer capacitors over a wide temperature range, *Nature.* 575 (2019) 468–472.
<https://doi.org/10.1038/s41586-019-1634-0>.
- [188] Y. Nouchokgwe, P. Lheritier, T. Usui, A. Torello, A. El Moul, V. Kovacova, T. Granzow, S. Hirose, E. Defay, Materials efficiency of electrocaloric lead scandium tantalate multilayer capacitors, *Scr. Mater.* 219 (2022) 114873.
<https://doi.org/10.1016/j.scriptamat.2022.114873>.
- [189] T. Hess, L.M. Maier, N. Bachmann, P. Corhan, O. Schäfer-Welsen, J. Wöllenstein, K. Bartholomé, Thermal hysteresis and its impact on the efficiency of first-order caloric materials, *J. Appl. Phys.* 127, 075103 (2020).
<https://doi.org/10.1063/1.5132897>.
- [190] Z. Li, H.H. Wu, J. Li, S. Wang, S. Qin, J. He, C. Liu, Y. Su, L. Qiao, T. Lookman, Y. Bai, Effects of thermal and electrical hysteresis on phase transitions and electrocaloric effect in ferroelectrics: A computational study, *Acta Mater.* 228 (2022) 117784. <https://doi.org/10.1016/j.actamat.2022.117784>.

- [191] Y. Nouchokgwe, P. Lheritier, T. Usui, A. Torello, A. El Moul, V. Kovacova, T. Granzow, S. Hirose, E. Defay, Materials efficiency of electrocaloric lead scandium tantalate multilayer capacitors, *Scr. Mater.* 219 (2022) 114873. <https://doi.org/10.1016/j.scriptamat.2022.114873>.
- [192] Y. Liu, J.F. Scott, B. Dkhil, Direct and indirect measurements on electrocaloric effect: Recent developments and perspectives, *Appl. Phys. Rev.* 3, 031102 (2016). <https://doi.org/10.1063/1.4958327>.
- [193] Y. Liu, H. Strozyk, B. Dkhil, E. Defay, Insight into electrocaloric cooling power in multilayer capacitors using infra-red camera, *Appl. Phys. Lett.* 109, 212902 (2016). <https://doi.org/10.1063/1.4968581>.
- [194] F.P. Incropera, D.P. DeWitt, T.L. Bergman, A.S. Lavine, *Fundamentals of heat and mass transfer*, Sixth Edition, John Wiley & Sons, (1996). https://doi.org/10.1007/978-3-031-28920-0_19.
- [195] A. Torelló Massana, *Electrocaloric coolers and pyroelectric energy harvesters based on multilayer capacitors of Pb(Sc_{0.5}Ta_{0.5})O₃*, Doctoral dissertation, University of Luxembourg, (2022).
- [196] S. Pandya, G. Velarde, L. Zhang, J.D. Wilbur, A. Smith, B. Hanrahan, C. Dames, L.W. Martin, New approach to waste-heat energy harvesting: pyroelectric energy conversion, *NPG Asia Mater.* 11, 26 (2019). <https://doi.org/10.1038/s41427-019-0125-y>.
- [197] G. Sebald, S. Pruvost, D. Guyomar, *Energy Harvesting from Temperature : Use of Pyroelectric and Electrocaloric Properties*, in *Electrocaloric Materials*, Springer, Berlin, Heidelberg (2014) 225–249. <https://doi.org/10.1007/978-3-642-40264-7>.
- [198] G. Yugandhar, G. Venkateswara Rao, K. Srinivasa Rao, Modeling and Simulation of Piezoelectric MEMS Sensor, *Mater. Today Proc.* 2 (2015) 1595–1602. <https://doi.org/10.1016/j.matpr.2015.07.086>.
- [199] S. Glinsek, L. Song, M. Gerard, O. Bouton, S. Girod, M. El Hachemi, B. Mandal, E. Defay, T. Granzow, J. Polesel-Maris, Autonomous low-energy communication module based on inkjet-printed transparent antenna, *Cell Reports Phys. Sci.* 4 (2023). <https://doi.org/10.1016/j.xcrp.2023.101685>.
- [200] N. Bassiri-Gharb, Y. Bastani, A. Bernal, Chemical solution growth of ferroelectric oxide thin films and nanostructures, *Chem. Soc. Rev.* 43 (2014) 2125–2140. <https://doi.org/10.1039/c3cs60250h>.
- [201] R. Schwartz, T. Schneller, R. Waser, H. Dobberstein, *Chemical solution deposition of ferroelectric thin films*, *Chem. Process. Ceram.* Second Ed. 4756 (2005) 713–742. <https://doi.org/10.1201/9781420027334.ch27>.

- [202] N. Godard, Inkjet-printed piezoelectric films for transducers, Doctoral dissertation, University of Luxembourg, (2020).
- [203] R.W. Schwartz, T. Schneller, R. Waser, Chemical solution deposition of electronic oxide films, *Comptes Rendus Chim.* 7 (2004) 433–461. <https://doi.org/10.1016/j.crci.2004.01.007>.
- [204] K. Brinkman, Y. Wang, M. Cantoni, D. Su, N. Setter, P.K. Petrov, Processing and properties of ferroelectric relaxor lead scandium tantalate $\text{Pb}(\text{Sc}_{1/2}\text{Ta}_{1/2})\text{O}_3$ thin films, *J. Mater. Res.* 22 (2007) 217–232. <https://doi.org/10.1557/jmr.2007.0023>.
- [205] G.F. Harrington, J. Santiso, Back-to-Basics tutorial: X - ray diffraction of thin films, *J. Electroceram.* 47 (2021) 141–163. <https://doi.org/10.1007/s10832-021-00263-6>.
- [206] V. Kovacova, S. Glinsek, S. Girod, E. Defay, High Electrocaloric Effect in Lead Scandium Tantalate Thin Films with Interdigitated Electrodes, *Sensors.* 22, 4049 (2022). <https://doi.org/10.3390/s22114049>.
- [207] V. Shabadi, M. Major, P. Komissinskiy, M. Vafae, A. Radetinac, M. Baghaie Yazdi, W. Donner, L. Alff, Origin of superstructures in (double) perovskite thin films, *J. Appl. Phys.* 116, 114901 (2014). <https://doi.org/10.1063/1.4895636>.
- [208] W. Zhou, R. Apkarian, Z.L. Wang, D. Joy, Fundamentals of scanning electron microscopy (SEM), *Scanning Microsc. Nanotechnol. Tech. Appl.* (2007) 1–40. https://doi.org/10.1007/978-0-387-39620-0_1.
- [209] R. Nigon, T.M. Raeder, P. Muralt, Characterization methodology for lead zirconate titanate thin films with interdigitated electrode structures, *J. Appl. Phys.* 121 (2017) 0–12. <https://doi.org/10.1063/1.4983772>.
- [210] A.B. Martínez, Photoferroelectric Effects in Polycrystalline Bismuth Ferrite Doctoral dissertation, University of Luxembourg, (2023).
- [211] R. Nigon, Internal electric fields and electrode effects in ferroelectric thin films for piezoelectric energy harvesting, Doctoral dissertation, École Polytechnique Fédérale de Lausanne, (2017).
- [212] C. Meola, G.M. Carlomagno, Recent advances in the use of infrared thermography, *Meas. Sci. Technol.* 15 (2004). <https://doi.org/10.1088/0957-0233/15/9/R01>.
- [213] Y. Nouchokgwe, Scale law on energy efficiency of electrocaloric materials, Doctoral dissertation, University of Luxembourg, (2022).
- [214] A.N. Smith, B.M. Hanrahan, Cascaded pyroelectric conversion: Optimizing the ferroelectric phase transition and electrical losses, *J. Appl. Phys.* 128, 024103 (2020). <https://doi.org/10.1063/5.0003301>.

- [215] Y. Xu, *Ferroelectric Materials and their Applications*, Elsevier, 1991.
- [216] Y.A. Cengel, M.A. Boles, M. Kanoğlu, *Thermodynamics: an engineering approach*, McGraw-hill, New York (2011).